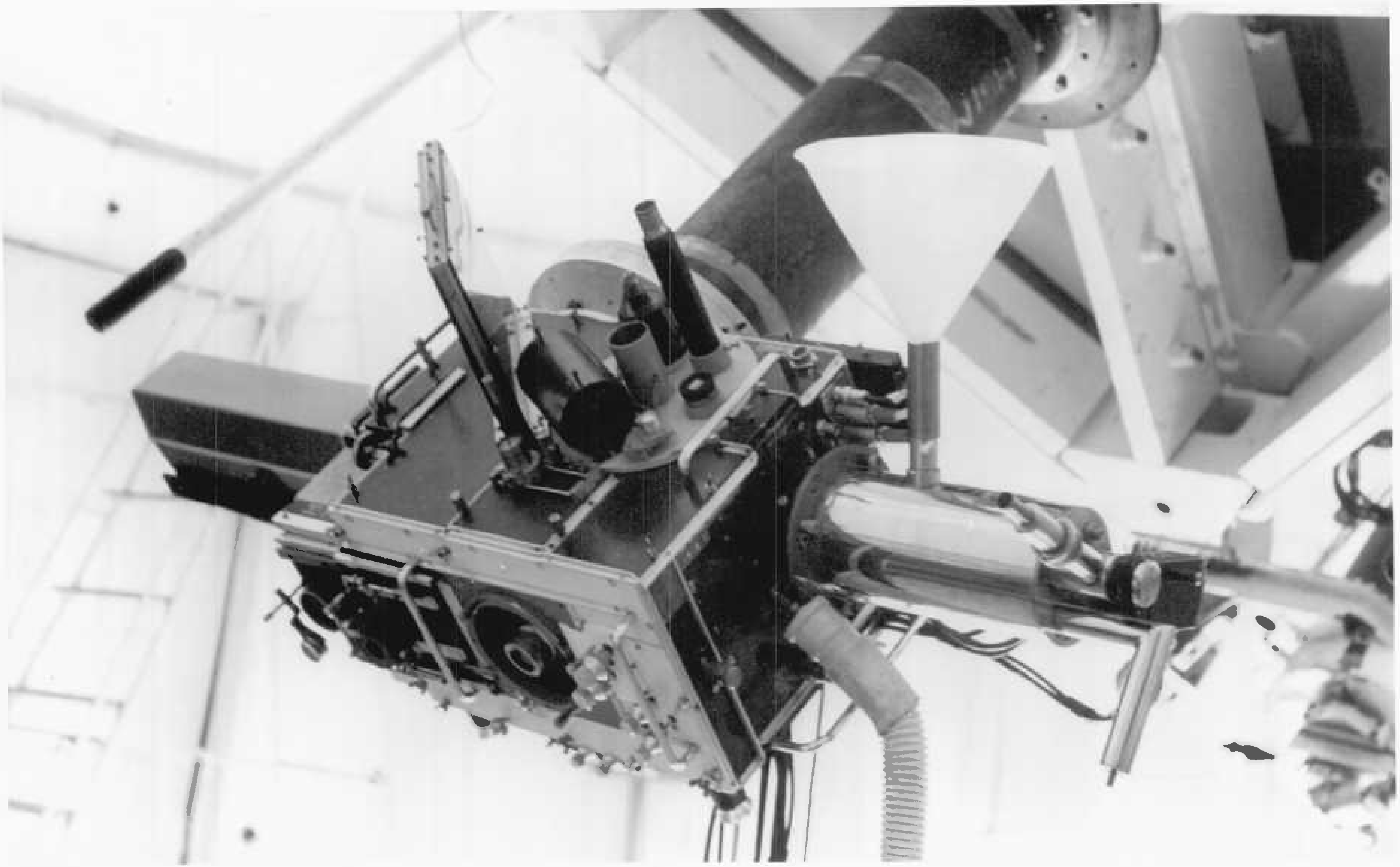

P9.1

GENERAL VIEW OF THE WIDE FIELD INFRARED PHOTOMETER (IRIS) AT THE F/12.8 FOCUS OF THE TENERIFE 60" FLUX COLLECTOR

A WIDE FIELD NEAR-INFRARED PHOTOMETER

by

Christopher James Baddiley, B.Sc.

October 1975

A thesis submitted for the degree of Doctor of Philosophy of the University of London and for the Diploma of Imperial College.

Astronomy Group
Physics Department
Imperial College
London S.W.7.

SYNOPSIS

This thesis concerns the development of a wide-field infrared photometer. The photometer was first designed as a broad-band radiometer for use as a reference channel of a field-compensated Michelson interferometer, but later evolved as a separate survey instrument for the detection of nebulae, globular clusters, comets and other extended astronomical infrared sources.

Details are given for a Moiré grid modulation system designed for intensity modulating a 25mm diameter optical beam at 400Hz, and an alternate disc-chopping system. Two pivoted-mirror, sky-scanning systems are also described; one involving the parallel-pivoted motion of two linked diagonal flats, and the other involving a twin spherical mirror arrangement. The latter system is capable of sky-comparison on a telescope with good definition, a 25mm field, and 25mm throw at frequencies up to 50Hz. A capacitance position-detection system and servo control used to control the mirror-scan square wave motion is also described. A semi-empirical relation for PbS detector and bias network optimisation is also developed and verified.

Astronomical observational data is given as obtained with this wide-field infrared photometer, including successful detection of a comet, nebulae and many globular clusters at λ 1.65μ and λ 2.2μ. Some possible astronomical applications and research topics are also discussed.

Acknowledgements

This thesis, described in the synopsis, was carried out over a six year period, during the first three of which (October 1969 to October 1972), the author was supported by an S.R.C. postgraduate research studentship while with the Astronomy group at Imperial College, London. The author continued the project on an out-of-hours basis from October 1973 to November 1975 while employed as an S.R.C. research fellow at the Royal Observatory Edinburgh and project officer for the A.A.T. Multi-Object Spectrograph project. The project remained supported by I.C. during this period, while the observing trip on the Tenerife 60" flux collector was sponsored by R.O.E., to whom the author wishes to convey his thanks.

The instruments described in this thesis were entirely designed by the author, and in the case of the sky-scanning photometer of chapter 5 and all chapters thereafter, the author carried out all the machining, soldering and construction.

The author wishes to acknowledge thanks to Professor J Ring for his continued support and advice, and also to Professor V C Reddish, for his help and encouragement, as well as to many others for their advice or occasional helping hand.

Submitted for examination for degree of PhD in Astronomy, and D.I.C., at Imperial College, London.

October 1975

C J Baddiley

R.O.E. Oct. 1975

CONTENTS:

CHAPTER 1

1. Astronomical extended sources of near infrared radiation; some observing techniques; a Mock interferometer; and the development of a field compensated Michelson Interferometer.

Contents:

ASTRONOMICAL EXTENDED SOURCES OF NEAR INFRARED RADIATION; SOME OBSERVING TECHNIQUES; A MOCK INTERFEROMETER; AND THE DEVELOPMENT OF A FIELD-COMPENSATED MICHELSON INTERFEROMETER

1.01 Introduction

This thesis mostly concerns the development of a wide-field near-infrared photometer but this chapter concerns the work carried out leading to its development, starting with observations of λ 0.6 μ spectra of diffuse nebulae with a Mock Interferometer (a modified 3m. Ebert spectrometer), and concurrently the development of a field compensated Michelson interferometer (F.C.M.I.) for continuation of the observed spectrum up to about λ 2 μ. Extended sources of infrared radiation are discussed together with their mechanisms and some observing techniques, but no detailed historical account of the subject of interferometry or related infrared astronomy is given, as the author considers this thesis long enough without it; an extensive background reading list is given at the end of this chapter.

1.02 Some problems of observing astronomical spectra in the infrared

Photomultipliers are limited in wavelength response to around λ 0.95 μ by the available energy potential of photocathode materials. Some extended S20 photocathodes may reach λ 1.0 μ but these are not commercially available. Semi-conductor radiation-sensitive devices have energy gaps corresponding to maximum sensitivity ranging from λ 1 μ for lead sulphide to λ 10μ for indium antimonide. All such semiconductor devices are very inefficient as compared with photomultipliers, although their sensitivities increase considerably on cooling.

Atmospheric emission, as given by a room temperature black body from graph F1.01, is well below the detection limit for a photomultiplier, see graph F1.02, but increases expontentially with wavelength in the near infrared to reach a peak near λ 10μ; this emission may be detected with a modest infrared detector at around λ 1.3μ and is shown by the curve of F1.03. At this wavelength, the air becomes effectively opaque, and an infrared detector will show rapid fluctuations in emission from small percentage temperature irregularities (see curves F1.03) (R1.05, R1.06). The curves F1.03 were plotted from the black body radiation function, and were later experimentally verified (see chapter 4). The principal atmospheric non-thermal emission component is produced by OH radical vibration bands, originating from the reaction $H + O_3 \rightarrow OH^* + O_2$, $OH + O \rightarrow H + O_2$; the OH transition (see table T1.1, Pardy R1.01) and resultant combined emission is shown in F1.04 together with the atmospheric abundances in F1.05. The airglow emission bands do not occur at certain wavelengths, leaving optical windows at λ 1.3μ, λ 1.65μ, λ 2.2μ, λ 5μ etc. (see F1.06).

The near infrared atmospheric sources have been studied by D. Pardy and others, see references R1.01 to R1.04, mostly with the aid of balloon born interferometers. A summary of the airglow emission bands is plotted in figures F1.02 and F1.03. The optical windows allow observation

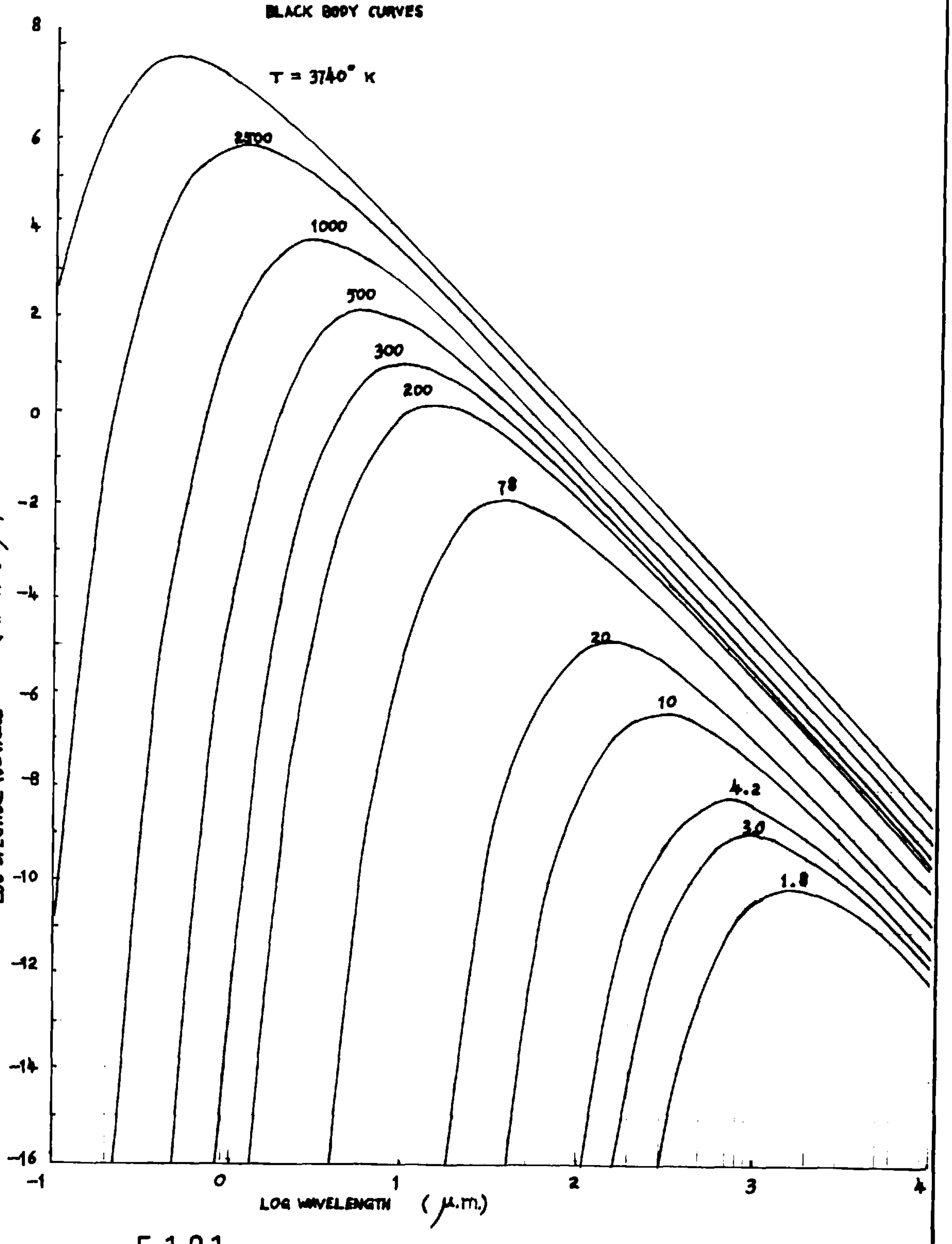

F. 1.01 BLACK BODY RADIATION CURVES.

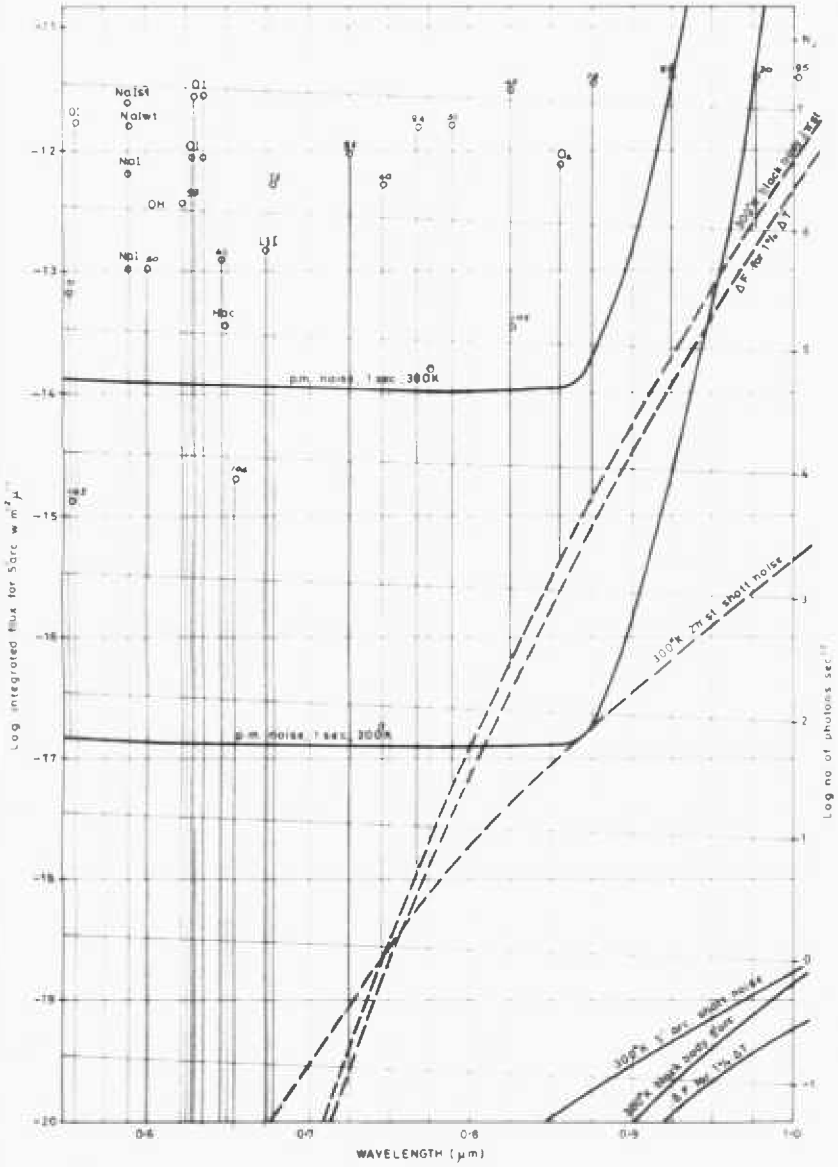

F.1.0 2 BLACK BODY CURVES AND NIGHT SKY EMISSION

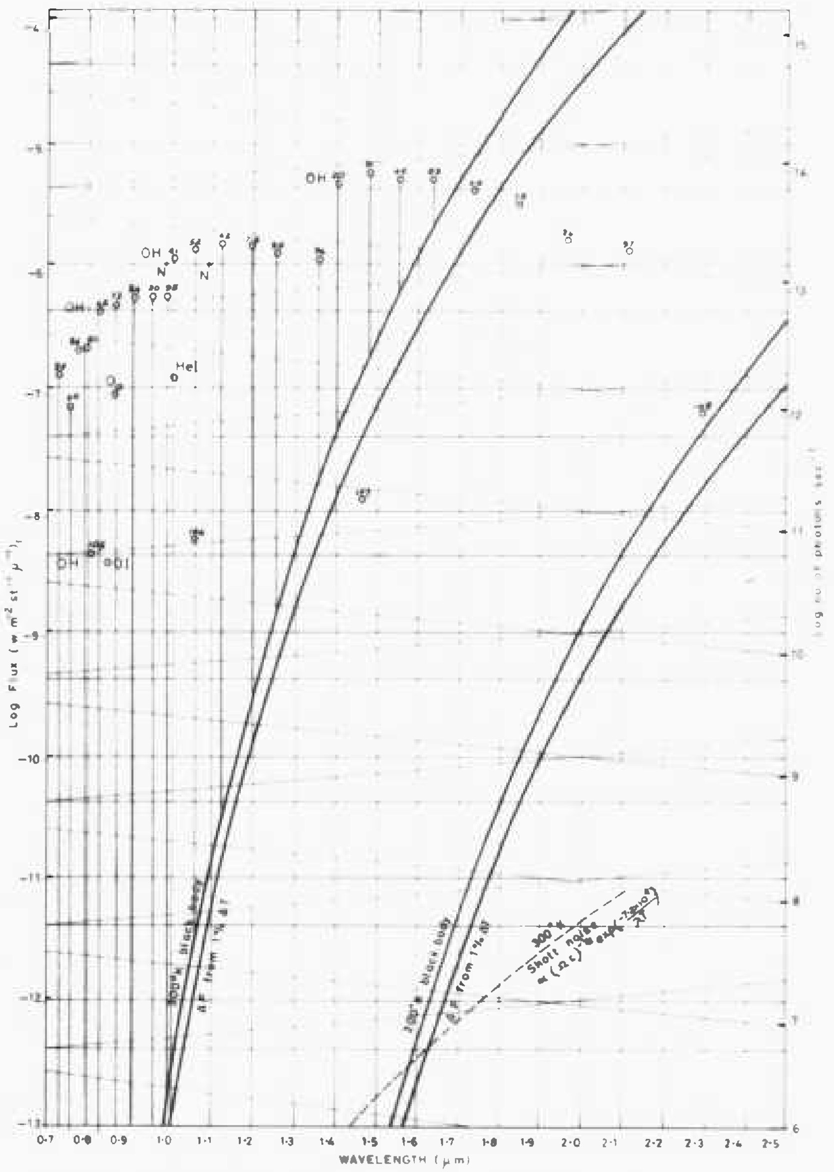

F.1.0 3 BLACK BODY CURVES AND NIGHT SKY EMISSION

T.1.1

OH Transition	Wave length (μ)
9–5	1·00
4–1	1·03
5–2	1·08
6–3	1·14
7–4	1·21
8–5	1·29
9–6	1·38
2–0	1·43
3–1	1·50
4–2	1·58
5–3	1·67
6–4	1·76
7–5	1·87
8–6	1·99

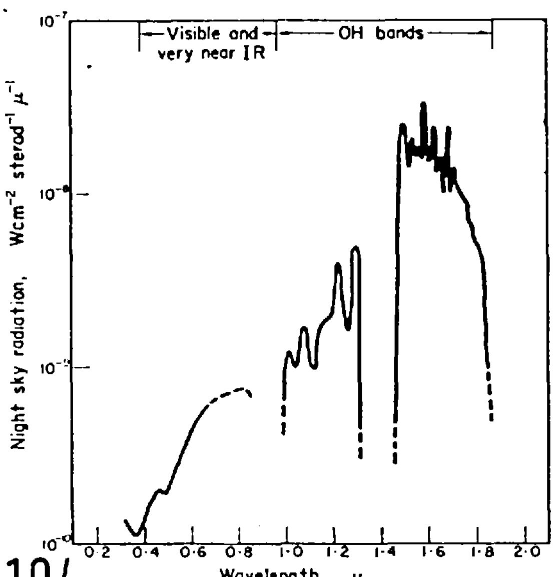

F.1.04

Radiation levels on a clear moonless night.

Night sky radiation in the infra-red

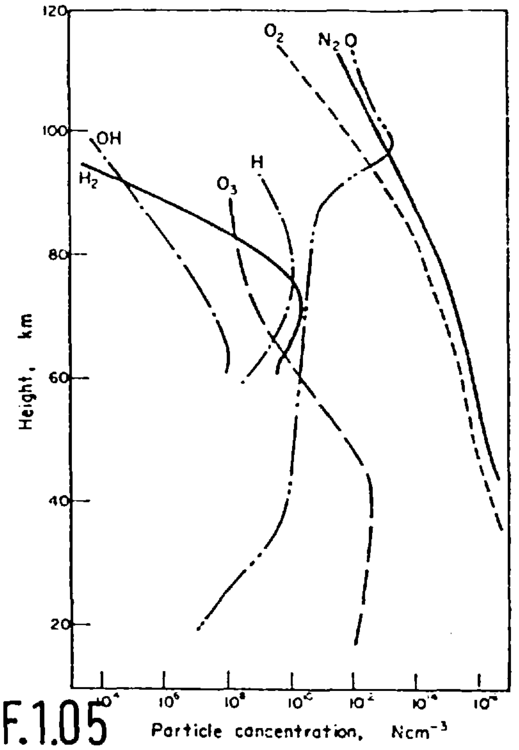

F.1.05

Concentration of upper atmosphere constituents.

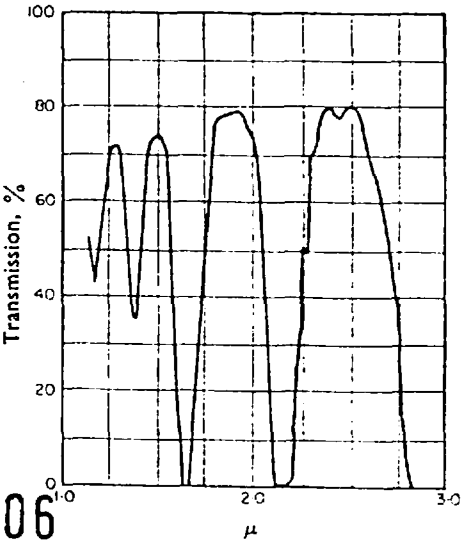

F.1.06

Atmospheric transmission 1–3 microns.

of astronomical sources, but the black body atmospheric emission beyond λ 1.3 μ is in general considerably greater than that from most other observed sources and reaches a peak at about λ 10 μ, and so sky-comparison techniques must then be employed.

1.03 Astronomical infrared extended sources

(a) Stellar sources

The diagram of F1.07 shows the observed radiation curves for several infrared astronomical sources; most of these resemble black body curves integrated over a restricted range of temperature as would be expected from stellar thermal sources, especially from red super-giants with extended atmospheres. Some sources such as R. Mon, μ. Ceph. and possibly the galactic centre show additional secondary peaks around λ 10 μ corresponding to a lower temperature secondary source such as an evelope of dust around the stars in question. Recent work by Neugebauer and Low(R9.01, R9.02) on the galactic centre also confirms the view that this emission is largely thermal in origin. There are some infrared emission line features produced by cool red giant stars (K, L, M class) which arise from C, N, & O, molecular band transitions; these stars sometimes show absorption features around λ 9 μ, where silicates are thought to be responsible.

These emission bands tend to average out when observing globular clusters or galaxies, leaving the dominant broad absorption features in the infrared thermal continuum. Globular clusters and galaxies are the subject of some discussion in chapter 9.

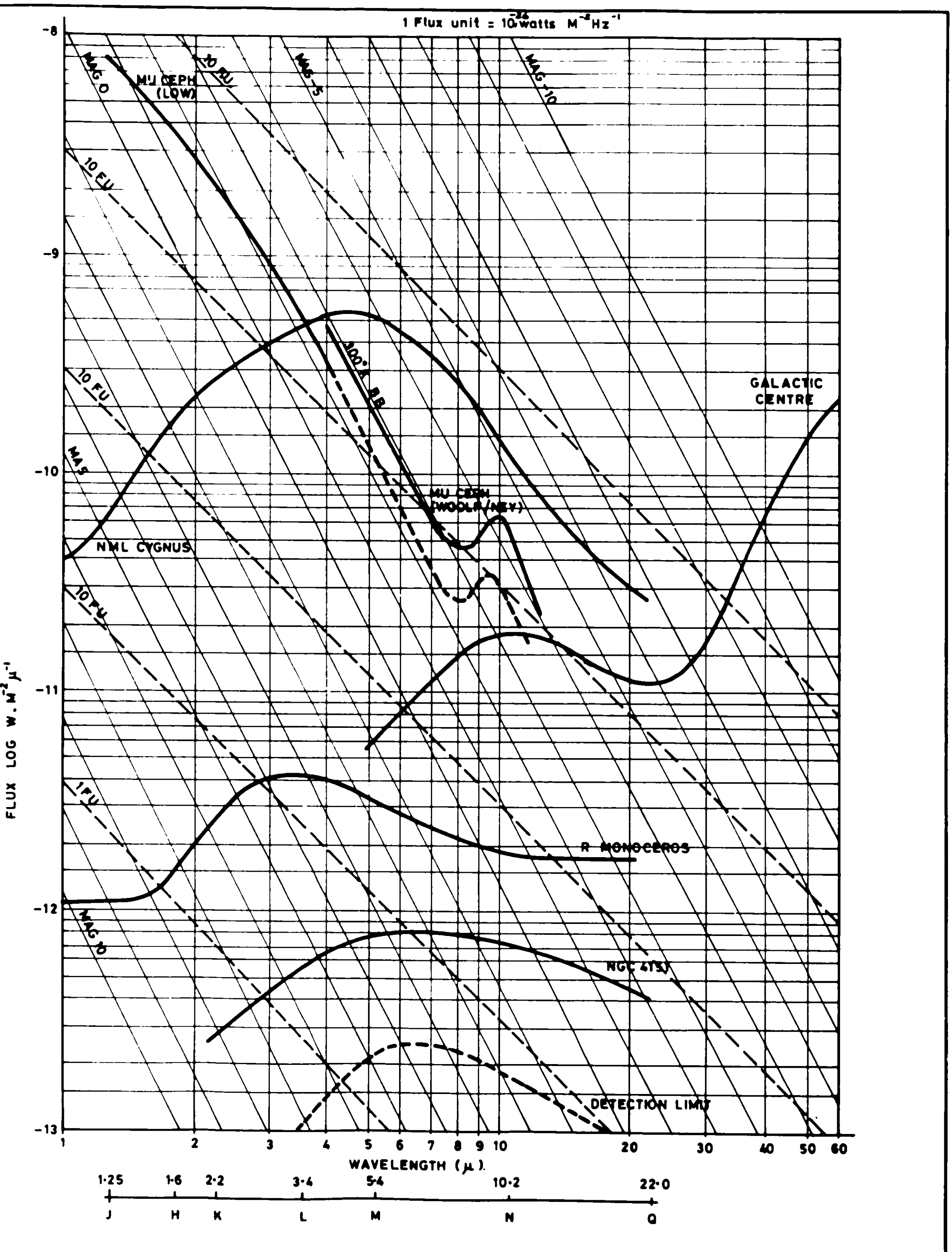

F.1.07 RADIATION CURVES FOR SOME ASTRONOMICAL INFRA RED SOURCES

Spectrum of planetary nebulae

Only the stronger lines are tabulated, and are relative to Hβ (= 100). The intensities represent planetary nebulae in general but wide differences are found, mostly concerned with T_*. t = line whose intensity increases with T_*; ~ = line whose intensity varies erratically for various nebulae; [ ] = forbidden line.

T12

λ	Elements and line components	Intensity
Å		Hβ = 100
3133	O III	30 t
3203	He II	10 t
3343	O III [Ne V] 3340–46	25 t
3435	[Ne V] 3425; O III 3444	20 t
3727	[O II] 3726·1, 3728·6	40 ~
3798	H I	5
3835	H I	7
3869	[Ne III]	50 t
3889	H I 3889·1; He I 3888·6	15
3968	[Ne III] 3967·4; H I 3970·1	30 t
4026	He I	2
4073	S II 4069, 4076	4
4101	H I 4102; N III 4097, 4103	25
4340	H I	40
4363	[O III]	10 t
4471	He I	5
4542	He II	2 t
4638	N III 4634, 4641	4
4686	He II	30 t
4725	[A IV] 4712, 40; [N IV]	6 t
4861	H I	100
4959	[O III]	300 t
5007	[O III]	800 t
5412	He II	6 t
5755	[N II]	10 ~
5876	He I	30
6302	[O I] 6300; [S III] 6311	30 ~
6364	[O I]	10 ~
6548	[N II]	70 ~
6563	H I	400
6584	[N II]	150
6678	He I	12
6726	[S II] 6716, 6731	15
7065	He I	20
7136	[A III]	50 t
7325	[O II] 7319, 7330	20

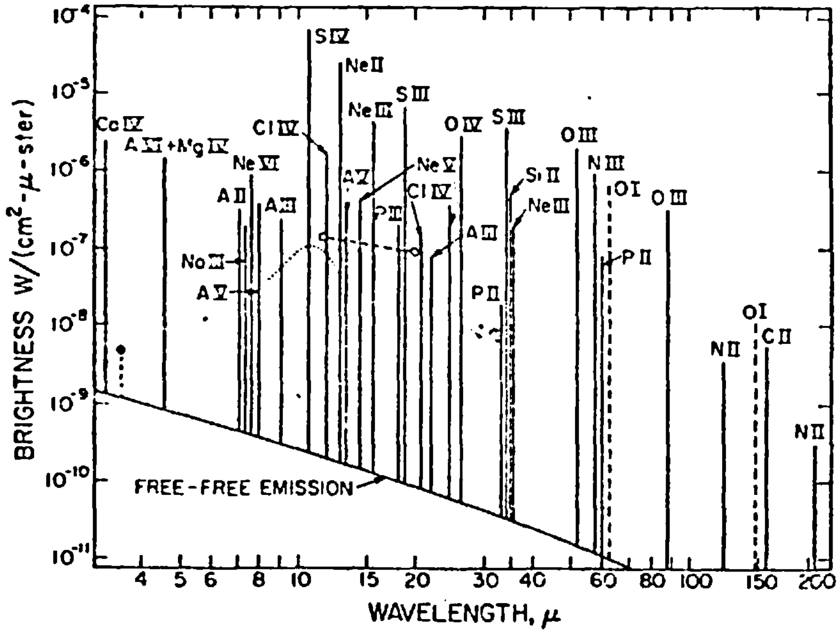

F.10 8

Fine-structure line intensities for the Orion Nebula averaged over 4′ of arc region. Free-free emission intensity obtained from extrapolation of the radio data with T_e = 7000° K. Circled cross, from Ney and Allen (1969), refers to the whole nebula (4′ of arc). Open circles, from same authors, refer to 26″ of arc region around the Trapezium. *Dotted lines*, observations of Stein and Gillett (1969) for 15″ of arc region around the Trapezium.

Table T.1.3 Observed intensities of infrared lines

NGC 1976. H II region. (Aller & Liller)

λ(μ)				λ(μ)			
0.6563	H I	Hα	350	0.9069	[S III]	$^3P_1-^1D_2$	72
0.6583	[N II]	$^3P_2-^1D_2$	55	0.9229	H I	P9	6
0.6716	[S II]	$^4S-^2D_{5/2}$	6	0.9532	[S III]	$^3P_2-^1D_2$	181
0.6730	[S II]	$^4S-^2D_{3/2}$	8	0.9546	H I	Pε	8
0.7065	He I	$2^3P-3\ ^3S$	13	1.0049	H I	Pδ	10
0.7136	[Ar III]	$^3P_2-^1D_2$	17	1.0830	He I	$2\ ^3S-2\ ^3P$	70
0.7319	[O II]	$^2D_{5/2}-^2P$	9	1.0938	H I	Pγ	20
0.7330	[O II]	$^2D_{3/2}-^2P$	9				

(Tables after Osterbrock)

Table T.1.4 Expected infrared photon emission hydrogen lines

H II region. T = 10000 °K

λ(μ)			λ(μ)		
0.656	3-2	188	7.459	6-5	20
...	...	...	4.654	7-5	7.8
1.876	4-3	66	3.740	8-5	4.1
1.282	5-3	21	3.297	9-5	2.5
1.094	6-3	9.9	...	...	...
1.005	7-3	5.6	...	...	...
0.955	8-3	3.5	12.37	7-6	13
...	...	...	7.502	8-6	5.5
...	...	...	...	...	...
4.052	5-4	34	...	...	...
2.626	6-4	12	19.06	8-7	10
2.166	7-4	6.1	11.31	9-7	4.7
1.954	8-4	3.6	...	...	...
...	...	...	...	...	...

Table T.1.5 Expected photon emission in collisional lines

H II region. T = 7300 °K. Low-density limit.

λ(μ)				λ(μ)			
0.7138	[Ar III]	$^3P_2-^1D_2$	6.8	18.7	[S III]	$^3P_1-^3P_2$	270
0.7321	[O II]	$^2D_{5/2}-^2P$	1.9	21.8	[Ar III]	$^3P_1-^3P_0$	22
0.7332	[O II]	$^2D_{3/2}-^2P$	1.6	33.6	[S III]	$^3P_0-^3P_1$	870
0.7753	[Ar III]	$^3P_1-^1D_2$	1.8	34.8	[Si II]	$^2P_{1/2}-^2P_{3/2}$	8100
0.9072	[S III]	$^3P_1-^1D_2$	4.1	36.1	[Ne III]	$^3P_1-^3P_0$	170
0.9535	[S III]	$^3P_2-^1D_2$	11	113	[O III]	$^3P_0-^3P_1$	5500
1.032	[S II]	$^2D-^2P$	2.0	122	[N II]	$^3P_1-^3P_2$	1700
6.983	[Ar II]	$^2P_{3/2}-^2P_{1/2}$	190	156	[C II]	$^2P_{1/2}-^2P_{3/2}$	2300
8.990	[Ar III]	$^3P_2-^3P_1$	100	174	[N III]	$^2P_{1/2}-^2P_{3/2}$	1000
12.8	[Ne II]	$^2P_{3/2}-^2P_{1/2}$	2700	204	[N II]	$^3P_0-^3P_1$	3900
15.4	[Ne III]	$^3P_2-^3P_1$	790	307	[O III]	$^3P_1-^3P_2$	4200

Table T.1.6 Expected infrared photon emission

H I region. T = 100 °K. 10% H_2

λ(μ)				λ(μ)			
28.2	[H_2]	0-2	4.0	147	[O I]	$^3P_1-^3P_0$	4.9
34.8	[Si II]	$^2P_{1/2}-^2P_{3/2}$	0.4	156	[C II]	$^2P_{1/2}-^2P_{3/2}$	140
63.1	[O I]	$^3P_2-^3P_1$	31				

Table I.1.7 Expected infrared photon emission

H I region. $T = 1000^{\circ}K$. 10% H_2

λ(μ)				λ(μ)			
8.05	[pH_2]	4-6	0.4	34.8	[Si II]	$^2P_{\frac{1}{2}}-^2P_{\frac{3}{2}}$	1.7
9.68	[oH_2]	3-5	18	63.1	[O I]	$^3P_2-^3P_1$	78
12.8	[pH_2]	2-4	30	147	[O I]	$^3P_1-^3P_0$	30
17.0	[oH_2]	1-3	97	156	[C II]	$^2P_{\frac{1}{2}}-^2P_{\frac{3}{2}}$	32
28.2	[pH_2]	0.3	4.2				

Table I.1.8 Resonance-fluorescence lines of H_2

$v' = 1 \rightarrow v'' = 0$

J'	J''	λ(μ)	J'	J''	λ(μ)
0	2	2.627	2	0	2.223
			2	2	2.413
1	1	2.407	2	4	3.004
1	3	2.802			

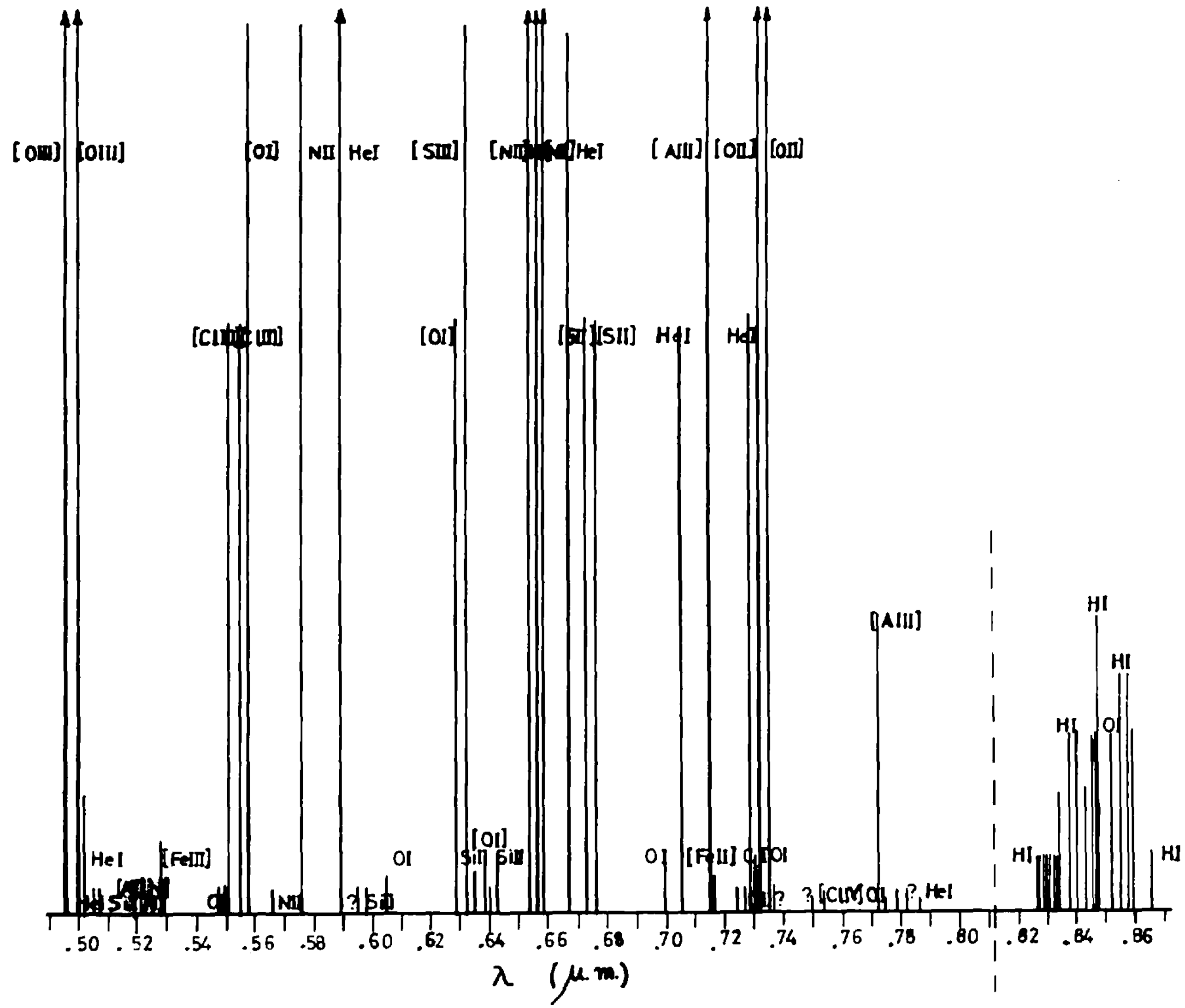

F.1.09 LINE SPECTRUM OF ORION NEBULA AS OBSERVED BY L.A. MORGAN,1971

(b) Planetary nebulae

Planetary nebulae show thermal (continuum) emission in the visible as a combination of degraded and reflected stellar radiation, as well as line emission, (R1.08) of which forbidden lines dominate. The strongest lines are $[0\ \mathrm{III}]_{\substack{4959\\5007}}$, $H\alpha_{6563}$, $H\beta_{4861}$, $[N\ \mathrm{II}]_{6584}$, (a list is given in table T1.2 (Allen, R1.07), and are usually produced by cascade processes from degraded Ly α stellar radiation; the heavier less abundant elements emit forbidden lines from non-collisional de-excitation. Infrared line emission is less common, though predictions have been made for $\lambda > 3\mu$ by Flower (R1.11).

The mechanisms for these infrared line sources are similar to those operating in diffuse nebulae; diffuse nebulae are the principal subject of interest for the instruments to be described in the remaining sections of this chapter.

Table TI.4 (Osterbrock, R1.28) shows the expected hydrogen lines for an HII region at 10000°K. Some helium lines are also expected, the most interesting is the λ 1.030μ HeI line, 2^3S-2^3P which is thermal-electron-collisionally excited and must encounter many scatterings before leaving a nebula. The line is thus very sensitive to electron density and anisotropies in the nebula; it has been observed by several authors (R1.20, R1.30, R1.31) and is found to be usually asymmetric as determined by local anisotropies in the radial velocities of the nebulous material.

The optical depth at the HeI 1.083 μ line is considerably greater than at HeI λ 0.389 μ which is weakened by absorption and partially converted to λ 4.296 μ 3^3S-3^3P.

Collisionally-excited and forbidden lines also occur in the infrared, and for collisional excitation, the infrared threshold is low and so is favoured.

Table T1.5 (Osterbrock, R1.28) shows the principal collisional lines expected, the strongest being $[NeII]_{12.8\mu}$ $[SiII]_{34.8\mu}$ and $[LII]_{1.56\mu}$; the table is based on collisional excitation, followed by photon emission. At higher electron densities some collisional de-excitation occurs which affects the relative intensity of different lines of an element at the same ionisation (for example the two [NII] $\text{lines}_{\lambda 174,\ \lambda 204}$). Cool HI regions are also expected to give infrared line emission from lower levels of excitation including hydrogen molecular bands, and these are sensitive to the temperature (see table T1.6 & T1.7, Osterbrock R1.28). There will also be infrared transitions from OH, CH, NH, and OH^+, CH^+ and NH^+. Resonance fluorescence lines are also possible for H_2, excited by Lyman α radiation and returning via the $\nu = 1$ vibration level. (Table T1.8).

The wavelength range with which this thesis is concerned is λ 0.7 μ to λ 2.2 μ and includes only a few possible nebular emission lines.

(d) Diffuse nebulae (λ 1 to 4 μ emission)

Some diffuse nebulae show $[SII]_{6717}$ emission, and some show $[OII]_{\substack{7319\\7330}}$ but the only strong line found beyond this is the $[He]_{10830}$ line as previously discussed. Several possible non thermal mechanisms of λ 1.0 to λ 4.0 μ

emission have been suggested; line emission from $1s^2$, $2s^2\ 2p^2\ {}^3P$ transitions would be expected from elements of this isoelectronic sequence. O^{+2} has line emission from the 'S to 'D transition at λ 0.4363μ, 'D to $3p_{j=2}$ at λ.5007μ, 'D to $3p_{j=1}$ at λ.4959μ and $3p_{\Delta j=1}$ transitions for $\lambda > 10\mu$; the 'S to 'D and 'D to 3p transitions will occur at long wavelengths for elements of lower ionisation energy, such as $Ne^+\ 1S^2\ 2S^2\ 2p^5\ {}^3P$. Transitions of this type will occur from np^q electron configurations where q = 1 to 5 but $\neq$ 4, q is more typically 1 to 3 but the maximum may occur of q = 5 to 6 in HII regions; the lower atomic number and lower ionisation elements are more abundant and hence give stronger emission. The thermal electron collisionally excited λ 1.0830μ and HeI 2^3S-2^3P line previously mentioned has been studied by various authors (R1.29 - R1.30) to determine electron densities in nebulae; this line emission is scattered many times in a nebula; there is some evidence that this line does not always appear symmetrical. The line arises from collisional transfer in the 2^2S to 2^3P transition. The strongest HeI line is expected to be 2'S-2'Pλ 2.059μ. Pachen lines (n = 3 to n = m, $3 \leqslant m \leqslant \infty$) from neutral hydrogen start at λ1.8751μ and follow at λ 1.2818μ, μ 1.0938μ etc. to the series limit at λ 0.8204μ. Observations of diffuse nebulae in the infrared have been made by various authors (R9.21 to R9.27) and line predictions are given by Osterbrock (R1.28).

The wavelength range with which this thesis is concerned (λ 0.7 λ 2.2 μ) includes only a few possible nebular emission lines. The figures F1.08 and F1.09 show the lack of available observed data for line emission between λ 0.9 μ and 4μ.

(e) Other infrared extended sources

At present, the radio loop structures observed by Meaburn and by Reay et al (R1.32, R1.33) have not been detected in the infrared, but would be well worth investigating.

Comets have been detected in the infrared (R1.34); most of this continuum is reflected solar radiation. The subject has not been intensively studied mostly due to the infrequent occurrence of bright comets and the limited field apertures of most infrared photometers.

1.04 The design parameters for infrared spectrometers

Near infrared and infrared radiation from astronomical sources is invariably detector noise-limited, as opposed to photon shot-noise limited in the visible and ultraviolet. Spectrographic work in the near infrared becomes very inefficient when wavelengths are observed successively with the low-sensitivity detectors available. The design of near-infrared spectrometers concentrates on maximising the instrumental resolution-throughput product and at the same time using the "Fellgett Advantage", whereby a signal-to-noise advantage of (no. of resolved spectral elements in the wavelength range)$^{\frac{1}{2}}$ is attained over monochromator type spectrometers, from observing the full wavelength range simultaneously. This advantage arises as the signal detected will be proportional to the integration time and to the number of simultaneously observed spectral elements, while the random noise, when detector limited, is only proportional to the square root of this integration time.

Instrumental throughput for an aperture may be defined as the product of the solid angle of the incident beam on that aperture and the area of that aperture. In order to achieve maximum transmission of the available radiation through an optical system, this product constant must be maintained for all apertures in the system. The quantity is more readily appreciated in its square root form, where for conservation, the product of any aperture diameter and the F ratio of the beam at this aperture must be maintained throughout the optical system. In practice, the telescope defines the throughput by the telescope F ratio and the available field of view at the telescope focal plane, which usually forms the input aperture stop for a following spectrographic system. Slit spectrographs are satisfactory only for single stellar-type sources where the slit width is comparable to the image size; usually the slit width is necessarily restricted to increase the spectral resolution at the price of a reduction of throughput. The near-infrared spectrographic study of extended sources such as diffuse nebulae requires a wide field of view as well as simultaneous observation of all spectral elements, and a throughput matched to this large field and telescope F ratio. The field of view or entrance aperture is usually geometrically restricted and so fast telescope foci are preferred in order to gain throughput; resolution must not

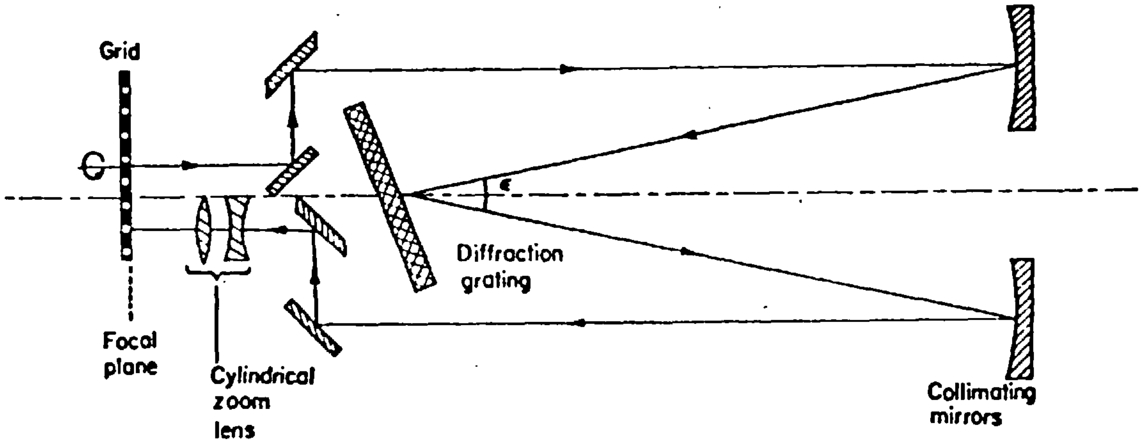

F.1.10a

Mock interferometer (3-m Ebert spectrometer).

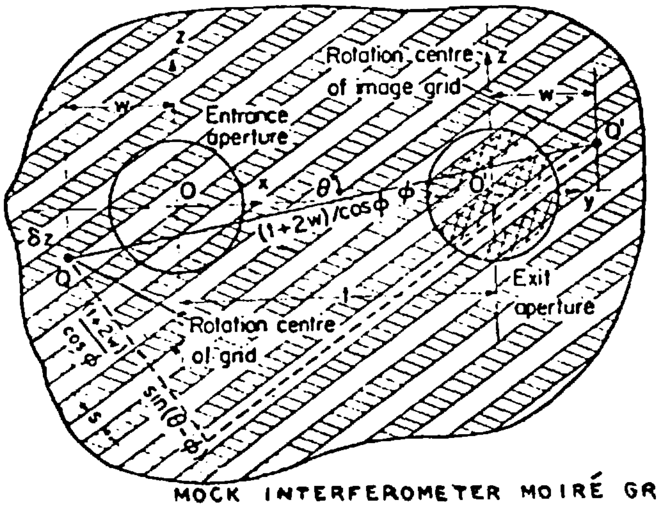

MOCK INTERFEROMETER MOIRÉ GRID

F.1.10b

Misplaced rotation centre of grid.

$$I = \frac{I_\lambda}{2}\Delta^2\left[\frac{\pi(\lambda - \lambda_0 + 2wd)\sin\theta}{2sd} + \phi_0\right]$$

F.1.10c

suffer as a result of this large throughput. Two such spectrophotometric systems briefly described here are the Mock Interferometer and the wide-field-compensated Michelson interferometer.

1.05 The Mock Interferometer

The Mock interferometer of J Ring and M J Selby is described in detail in references (R1.35, R1.36) and is shown in diagram F1.10a; it consists of a 3m. Ebert spectrometer with the conventional input slit replaced by a Moiré grid in the telescope focal image plane. The dispersed image of this grid and field stop is superimposed onto the grid and the resultant Moiré fringes imaged onto an infrared-sensitive photomultiplier; the Moiré grid is rotated about the principal optic axis in steps, and the transmitted radiation received on the photomultiplier recorded as samples. The grid and imaged grid are shown in diagram F1.10b, together with the output transmission relation (F1.10c); the samples are deconvoluted with the transmission function given (in a computer), to restore the original spectrum. This mathematical process is similar to that used in the spectrum restoration transformation of an interferogram; here the Moiré fringe pattern takes the place of the interferogram, hence the use of the name 'Mock'.

This system was used with the 40" flux collector at the Imperial College outstation, Silwood Park Ascot, to observe diffuse nebulae in λ 0.65 to λ 0.9μ; the author's part mainly being that of an observing assistant.

Some spectra were obtained from the brighter diffuse nebulae showing several spectral forbidden nebular emission lines including those of [SII] and [SIII]. The intensity ratio of $[SII]_{6717}/[SII]_{6731}$ is a particularly sensitive indicator of electron density, and unlike most other lines, is not a function of electron temperature; some more work on this is discussed in chapter 4.

1.06 A field compensated Michelson Interferometer

(a) Resolution-throughput advantage

Figure F1.11 shows the resolution-throughput product of several types of spectrometer as a function of resolution. The case of the grating-slit spectrograph has already been discussed; the increased field of view of a standard Michelson spectrometer has a x 10^2 advantage in resolution throughput product (see figure F1.11), while a spherical Fabry-Perot etalon system resolution-throughput product varies according to the resolution, and is always greater than the corresponding Michelson interferometer product. Field compensation for a Michelson interferometer gives a further advantage in resolution-throughput product over the Michelson interferometer; this is at least a further $\sim$ x 10^2 for a resolution of 10^4; a field compensated Michelson interferometer then has a $\sim 10^2$ advantage over the classical spectrometer (R1.37). Such an instrument was built by J.W Schofield with the function of observing the λ 0.7 to 2.0μ spectrum of large bright diffuse nebulae; the author's part in this instrument was mostly as an assistant in the later stages of construction. The advantage of such an instrument only applies so long as the source fills the entrance aperture, which in this case was approximately 90mm diameter. Such a high resolution Michelson interferometer has been built and successfully operated by P Connes (R1.39) for observing near infrared planetary spectra at high resolution.

(b) Principle of field compensation

There are a number of possible designs for field compensated Michelson interferometers, which are discussed in a paper on this subject by J Ring and J W Schofield (R1.37); the system built by J W Schofield follows Hertz first design (R1.44) and is shown in figure F1.12a.

The interposing of the double glass wedge shown geometrically foreshortens that arm of the interferometer; the apparent angular size of the moving mirror subtended at the exit aperture may then be kept equal to that for the fixed arm mirror also observed from the output aperture, for all positions of the moving mirror. Preservation of this relationship for all path differences increases the throughput of the instrument as previously discussed. Figure F1.12b shows a ray trace through a compensation block before a mirror; varying the thickness 'E' of this block accordingly varies the foreshortening distance 'D'.

The optical path difference between ray A CH and ray A KF (without the block) may be determined.

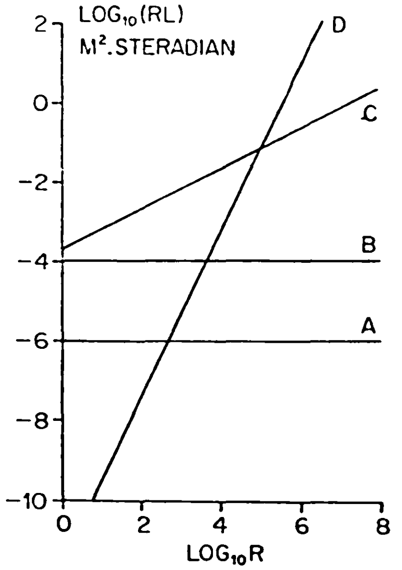

F.1.11 Resolution–luminosity products of spectrometers with common aperture $1/(2\pi)$ cm². The curve for the field-compensated Michelson is conservative. (A) Grating. (B) Classical Michelson. (C) Field-compensated Michelson. (D) Spherical Fabry-Perot.

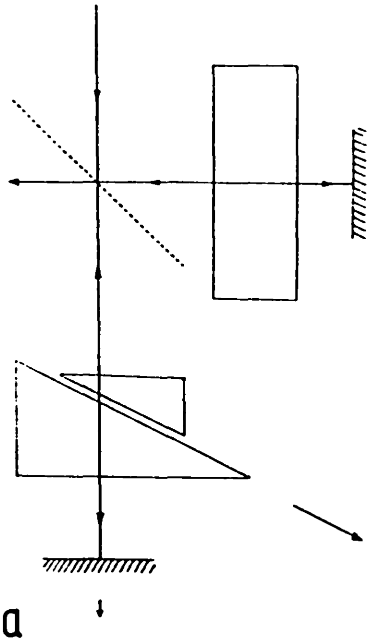

F.1.12a Mertz's first system. The plane parallel glass block is to give a large field at zero path difference, since the two wedge prisms cannot be reduced to zero thickness.

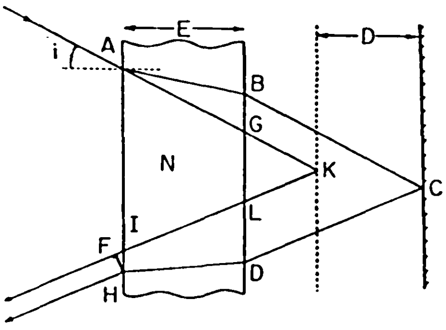

F.1.12b Ray trace for Mertz's first system.

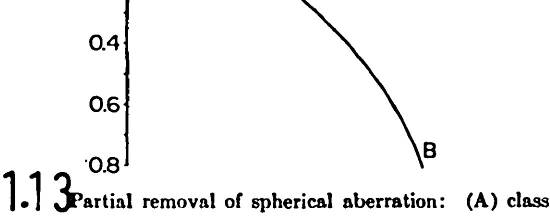

F.1.13 Partial removal of spherical aberration: (A) classical Michelson; (B) total removal of the i^2 term; (C) removal of all terms at $i \doteq 8.5°$ by changing the ratio of displacements by 1%.

$$\text{optical path AKF} = \frac{2E}{\cos i} = \frac{2\chi}{\cos i} + FI \qquad \text{E1.01}$$

$$\text{displacement AI} = 2E \tan i + 2\chi \tan i \qquad \text{E1.02}$$

$$\text{optical path ACH} = 2\eta \frac{E}{\cos r} + \frac{2\chi}{\cos i} + \frac{2D}{\cos i} \qquad \text{E1.03}$$

$$\text{where } \eta = \frac{\sin i}{\sin r} \qquad \text{E1.04}$$

$$\cos r = \frac{1}{\eta} (\eta^2 - \sin^2 i)^{\frac{1}{2}} \qquad \text{E1.05}$$

Displacement AH =

$$2E \tan r + 2\chi \tan i + 2D \tan i \qquad \text{E1.06}$$

Then displacement IH

$$= 2E(\tan r - \tan i) + D \tan i) \qquad \text{E1.07}$$

$$\text{and so } FI = 2\,(E\,(\tan r - \tan i) + D \tan i)\, \sin i \qquad \text{E1.08}$$

The total path difference is then

$$\Delta = 2E \left\{ \frac{\eta}{\cos r} - \frac{1}{\cos i} \right\} + \frac{2D}{\cos i} - 2(E(\tan r - \tan i) + D \tan i) \sin i \qquad \text{E1.09}$$

$$= 2E \left\{ \frac{\eta^2}{(\eta^2 - \sin^2 i)^{\frac{1}{2}}} - \frac{1}{(1 - \sin^2 i)^{\frac{1}{2}}} \right\} + \frac{2D}{(1 - \sin^2 i)^{\frac{1}{2}}} \qquad \text{E1.09}$$

$$-2E \left\{ \frac{\sin^2 i}{(\eta^2 - \sin^2 i)^{\frac{1}{2}}} - \frac{\sin^2 i}{(1 - \sin^2 i)^{\frac{1}{2}}} \right\} - \frac{2D \sin^2 i}{(1 - \sin^2 i)^{\frac{1}{2}}} \qquad \text{E1.10}$$

$$= 2E \left((\eta^2 - \sin^2 i)^{\frac{1}{2}} - (1-\sin^2 i)^{\frac{1}{2}} \right) + 2D\,(1 - \sin^2 i)^{\frac{1}{2}} \qquad \text{E1.11}$$

This may be written

$$2E\,((\eta^2 - 1 + \cos^2 i)^{\frac{1}{2}} - \cos i) + 2D \cos i \qquad \text{E1.12}$$

when $i = 0$, $\Delta_o = 2E\,(\eta - 1) + 2D$ E1.13

If we require compensation for i^2, then we must equate i^2 terms to zero.

then $-\frac{Ei^2}{\eta} + Ei^2 - Di^2 = 0$

Then $D = -E\,(\frac{1}{\eta} - i) = \frac{E}{\eta}\,(\eta - 1)$ E1.14

The spherical aberration is then

$$\Delta = \Delta_o\,(1 + i^4/8\eta^2) \qquad \text{E1.15}$$

and the chromatic aberration is

$$\Delta = \Delta_o \left\{ \frac{1 + \eta\,\delta\eta}{\eta^2 - 1} + \frac{\delta\eta\, i^2}{2\eta(\eta^2 - 1)} \right\} \qquad \text{E1.16}$$

The wavefront error is shown in graph F1.13 and shows that at a resolution of 10^4 the maximum off axis angle (or entrance aperture half angle) is 10°., while that for an uncompensated Michelson interferometer with a 2D cos i path difference is a few arcmins. For a similarly chromatically limited angle of 10°, the compensated system must be limited in spectral range to

$\Delta\ \lambda\ 0.2\mu$ in the visible, but with a throughput advantage of ~400 (see Fl.11) over an uncompensated system at $R = 10^4$.

(c) The field compensated Michelson Interferometer

The instrument built by J W Schofield followed the Mertz design shown, and had a 90mm entrance aperture and a resolution of 10^4. Thickness of the glass split prism compensation block was varied by moving one prism relative to the other parallel to their interface as shown; the fixed block in the fixed arm compensates the finite thickness of the wedge block, such that a condition of a compensated zero path difference for two arms may be achieved with the wedge in position. The wedge location was servo controlled to the mirror slide; a capacitance bridge gap detector (R1.38) measured the relative position of the wedge and mirror, which were respectively on air bearing slides and controlled by linear motors. The moving mirror optical path position was monitored with a photomultiplier from the interference fringes produced with a narrow He-Ne laser beam passing along the principal axis of the system. A second servo system locked the moving mirror onto the respective fringes, and its motion was stepped at single fringe intervals with a total displacement range of approximately 1 cm.

The laser beam was introduced at the entrance aperture, and removed at the exit aperture via small diagonal flats, such that the remaining field was available for the infrared radiation to be detected.

The two Michelson mirrors were of cube-corner design, such that when correctly arranged a small tilt in the carriage slide motion would give rise to a displacement of the beam and not a tilt, and so the compensation was unaffected. The system included a collimation lens for an F/5 input beam after the entrance aperture, and a spherical-mirror beam convergence system to reduce the 90mm output beam onto a 0.8mm diameter uncooled lead sulphide detector (see next chapter).

In order to detect and amplify infrared radiation, the radiation must be modulated in some manner with some carrier frequency; such a modulated signal is less sensitive to atmospheric turbulence, especially when detected with a synchronous filter. The system of Connes uses a tilted glass block in the beam to provide modulation of the fringes, while in this case the 'fixed' corner-cube was vibrated over a small fraction of a wavelength at 400Hz. The detection and servo systems were then operated with this carrier frequency.

It was found necessary to develop elaborate anti-vibration mountings to isolate the optical table from ambient vibrations, and both the moving carriages then required viscous damping baths to inhibit their motion. Some time was spent mirror aligning and producing satisfactory compensated fringes; the development of this instrument with the principal intention of producing near infrared spectra of NGC (1976) proved to be very long term.

Delays in completion of this instrument gave opportunity for the author to concentrate on the development of the infrared detection system necessary and also the development of a reference channel to simultaneously monitor the overall input radiation level during mirror scans.

This latter instrument was necessary as the Michelson Interferometer was only equipped with one exit aperture, and so each fringe sample would require to be divided by the reference monitor output in order to eliminate sky opacity variation; this monitor became a separate survey instrument and became the principal concern of the author, and is the subject of this thesis.

Since the time of the development of the field-compensated Michelson Interferometer, a second system has been built with a further X10 improvement in throughput with both moving mirror and compensation block mounted on the same carriage (see R1.35); this instrument may be used for Raman spectroscopy.

R1.07 A 40" flux collector with a fixed focus

This instrument, shown in figure F1.13a was placed at Silwood Park, Ascot; it was used with the Mock interferometer and Michelson interferometer previously described, both spectrometers required a fixed focus with a fast beam and the flux collector was built with this in mind. The author's concern with this instrument was mostly as a principal user but he was also responsible for its initial astronomical axial alignment and some operational refinements. The flux collector was again mostly the concern of J W Schofield, and proved a useful test-bed for larger instruments. Radiation from the sky is reflected by a set of six flats 'A' (F1.13b) on a steerable frame, to a fixed vertical paraboloid 'B' 40" in diameter. with an F/5 prime focus located in an adjoining hut 'C'. The flat frame 'A' is driven on a polar axis at half siderial rate, while the declination axis is also driven through the declination half angle at the appropriate rate (tables were provided) in order to keep the image of the object of interest at 'C'.

Gravitational twisting of the tessellated flat frame proved to be quite severe, and there were also some mechanical problems with the drive; frequent mirror alignment proved necessary. In principle, the instrument is satisfactory, but in practice proved problematical, although the system was used for all the observations made with the Mock interferometer and for trials made with the radiometer to be described.

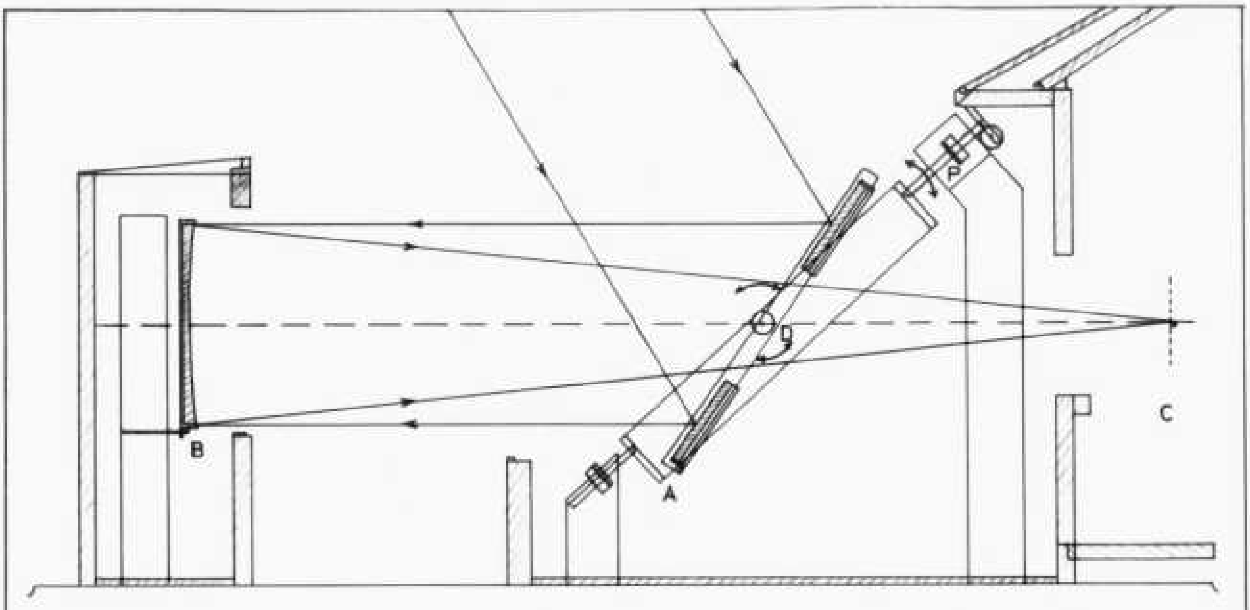

F.1.13a ELEVATION OF 40" FLUX COLLECTOR

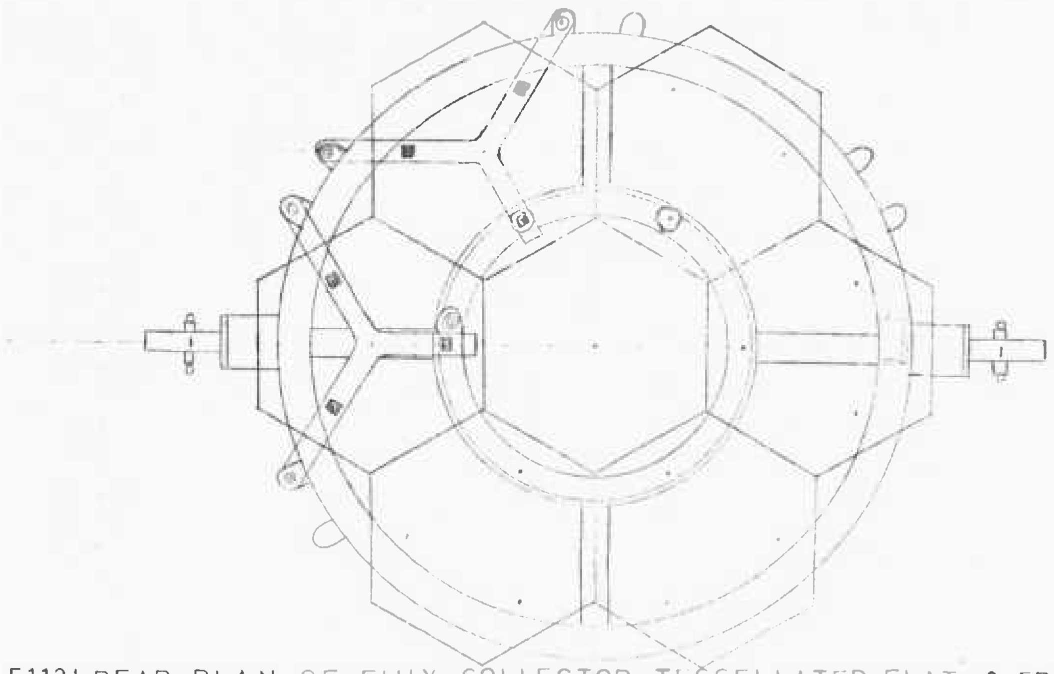

F.1.13b REAR PLAN OF FLUX COLLECTOR TESSELLATED FLAT & FRAME

References for Chapter 1

Atmospheric infrared emission

R1.01 Pardy, D. 'Night sky radiation in the infrared'. Infrared P. (1968), 8, 89-99

R1.02 Krosavosky, V.I., Shefrov, N.N., Yarin, V.I. 'Atlas of the airglow spectrum λ 3000 Å - 12400 Å'.

R1.03 Gush, H.P. 'The emission spectrum of the night airglow 2 to 4μ'. Ph. Tr. R. Soc. A, 1150, 264, 161-169

R1.04 Harwitt, M. Kuhrmannk, Werner, M. 'Near infrared night sky background'. Phil. Tr. R. Soc. A, 1150, 264, 273-278

Optical Scintillation

R1.05 Jurgen, R., Meyer-Arendt. 'Optical Scintillation: a summary of the literature'. U.S. Dept of Commerce, N.B.S. AD 614056

R1.06 Edgar, R.F. 'Turbulence and resolution in astronomical photography'. Technical Note 4 E.O.A.R. U.S.A.F.

Planetary Nebulae

Summary of observations in visible

R1.07 Allen, C.W. 'Astrophysical Quantities'. (13 Athlore Press).

R1.08 Allen, L.H. 'Gaseous nebulae'. I.A.P.S. 3, Chapman & Hall

Theory - Visible line emission

R1.09 Seaton, M.J. 'Planetary Nebulae'

R1.10 Flower, D.R. 'The Ionization structure of planetary nebulae'. Vols. I-VIII, Mon. Not. R. astr. Soc. (1969) 146

Theory infrared line emission

R1.11 (R9.20) Flower, D.R. 'On the infrared line spectra of planetary nebulae'. Mon. Not. R. astr. Soc. (1970), 147, 245-252

Observations of infrared emission

See R9.16 to R9.19

Diffuse nebulae - visible spectra

R1.12 Johnson, H.M. 'Spectrographic observations of galactic emission regions and nebulae'.

R1.13 Fa3e, B.Ф. Шaun, Г.А. 'КАТАЛОГ ЭМИССИОННЫХ ТУМАННОСТЕЙ' Izvestiya Krymskaya Astrofizicheskaya Observatoriya (1955) 1, 11-29

R1.14 Johnson, H.M. 'Diffuse Nebulae'.

R1.15 Meaburn, J. 'A search for nebulosity in high galactic radio spurs'. jur Astrk (1967) 65, 93-104

R1.16 Lozinskaya, T.A. & Esispov, V.F. 'Spectrophotometry of three filamentary nebulae'. Sov. Ast. A.J. (1971) 15, 3, 353-357

Orion nebula - visible spectra

R1.17 Margan, L.A. 'The emission spectrum of the Orion nebula in the wavelength range 4959 to 8665 Å'. Mon. Not. R. astr. Soc. (1971), 153, 393-399

R1.18 Johnson, H.M. 'Emission lines in the Orion nebula; Diffuse Nebulae C2'.

R1.19 Grandi, S.A. 'Observations of the starlight excited lines in the Orion Nebula'. Ap.J. (1975), 199, L43-L46

R1.20 Robbins, R.R. 'The Helium spectrum and dust in the Orion nebula'. Ap.J. (1970), 160, 519-530

R1.21 Balick, B. 'The structure of the Orion nebula'. Astron. Soc. Pac. (1974), 86, 616-634

Orion Nebula - infrared radiation

R1.22 Rieke, G.H. & Low, F.J. 'High resolution maps of the Kleinmann-Low nebula in Orion'. Ap.J. (1973), 186, L7-L11

R1.23 Becklin, E.E., Neugebauer, G., Wynn-Williams, C.G. 'On the nature of the infrared point source in the Orion Nebula'. Ap.J. (1973), 182, L7-L9

R1.24 Stein, W.A., Gillett, F.C. 'Spectral distribution of infrared radiation from the trapezium region of the Orion nebula'. Ap.J. (1969), 155, L197-199

Theory (infrared emission)

R1.25 Krishna, K.S.S. 'Infrared radiation from grains in Orion'. Astron. and Astrop. (1971), 14, 405-407

R1.26 Schiffer III, F.H., Mathis, J.S. 'The scattering of dust in the Orion nebula'. Ap.J. (1974), 194, 597-608

Infrared line emission theory

R1.27 Petrosian, V. 'Infrared line emission from HII regions. Ap.J. (1970), 159, 833-846

R1.28 Ostebrock, D.E. 'Expected infrared spectra of gaseous nebulae'. Ph. Tr. R. Soc. A. (1969), 1150, 246, 241

The 10830 line in nebulae

R1.29 Vaughan, Jr, A.H. 'The He I 10830 line in planetary nebulae and the Orion nebula'. Ap.J. (1968), 154, 2951-2968

R1.30 Robbins, R.R. 'The profile of the He I λ10830 in NGC 7027 and the Orion nebula'. Ap.J. (1970), 162, 507-511

R1.31 Persson, S.E. 'He I λ 10830 in gaseous nebulae'. Ap.J. (1970), 161, L51-L55

Other possible extended infrared sources

R1.32 Haslam, C.G.T., Kahn, F.D., Meaburn, J. 'Loop structures : a review and interpretation of the observations.' Astron and Astrop. (1971), 12, 388-397

R1.33 Reay, N.K. 'Association of night sky $H\beta$ emission with the cetus arc radio region'. Mon. Not. R. astr. Soc. (1971), 151, 299-306

Comets

R1.34 Maas, R.W., Ney, E.P., Woolf, N.J. 'The 10 micron emission peak of comet Bennett 1969i'. Ap.J. (1970), 160, L101-104

Mock Interferometry

R1.35 Selby, M.J. 'Mock Interferometer I theory, II construction and tests'. Infrared P. (1966), 6, 21-43

R1.36 Selby, J., Thorpe, L.W. 'A telescope mounted mock interferometer for use on extended sources'. J.de.P. Calloque suppl. 3-4, 28. 2-144

Michelson Interferometers

R1.37 Schofield, J.W., Ring, J. 'Field compensated Michelson spectrometers'. Ap. Opt. (1972), 11, 3, 507-516

R1.38 Schofield, J.W. 'A linear capacitance micrometer'. J.S.I. (1972), 5, 822-825

R1.39 Connes, P. 'Spectroscopie astronomique par transformation de Fourier'. Colloque C2 suppl. (1967) 3-4, 28, C2-120

R1.40 Ring, J., Stephens, C.L. 'The application of Michelson interferometers to high resolution astronomical spectrometry'. Mon. Not. R. astr. Soc. (1972), 158, 5p-9p

R1.41 Brault, J.W., White, O.R. 'The analysis and restoration of astronomical data via the fast Fourier transform.' Astron.and Astrop. (1971, 13, 169-189

General interferometry and spectroscopy

R1.42 Born & Woolf. 'Principles of Optics'. Pergamon

R1.43 Steel, W.H. 'Interferometry', C.U.P.

R1.44 Mertz, L. 'Transformations in Optics'

R1.45 Brault, J.W., White, O.R. 'The analysis and restoration of astronomical data via the fast Fourier Transform'. Astron. and Astrop. (1971), 13, 169-189

R1.46 Jacquinot, P. 'The luminosity of spectrometers with pressure gratings and Fabry-Perot etalon'. J.Opt.Soc. Am (1954), 44-761

THE ORIGIN, AND CONSTRAINTS FOR A WIDE FIELD RADIOMETER AND SOME DESIGNS FOR FOCAL REDUCERS

2.01 The F.C.M.I. compensation channel and its constraints

The F.C.M.I. was a single exit beam instrument, and so a reference channel was necessary in order to monitor sky transparency changes during the mirror scan of any astronomical source; each F.C.M.I. fringe sample could then be divided by the corresponding compensation channel signal to eliminate sky transparency fluctuations. Such a compensation channel would be mounted prior to the telescope focus and measure an integrated value for the whole field seen by the F.C.M.I.; this could be achieved by the use of a pre-focal beamsplitter. The distance between the telescope house wall, and the focus was approximately 370mm, and with an F/5 telescope beam converging to a 91mm field, any design involving a very large beamsplitter further up the beam was considered impractical. A 400mm pre-focal space was just sufficient to insert a 45° diagonal flat to bring the reflected beam focus clear of the incoming telescope beam; the reflected focus could then be reduced by any of a number of possible optical arrangements. The distance available perpendicular to the beam in the horizontal plane was limited only by occasional window struts and a narrowing due to the optic axis of the telescope being slightly inclined to the wall normal. The F.C.M.I. base plate would present an effective obstacle to access of such a compensation device; any chopping or sky-

CHAPTER 2

2. The origin and constraints for a wide field radiometer and some designs for focal reducers.

Contents:

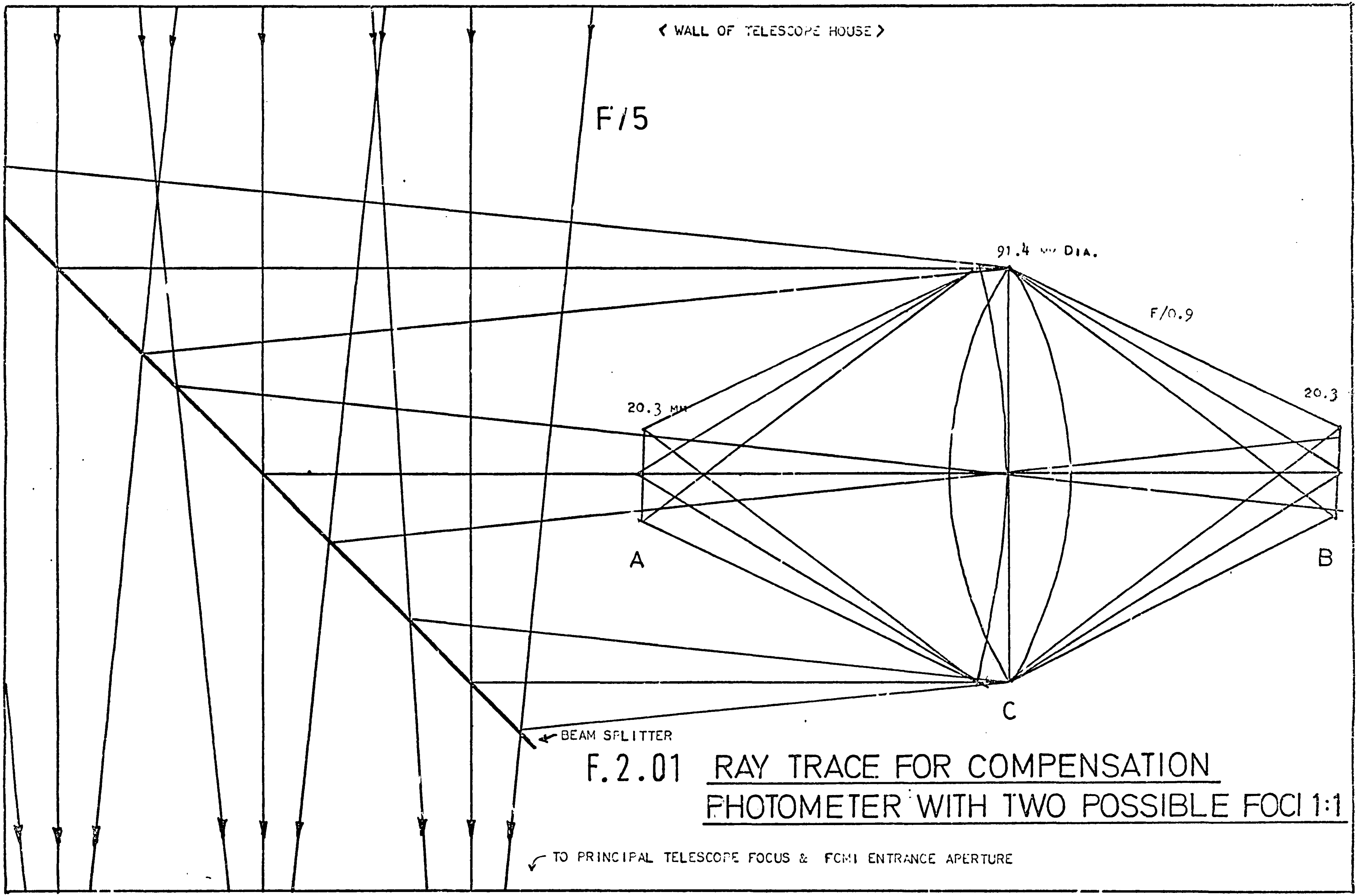

F.2.01 RAY TRACE FOR COMPENSATION PHOTOMETER WITH TWO POSSIBLE FOCI 1:1

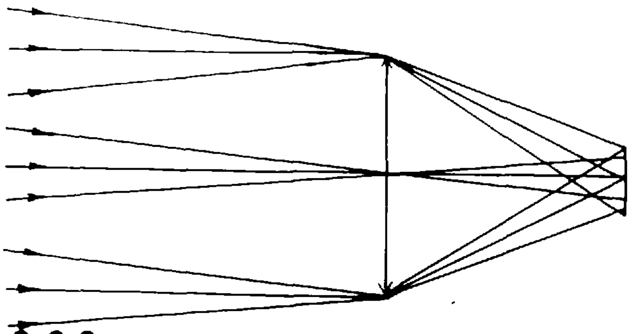

F.2.02 SIMPLE LENS

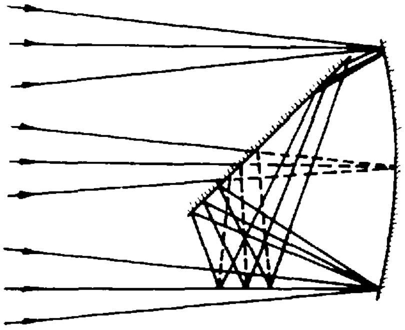

F.2.03 NEWTONIAN (SPHERICAL PRIMARY).

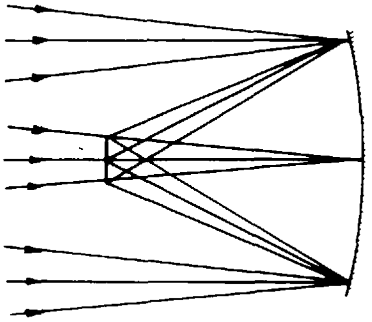

F.2.06 PRIME (SPHERICAL PRIMARY)

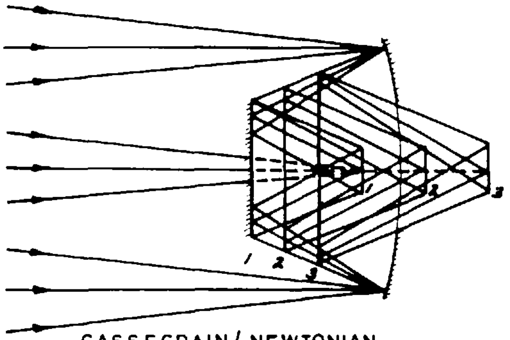

F.2.04 CASSEGRAIN/ NEWTONIAN (SPHERICAL PRIMARY)

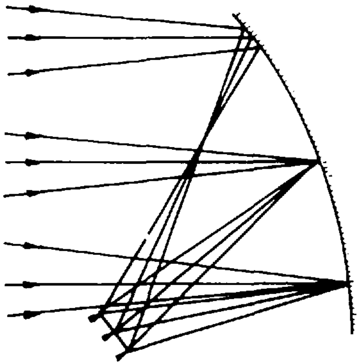

F.2.07 OFF-AXIS-PARABOLOID

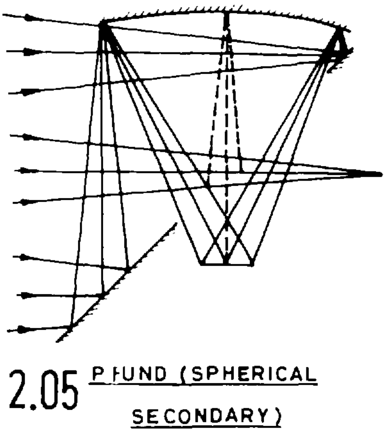

F.2.05 PFUND (SPHERICAL SECONDARY)

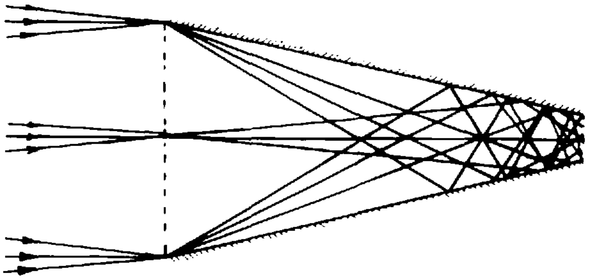

F.2.08 LIGHT CONE

5:1 REDUCTION SYSTEMS MINIMISING OBSCURATION

comparison system used in the compensation channel should not interfere with the F.C.M.I., and so it was decided to regard this instrument as a separate isolated self-contained unit, and as the instrument was to observe all wavelengths covered by the F.C.M.I. simultaneously, was given the name 'radiometer'. The principal sections of the radiometer are: optical system, modulation system, and detection electronics system; these will be discussed separately. The remainder of this chapter is concerned with the various possible optical systems that can be used to reduce a 91mm field down to a 20mm field (not necessarily an image), as required by the largest available PbS plate detector. The reflectivity of the beamsplitter necessary to give the optimum signal/noise in the divided and convoluted Fourier transformed F.C.M.I. interferogram was the subject of some calculation, which proved inconclusive. It was finally decided to conduct practical experiments with different reflectivities in order to establish the optimum; as the F.C.M.I. did not become operational these experiments were not executed.

2.02 Possible reduction systems for the radiometer

Two simple reduction systems are shown in fig F.2.01 together with the necessary constraints on space and location of the beam splitter; this diagram is a scale plan of the originally proposed optical table base, seen at the level of the optic axis, some 100mm above the base. The F.C.M.I. entrance aperture is coincident with the main telescope beam focus, below the lower edge of the diagram. The optical element C is either a lens to give an image of the telescope objective mirror at B, or is a mirror to give a similar image at A; in both cases, the F ratio required to give the 4.5:1 reduction is F/0.9. Both systems were tried, as will be mentioned later, but the mirror system has the distinct disadvantage of self-obscuration and very limited space for a detector assembly.

Figures F2.02 to F2.08 show the various reduction systems considered, all but one (F2.08) giving reduced images of the telescope objective. The principal disadvantage of the lens shown in figure F2.02 is that the necessary low F ratio will give rise to large aberrations including chromatic aberrations not common to the mirror systems.

In figures F2.03 to F2.05 various two mirror systems are shown; all suffer from excessive self-obscuration when reducing F/5 to F/0.9, and the focus in the Newtonian system F2.03 does not even clear the main beam. Of the Cassegrain (F2.04) and Pfund (2.05) systems, the Cassegrain is a little more versatile but in the three possible secondary mirror positions shown, 3 shows excessive obscuration, and focus 2 is only just accessible, still with bad obscuration. The prime mirror focus F2.06 has been previously discussed; it offers the least obscuration providing the detector assembly is very restricted in size.

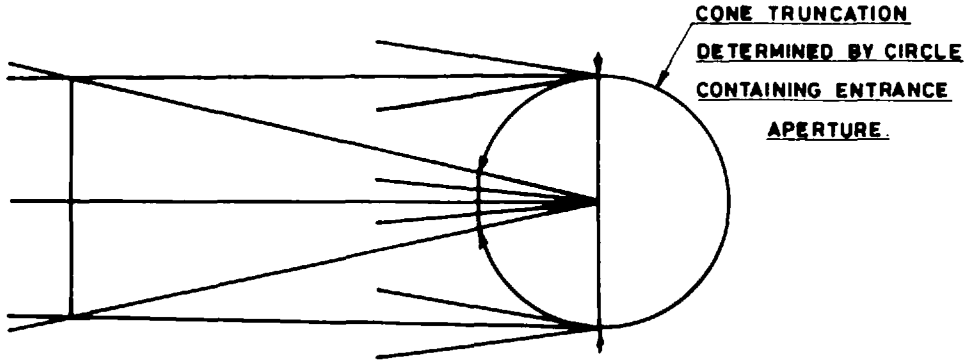

F.2.09 CONSTRUCTION DIAGRAM FOR 5:1 LIGHT CONE

The light cone (F2.08) requires much of the light to suffer multiple reflections and subsequent attenuation and so is rather inefficient; the gradient of the cone is controlled by the required exit aperture and the input aperture. The construction diagram for a light cone for a parellel input beam is shown in F2.09; the circle shown is constructed with a diameter equal to that of the entrance aperture and the required exit aperture is constructed on its circumference; the minimum cone length to avoid total internal reflection is given from the intersection of the circle radius through the exit aperture limit and the projected entrance aperture shown. The number of sides of an inscribed polygon, of side length equal to the aperture, in a quadrantof the circle is then equal to the number of reflections of the beam to produce a beam reorientation of 90^{o}. The F/5 converging beam requires a proportionally less convergent cone in order to avoid total back-reflection. Light reflection losses in such a system can be high; this is unsatisfactory as the likely astronomical sources are scarce in infrared photons, and infrared detectors are inefficient as compared with photomultipliers.

An off axis spherical mirror arrangement suffers from excessive aberrations (bad image spread), but an off axis paraboloid may not (F2.01).

2.03 Optimisation of an off axis parabolic mirror

The reflection properties of an off-axis paraboloid were investigated; the requirement being that all the light is reflected out of the main beam

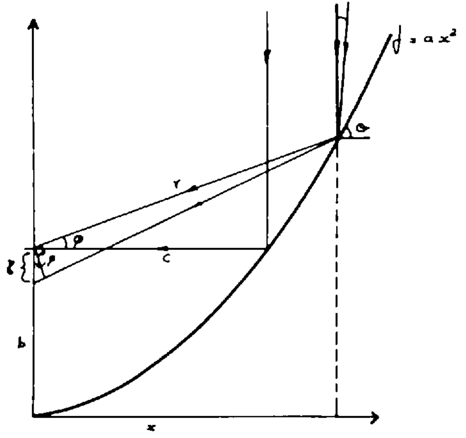

BEST FIT PARABOLIC MIRROR, REFLECTING A SKEW RAY INTO A FINITE APERTURE WHILE REFLECTING THE RAY OUT OF THE WAY OF THE INCIDENT BEAM.

F. 2.10

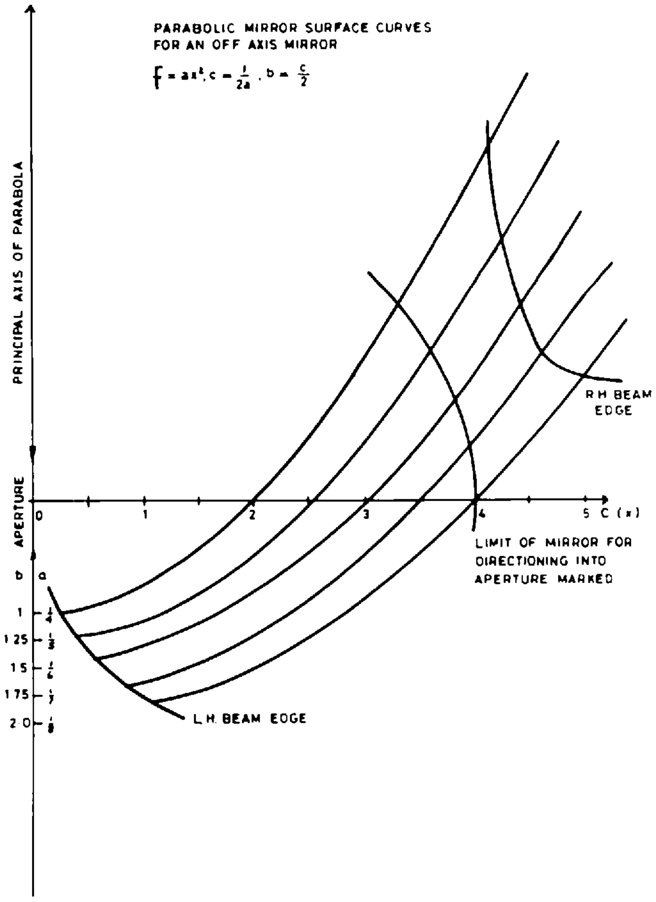

F. 2.11

RAY LOCATION CURVES GIVEN BY:-

$$L_C(x) = \frac{x^3}{4c^2} + \frac{x}{2} + \frac{c^2}{4x}$$

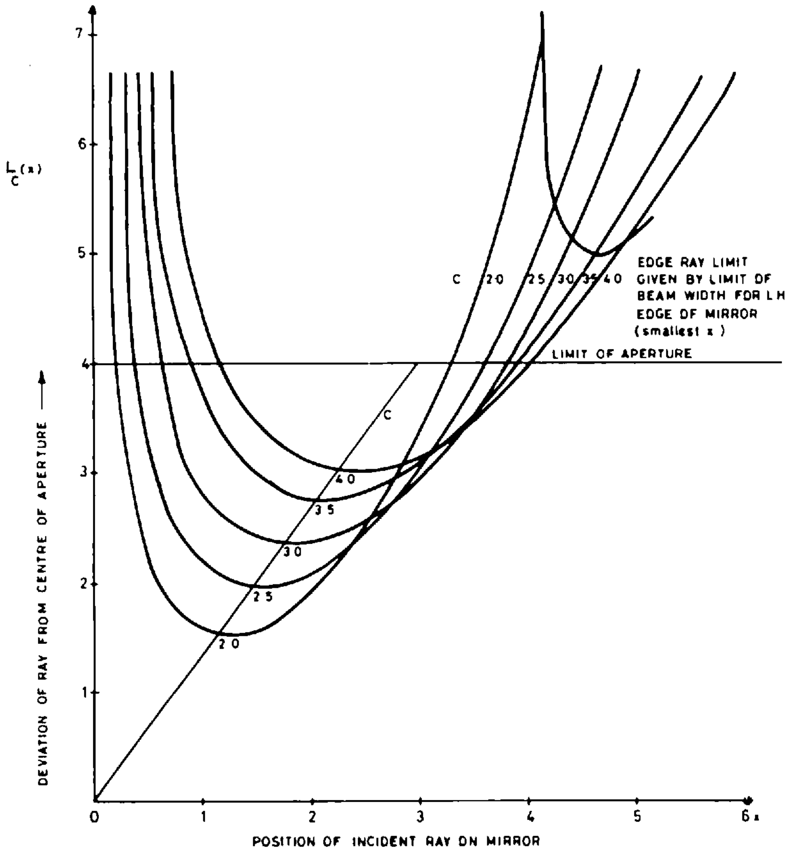

F. 2.12

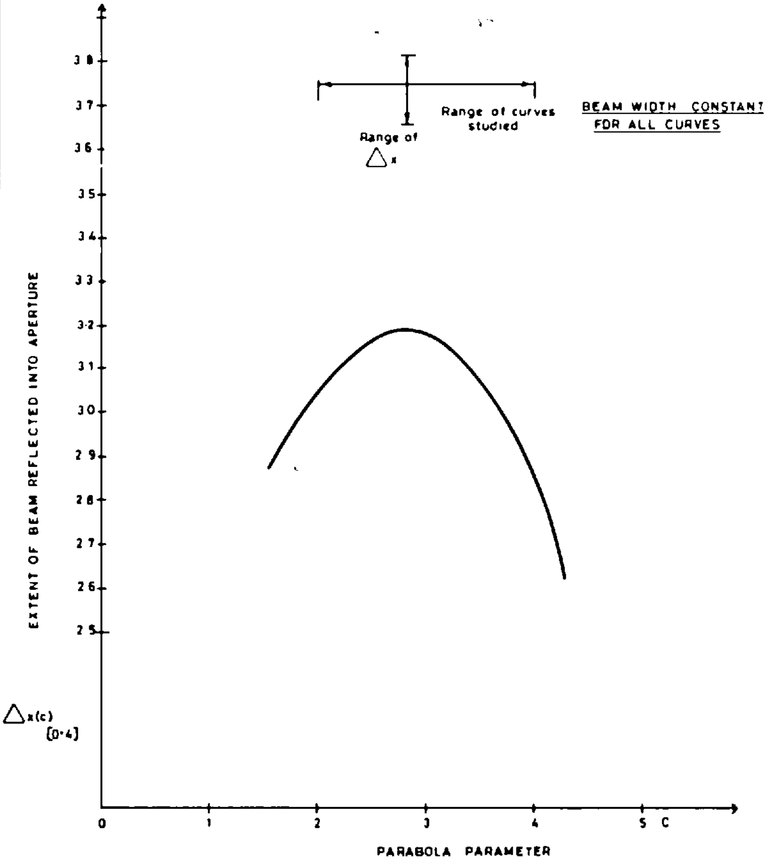

$\Delta x(c)_{[L]} = X_1 - X_2$ where X_1, X_2 are two + ve. roots of

$$x^4 + \frac{c^2}{2}x^2 - 4Lc^2x + c^4 = 0$$

F. 2.13 ***PARABOLA BEST FIT OPTIMISATION*** and through an aperture 20mm in diameter (see figure F2.10). In this analysis, l = distance from the aperture centre, and $l/\tan\alpha$ gives a convenient scale parameter $\equiv L$, where $2\tan\alpha$ is the F ratio of the input beam (for F/5, $\tan\alpha = 0.1$). The parabolic curves are all arranged such that a ray parallel to the parabola axis will be reflected normally when it corresponds to the aperture centre normal (see F2.10). The family of curves is defined by either proportional constant 'a' or 'c'; the limits of these curves given by the directivity condition of the reflected beam, together with their efficiencies, are here determined. An optimum curve is found from the family to give maximum reflection into the aperture; no curve reflects all the available light into this aperture.

The function $f = ax^2$ E2.01

has a first derivative $f' = 2ax = \tan\theta$ E2.02

When $f' = 1$, $x_1 = \frac{1}{2a}$, $f_1 = \frac{a}{4a^2} = \frac{1}{4a}$

Then $c = \frac{1}{2a}$, and $b = \frac{1}{4a} = \frac{c}{2}$, $b = ac^2$

Now $l = r\tan\alpha/\cos\phi$ E2.03

$$r^2 = x^2 + (f - b)^2 \qquad \text{E2.04}$$

$$= x^2 + f^2 - 2bf + b^2$$

$$= x^2 + a^2x^4 - 2bax^2 + b^2$$

$$= a^2x^4 + x^2(1 - 2ab) + b^2 \qquad \text{E2.05}$$

And is used to determine the accommodated input beam limits in figure F2.12.

$$\cos\varphi = x/r, \text{ then } r/\cos\varphi = r^2/x \qquad \text{E2.06}$$

Centre of the aperture,

$$\text{Then } L(x) \equiv l/\tan\alpha = a^2x^3 + x\,(1 - 2ab) + b^2/x \qquad \text{E2.07}$$

and replacing $a = \frac{1}{2c}$ and $b = \frac{c}{2}$

then $2ab = \frac{1}{2}$, $1 - 2ab = \frac{1}{2}$

$$a^2 = \frac{1}{4c^2}, \; b^2 = \frac{c^2}{4}$$

$$\text{Then } L(x) = \frac{x^3}{4c^2} + \frac{x}{2} + \frac{c^2}{4x} \qquad \text{E2.07}$$

see figure F2.12

For an F/5 beam, $\tan\alpha = 0.1$

c is a constant for a given curve.

$$\text{Then} \quad \frac{\partial L}{\partial x} = \frac{3x^2}{4c^2} + \frac{1}{2} - \frac{c^2}{4x^2} = 0 \text{ for an extrema} \qquad \text{E2.08}$$

and if $x \neq 0$,

$$x^4 + \frac{2}{3}c^2x^2 - \frac{1}{3}c^4 = 0$$

$$x^2 = \frac{-c^2}{3} \pm c^2\sqrt{\frac{4}{9}} = \frac{1}{3}c^2 \text{ or } -c^2 \qquad \text{E2.09}$$

Only the positive root is acceptable,

then $x = c/\sqrt{3}$ is the minimum L point

Substituting in E2.07

$$\check{L} = \frac{c}{12\sqrt{3}} + \frac{c}{2\sqrt{3}} + \frac{3c}{4\sqrt{3}} = \frac{4c}{3\sqrt{3}} = \frac{4}{3}\, x_{\check{L}} \qquad \text{E2.10}$$

Allowing c to vary but holding x constant ;

from E2.07

$$\frac{\partial L}{\partial c} = -x^3/_{2c^3} + c/_{2x} = 0 \text{ for an extrema} \qquad \text{E2.11}$$

Then $c/x = x^3/c^3$

$$x^4 = c^4$$

and so x = c, for the positive root minimum L point E2.12

Substituting in E2.07

$$\check{L}_{(c)} = \frac{c}{4} + \frac{c}{2} + \frac{c}{4} = c_{\check{L}} = x \qquad \text{E2.12}$$

Now let there by an $L_{\hat{m}}$,(L_{max}) and $L_{\check{m}}$,(Lmin.), then there is an $x_{\hat{m}}$ and $x_{\check{m}}$.

The maximum value of x for a given L is given by: $L \leqslant L_{\hat{m}}$

Then from E2.07

$$\frac{x^3}{4c^2} + \frac{x}{2} + \frac{c^2}{4^x} \leqslant L_{\hat{m}}$$

hence $x^4 + 2c^2 x^2 + 4c^4 - 4c^2 Lx \geqslant 0$ E2.13

$$c^4 + c^2 (2x^2 - 4Lx) + x^4 \geqslant 0$$

$$c^2 \geqslant 2Lx - x^2 \pm 2x \sqrt{L^2 - Lx}$$ see figure F2.13

For real positive roots, then: $L > x$, hence the smallest real 'c' occurs when $L = x$, and then $c = x$.

For a given position 'x' across the incoming beam, the smallest value of the deviation parameter 'L' occurs when $L = x$ and then $x = c$.

Summary:

The function $f = ax^2$, with focal distance $b = \frac{1}{4a}$, is plotted as a set of curves with various b, in figure F2.11. The intersection points of the curves with the extreme edges of the F/5 beam are shown, together with the limits for which the light is reflected into the aperture, as given by E2.05.

Deviation parameters for each parabola are shown in figure F2.12 as determined from E2.07; the maximum beam coverage is determined by E2.13, as shown in F2.13; the optimum is then for the curve $c = 3$, then $b = 1.5$. This curve can be seen in F2.11; there is still a significant light loss from the side of the mirror not reflecting all that light into the aperture.

Such a mirror could be manufactured by turning a mould out of wood, or similar medium, to a template; a plastic replica mirror could be moulded and then aluminised.

The CALCOMP graph plotter was used to draw up the optimum curve for the template; a best fit circle was also obtained.

This reduction method was considered unsatisfactory, again for reasons of light loss (as shown, a large proportion of the incident radiation does not pass through the exit aperture).

2.04 Focal reduction systems using lenses

The function of a focal reducer is to produce a reduced scale image of the original field; - the system may or may not include a collimated beam section for the introduction of interference filters or dispersive elements. In the case considered here, there is no need to produce an image of the original field; it is more advisable to image the objective onto the detector, as this gives a more uniform instrumental field profile.

(a) A simple focal reducer without collimated beam

A simple focal reducer is shown in figure F2.14; this system does image the field with a 4.5:1 reduction and requires only one addition lens; the system does not provide for a collimated beam space. The advantage of this system over the simple lens is mostly due to increased total focal distance for the same scale reduction with the simple lens; this system was used for the second instrument built,and is described in chapter 4.

F. 2.14 A FOCAL REDUCER WITHOUT COLLIMATED BEAM

F.2.15

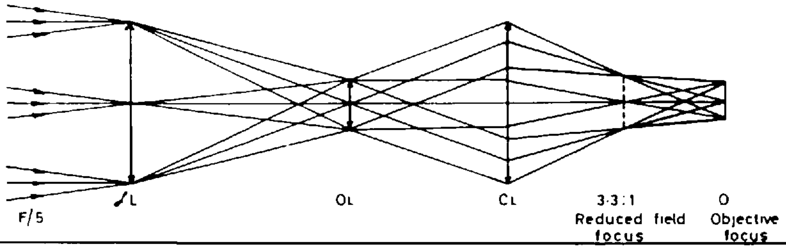

System requiring powerful reduction lens.

F.2.16

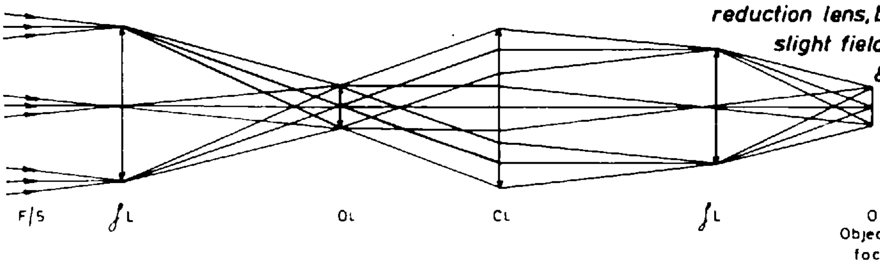

System with less powerful reduction lens, but only slight field reduction & with second objective focus.

F/5 FOCAL REDUCERS INCLUDING A COLLIMATED BEAM

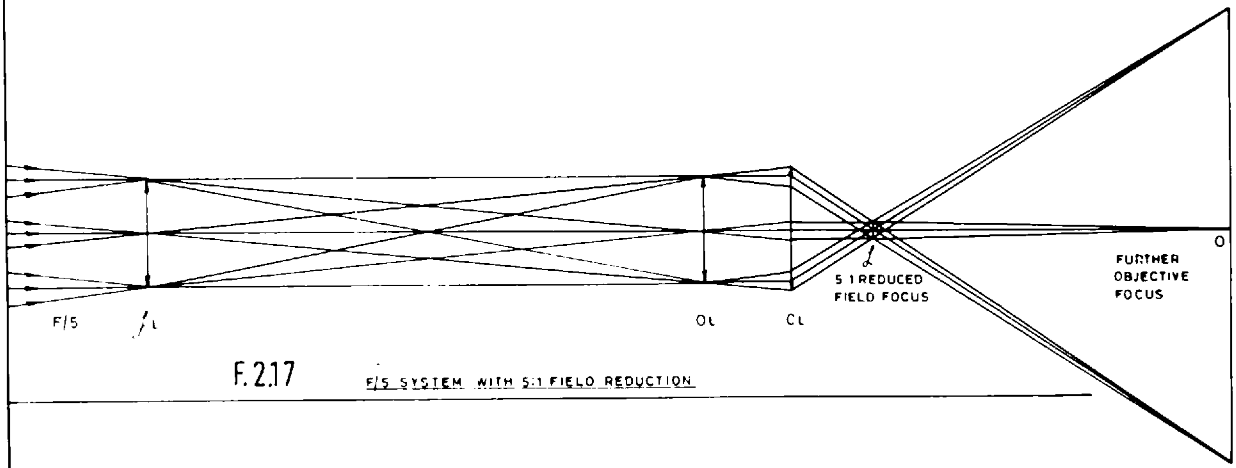

F.2.17 F/5 SYSTEM WITH 5:1 FIELD REDUCTION

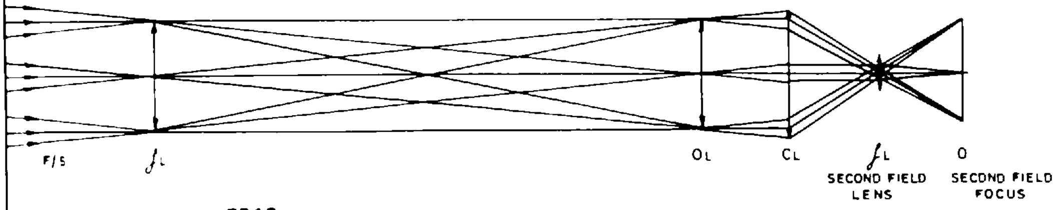

F.2.18 F/5 SYSTEM WITH 5:1 FIELD REDUCTION AND A 1:1 SECOND OBJECTIVE FOCUS

F/5 5:1 FOCAL REDUCERS INCLUDING A COLLIMATED BEAM

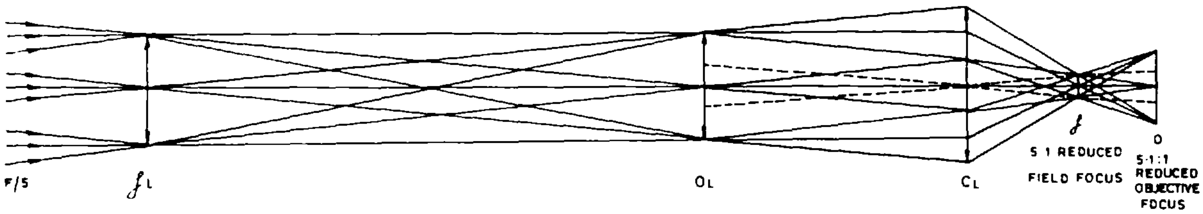

F.2.19 F/5 SYSTEM WITH 5 1 FIELD REDUCTION

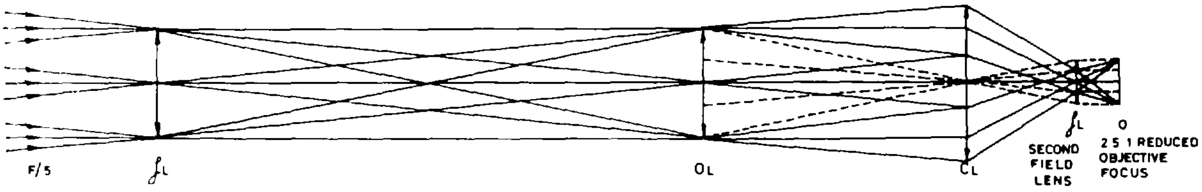

F.2.20 F/5 SYSTEM WITH 5 1 FIELD REDUCTION AND A FURTHER 5 1 OBJECTIVE APERTURE REDUCTION AT F/10.

F/5 FOCAL REDUCERS INCLUDING A COLLIMATED BEAM. CASES WITH AN EXTENDED COLLIMATED BEAM SHOWING ADVANTAGES IN OBJECTIVE SCALE REDUCTION

(b) Focal reducers with collimated beams

Two systems imaging the objective are shown in figures F2.15 and F2.16; both contain collimated beam spaces but neither collimated beam is of much practical use due to the extreme beam divergence in each case. The beam divergence at any aperture is determined by the conservation of throughput : $\sqrt{A\Omega}$ = constant, as given by the product of the telescope F ratio, and the field diameter. Any reduction in aperture in the system from the 91mm will inevitably lead to divergences greater than F/5. The input parameters of F/5 and 91mm field are too severe for any common infrared interference filter; most such filters will operate to specification only in a slower beam convergence than F/5 and are available only up to 25mm diameter. This is not a severe limitation, as the instrument was intended only for use over broad-band without interference filters; these constraints are thus acceptable for a radiometer, but unacceptable for a photometer where narrow bandwidth interference filters are used. The system of F2.16 has a weaker projection lens 'C_L' than shown previously, and has a second field lens, while the system of F2.15 requires a single powerful projection lens and gives a 3.3:1 reduced field image as well as a small scale objective image. The lens 'C_L' has been used to project the field or objective image without scale change.

Figures F2.17 and F2.18 show focal reducers with weak field lenses and large diameter collimated beams with 5:1 field reduction, but with unsatisfactory objective image reduction; note that the introduction of a second powerful field lens in F2.18 considerably reduces the second objective image scale, but still by an insufficient amount to justify the complexity.

A photometric system with interference filters can only be designed by a reduction in the field stop diameter or F ratio or both. The system shown in figure F2.17 was built for the photometers to be described in chapter 5, though in this case the telescope F ratio was F/5 or F/8, and the detector was placed at the reduced field focus 'f' which is a 5:1 reduction of the 25mm diameter field lens stop $'f'_L$. Note that this system has a reduced field of view to those previously described, and so can accommodate 25mm diameter interference filters in the collimated beam without excessive filter band-width broadening or shifts. The exit stop arrangement was designed for use with 4.0 to 5.0mm detectors in a cryostat, where a reasonable back-focal distance was essential to accommodate the cryostat window.

Figures F2.19 and F2.20 show the effect of extending the collimated beam space of figures F2.17 and F2.18, while in F2.19 maintaining the field reduction of 5:1. The system of F2.19 was also built, as a modification to the F2.17 arrangement, but here the input telescope beam was restricted to F/12.8, which enabled the projection lens $'C_L'$ to be considerably reduced in size (the stops for F/12.8 are shown dashed in F2.20) and so accommodated inside the cryostat. This system is further discussed in chapter 7.

Figure F2.20 is a modification of F2.19 to produce a further 2.5:1 reduction of the objective image by the use of a second field lens f_L; with an F/12.8 input beam, and 25mm field stop, the reduced objective focus stop is 4.0mm. This system has the advantage over that of F2.19 of a flatter instrumental profile, but introduces more loss of light by way of the additional optical element. Again this arrangement is suited for use with a cryostat cooled detector, with a clear 25mm cryostat window; this is discussed in chapter 7.

2.05 Summary of reduction systems

The requirement of a 91mm 4.5:1 beam width reduction of an F/5 telescope beam is restrictive on the choice of a reduction system. The simplest and most practical system for a radiometer is either the simple short focus lens (F2.02) or the spherical mirror used at its prime focus (F2.06); all other mirror systems suffer from excessive self obscuration, and an off axis paraboloid or a light cone is inefficient. In either the simple lens or spherical mirror case, the image is of the objective, which for infrared detection purposes is preferred, but the original image may be restored on the same scale as the objective image by inclusion of an objective lens as in F2.14; this additional axial distance of the focus may be of benefit in some cases. Collimated beam focal reducers are not satisfactory for the radiometer, but prove to be satisfactory for a 25mm F/5 to F/12.8 input beam, as in the photometer of chapter 7, where a cryostat was used together with interference filters. The system of figures F2.17 or 2.19 may then be used to give a reduced field focus, or those of F2.18 or F2.20 may be used to give a reduced objective focus.

The systems used in the two infrared radiometers, with uncooled detectors, to be discussed in chapters 3 and 4, are those of the spherical mirror with prime focus, F2.06, and the simple lens, F2.02, respectively; the latter was later adapted to the simple focal reducer of F2.14 for use with a photomultiplier. The system used for the infrared photometer of chapter 5 was that of the focal reducer with collimated beam, figure F2.18, later modified to F2.19; however the system of F2.20 is considered to be preferable and a worthwhile future modification.

2.06 Related work on focal reduction systems (included here for convenience)

A detailed survey of focal reduction systems has been undertaken as a project, now concluded, at R.O.E. for the proposed A.A.T. multi-object spectrograph. An extensive reference list, R2.01 to R2.15, is provided here for further reading on the design of focal reduction systems and spectrograph cameras.

A full historical review of the subject of focal reduction systems is given in chapter 2 of "A.A.T. Multi-Object Spectrometer project" : Design Study Report, ROE 1974, C.J.B.(R2.16). In this case, the focal reduction system was to reduce a 185mm field at the F/8 Ritchey Chrétien focus of the A.A.T. to at 35mm field reduced image with 30μ resolution, to be accommodated by the photocathode of an image tube; the system was to include a collimated beam containing a 125mm diameter objective aperture stop followed by a dispersive element of ones choice (normally a 600 line/mm transmission diffraction grating). In the 'A.A.T. Multi-Object Spectrometer design specification', ROE 1974, C.J.B. (R2.17), a system was proposed using a field lens, Tessar type collimator, and Wynne Schmidt-Cassegrain camera. Contracted work to Grubb Parsons and Professor C. Wynne produced a final practical system as described in the Grubb Parsons 'Multi-Object Spectrometer design study report I and II, (R2.18, R2.19), mostly achieving 12μ spatial resolution from λ 0.37 μ to λ 0.50 μ wavelength range, with a standard spectral resolution of 10 Å, with a 20 arcmin field on the A.A.T. and a 1 hour exposure magnitude limit of m18.5 to m19; it would be used with a focal plane mask with 1 arc sec apertures to remove the sky background light. The instrument would have various uses, but was principally designed for simultaneous spectrography of feint clusters of galaxies.

References for Chapter 2

R2.01 Courtes, G., c.r. le bd seanc Acad. Sci. Paris 234, 506-2424

R2.02 Ring, J. Courtes, G. 'Astronomical Optics Col. Manchester (1955)'

R2.03 Ring, J. Col. Bellevue (Mar. 1958), J. de Physique, 19

R2.04 Meinel, A.B. 'An F/2 Cassegrain Camera'. Ap. J. (1956) 124, 652

R2.05 Courtes, G. 'Methodes d'observation et etude del'hydrogene interstellaire en emission'. Ann. d'Astrop. 23, No. 2, 115

R2.06 Courtes, G. 'Quelques realisation instrumentales en France' 5, (1966), No. 9, 1349

R2.07 Meaburn, J. (ref. Ring, J., Woolf, N. 1958). 'Cameras and filters for nebula photography'. Astrop. Space Sci. (1968)

R2.08 Wilson, R.N. 'Large Telescope Design', 155, R.M. West ed. Geneva 71

R2.09 Serkowski, K. 'Some possibilities of increasing the efficiency of optical telescopes'. The Observatory. 87, 961, 259

R2.10 Gascoigne, S.C.B. 'Some recent advances in optics of large telescopes'. Q. Jl R. ast. Soc (1968), 9, 98-115

R2.11 Gascoigne, S.C.B. 'Recent advances in astronomical optics.' App. Optics (1973), 12, 1419

R2.12 Reddish, V.C. PILOT 8 Report

R2.13 Reddish, V.C. PILOT 18 Report

R2.14 Wynne, C.G. 'Five spectrograph camera designs.' Mon. Not. R. Ast. Soc. (1972), 157, 403-418

R2.15 Wynne, C.G. 'Spectrographic cameras of the Maksutov and related types' Auxiliary Instrumentation for large telescopes conference - CERN/ESO (May 1972).

R2.16 Baddiley, C.J. 'A.A.T. Multi-Object Spectrometer Project : Design Study Report'. (ROE 1974)

R2.17 Baddiley, C.J. 'A.A.T. Multi-Object Spectrometer Design Specification.' (ROE 1974)

R2.18 Wynne, C. 'Multi-Object Spectrometer Design Study Report Stage I.' Grubb Parsons. (1974)

R2.19 Wynne, C. 'Multi-Object Spectrometer Design Study Report Stage II'. Grubb Parsons (1974)

CHAPTER 3

3. Grid light modulators and the first radiometer.

Contents:

GRID LIGHT MODULATORS AND THE FIRST RADIOMETER

3.01 Modulation systems: the requirements and some methods

The first radiometer was based on the optical configuration shown in figure F2.01, using the prime focus of a 91mm diameter spherical mirror at F/0.9. A 20mm square PbS plate detector was to be used at the prime focus, mounted on the face of a 26mm diameter cylinder containing a bias resistor and preamplifier identical to that proposed for the F.C.M.I. output. Manufacturer's data on the PbS detector showed the optimum signal/noise to be at a carrier frequency of 400Hz at room temperature. The requirement was then for a modulation unit capable of chopping at least a 25mm field at 400Hz such that the detector may see alternately the source and a blank reference at this carrier frequency.

There are several methods of achieving alternate transmission and absorption of light over a large field (R3.01). The obvious choice of a rapidly rotating disc containing equi-spaced holes (R3.04) was temporarily avoided, as it was feared that without particularly good isolation it would give rise to unacceptable vibration of the F.C.M.I. table; such a rotating disc radiometer was in fact built as described in chapter 5. A possible alternative would have been a Kerr cell system, but the expected transmission and efficiency was not considered sufficient (R3.02, R3.04 and R3.05). This chapter is concerned with vibrating vane and grid systems to give the required 100% modulation of the 26mm field at 400Hz.

3.02 A tuning fork chopper

A commercial 'Accutron tuning-fork' mounted with 4mm wide x 10mm long vanes was set up covering the face of a 20mm PbS detector and was used in some trials at the focus of the optical mirror arrangement of F2.01, but was found unsatisfactory for several reasons:

The maximum relative tine motion amplitude gave approximately an 2mm maximum tine separation gap, and the times when closed did not cover the detector, (the diameter of the light beam clear of the detector in F2.01 was at least 2.6mm); the tine motion was accurate, leading to a non-parallel sided gap; the angle between the waves varied according to wave separation. The fork was driven by a small amplifier and solenoid arrangement; the drive signal was obtained from a magnetic pick-up coil close to one of the tines, hence the fork was driven in resonance and was self-stabilising in amplitude. Little vibration was transmitted from the fork assembly; the fork assembly, and also the detector assembly were mounted by a cross system of tension wires to a frame, which effectively eliminated acoustic pick-up at the detector and also vibration on the base plate.

Several modifications to the wave shape and tine drive system were attempted all in order to increase the tine amplitude and increase the effective radius of the arcuate motion; none of these attempts proved successful and the system was finally abandoned.

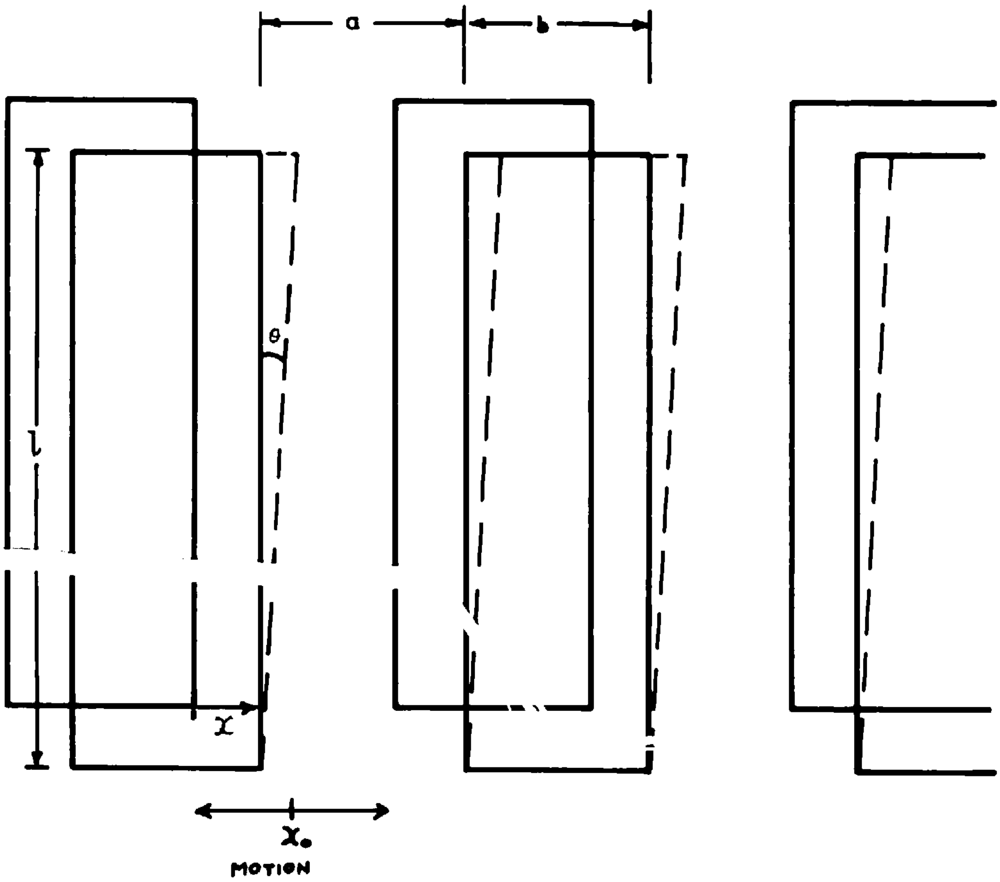

F. 3.01 MOIRÉ GRID PARAMETERS

3.03 Moiré grid modulation systems

Light chopping over large apertures may be performed with small amplitudes by the use of two identical Moiré grids. The grids are superimposed with the grids parallel, then the relative grid displacement required to produce maximum change in the integrated light transmission through the grids is just one half grid spacing. A study was made of the effect of non-parallel and also curved grids, vibrated with non-sinusoidal periodic waveforms. Figure F3.01 shows an enlargement of a section of a Moire grid; in a general case, the grids will not be precisely parallel. It can be shown that slight tilt of the grids produces a reduction in the maximum possible transmission amplitude by an amount $\frac{l \tan \theta}{2a}$ where 'θ' is the tilt angle. When the two grids are coincident, then the transmission takes a maximum corresponding to a 50% light obscuration by the coinciding grids. The maximum obscuration is for the two (1:1, a = b) grids to lie between each other, transmission then being zero; the displacement necessary for this is one half grid spacing, (a), implying that the equilibrium position for a periodic motion must be that to produce 50% overlap (i.e. the transmission gap is then $\frac{a}{2}$). Any departure from this condition, such as the amplitude of maximum displacement exceeding 'a' or the mean position x_0, $\neq \frac{a}{2}$, will result in the generation of a second harmonic term in the transmission waveform. For example, if the equilibrium mean position were $x_0 = 0$, (grids coincident), then a sinusoidal displacement of total amplitude 'a' will give rise to a 50% decrease in modulation amplitude of the light, with modulation at twice the drive frequency. Second harmonic of the carrier frequency is rejected by the synchronous rectifier, and so amounts to a loss of signal. It is clear that the setting up condition of such a Moiré grid, and the displacement motion amplitude, are particularly critical. A Moiré grid as described, can be used to modulate light over a large field area, with only a small displacement motion. The amplitude of motion required is given by the grid spacing; a very fine grid spacing requires a similarly small amplitude of motion but requires great care in setting up. A 0.25mm broad grid line with 0.5mm spacing was selected for the 26mm field, and the grid and its replica was constructed as a high contrast photographic negative reduction of an 1:1 mark-space ink line grid. Then a 0.25mm relative grid displacement would produce the maximum 50% light modulation; however, for 5% repeatability, the vibration amplitude and mean grid position would have to be stable to 12 μ. An additional problem arises from the high F convergence of the optical beam from the mirror of figure F2.01; this will lead to indefinite shadowing of the first grid onto its replica, unless the two grids are effectively in the same place. The photographic negative grids, used in the radiometer to be described, presented noticeable attenuation of light from the two layers of negative emulsion in excess of the inevitable 50% light loss from the grids themselves.

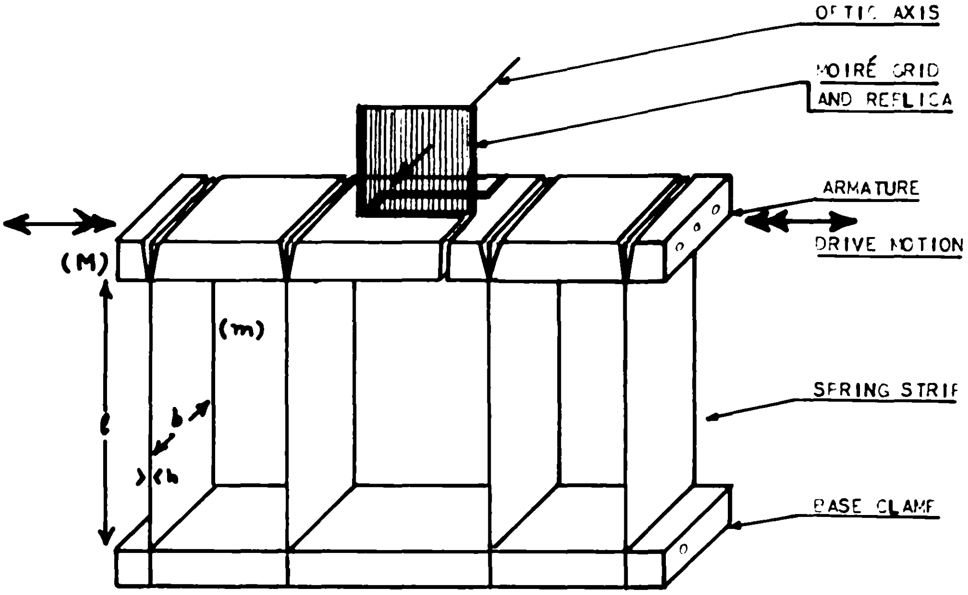

F. 3.02

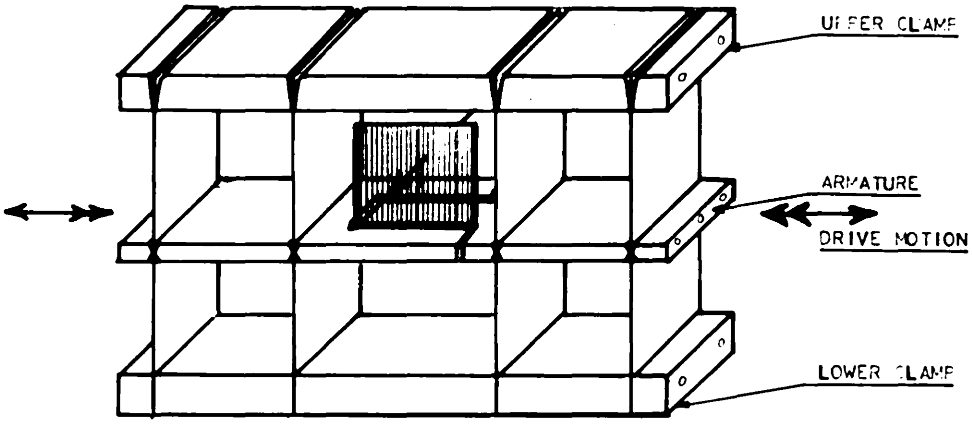

F. 3.03

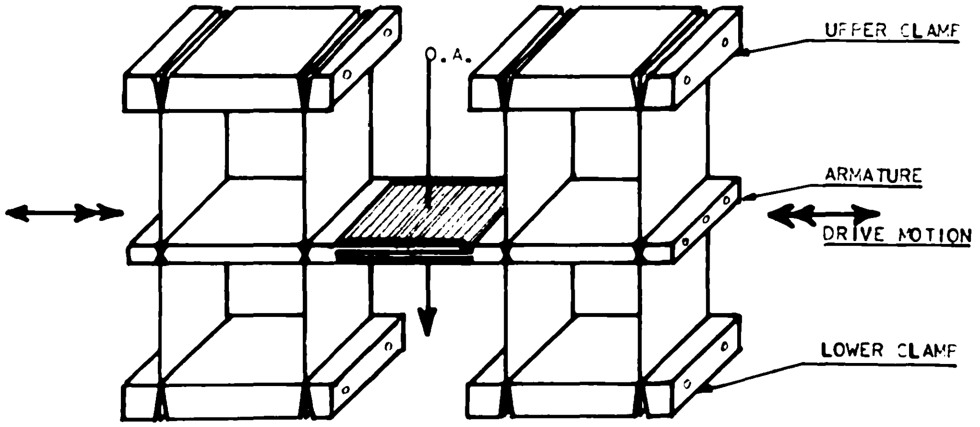

F. 3.04

PARALLEL, PLANAR RESONATORS FOR A MOIRÉ GRID

3.04 Resonant systems producing parallel armature motion

In order to obtain intensity modulation of a radiation beam with a Moiré grid, some suitable means of constrained linear vibration must be found. This section discusses some possible mechanical arrangements to produce this required constrained motion. Any departure of such motion from linearity will produce misalignment of the grids with a consequent introduction of harmonics into the modulation profile; resonant systems are considered preferable to non-resonant systems in order to meet the otherwise large power requirement for an amplitude of the order of 0.3mm at the detector optimum operating frequency of 400Hz.

Frequency and power function

A comparison is here made of three spring cantilever arrangements as shown in figures F3.01 and F3.03, with a view to their relative power consumptions.

(a) Free ended spring cantilever of F3.02

Consider a single spring cantilever as in F3.02, with length l, thickness h, width b and spring mass m, load mass M displaced by x from equilibrium.

The force F to give a displacement y of the free end of two cantilevers is

$$F = \frac{2\,(3EI)}{l^3} \qquad \text{E3.01}$$

$$\text{where } I = \frac{bh^3}{12} \qquad \text{E3.02}$$

For a simple harmonic motion:

$$\ddot{x} + \frac{k}{\mathfrak{m}} x = 0 \qquad \text{E3.03}$$

where $k \equiv \frac{F}{x}$ E3.04

and $f = \frac{\omega}{2\pi} = \frac{1}{2\pi} \frac{k^{\frac{1}{2}}}{\mathfrak{m}^{\frac{1}{2}}}$ E3.05

power $p = \frac{f}{Q} \int_{0}^{\hat{x}} F dx$ E3.06

From E3.01, E.302, E3.06 for S.H.M. $p = \frac{f}{Q} \frac{k\hat{x}^2}{2}$ E3.07

Then from E3.05 $p = \frac{2\pi^2 \mathfrak{m}}{Q} f^3 \hat{x}^2$ E3.08

In the case of F3.02

from E3.01, E3.02 and E3.04 $k = \frac{2\ (3E\ bh^3)}{12\ l^3} = \frac{Eb}{2}\left(\frac{h}{l}\right)^3$ E3.09

The inertial mass $\mathfrak{m} = \frac{2}{3}\frac{m l^2 + M l^2}{l^2} = \frac{2}{3} m + M$ E3.10

where l is the radius of giration

Then from E3.05 $f = \frac{1}{2\pi} \frac{(Eb)^{\frac{1}{2}}}{2^{\frac{1}{2}}} \frac{\left(\frac{h}{l}\right)^{3/2}}{(M + 2m/3)^{\frac{1}{2}}}$ E3.11

and from E3.08, E3.09

$$p = \frac{2\pi^2}{Q} \left(M + \frac{2}{3} m\right) f^3 \hat{x}^2 \qquad \text{E3.12}$$

(b) Two constrained but not clamped cantilevers, motion about centre

This may represent F3.03 where the upper pivots are not tightly clamped.

The inertial mass of half the armature about the centre is

$$2 \, \frac{1}{3} \left(\frac{m}{2}\right) \frac{l^2}{4} + \frac{M}{2} \, \frac{l^2}{4} = \frac{m}{3} + \frac{M}{2} \qquad \text{E3.13}$$

The force for the two halves is then

$$F = 2 \times 2 \times \frac{3Eb}{12} \, \frac{h^3}{(l/2)^3} = 8 \, Eb \left(\frac{h}{l}\right)^3 \qquad \text{E3.14}$$

and

$$k = 8 \, Eb \left(\frac{h}{l}\right)^3 \qquad \text{E3.15}$$

Then from E3.05

$$f = \frac{2^{\frac{1}{2}}}{\pi} \quad \frac{(Eb)^{\frac{1}{2}}}{\left(M + \frac{2}{3} m\right)^{\frac{1}{2}}} \left(\frac{h}{l}\right)^{3/2} \qquad \text{E3.16}$$

and from E3.08

$$P = \frac{2\pi^2}{Q} \left(M + \frac{2}{3} m\right) f^3 \hat{x}^2 \qquad \text{E3.17}$$

(c) Two clamped cantilevers, motion about centre

These may be represented by, F3.04 with both ends clamped.

The force constant from the accurate motion is as in E3.15.

$$k_1 = 8\,Eb\left(\frac{h}{l}\right)^3 \qquad \text{E3.18}$$

But there is an additional term due to tension produced in the spring.

The tensional spring force from one half spring is

$$E\ hb\left\{\frac{\Delta l/2}{l/2}\right\} \qquad \text{E3.19}$$

and $$\frac{\Delta l}{l} = \frac{(l^2+x^2)^{\frac{1}{2}}}{l} - \frac{l}{l} = \left(1+\frac{x^2}{l^2}\right)^{\frac{1}{2}} - 1 \qquad \text{E3.20}$$

horizontal tensional force is then:

$$Ehb\ \frac{y}{(l^2+x^2)^{\frac{1}{2}}}\ \left((1+x^2/l^2)^{\frac{1}{2}} - 1\right) = \frac{EhB\,x}{l}\left(1 - (1+x^2/l^2)\right)^{-\frac{1}{2}} \qquad \text{E3.21}$$

Then the total tensional horizontal force is

$$F_2 \simeq 4\ \frac{Ehb\ x}{l}\ \frac{x^2}{2l^2} = 2\,Ehb\left(\frac{y}{l}\right)^3 \qquad \text{E3.22}$$

Then $F = 8Eb \left(\frac{h}{l}\right)^3 x + 2\,Ehb \left(\frac{x}{l}\right)^3$

$$= 8\,Eb \left(\frac{h}{l}\right)^3 \left(1 + \frac{1}{4}\left(\frac{x}{h}\right)^2\right) x \qquad \text{E3.23}$$

The equation of motion is

$$\ddot{x} + \frac{8Eb \left(\frac{h}{l}\right)^3 x + 2\,Ebh \left(\frac{x}{l}\right)^3}{(M + \frac{2}{3}m)} = 0$$

$$= \ddot{x} + \frac{8\,Eb \left(\frac{h}{l}\right)^3 \left\{1 + \frac{x^2}{4h^2}\right\} x}{(M + \frac{2}{3}m)} = 0 \qquad \text{E3.24}$$

This contains higher harmonics but has a fundamental frequency

$$f_o = \frac{1}{\pi}\; 2^{\frac{1}{2}} \frac{(Eb)^{\frac{1}{2}} \left(\frac{h}{l}\right)^{3/2}}{(M + \frac{2}{3}m)^{\frac{1}{2}}} \qquad \text{E3.25}$$

and

The power $p = \frac{f_o}{Q} \int_0^{\hat{x}} F\, x\, dx$

$$= \frac{f_o}{Q} \int_0^{\hat{x}} f_o^2\, 4\pi^2 (M + \frac{2}{3}m)\left(1 + \frac{x^2}{4h^2}\right) x \; dx$$

then $$p = \frac{f_o^3}{Q}\; 2\pi^2 (M + \frac{2}{3}m)\left(1 + \frac{\hat{x}^2}{8h^2}\right) \hat{x}^2 \qquad \text{E3.26}$$

Summary Table 3.1

	a Free cantilever	b Constrained cantilever	c Clamped cantilever
k	$\frac{Eb}{2}\left(\frac{h}{l}\right)^{3}$	$8\,Eb\left(\frac{h}{l}\right)^{3}$	$8\,Eb\left(\frac{h}{l}\right)^{3}\left(1+\frac{1}{4}\left(\frac{x}{h}\right)^{2}\right)$
f_o	$\frac{(Eb)^{\frac{1}{2}}\left(\frac{h}{l}\right)^{3/4}}{2M2^{\frac{1}{2}}(M+\frac{2}{3}m)^{\frac{1}{2}}}$	$\frac{2^{\frac{1}{2}}(Eb)^{\frac{1}{2}}\left(\frac{h}{l}\right)^{3/2}}{M(M+\frac{2}{3}m)^{\frac{1}{2}}}$	$\frac{2^{\frac{1}{2}}(Eb)^{\frac{1}{2}}\left(\frac{h}{l}\right)^{3/4}}{M\,(M+\frac{2}{3}m)^{\frac{1}{2}}}$
$\bar{p}$	$\frac{2\pi^{2}}{Q}(M+\frac{2}{3}m)f^{3}\hat{x}^{2}$	$2\pi^{2}(M+\frac{2}{3}m)f^{3}\hat{x}^{2}$	$\frac{2\pi^{2}}{Q}(M+\frac{2}{3}m)\left(1+\frac{1}{8}\left(\frac{\hat{x}}{h}\right)^{2}\right)f^{3}\hat{x}^{2}$
relative $\left(\frac{h}{l}\right)$ for same f		${}^{1}/_{4}{}^{2/3}$	${}^{1}/_{4}{}^{2/3}$
relative k for same f		1	$1+\frac{1}{4}\left(\frac{x}{h}\right)^{2}$
relative p for same $f, \hat{x}$		1	$1+\frac{1}{8}\left(\frac{\hat{x}}{h}\right)^{2}$

3.05 Resonant systems producing parallel motion: relative advantages

The first and second systems discussed (a, b) are not linearly constrained, unlike the third system (c), in that they have arcuate motion in the vertical plane as shown, but have a smaller power rating for a given amplitude and less harmonic content in the motion than that of system 'c'. For small amplitudes the arcuate motion is slight, but at a high-frequency resonance such as 400Hz. the spring thickness must be comparatively large so as to permit resonance with long spring lengths, thus maximising the arc radius.

The third system discussed ensures parallel linear motion of the grids, (the motion is constrained to a vibration along a straight line). In order to produce a comparable deflection, as in the first system, the tensional strain forces in the springs will be significant (see table T3.1), due to the necessary stretching of the springs where both ends on the springs are clamped; this also leads to a vibration of high harmonic content. In the event of one of the ends of each spring being constrained but not clamped, as in b, the strain forces are reduced and hence the harmonic content is lowered, but the motion is no longer linear. Concerning vibration to the supporting framework, it was considered that as the double-clamped end system'c'is symmetrical, and the line of symmetry is along the axis of vibration, then this system, when balanced along the axis by a similar one in antiphase, gives the least transmitted vibration, provided the displacement is very small, i.e. ($\hat{x} < h$).

F.3.05a

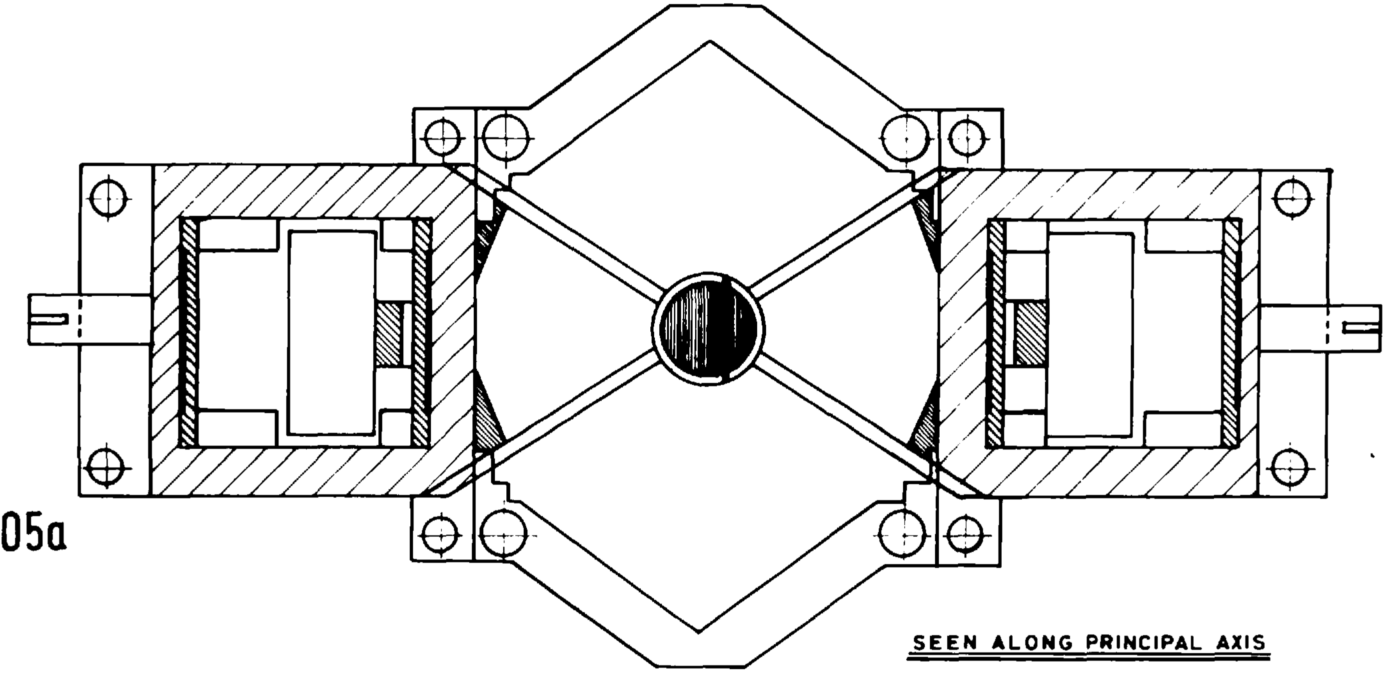

F.3.05b

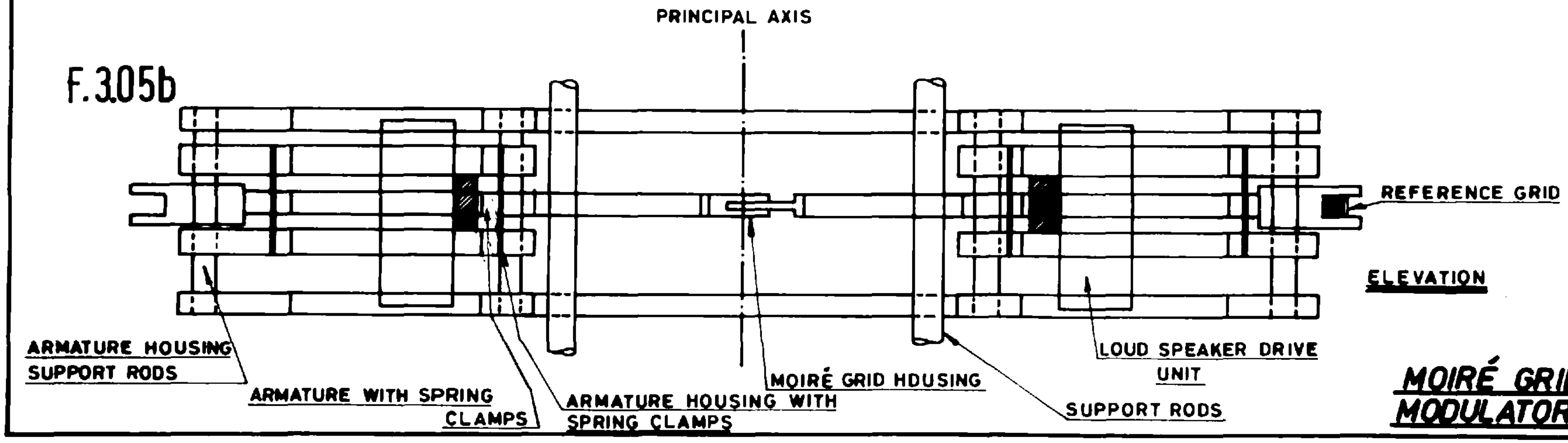

MOIRÉ GRID MODULATOR

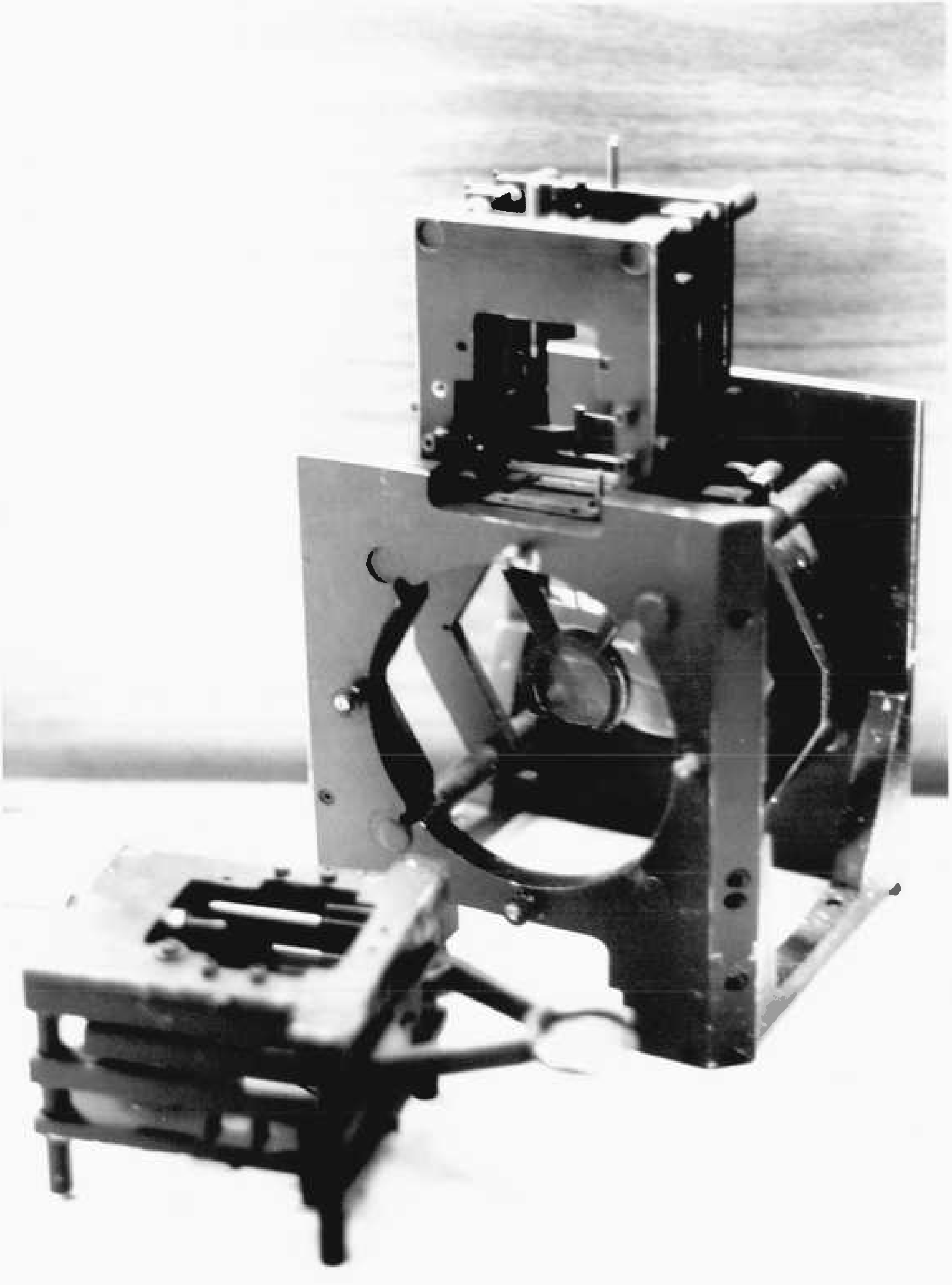

P3.1

THE MOIRÉ GRID RADIATION MODULATOR AS USED IN THE FIRST RADIOMETER

3.06 The clamped spring cantilever system of the first radiometer

The design selected for the radiometer was based on system 'b' or 'c' depending on whether the spring ends were to be clamped or just constrained. Two solenoids were used to drive the two resonant systems shown in figures F3.05a, F3.05, and photograph P3.1; each solenoid was supported between two parallel frames which also carried the spring clamps. The separation of the frames could be adjusted by sliding them on the steel rods running into holes in the frames. The framework was made of aluminium and the spring clamp jaws of brass, while the springs were made of 0.5" x 15 thou. spring steel; the frames were separated by about 2cm with a similar but lighter frame clamped midway, supporting an armature to the grid frame. The solenoid was attached to the centre frame close to the plane of the front two of the four supporting springs. The two opposed resonant systems were rigidly connected by an extension of the clamping frames, and the armatures projected across the optical beam in 60^{0}, 120^{0}, 60^{0}, and 120^{0} orientation, see F3.05a and P3.1. The grid support frame ring was about 30mm in diameter and cut away such that the ring of one vibrator armature fitted in the slot of the other armature to maintain coplanar centres of mass for the two vibrators. The general scale and extent of the armatures of the system was dictated by the available space and size of the optical beam. Small counter-weights were fitted at the opposite ends of the armatures to the grid supports, and one of these weights was fitted with a 5mm square grid and duplicate grid fixed to the outer supporting frame, for use in the reference channel detection system.

3.07 (a) The general layout of the radiometer

The optical layout was dictated by the limited available space between the wall of the observing room and the focal plane of the 40" F/5 telescope at Silwood Park Ascot, arranged as previously discussed and given in figure F2.01. The focal plane was to form the entrance pupil of the F.C.M.I., and so the whole photometer had to be confined to a 330mm gap between the telescope observing room wall and the F.C.M.I. table. In order to accommodate the same field as the F.C.M.I.; the field stop of the photometer was 1^{o}, or 92mm, at F/5, and reduced onto the detector of 20mm square. As previously discussed, the design most suited for a very limited space, where self-obscuration is not of prime importance, is that of a parabolic mirror. In this case a spherical mirror was used, with a radius of curvature of 83mm and a diameter of 92mm. A beam splitter was placed diagonally in the main beam to reflect some of the incident light through 90^{o} clear of the main beam. It was necessary to place the diagonal flat as far up the beam as space would allow, such that the reflected focal plane was as far from the main beam as possible; the flat was thus rather large, but gave sufficient clearance from the focal plane to allow room for the above spherical mirror and a further 30mm clearance after the reduced image. The spherical mirror was placed in the focal plane, such that the reduced image was that of the telescope primary mirror; the resultant focal ratio was then F/0.9. By arranging the grid supports and detector supports radially, the obscuration produced by the struts is minimised (essentially self-obscuration). The 26mm diameter, 0.25mm pitch grids were mounted just before the detector with the two sets of grids in close contact so as to minimise scale change effects from the highly convergent beam. The mirror cell holder was designed to be fairly rigid and also to support the four horizontal rods holding and locating the whole vibrator supporting frame; the vibrator frame and grid position could thus be easily adjusted along the optical path.

All optical components were screwed down onto a base plate, but due to the limited width of this plate, the vibrator system had to be mounted in a vertical plane, with one vibrator assembly projecting underneath the base plate. The beamsplitter frame was designed for easy adjustment of tilt and rotation, and easy removal of the mirror. An eyepiece was placed in the focal plane on axis of the main beam; the detector was supported on a block of Tufnol mounted on the end of an aluminium cylinder, supported by two sets of four radial wires in tension, thus minimising acoustic vibration transmitted to the detector.

(b) The wavelength response

A Kodak gelatine red filter was placed between the grids and the detector, limiting the wavelength response in the visible to a minimum wavelength of $\lambda 0.75\mu$; no other filters were used as the radiometer was required

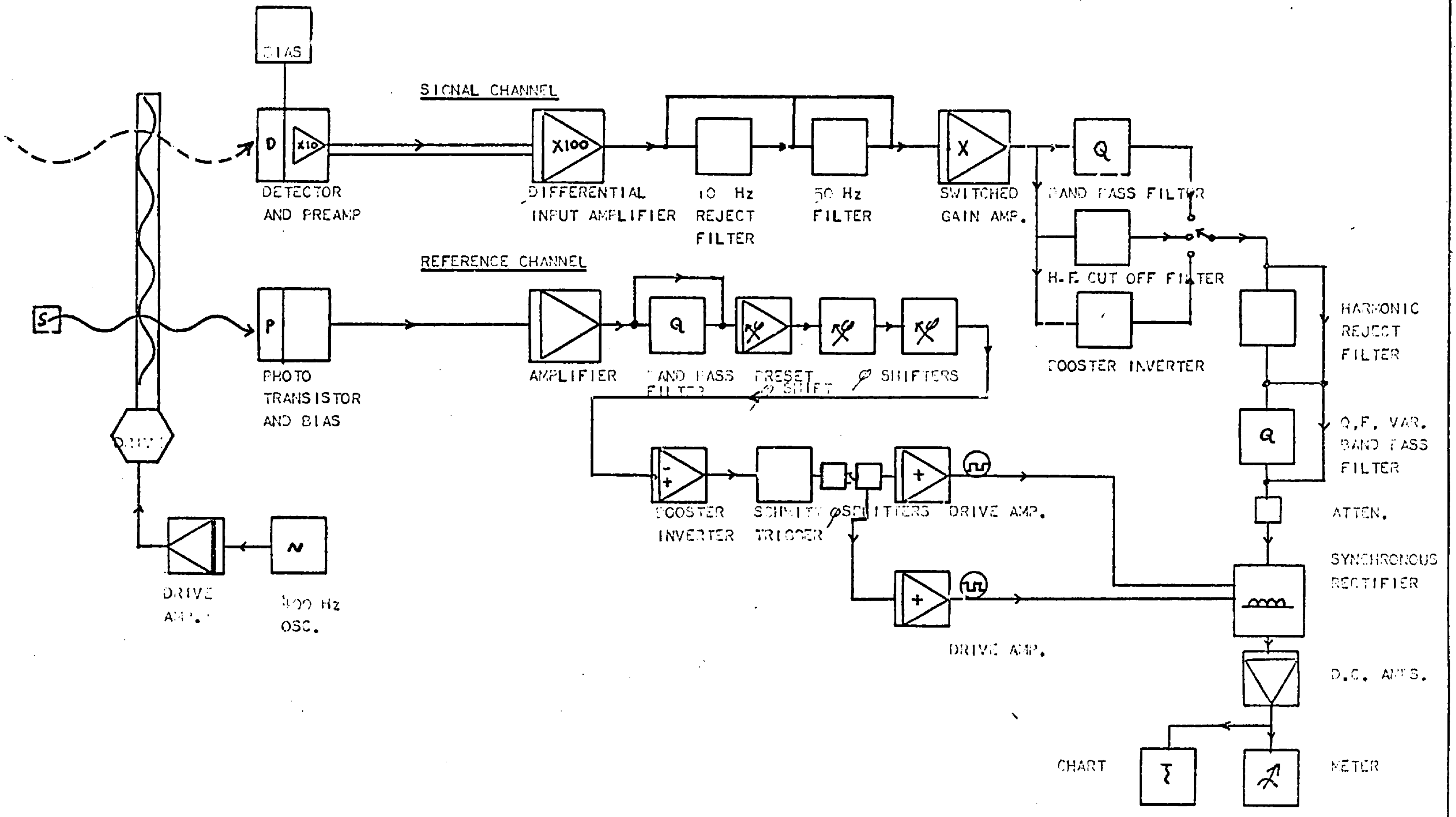

F.3.06 **BLOCK LAYOUT OF RADIOMETER CIRCUITS** as much as possible to simulate the wavelength response of the F.C.M.I.; besides this, the F ratio of the reduced image excluded the use of interference filters. The sensitivity of the plate detectors reaches a maximum at about $\lambda 2\mu$ and falls dramatically after $\lambda 2.4\mu$; the acetate base of the photographic film, like glass, limits the transmission response to about $\lambda 2.5\mu$.

3.08 The Radiometer electronic circuits

An experimental circuit was built, as given in the block diagram F3.06; this is conveniently broken down into a signal channel, reference channel and drive unit; the circuit details were modified over a period of time, and the final version is discussed in detail in chapters 6 and 7.

(a) Signal channel

The detector bias battery was of a symmetrical earth design with switched attenuators such that the normal voltage level of the detector-bias resistor junction was close to zero. The preamplifier mounted close to the detector was A.C. coupled to this junction, and was of a simple F.E.T. follower design followed by a X10 voltage gain stage to drive the line to the main amplifiers. The main amplifier had a common mode rejection input, switched preset gain, and several experimental filters for rejecting mains hum and selected harmonics of the carrier frequency.

(b) Reference channel

The original photo transistor output signal was amplified and filtered in the first reference channel stage; a duplicate optional Q band pass filter to that in the signal channel maintained the relative phase relation between the signal channel. Two phase shifters, one coarse and one fine, were used to adjust the two channels to the same phase; several operational amplifier designs were tried but that finally selected used a single transistor, (see chapter 6). This was followed by a drive amplifier and a Schmitt trigger (later abandoned) then a phase splitter to two drive amplifiers. Rectification was achieved with a standard synchronous rectifier circuit switched by the reference drive amplifiers. Several synchronous rectifier designs were tried and compared for their relative suppression of random noise and side bands; the one finally selected is discussed in chapter 6; a range of time constants was provided in steps of X10 up to 100 seconds. The D.C. output signal was usually monitored with a meter and chart recorder.

(c) Drive Circuits

A low frequency oscillator was built, together with a power amplifier, to drive the two loudspeaker electromagnets at 400Hz. It was later found necessary to provide a preset power amplifier gain setting and a fine frequency control on the oscillator. The loudspeaker coils were wired electrically in parallel and in phase, but were geometrically opposed when located in the vibrator frame.

(d) Artificial source

For test purposes, it was found necessary to build a small artificial star, consisting of a small bulb and tapered light pipe, placed in front of the field lens and powered from a stabilised supply.

3.09 Tests and modifications to the radiometer

The spring clamp frames were adjusted to be parallel and the armature made to lie midway between the two frames; this was achieved by inserting a pair of identical spacer blocks in the spring gaps during tightening of the clamp screws.

On application of the drive voltage to the electromagnets, it was soon established that the resonance was about 15% lower than that predicted (400Hz); this was corrected by iterative reduction of the resonance gap (or effective spring length). The resonances were found to have a high Q, and the two armatures had noticeably different resonance frequencies, such that for a given power the amplitude of motion of the two armatures differed by several fold, and the slightest change in temperature such as that produced by vibration energy dissipation, or any sign of metal fatigue, would produce a large relative amplitude change from the rapidly changing phase function of resonance. It was also found difficult to preserve the positional stability of the grids to the required 12μ accuracy. Relative amplitude change effects produced by high Q phase shifts may be eliminated by clamping one grid armature and only allowing the other one to move; the maximum resultant amplitude is then halved, which in the case studied proved insufficient amplitude for an efficient modulation, even with maximum power delivery. A finer grid pitch spacing would have overcome this problem, but this would require a corresponding increase in positional accuracy.

Some considerable pickup interference was noticed on the detector when the drive was on; it was found that this could be reduced by screening the detector with a horizontal coarse earthed wire grid, and it could be effectively eliminated by application of a small voltage to the Moiré grid armature, with respect to the earthed base plate.

The overall maximum transmission for the grid was considerably less than the expected maximum of 50%, due to attenuation by the two layers of negative emulsion; and as a result of this, and the effects of metal fatigue and amplitude and phase stability, this mode of chopping was finally abandoned in favour of the traditional disc method.

A list of references for light modulation techniques is given.

References for Chapter 3

R3.1 Ellis, Band, Walton, A.K. 'Optical Modulators, a Survey of the Literature'.

R3.2 Cranemeyer, D.C. and Spanberger, L.R. I.R.'Transmittance + Kerr Effect of nitrobenzene.' J. Opt. Soc. Am (1961) 51, 1061

R3.3 Keith, K.H. and Jones, O.C. 'The modulation of light at extreme frequencies'. J.S. Ins. (1965), 42, 729

R3.4 Baybulator, K.M. 'Modulation of light beams of annular section'. Soviet J. apt. Tech. (1969), 36, 672

R3.5 Moss, T.S. 'Methods of modulating infrared beams - a comparison of solid state systems', J. Infra. Phys. (1962), 2, 129

CHAPTER 4

4. The disc-chopper near-infrared radiometer and photometer.

Contents:

THE DISC-CHOPPER NEAR-INFRARED RADIOMETER AND PHOTOMETER

4.01 Design of the first disc and motor housing

The optical arrangement of the grid radiometer as previously described cannot be used with a disc chopper arrangement, as the obscuration from the disc would effectively block out half of the input beam; after considering the various alternatives of F2.02 to F2.05 and F2.07, F2.08, it was decided to build a simple lens arrangement of F2.01, where the beam splitter was replaced by an aluminised flat, and the plane of the disc was placed just before the objective image. A base was built around the base plate, with a large mains-powered motor housed above the optic axis. The disc was about 230mm in diameter with 35mm diameter holes (8) at 70mm intervals; the disc should ideally rotate at 3500 r.p.m., but in practice would only achieve 2000 r.p.m.,with a corresponding reduction in modulation frequency.

The 20mm PbS plate detector was mounted on the end face of a short cylinder located by rubber anti-vibration mountings to an outer concentric cylinder, which in turn projected from the end wall of the radiometer box. A F.E.T. preamplifier was mounted on the back of this detector housing, also containing the necessary bias resistor arrangement, while the bias battery box and amplifier boxes were connected by long cables. A phototransistor and light source were used as before for detection of the disc hole positions and for operation of the reference switching of the synchronous rectifier.

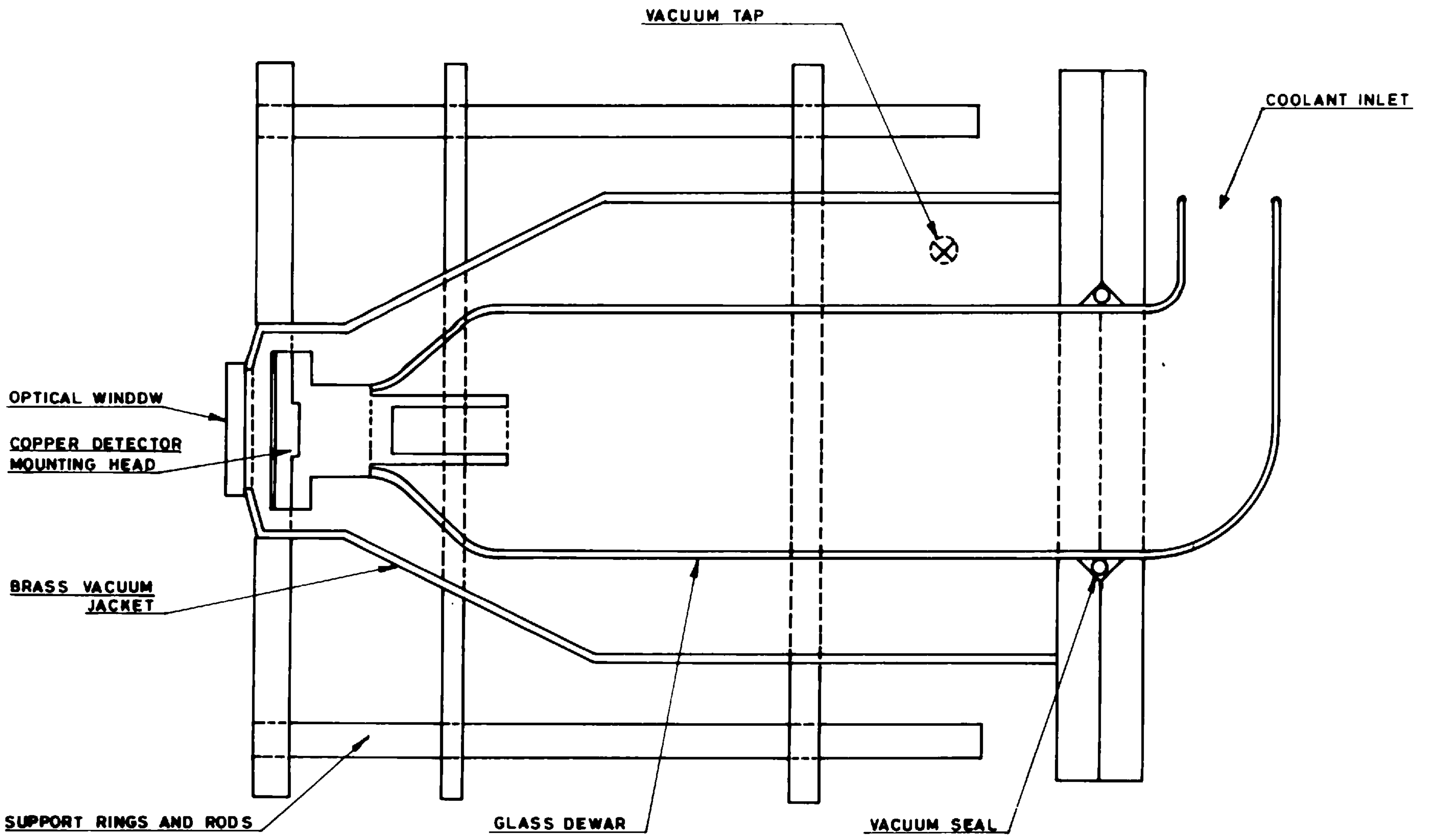

F.4.01 THE ORIGINAL CRYOSTAT

4.02 Operation of the disc-chopper radiometer

This system was operated on the Silwood Park 40" flux collector, from which it was shown that bright astronomical infrared sources such as planets could be detected up to $\lambda 1.35\mu$ as defined with an A.D.P. 1.35μ roll-off filter, beyond which thermal drift from the reference disc and rapid emission fluctuations dominated, see figure F1.03. The near infrared scattering function of atmospheric water vapour was confirmed, where the moon provided a convenient source.

4.03 Cryostat design for the disc-chopper radiometer

In order to increase the sensitivity of the detector, it was decided to build a cryostat capable of accommodating the 25mm F/0.9 beam. The cryostat consisted of a glass dewar mounted in a brass vacuum jacket, with a 27mm diameter optical window, as shown in figure F4.01; the detector mounting block was made of high conductivity copper in two parts, such that the detector mounting flange could be unscrewed from the remaining head.

The 20mm square detector was not suitable for cooling, and was replaced with a 5mm square cooled type, cemented onto the detector flange with low temperature 'araldite'. A bias resistor was fixed to the reverse side of the copper head flange, connected to the detector via feed-throughs; the biasing arrangement was supplied from a bias battery, connected, together with the preamplifier, via more feed-throughs in the end vacuum flange.

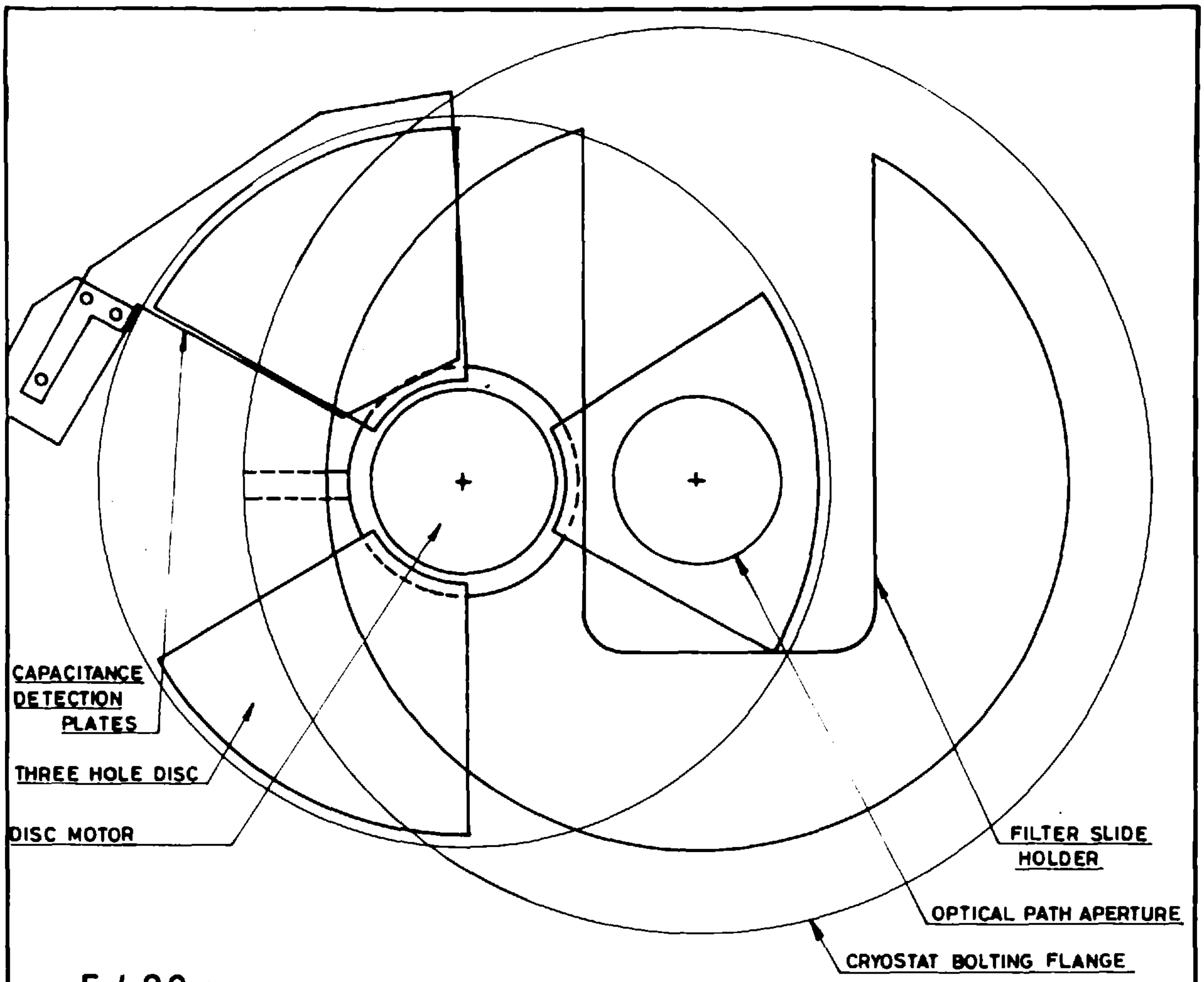

F. 4.02a

ELEVATION (SUPERPOSITION)

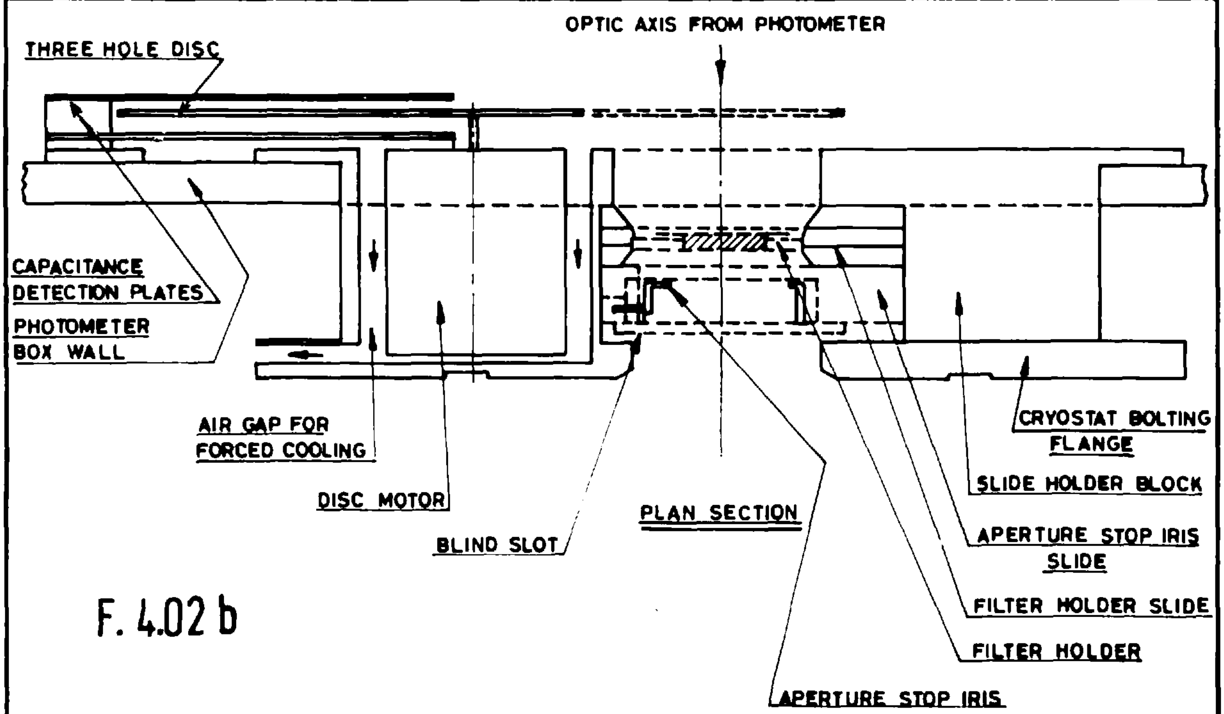

F. 4.02 b

FILTER SLIDE HOLDER, DISC, MOTOR AND CRYOSTAT FLANGE

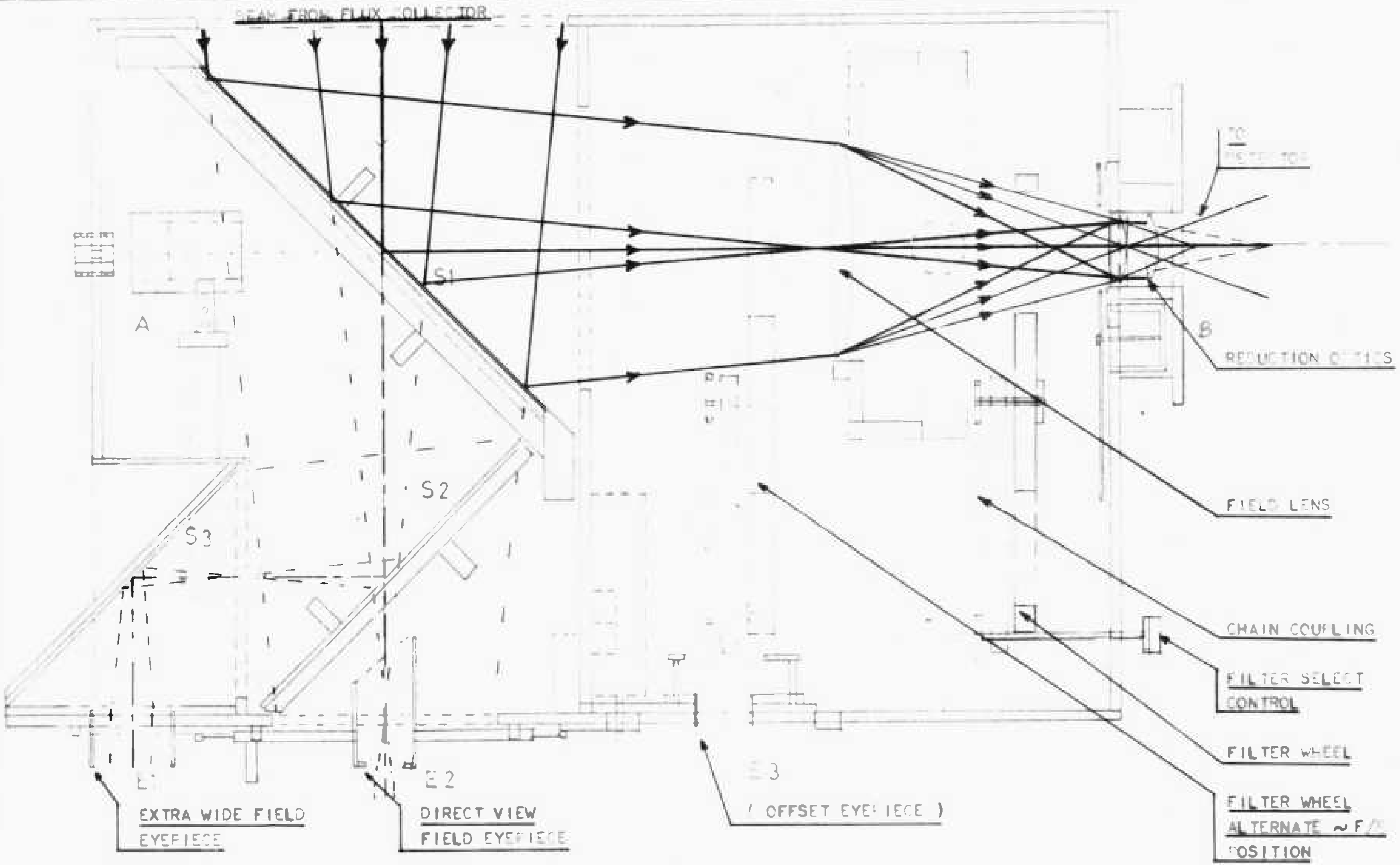

F. 4.03 **PHOTOMETER LAYOUT : PLAN**
VISIBLE-WAVELENGTHS, FILTER PHOTOMETER

4.04 Changes to optical arrangement

In view of the sixteen fold reduction in detector area, it was decided to image the field onto the detector, thereby reducing the field of view from 0^{o} to 15 arcmins, but maintaining the throughput at the objective image; the optical arrangement was thus modified to that of figure F2.4 by placing a 25mm diameter ~ F/1 lens at the objective image plane, and moving the detector plane back some 30mm.

4.05 Changes to the disc-chopper, disc detector, and mounting flange

The additional 30mm of optical path and reduced field of view suggested that the instrument could also be used as a wide-field photometer. It was therefore decided that the new cryostat mounting flange should include a filter slide holder, and that the additional objective lens should also be mounted on a slide in this slide holder space. The original disc and motor were replaced with a smaller three hole disc and 25mm diameter high speed motor mounted in a cavity in the new flange block as shown in figures F4.02 and F4.03; this disc and motor were cooled by forced air via an air exhaust pump, where the air was made to flow from the photometer box, over the disc, and then over the motor. It was hoped that this air cooling would help stabilise the thermal drift problem of the reference disc; and by the use of the small motor with good anti-vibration radial supports, the transmitted vibration would be reduced to a more acceptable level. The general layout of this radiometer/photometer was as shown in figure F4.03, for which the field lens was appropriately stopped down. The phototransistor disc detector was replaced by a capacitance detection system; two metal capacitor plates, electrically connected, were placed either side of the disc shown in figure F4.02a and F4.02b. Variation of the capacitance between the plates and the earthed motor disc was determined by means of a 450 Hz L-C 30v oscillator connected to the capacitor plates, in series with a 10K resistor, the modulated carrier voltage across the resistor was diode-rectified and filtered to leave just the amplified modulation voltage, which in turn was used as the reference signal. The double nature of the capacitance detection plates seen in figure F4.02b considerably reduces the amplitude-modulation effect produced by 'disc wobble resonances'; the gap-width of one plate to earth changes covariantly with the other plate gap-width, but cancellation of gap-width variation is not complete as capacitance is an inverse function of gap-width. Radial edge slots were used in the disc as opposed to circular ones because of their relative improvement in signal transmission due to their symmetry with the blank areas of disc.

4.06 Operation of the second disc-radiometer/photometer

This instrument was successfully used on the Silwood Park 40" flux collector. Thermal drift from the improved disc arrangement was found to be much reduced, but detection was still limited to λ 1.35 μ as determined with an A.D.P. roll-off filter, observed with the dry ice and acetone cooled PbS detector, beyond which local atmospheric thermal emission gave excessive noise readings (see reference R4.01); this confirms the expected sky emission curves as given in figure F1.03.

The increased system sensitivity in the near infrared achieved by cooling the detector balanced the decrease from the reduction in field of view, but some bright infrared stars were successfully detected. Much difficulty was experienced with the glass-metal seal of the detector head, which periodically shattered, spraying the dry ice and aceton coolant over the detector.

4.07 The case for two instruments

It was clear that the F.C.M.I. detection system would run into the same problems as that of the radiometer, and it was decided to continue with the development of the radiometer in its own right as a separate survey instrument, and adapt it to photometric use.

No extended nebulous infrared sources were detected short of λ 1.35 μ, and none beyond this because of the atmospheric emission; it was thus decided that the instrument should be made adaptable for use 1) as a visible to very near-infrared very wide field photometer using a cooled near-infrared photomultiplier with an S11 or S20 photocathode for the study of nebulous [SII] emission and 2) as a wide-field infrared photometer for operation at the atmospheric windows of λ 1.65 μ and λ 2.2 μ. The design and construction of the infrared photometer using sky comparison chopping to eliminate sky background, is described in the following chapters.

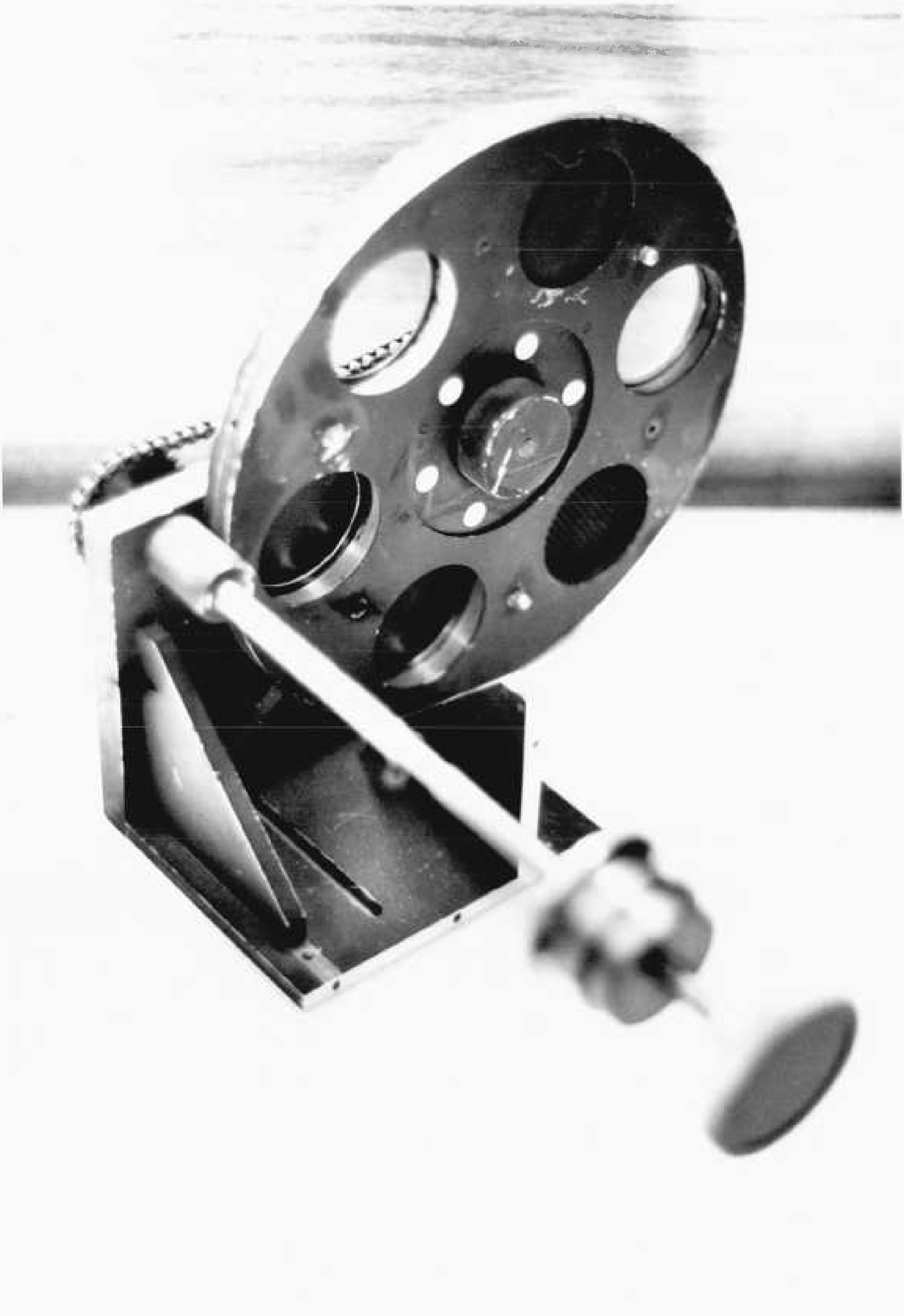

P4.1

THE FILTER WHEEL AS USED WITH THE PHOTOMULTIPLIER FILTER PHOTOMETER

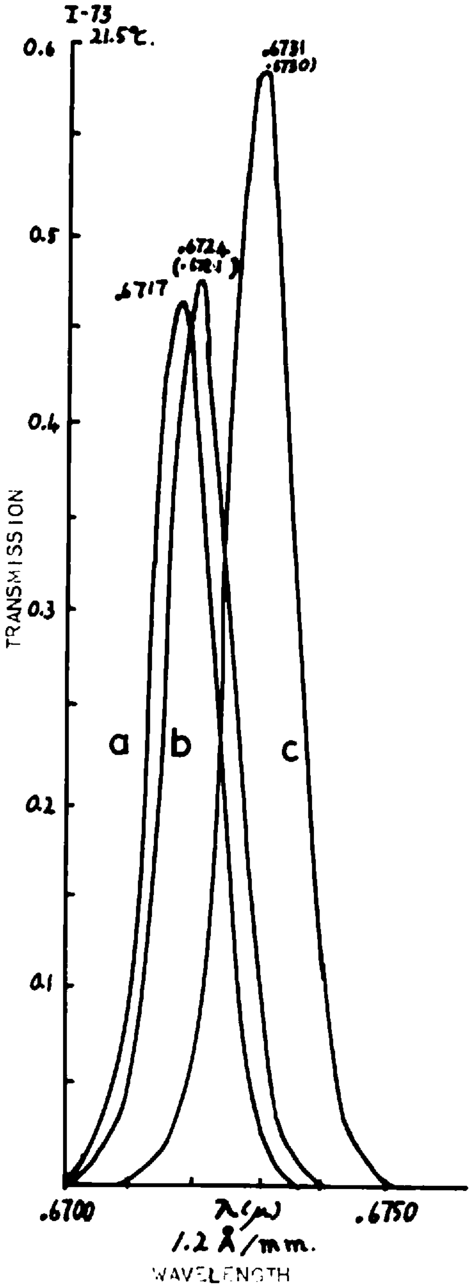

F. 4.04 a

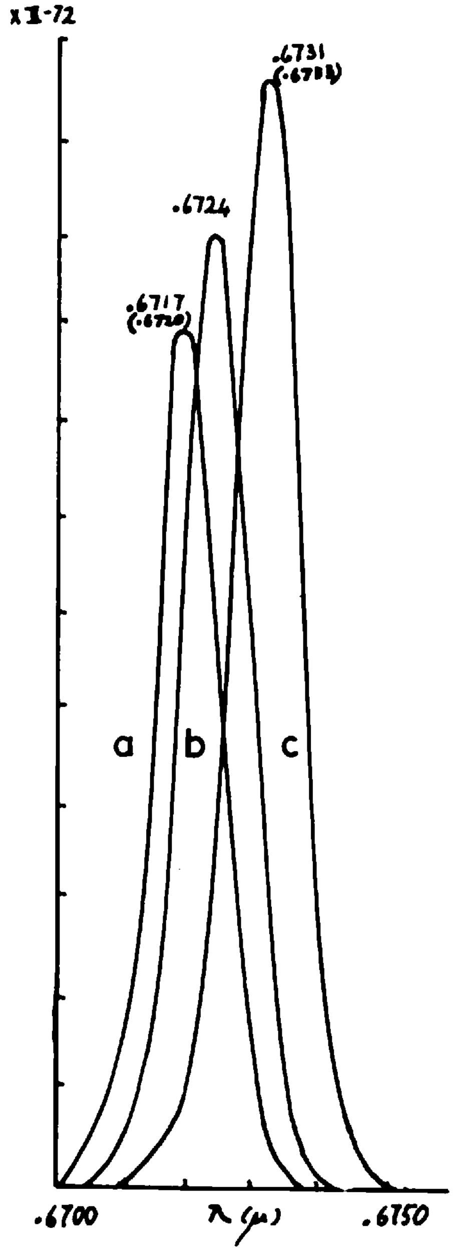

F. 4.04 b

[S II] FILTER PROFILES

4.08 A two-fold program of nebular photometry

Amongst the numerous papers by M.J. Seaton (see refs. R4.01, R4.02) on nebular-line-ratio theoretical values and relations, he suggests that $[SII]_{6717}/[SII]_{6731}$ is a particularly good indicator of electron temperature, and is relatively insensitive to electron density, unlike most other line-ratios. [SII] emission has clearly shown up in several bright diffuse nebulae from measurements made with the Mock interferometer, when used on the 40" flux collector, and also has been studied by other authors (see refs. R4.05 to R4.07); it was therefore decided to attempt to measure the [SII] line ratios at different points in the Orion nebula in order to establish an electron temperature distribution, and to compare the results with those by other authors using other lines, and also to follow this up with similar infrared measurements.

4.09 The construction of a red to infrared wide-field photometer

Two infrared sensitive photomultipliers were compared under optimum conditions, when cooled in the photomultiplier cooler previously discussed. Of the two photomultipliers tested, an RCA 'Quanticon' C300E and a C31034, the C31034 had a relative signal-to-noise advantage of 40, but a rather restricted photocathode area (4mm x 10mm).

A filter wheel as shown in photograph P4.1, was built to accommodate three 38mm diameter [SII] filters, one for each of the two [SII] nebula emission lines, (filters: $\lambda\ 0.6717\mu$, $\Delta\lambda\ 0.0022\mu$, and $\lambda\ 0.6731\mu$, $\Delta\lambda\ 0.0022\mu$), and one to monitor the continuum between these lines, ($\lambda\ 0.6724\mu$, $\Delta\lambda\ 0.0022\mu$) (see figure F4.05). This filter wheel could be placed either before the field lens in the F/5 beam thereby restricting the field to 38mm (25 arcmins on the 40" flux collector), or after the field lens working with a field size determined by the photocathode, but with a more severe F ratio (depending on the field). This arrangement is shown in figure F4.03; the electronics used was that of the photometer but with a more appropriate photomultiplier preamplifier.

It was principally with this light-sensitive system in mind that the disc phototransistor detection system was replaced with the capacitance detection system. It was also found necessary to light-seal the photometer box, and supply the entrance aperture to the photometer with a long horn baffle.

4.10 Operation of the [SII] filter photometer

The [SII] filter photometer was successfully operated on the 40" flux collector, and data obtained of $[SII]_{6717}$ and $[SII]_{6731}$ intensities for the Orion nebula, M42, trapezuim region, with a 2 x 6 arcmin^2 field. This data could not be related to the electron temperature without careful subtraction of the continuum intensity, as monitored with the third filter.

The λ 6717 Å and λ 6731 Å filter profiles as shown in figure F.404 are satisfactory in having little common overlap, while the 6724 Å filter used for continuum measurements is unsatisfactory due to the excessive overlap of the wings with the two other filters. Data could not be satisfactorily interpreted for the continuum due to this particularly excessive overlap, and no other filter was available.

Problems were also experienced with the flux collector drive reliability and also in maintaining the required pointing accuracy of the flux collector six flat mirrors.

The optical requirements of this photometer thus exceeded the specification of the available flux collector; upgrading the flux collector was considered, but it was decided that the time and effort involved would be more profitably spent on development of the infrared wide-field photometer in readiness for the following winter. The infrared photometer considered could be of modular construction, such that the filter and photomultiplier system could be replaced if required. Such an instrument would then be very versatile and could cover a wavelength range from visible wavelengths out to the $\lambda\ 1.3\mu$ atmospheric limit or the $\lambda\ 2.4\mu$ glass absorption limit, with a field of view ideally suited for observation of nebulae, comets or possibly radio arcs.

4.11 Adaptation of an 'Oxford Instruments' photomultiplier cooler for use as a cryostat for the infrared photometer

Several variations on the previously described cryostat were attempted, including replacing the glass dewar with a brass cylinder, all without much success; which lead to the construction of a replacement cryostat assembly. The 'Oxford Instruments' photomultiplier cooler previously used with the'quanticon'tubes was adapted for use as a cryostat; a preamplifier was fixed to the valve plate, and a brass cylinder, previously mentioned, inserted in the photomultiplier cooling jacket section; this brass

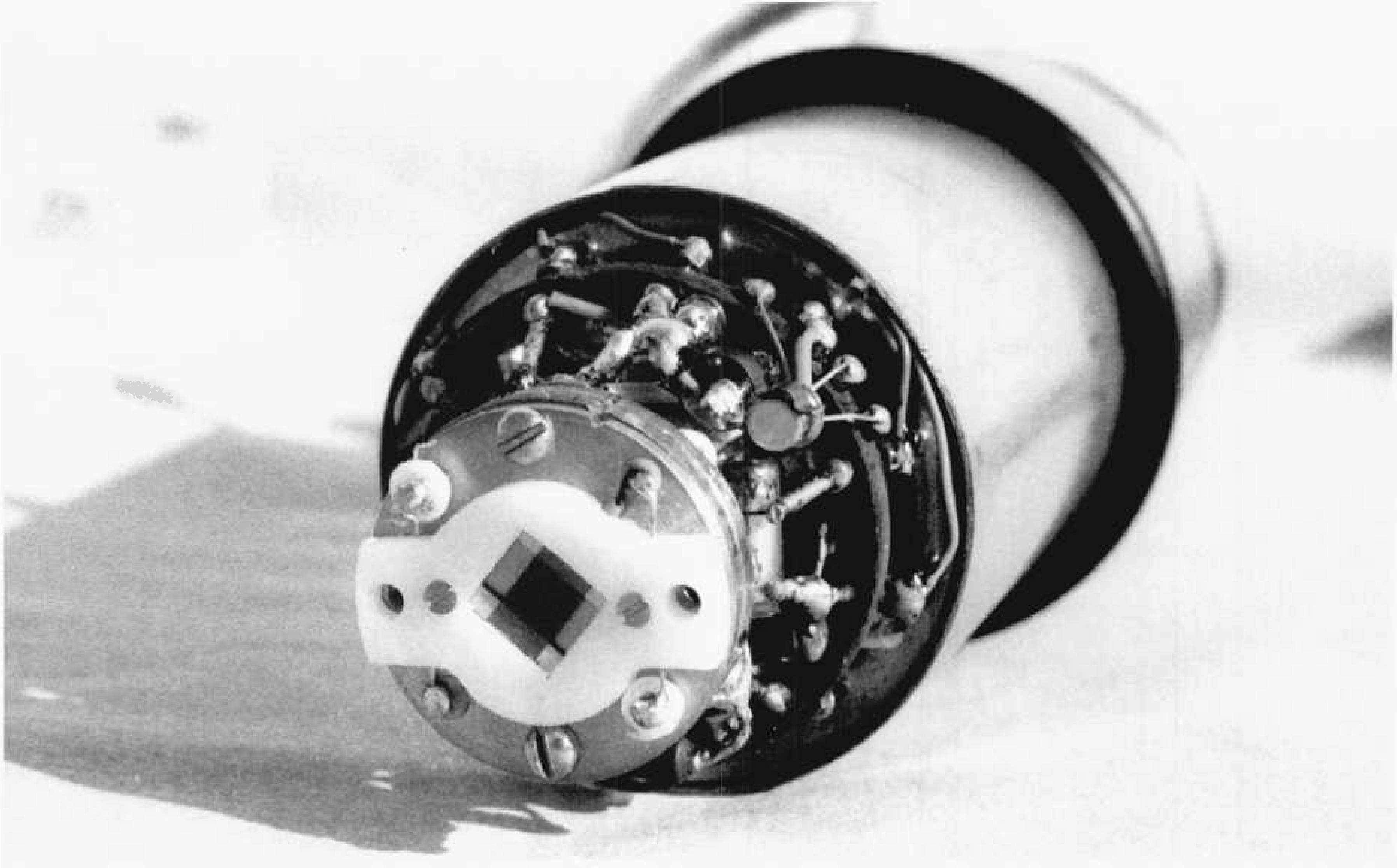

P4.2

THE DETECTOR MOUNTING FLANGE WITH INTERCHANGEABLE MOUNTS, AND THE BIAS NETWORK WITH FET.

cylinder was wrapped with brass shim to ensure a tight fit and consequent satisfactory thermal conduction path to the cooling jacket. One end of this cylinder was sealed off and mounted with the copper detector head unit as before with interchangeable detector mounts, now fitted with a rigid terminal ring tag array on which a bias resistor and the first pre-amplifier F.E.T. follower stage were mounted (see photograph P4.2).

The vacuum vessel was fitted with a 38mm diameter window and the detector head flange could be positioned about 10 milimeters back from this window, which allowed the rapidly converging 5mm diameter photometer/ radiometer beam to be accommodated. Unfortunately, the photomultiplier window was recessed from the cryostat bolting flange, which prevented the detector being correctly located at the reduced field focus; the cryostat was thus modified with a smaller window and short 6mm diameter light pipe to reflect the light from the focal plane just inside the window to the detector plane, with a slight consequent loss of light (0.75 transmission at (λ 2.2 μ).

This cryostat was capable of satisfactory performance up to the λ 2.4 μ glass absorption band; the wavelength detection limit was in practice determined by the atmospheric thermal opacity to λ 1.3 μ when disc chopping. The further development of this equipment to operate at longer wavelengths is described in the following chapters.

References for Chapter 4

Planetary nebulae

R4.01 Saraph, H.E., Seaton, M.J. 'Electron densities in planetary nebulae.' Mon. Not. R. astr. Soc. (1970), 148, 367-381

R4.02 Seaton, M.J. 'Planetary Nebulae' pp. 341-354

R4.03 Lowrie, R.' On the electron temperature in HII regions.' Astron. and Astrop. (1970), 6, 460-463

R4.04 Perinattor, M.' Temperature and density in gaseous nebulae.' Astron. and Astrop. (1971), 10, 421-433

Orion Nebula

R4.05 Danks, A.C.' Observations of the [SII] doublet 6717 Å in Orion.' Astron. and Astrop. (1970), 9, 175-180

R4.06 Dapita, M.A., Gibbons, A.H., Meaburn, J.' Measurements of the electron temperatures in M42 from the profiles of Hα [NII], Hβ [0 III].' Astron. and Astrop. (1973), 22, 33-39

R4.07 Danks, A.C., Meaburn, J.' The variations of the electron density throughout the Orion nebula.' Astrop. and Sp. Sc. (1971) 11, 398-406

Key to figures F5.09, F5.10,(and 5.04 - 5.11)

a	Field lens scanning pre-focal stop
b	Field lens and telescope focal plane
c	Sliding mirror module first diagonal flat
d	Sky comparison vibrating spherical mirror and objective focus
e	Optional iris stop
j	Optional filter slide
g	Field twin spherical mirror
g'	Field iris stop
h	Second sliding mirror module diagonal flat, with three preset locations h1, h2, and h3
k	Chopper-disc and detection plates
l	Collimator compound lens
m	Filter holder and slide
n'	Objective stop
n	Reduction lens
p	Cryostat window
q	Cryostat light pipe
r	Detector and mounting head
t	Reference lamp field widening lens slide
u	Viewing eyepiece field stop
v	Viewing eyepiece (replaced with reference lamp in F5.06 to F5.08)

THE DESIGN AND CONSTRUCTION OF TWO SKY-COMPARISON SYSTEMS FOR THE INFRARED PHOTOMETER, AND SOME OBSERVATIONS MADE WITH THE SECOND SYSTEM

5.01 Introduction: a discussion on sky-comparison techniques

The need for a sky-comparison system for detection of astronomical sources beyond λ 1.3μ was demonstrated in chapter 4. Two such systems were visualised, designed and constructed simultaneously; both systems are in modular form and are bolted into the photometer box shown in figure F4.04 as alternatives to the field lens and filter wheel arrangement of F4.04; however the disc, motor and filter slide arrangement remain unaltered.

The conventional method for sky-comparison is to vibrate the telescope secondary, or if this is not possible, then to vibrate the diagonal pre-focal flat, in the photometer along its normal. This produces a serious defocusing affect, and is not successful where a throw of 25mm is required. Some thought was given to possible systems using a mirrored rotating disc as diagonal flat, possibly with holes and a back mirror, or just a system of alternating displaced mirrors on a disc. It was decided that such arrangements would produce serious defocusing effects, and that it would be more profitable to consider pivoted mirror arrangements whereby light lever amplification might be employed.

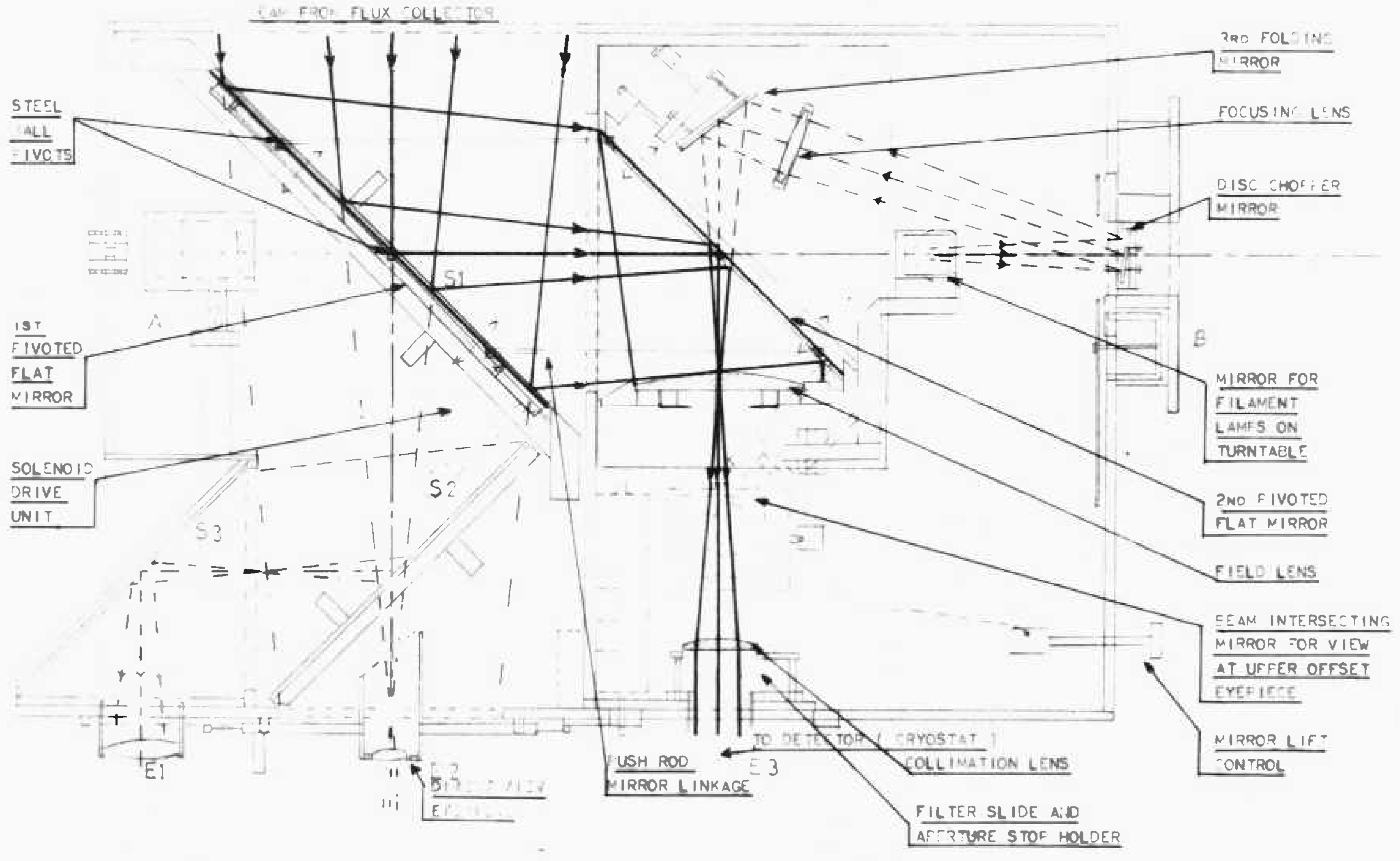

F.5.01 **PHOTOMETER LAYOUT : PLAN**
DOUBLE - PIVOTED - MIRROR SKY COMPARISON MODULE

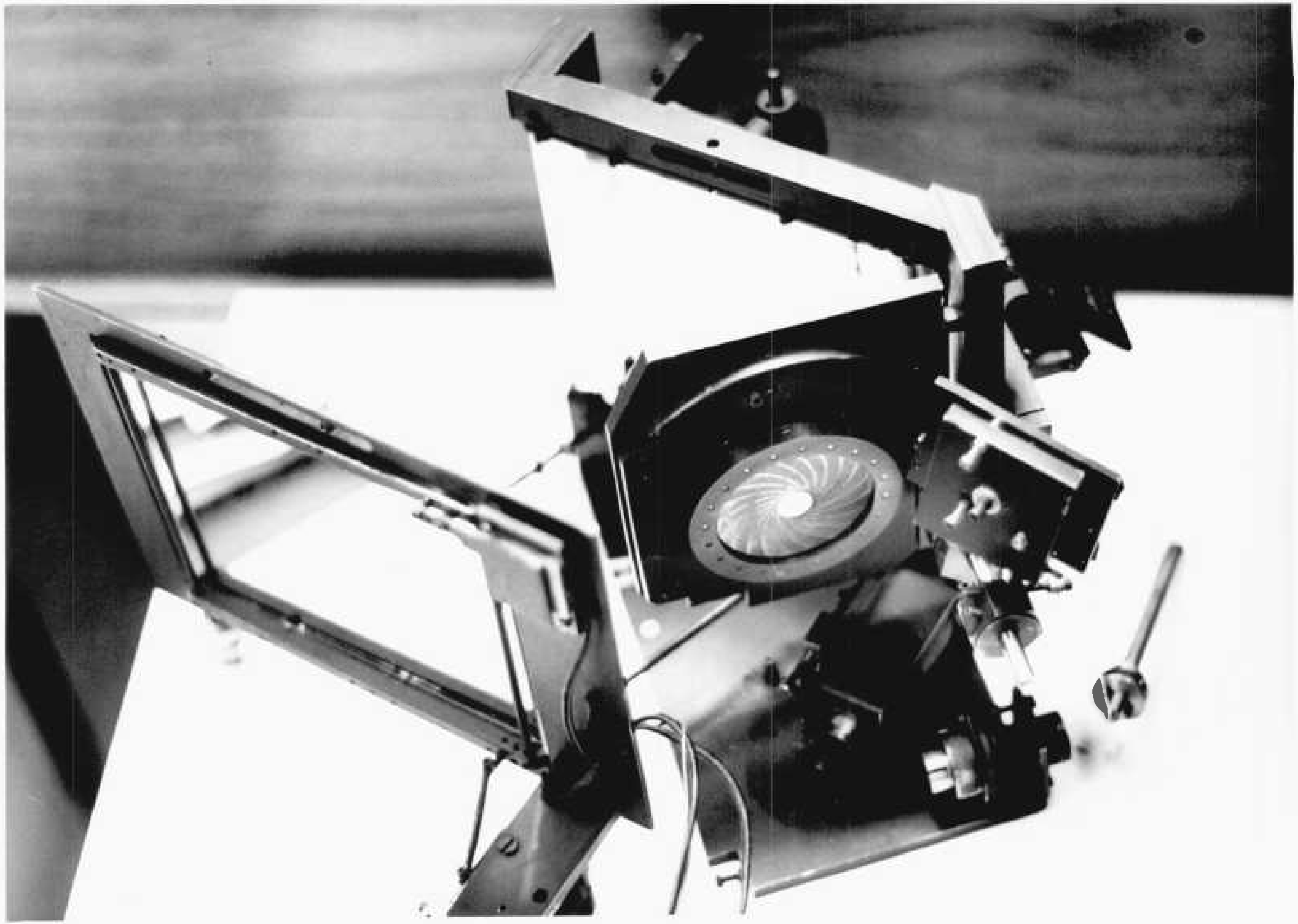

P5.1

THE PARALLEL PIVOTED MIRROR SKY COMPARISON SYSTEM, SEEN FROM THE FIELD-STOPSIDE

5.02 The basic optical system

It was decided that the system should be designed for use on any telescope operating around F/5 to F/10 at a Ritchey-Crétien or Cassegrain focus, and with a field restricted to 25mm of focal plane. These conditions enabled some improvements to be made to the optical arrangement of F2.14, such that infrared narrow-band interference filters could be used, without excessive band-width broadening and shifts. The system of F2.14 was therefore changed to that of F2.17, with the final reduced field plane, as before, coincident with the entrance aperture of the cryostat light pipe; the original field lens was replaced by a better quality lens of 65mm diameter and again 128mm length; the collimator lens was placed just before the filter slide holder.

5.03 The parallel mirror system

The fixed mirror S1 of F4.04 (which replaced the beam splitter of the original radiometer in F2.01), was replaced by a frame, with steel ball and socket pivots, such that this frame could execute small oscillations about a vertical line through the mirror frame. The aluminised face of the mirror, placed in this pivoted frame, was arranged to be flush with the pivot axis, such that incident pre-focal, converging radiation from a telescope would be reflected through $90^{\circ} \pm$ twice the tilt angle of the mirror; this arrangement can be seen in figure F5.01. The reflected beam is then reflected through 90° by a second similar pivoted mirror to bring the radiation to a focus on the newly located field lens (see photograph P5.1); the optical system of F2.17 was duplicated along this axis, with a similar filter slide holder and cryostat mounting flange at E3. The two pivoted mirrors were mechanically linked by ball-ended, adjustable length, push rods, held in position by compression,transmitted through the pivoted frames (this arrangement forms a parallelogram of forces). Two spring-loaded solenoids, with lever linkages, one to each of the frames, provided the necessary driving force, and the solenoids were driven in resonance via a step-up transformer from a power amplifier and 30Hz oscillator. The second mirror takes out the beam tilt produced by the first mirror, but leaves the displacement produced by the mirror separation; the field lens thus receives radiation from alternating fields produced by the transverse displacement of the incident beam.

Displacement amplitude was limited to only 5mm at 30Hz on maximum drive power; however this could be increased by further separating the two pivoted mirrors; the displacement is proportional to the separation. In this case it was not possible to increase this mirror separation due to the limited space available; the system, was very successful for up to 5mm displacement, but was not considered to meet the requirements of wide field scanning.

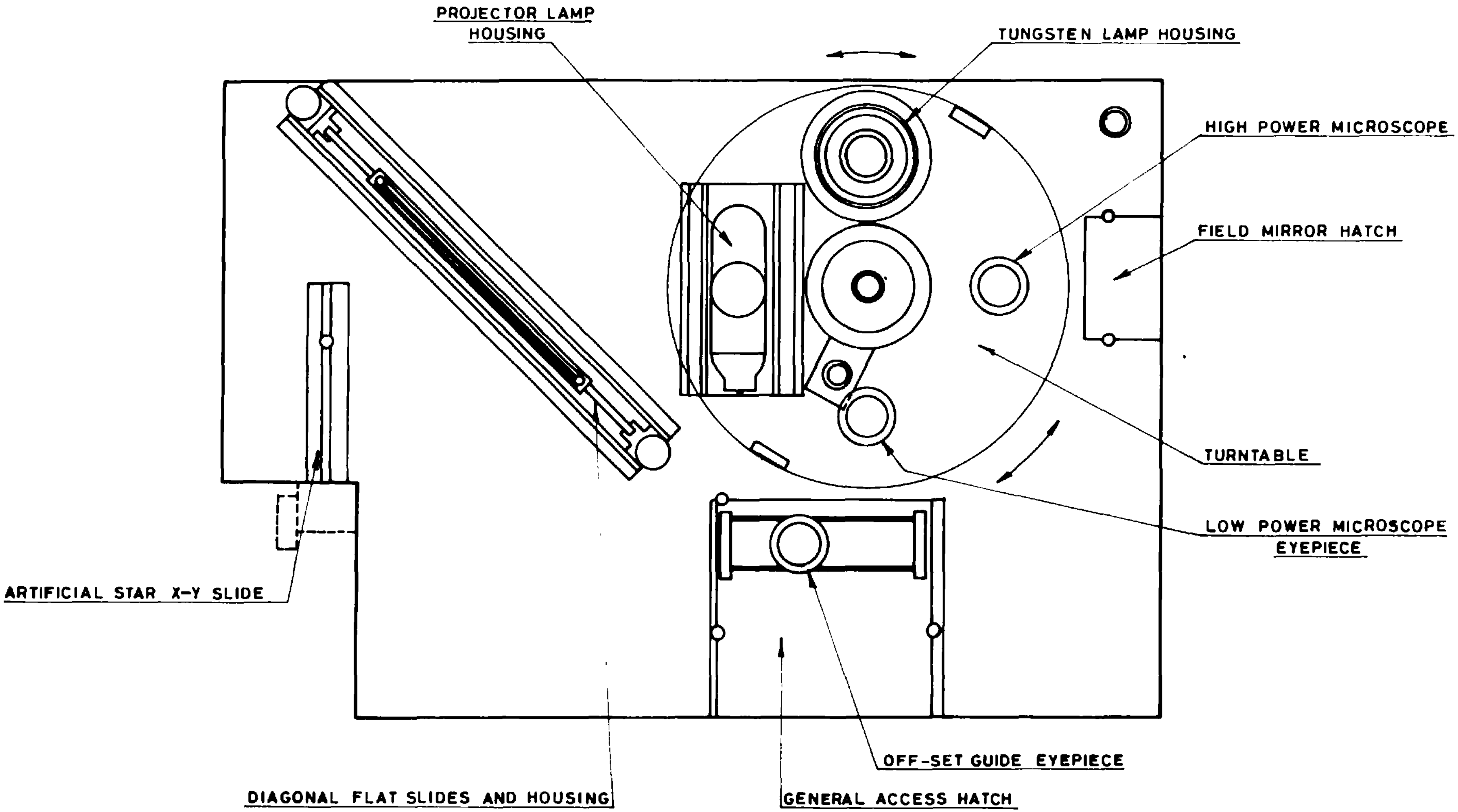

F.5.02 ***PHOTOMETER BOX ; TOP PANEL LAYOUT***

5.04 Reference lamp for the parallel mirror system

The lid of the photometer box was provided with a turntable including two reference tungsten lamps; either of these, when located over the entrance hole in the lid, would supply a convenient source for testing the system. The radiation was reflected in the box via a diagonal flat to the disc-chopper, behind which was placed a second adjustable tilted flat, mounted in the slide holder 'B'. This flat reflected the radiation back through the disc holes to a third flat (as shown in F5.09) just behind the second pivoted flat, thereby bringing this radiation onto the instrument optic axis. The field lens was equipped with an iris stop, and a small pivoted diagonal flat could intersect the beam after the field lens to bring the field into view of an eyepiece mounted in the lid (labelled offset guide eyepiece in F5.02).

5.05 The double spherical mirror sky-comparison system general layout

The optical module location in the photometer box can be seen in figure F5.03; the field lens is returned to its original location, with the optical system of F2.17 and cryostat attached at 'B'. A diagonal flat before the first focus, containing a 30mm x 90mm slot, was used to reflect that radiation not seen by the detector in the neighbouring fields, to a convenient focus on an illuminated grid. This focus was observed via a sliding diagonal flat from the offset guide eyepiece in the lid.

The principal beam, passing through the slot, could be sent directly through the lens system of F2.17 via the disc chopper to the cryostat, as shown in the vertical section diagram F5.04; or, by lowering a hinged mirror's'from location's2'to location's1'on the main mirror module to be described, the light could be directed to the centering eyepiece (low power or high power) on the lid turntable of F5.02. (see figure F5.05).

The mirror's'is mounted on a slide such that it may be interchanged with a different flat arrangement as shown in F5.06. Here, one of the reference lamps is in place of the centering eyepiece, and its radiation is reflected by a mirror in location'h2'into the collimator, remaining optical system, and cryostat; a substitute field lens is seen under the lamp housing, but in order to cover a 25mm field, a field widening lens on a slide is positioned in the beam, as shown in figure F5.07.

The arrangement also applies to the second reference lamp, as shown in figure F5.08.

5.06 The sky comparison optical system for the photometer

The principal sky comparison mode arrangement is shown in figure F5.09; it was designed for operation at F/5, but the cryostat is limited to an F/8 telescope beam, with the same lens arrangement as F5.08 etc., but with the three location pivoted mirror 'h' now located in location

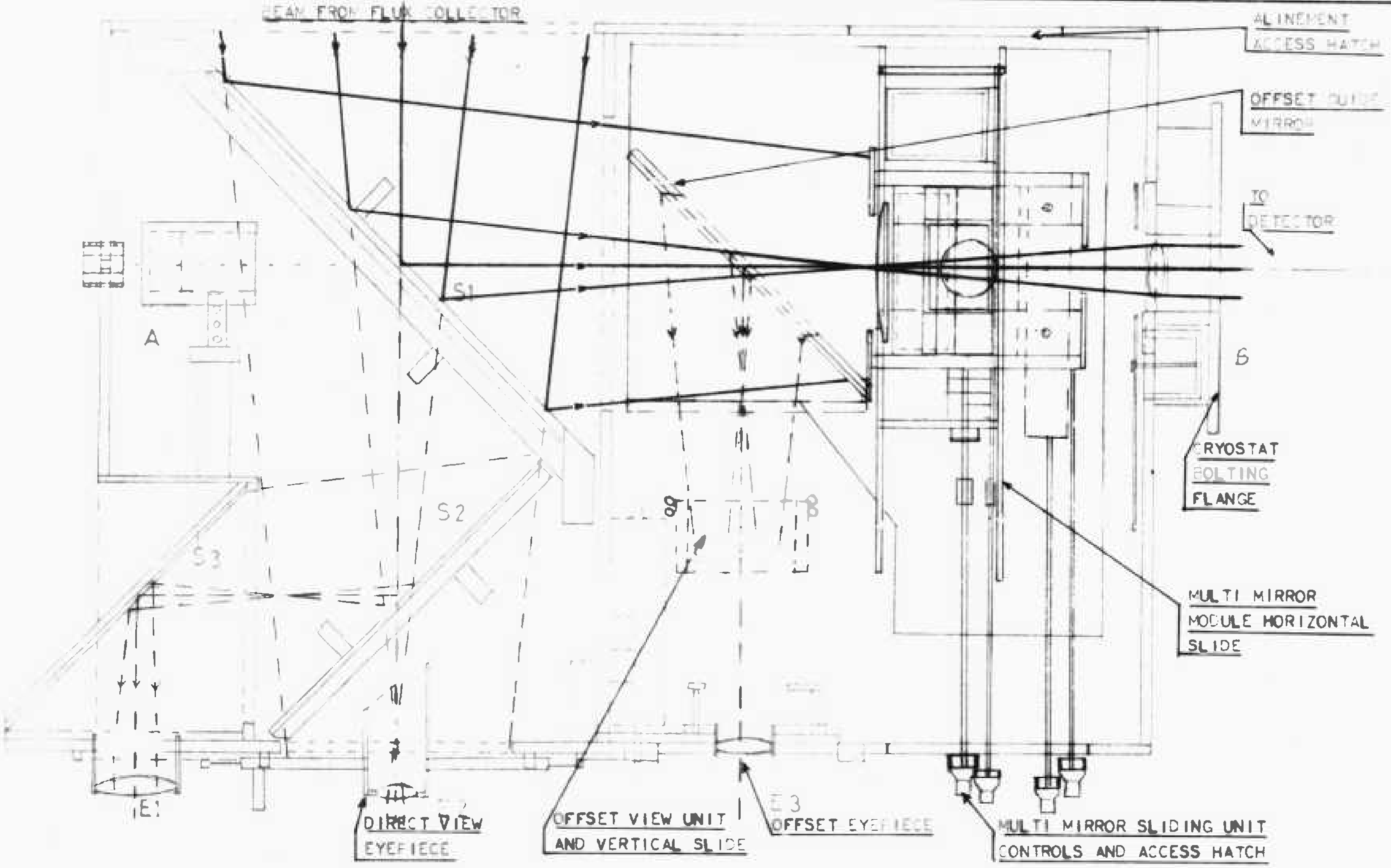

PHOTOMETER LAYOUT : PLAN

F.5.03 **MULTI-MIRROR MODULE COMPLETE UNIT WITH OFFSET MIRROR UNIT**

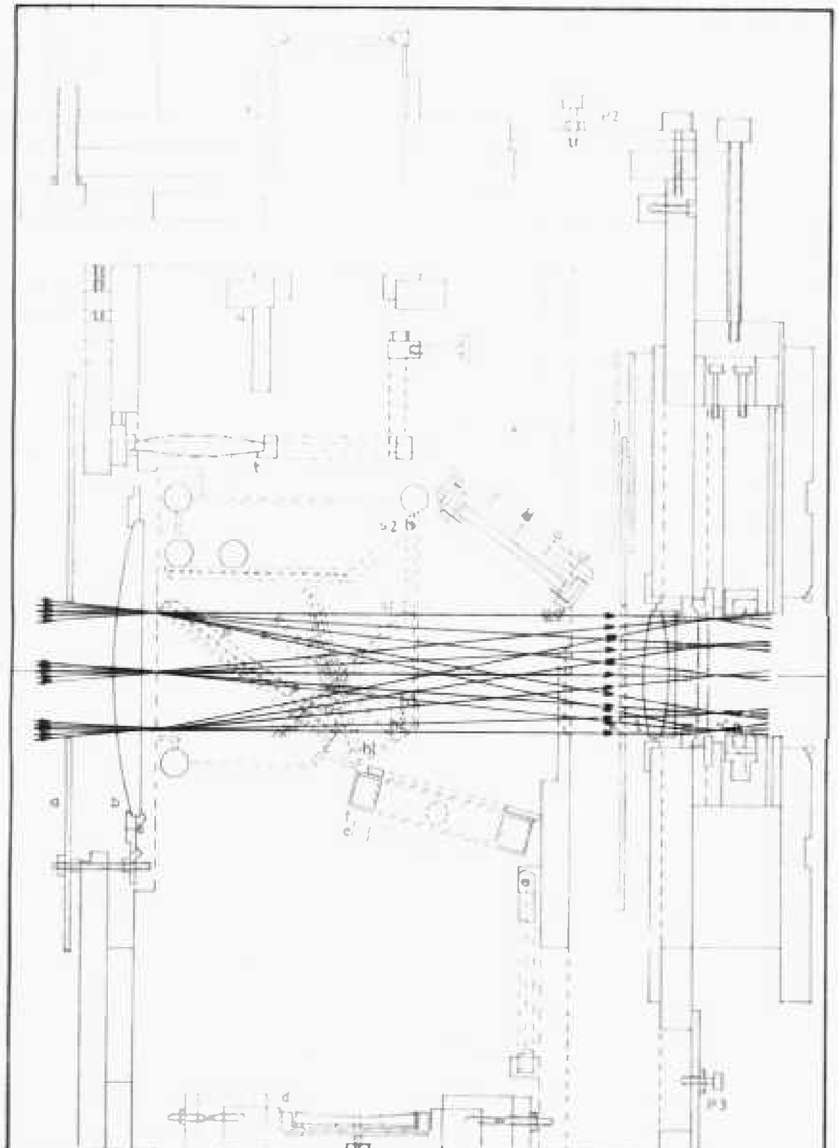

F.5.04

F/5)
F/8) BEAMS ON THE DIRECT PATH AVOIDING MULTI MIRROR OPTICS

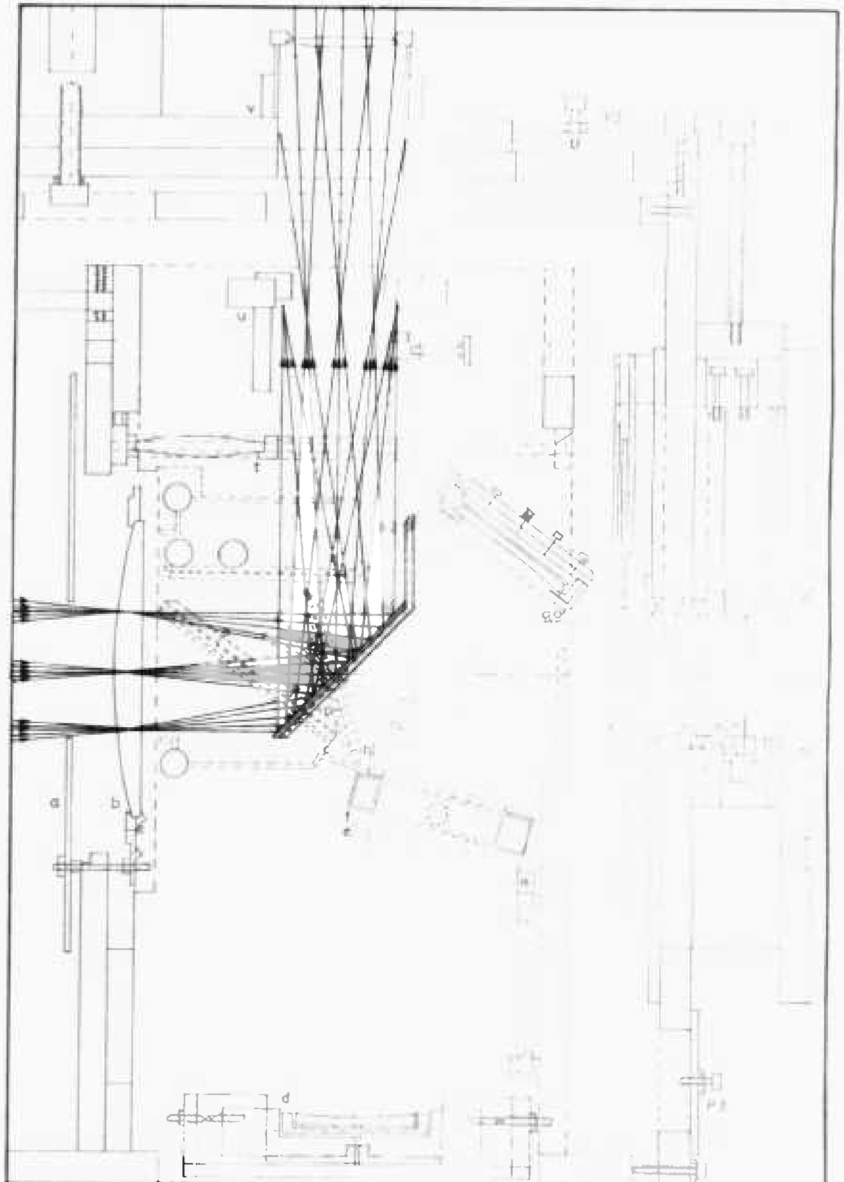

F.5.05 F/5)
F/8) BEAMS DIRECTED TO EYEPIECE

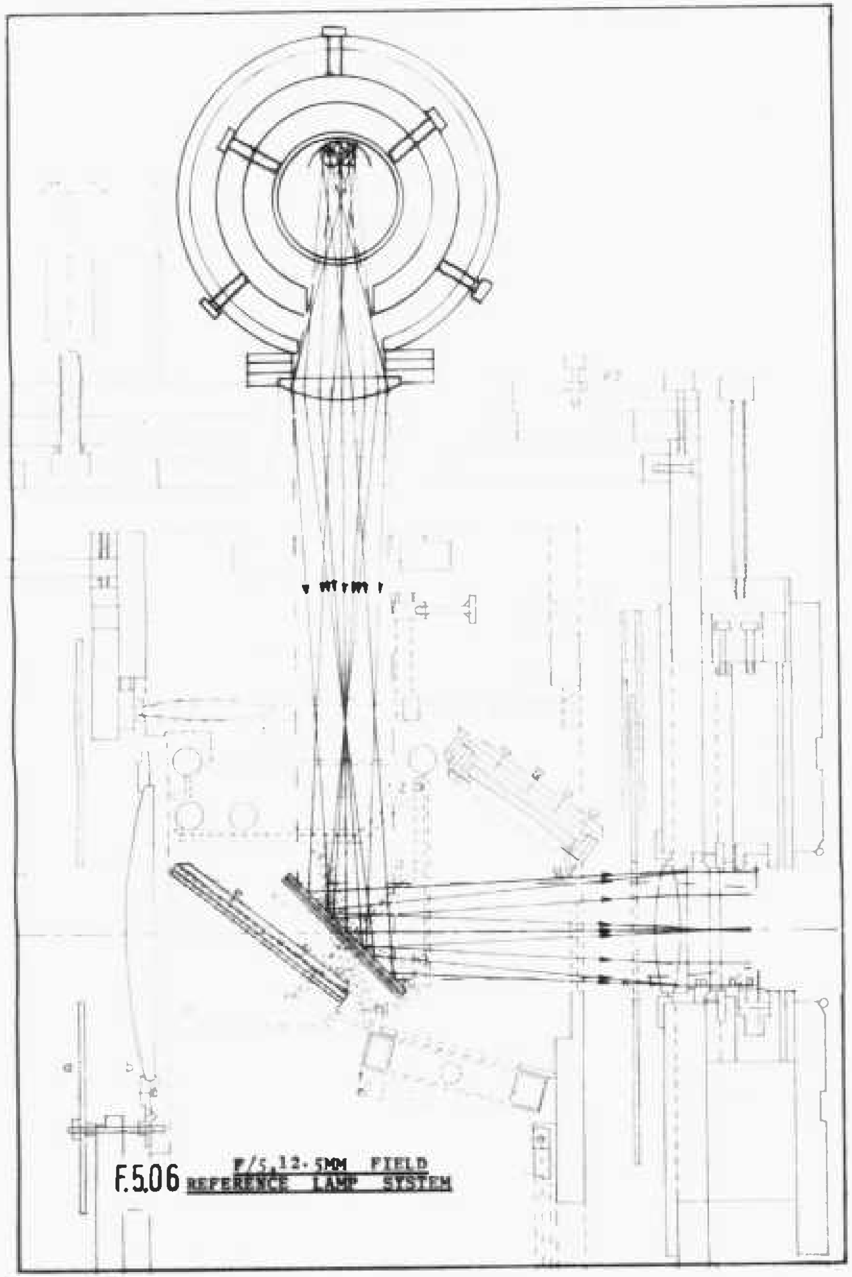

F.5.06 F/5, 12.5MM FIELD REFERENCE LAMP SYSTEM

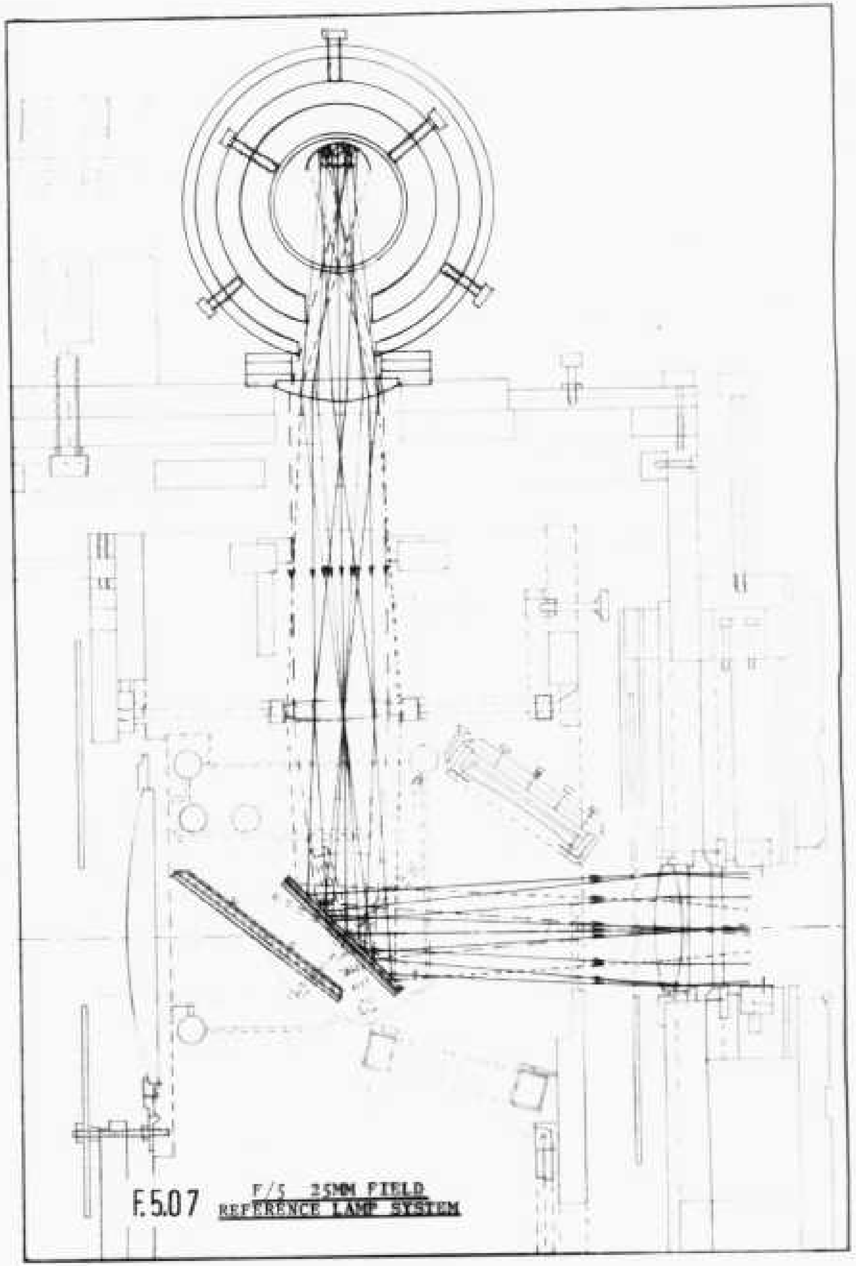

F.5.07 F/5 25MM FIELD REFERENCE LAMP SYSTEM

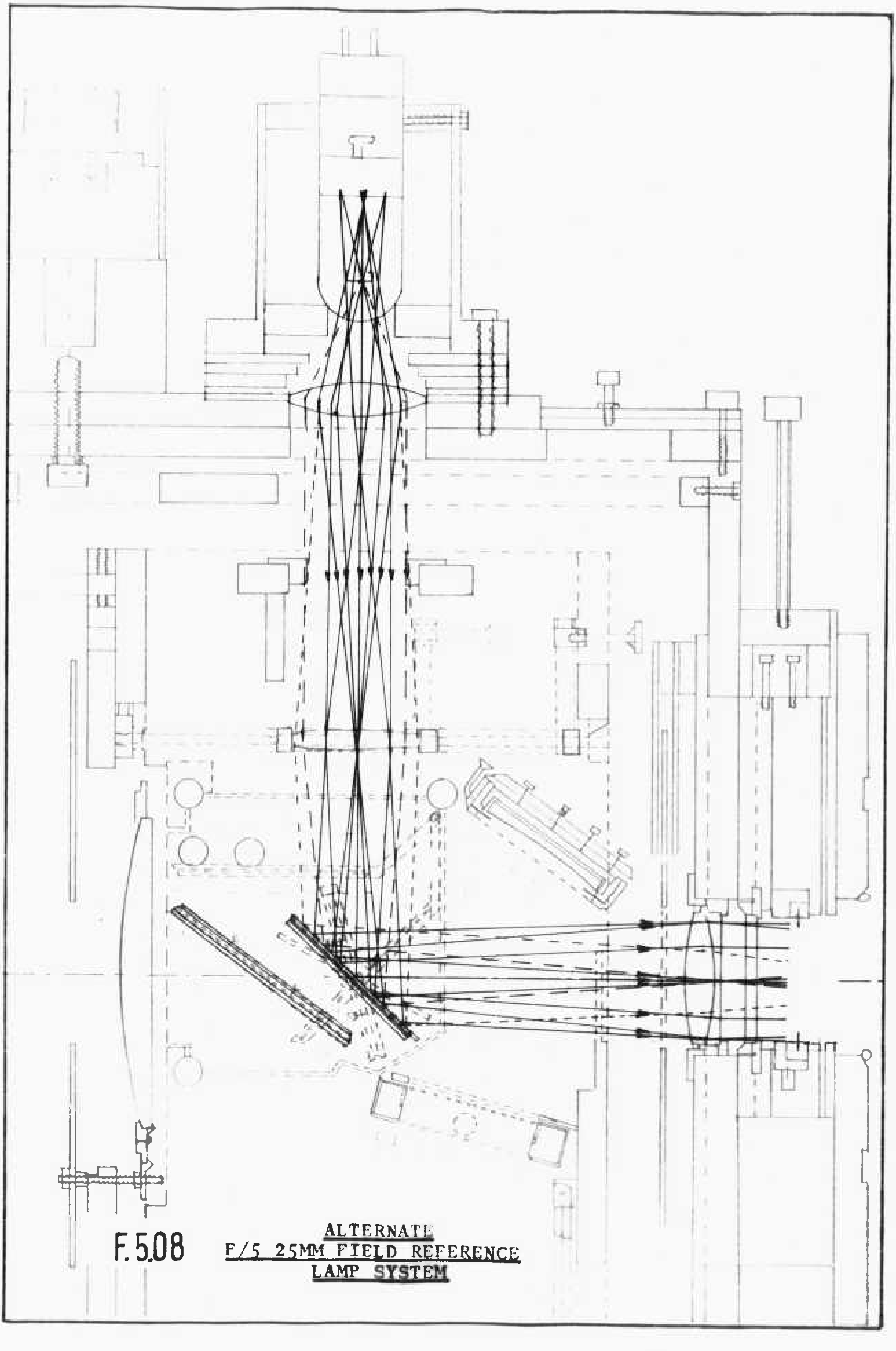

F. 5.08

ALTERNATE
F/5 25MM FIELD REFERENCE
LAMP SYSTEM

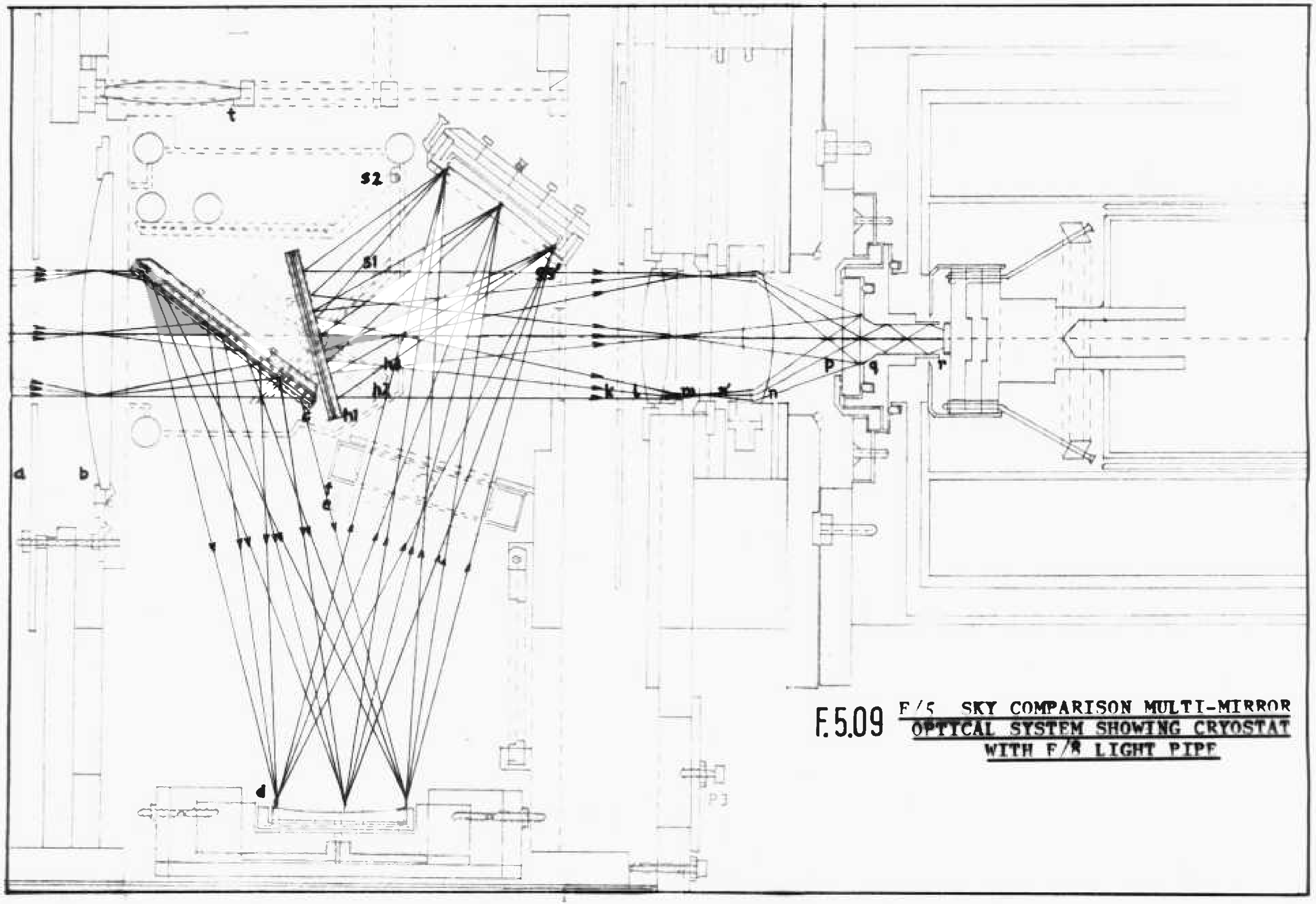

F.5.09 F/5 SKY COMPARISON MULTI-MIRROR OPTICAL SYSTEM SHOWING CRYOSTAT WITH F/8 LIGHT PIPE

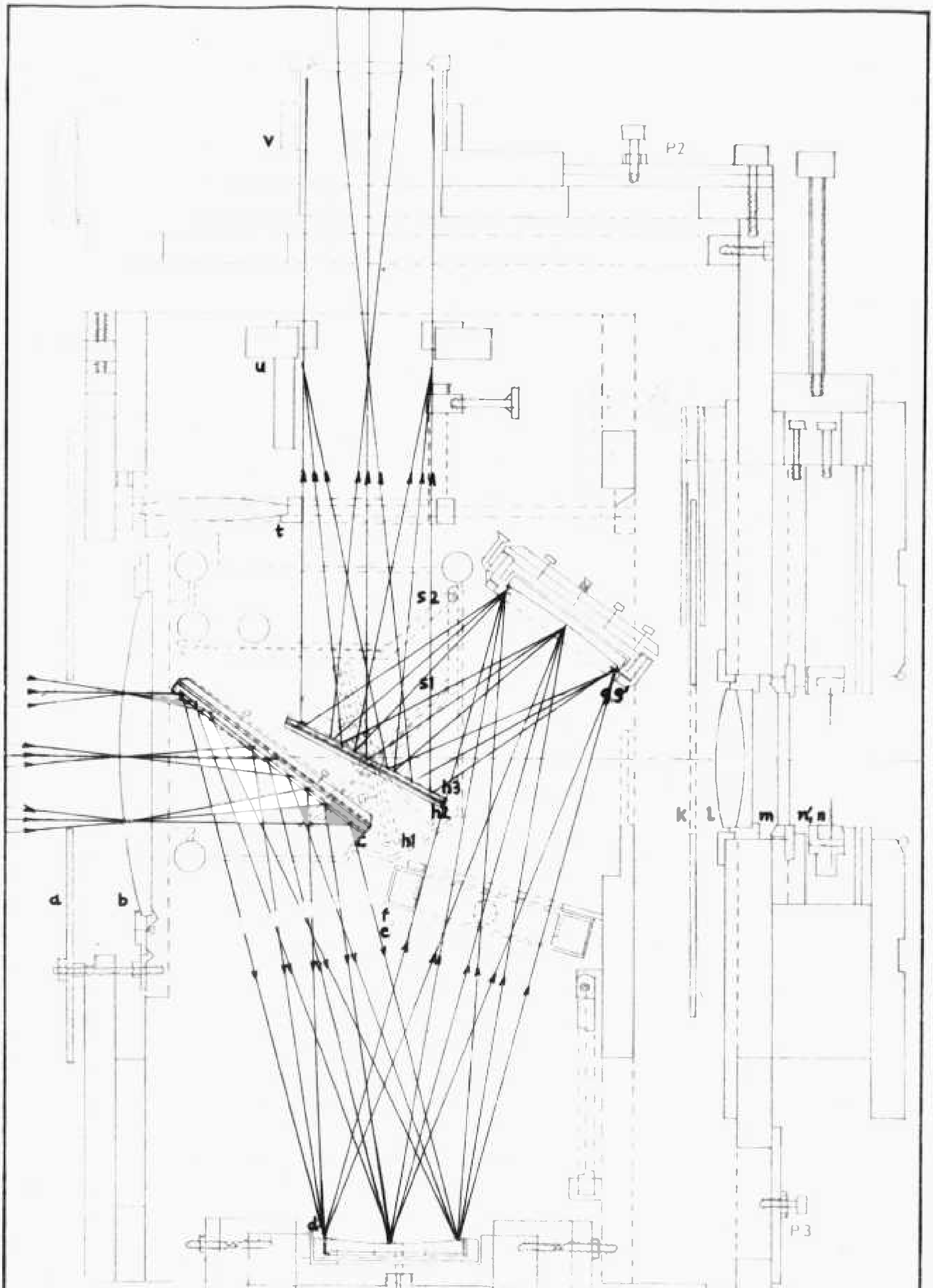

F.5.10

F/5 BEAM DIRECTED TO EYEPIECE VIA MULTI MIRROR OPTICS 'hl'. Radiation, restricted by the slot stop 'a', is brought to a focus on the field lens 'b'; thereafter it is reflected by diagonal flat 'c' to produce an image of the primary objective on the spherical mirror surface 'd'. This mirror, in a rigid frame, screwed firmly to the base plate, is vibrated about its pivot points 'd'' , 'd''' about an axis across its face and in the plane of incidence; the radius of curvature of the mirror is equal to the focal distance of the field lens, hence the reflected sky-beam from this mirror is made to form an image of the field lens and field on the twin spherical mirror 'g'. Between 'd' and 'g', the beam may be restricted by a hinged iris stop, or filtered (filter slide 'f'), but these are not usually used. The field image formed on the cross wires of mirror 'g' appears displaced according to the tilt of mirror 'd', such that a total vibration of 1.2mm at the edge of mirror 'd' is sufficient to give a field lateral displacement amplitude of 25mm. Mirror 'g' is provided with an iris stop; adjustable from 26mm to 3mm diameter, (access is via a hatch in the photometer box lid) and forms a fixed field stop. The reflected beam is then directed by the three position flat in location 'hl', to the collimator lens 'l', along the same path and to the same (but inverted) focus as that obtained without the mirrors 'c' and 'h' (see figure F5.04). In diagram F5.09, the optional disc-chopper is shown at 'k', and an interference filter 'm' is located in the collimated beam just before the aperture stop iris 'n''. The reduction lens 'n' produces a reduced field image just inside the cryostat window 'p', but the light pipe 'q' is not capable of accommodating the full beam width for an F/5 objective stop; the detector is located at 'r'.

Filter slides can be exchanged as before (the slide holder has been described previously), and the iris aperture stop 'n' is adjustable to suit the F ratio of the telescope. The cryostat window vacuum seals, designed and machined by the author, were found to be satisfactory, and no icing or misting up of the window was ever experienced.

When mirror 'h' is located in position 'h3', the beamed radiation from field mirror 'g' is diverted to a focus, seen by the centering eyepiece 'v' on the lid turntable, such that the field image may be observed through the vibrating mirror system (see figure F5.10).

This system was found to be very successful; image quality was particularly satisfactory (unnecessarily so), and the total light loss from the four mirrors involved was quite small (for the four mirrors, transmission at λ 1.65 μ = 0.63, and at λ 2.2 μ = 0.70). The transmission figures were determined with a PbS detector, reference source, and the disc-chopper, with the multi-mirror slide in position (h1), as compared with the same removed. Alignment of the mirrors is fairly straightforward, but requires the initial assistance of a laser; all the mirrors are mounted with spring loaded three point adjustment; again the direct beam arrangement was found to be useful as a reference for alignment.

The sliding mirror module can be seen in photograph P5. 2, seen from the input side showing the fixed diagonal flat 'c'; photograph P5. 3 shows the same unit from the reverse, where the three position flat 'h' can be seen, together with the central rods and location drum.

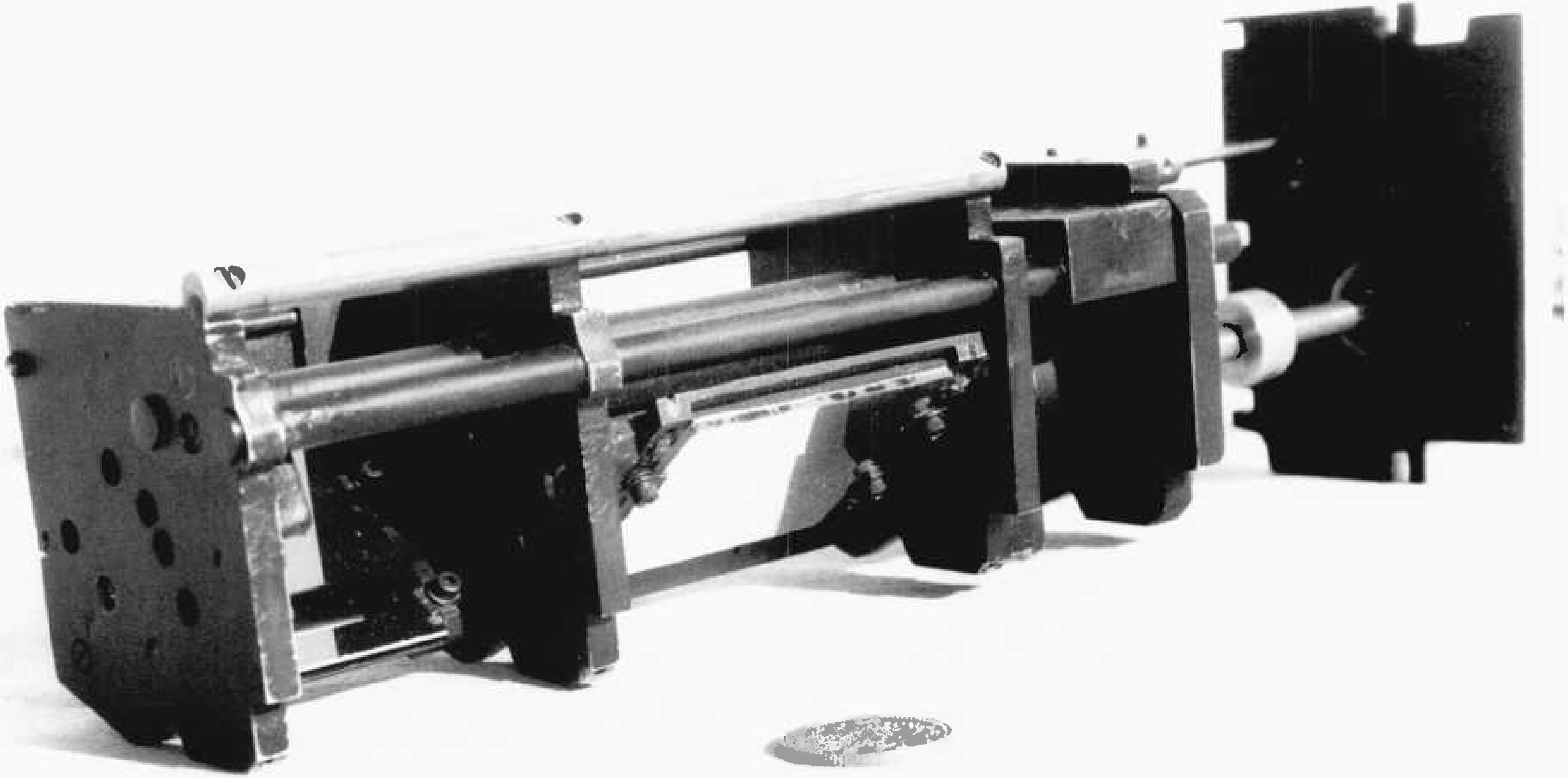

P5.2
THE MULTI-MIRROR SLIDING MODULE, SHOWING THE FIRST DIAGONAL FLAT OF THE UNIT

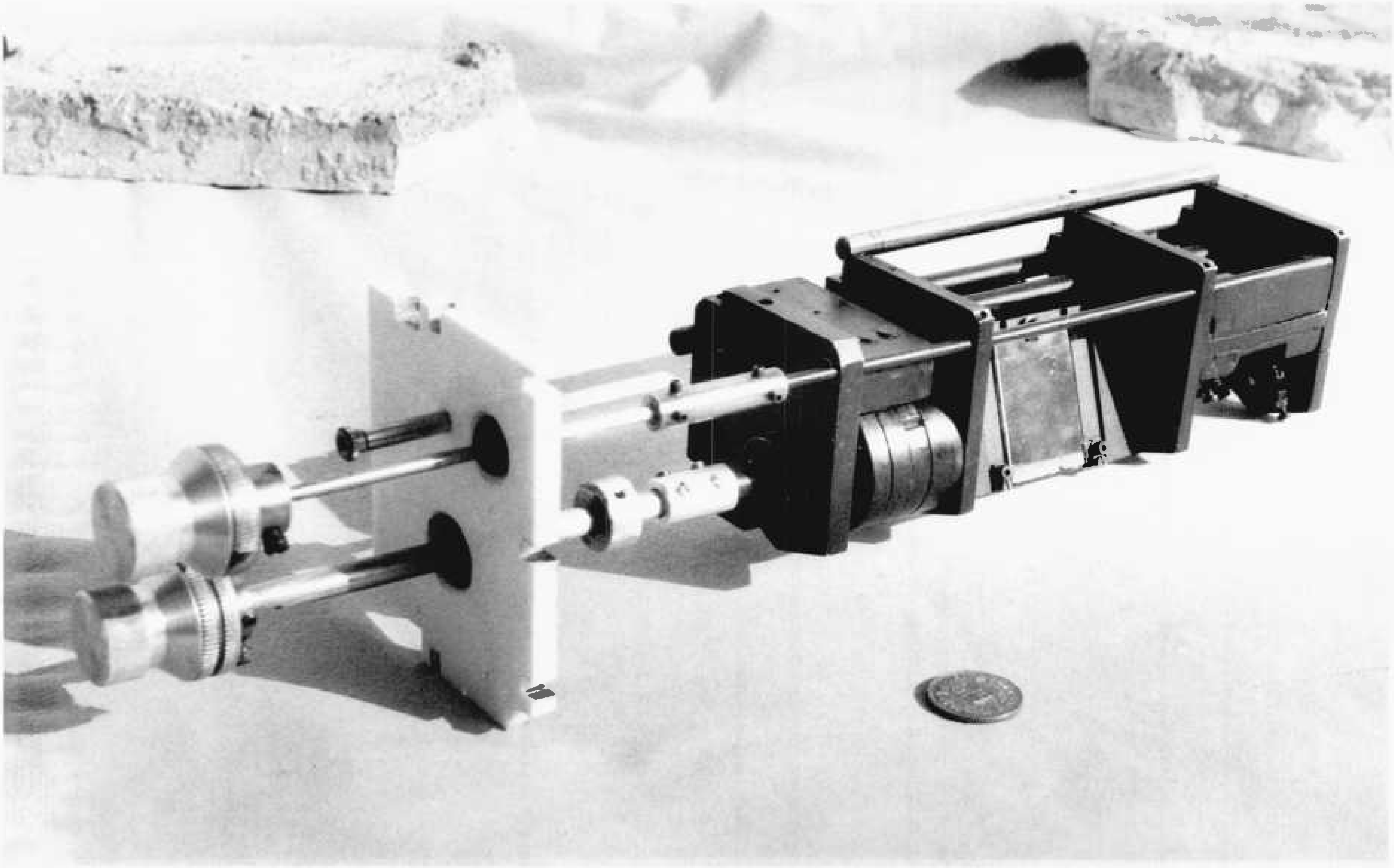

P5.3

THE MULTI-MIRROR SLIDING MODULE, SHOWING THE THREE POSITION DIAGONAL FLAT

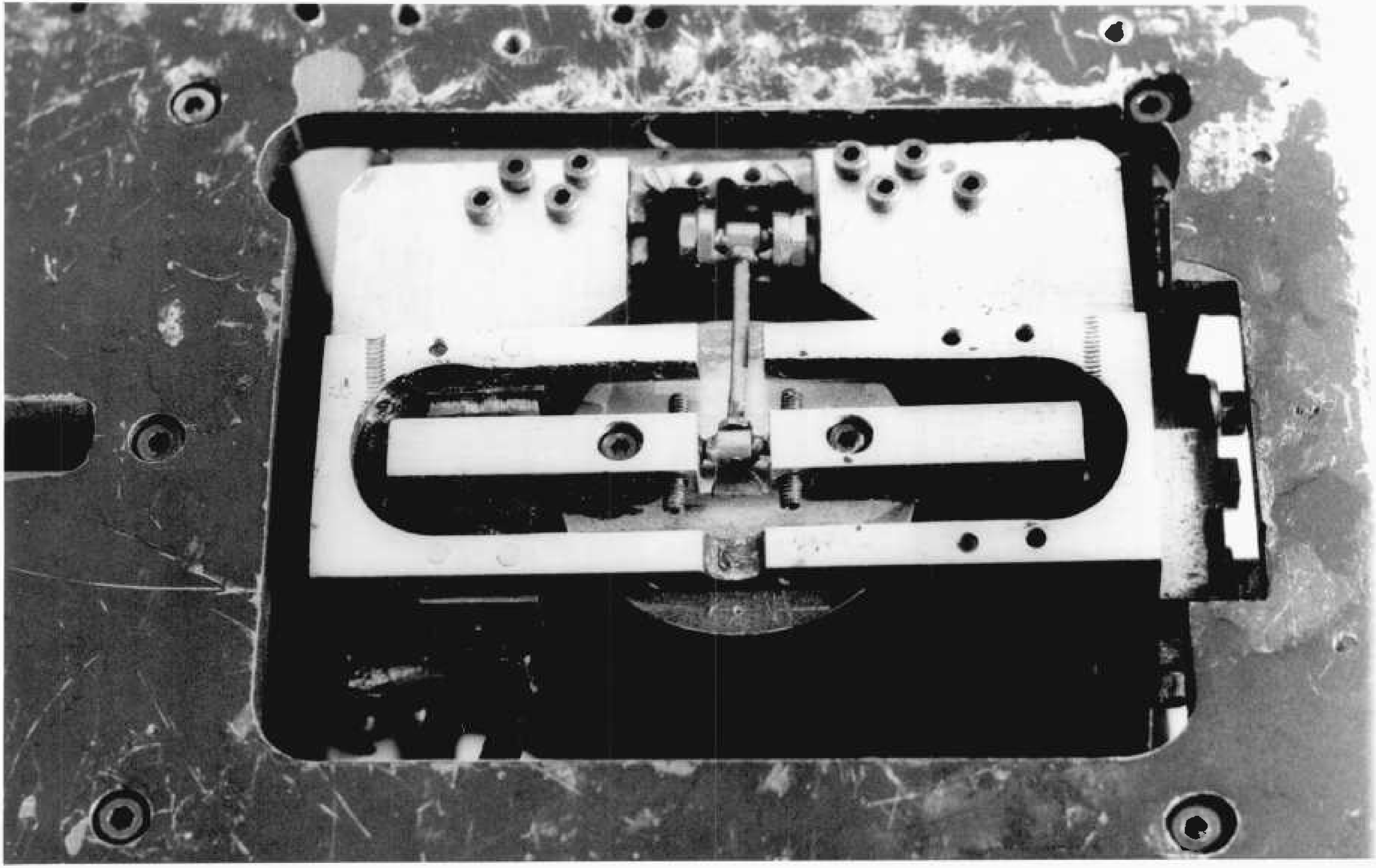

P5.4

THE MIRROR DRIVE LINKAGE SEEN FROM UNDER THE BASE

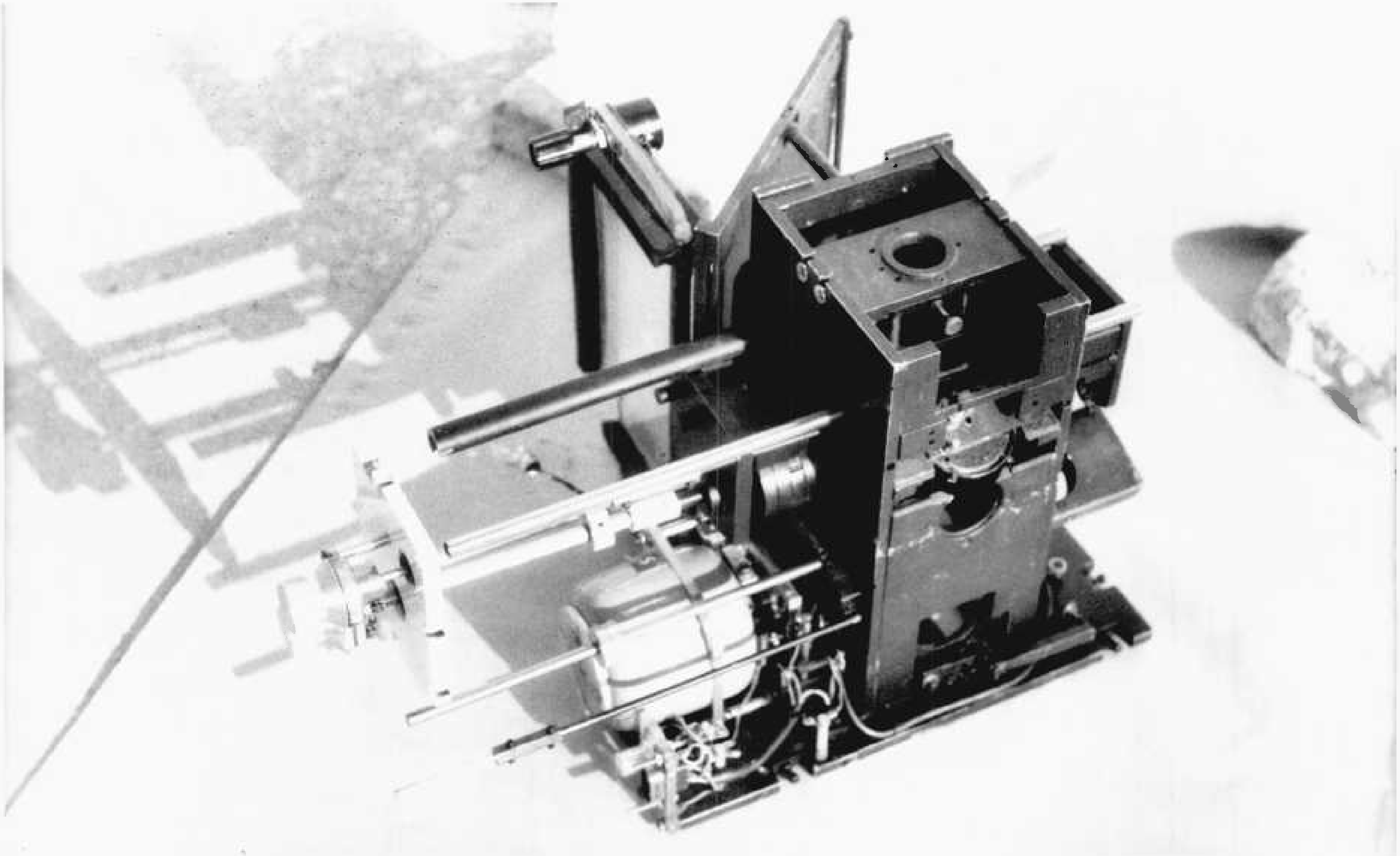

P5.5
THE DOUBLE SPHERICAL MIRROR SKY COMPARISON MODULE

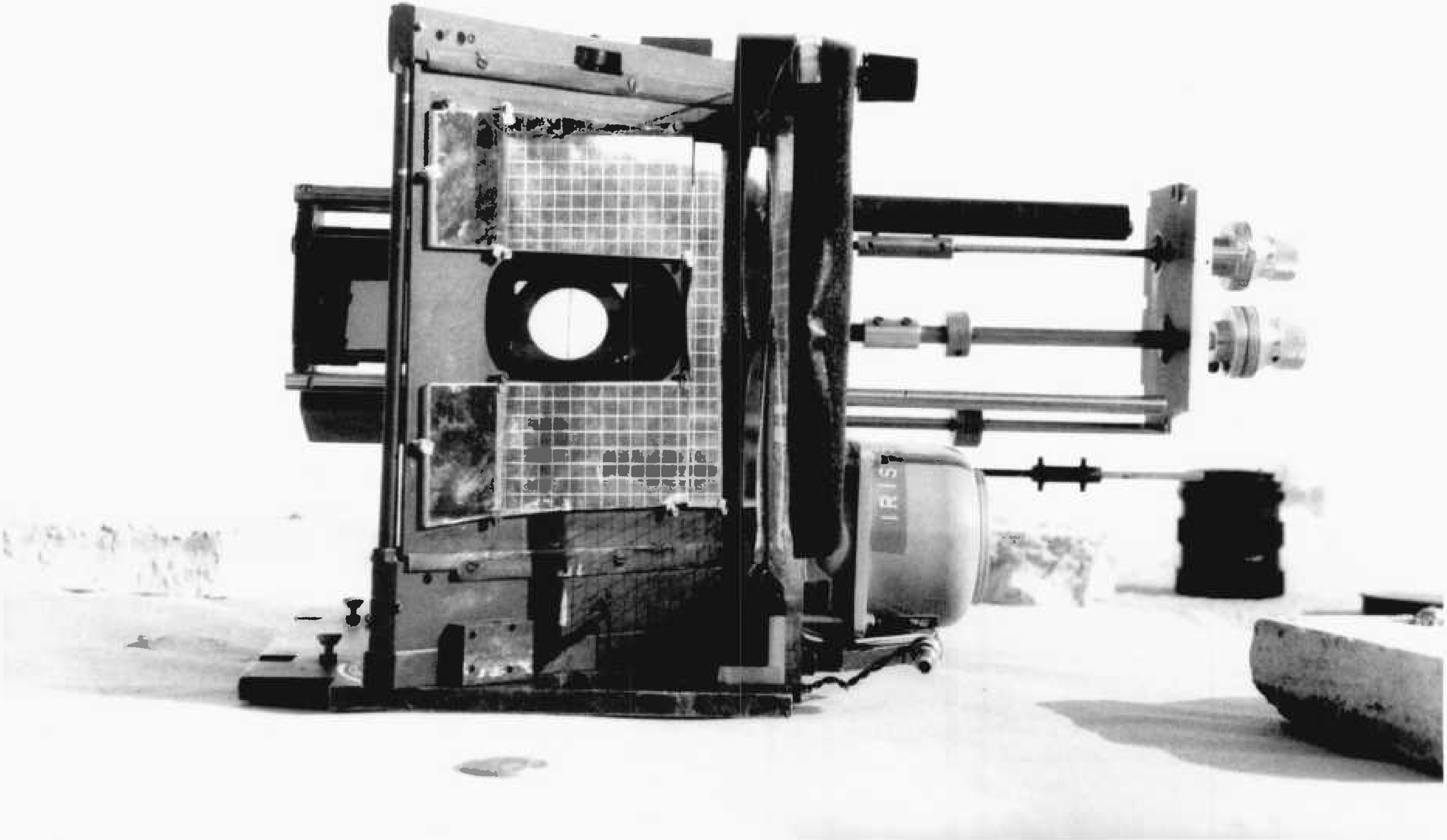

P5.6

A VIEW OF THE FIELD MIRROR CROSS WIRES SEEN VIA THE PRINCIPAL AXIS OF THE DOUBLE SPHERICAL MIRROR SKY COMPARISON MODULE

5.07 The mirror drive, linkage and general assembly

The vibrating pivoted mirror was driven from a spring loaded solenoid as before; the solenoid pole piece was mounted on a screwed carriage for positional adjustment, and the solenoid armature was guided through a simple thrust bearing to a ball-pivoted arm connected to the mirror armature, as shown in photograph P5. 4. This solenoid was driven via a step up transformer at 30Hz, where the resonance of the spring was 20Hz; the solenoid was driven close to resonance, in order to maintain a good amplitude of motion with little power, but not at resonance, in order to maintain amplitude stability. A solenoid is normally a rectifying device; its armature is magnetically attracted for both half cycles of the drive current. The necessary repulsion action is provided by the spring, and the overall motion has a high harmonic content with a fundamental frequency of twice the drive frequency; magnetic hysteresis leads to alternate cycles of motion with different amplitudes. Much power is dissipated in magnetic hysteresis heating and in the high harmonics, and so this is not a satisfactory method of operation.

This is all overcome by biasing the solenoid, in this case with 100v bias; the drive current then modulates this bias current to produce a single-polarity magnetic field, modulated by the drive field. The solenoid armature reaches an equilibrium with the permanent field by compression of the spring, and this net magnetic attraction varies at the drive frequency, thus providing a motion, at the drive frequency, of a much lower harmonic content; the armature and mirror position could be offset by changing the bias current. A capacitor plate was fixed to the solenoid armature and a similar parallel plate to the base; the varying gap width gave rise to a capacitance variation, detected by the capacitance detection circuit of the reference channel.

This system was found to give satisfactory sinusoidal amplitude of up to 0.8mm for the solenoid armature at 30Hz (corresponding to 25mm amplitude displacement in the telescope focal plane), for short periods of time at fixed orientation of the photometer. In practice, on the Cassegrain focus of a telescope amplitude changes in the mirror motion were noticeable over a period of a few minutes, brought about partially by magnetic and frictional power dissipation heating in the solenoid, and partially from changes in the orientation of the telescope (gravity force reorientation on the spring loaded solenoid armature).

The double spherical mirror module assembly can be seen in photograph P5. 5, but here the solenoid has been replaced with a loudspeaker type drive unit; this drive unit was a later refinement, to be discussed in chapter 7, and not present in the instrument described at this stage. Photograph P5. 6 shows a view of the central field mirror cross-wires, as seen via the other mirrors, along the principal optic axis of the module, through the field lens; the grid system seen reflected in the prefocal-slotted diagonal flat is from the offset focal plane system. The mirror control

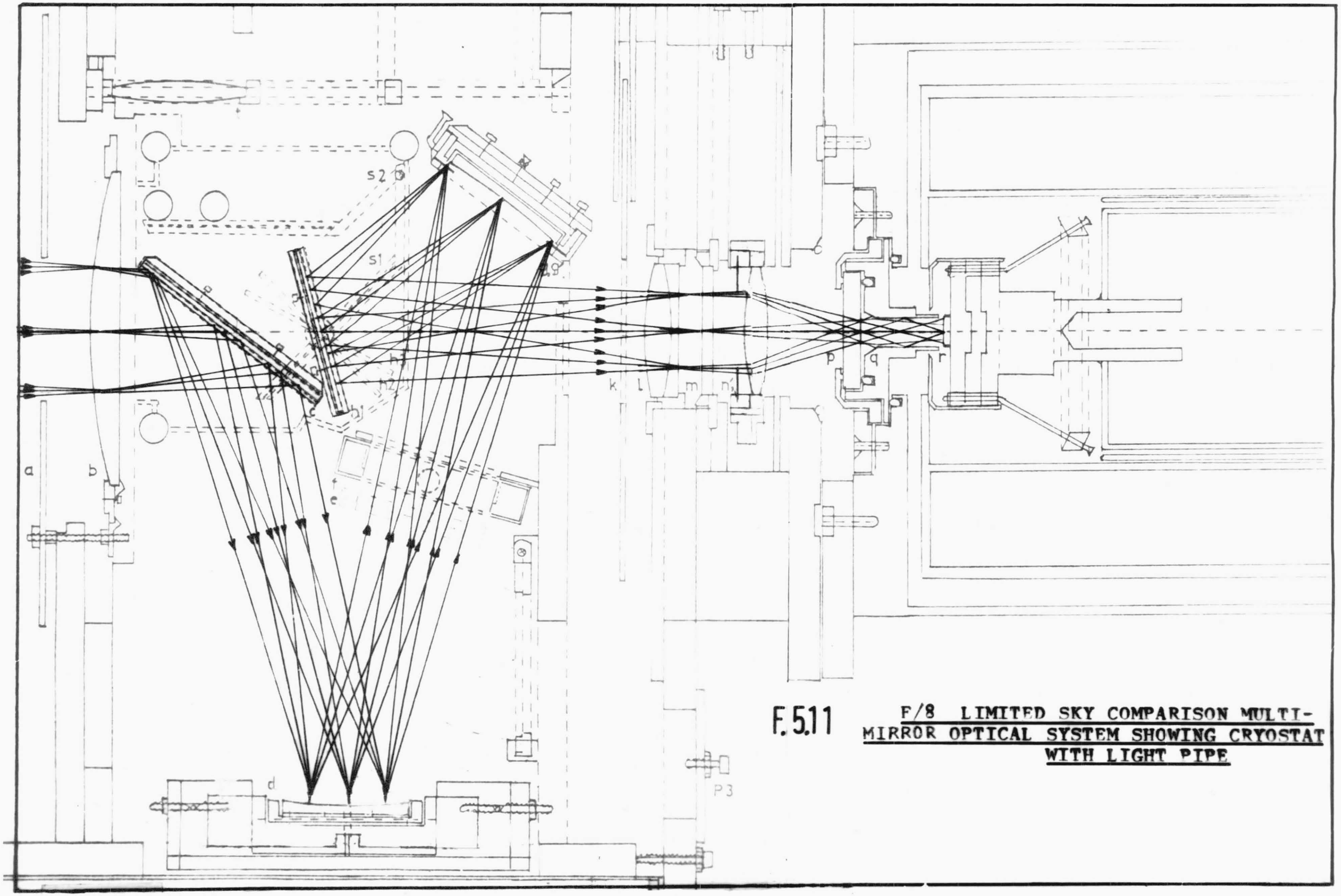

F. 5.11 F/8 LIMITED SKY COMPARISON MULTI-MIRROR OPTICAL SYSTEM SHOWING CRYOSTAT WITH LIGHT PIPE rods on the sliding module can be seen extending on the right hand side, while the alternate direct view mirror 's' can be seen projecting to the left; in this latter mode, the slide is relocated with the control rods then extended further to the right; the sliding module may be completely removed for storage etc. via a side hatch in the photometer box; the vibrating mirror unit is similarly accessible via another side hatch.

5.08 Preparation for use of this photometer on the R.O.E. 20" telescope

The instrument, as described, was adapted for use on the 20" R.O.E. telescope at the Ritchey-Chrétien F/8 Cassegrain focus. Most of the electronics was improved at about this time (1973 to 1974) and is discussed in detail in chapter 6. An adaptor plate was built for the photometer to interface with the telescope; unfortunately, the prefocal clearance necessary for the photometer and adaptor was 400mm, which was out of range for the telescope, and so some 20mm spacers were made up, to relocate the telescope secondary mirror in order to produce the required focus. Some small improvements to the cross wire illumination systems, and other small refinements to improve the ease of use of the instrument, were also carried out at this time. The F/8 telescope beam enabled all the radiation incident on the 25mm field to be accommodated by the cryostat light pipe and detector, but in practice only 13mm diameter interference filters were available, which further stopped-down the beam. Figure F5.11 shows the optical arrangement with the F/8 telescope beam. The cryostat was used as previously described, wirh an 'Infrared Industries' PbS detector of 5mm x 5mm area, type B3SA8.

5.09 Observations with the photometer on the R.O.E. 20" telescope

Observations were made on this telescope from late December 1973 into January 1974, during the national power emergency; several cold clear nights were experienced. It was found, contrary to expectations, that the detector when cooled gave worse signal/noise than at room temperature, while biased with a matching load resistor in each case, but gave a five-fold improvement on the room temperature performance when mismatched in the cooled state with a 5M to 15M bias resistor (the cell resistance was 180M at ~ 200°K). The bias voltage required to double the zero voltage noise was then found to be only a few volts (as opposed to about 40 volts at room temperature with an 1M cell resistance); the reason for this was later the subject of much investigation, and is discussed fully in chapter 8.

Observations were made of the Orion nebula M42 (NGC 1976), the diffuse nebula in Monoceros (NGC 2264), several red giant stars including Betelgeux and Arcturus, as well as comet Kohoutek. α Ori was used to obtain an instrumental profile; the star was allowed to drift across the field and the detected signal recorded on a chart recorder; the resultant profile would be ideally a box function for the light pipe, convoluted with a sinusoid cycle for the sky-comparison scan profile, but in practice included a strong gaussian component. The best signal to noise with a 10 second integration for α Ori was about 10 at λ 1.65μ, and less at 2.3μ, while on some apparently clear nights no signal could be detected. M41 gave no clear signal, but

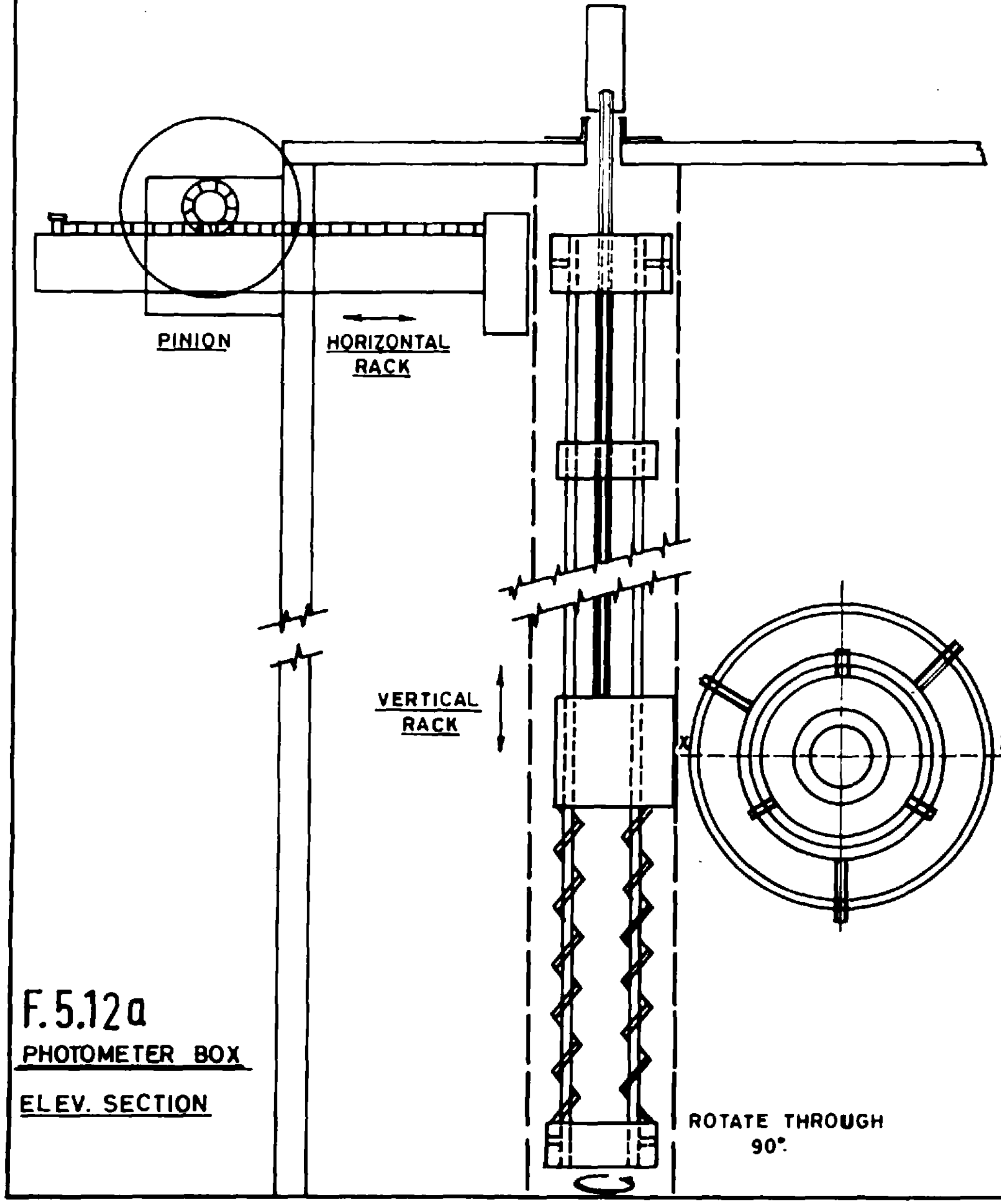

F. 5.12a

PHOTOMETER BOX

ELEV. SECTION

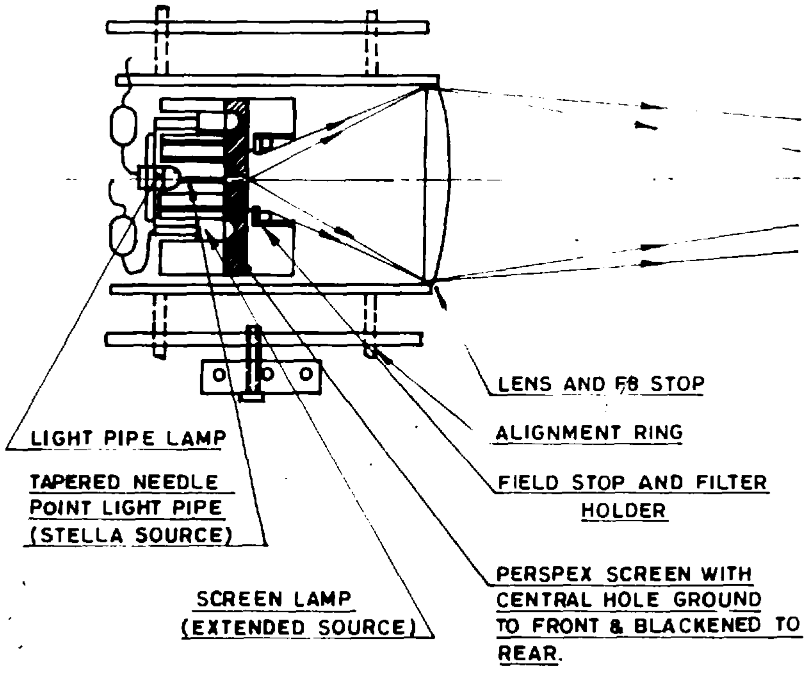

F. 5.12b CROSS SECTION X-X′

THE ARTIFICIAL STAR AND SLIDE

the nucleus of comet Kohoutek was observed on the 13 January 1974 to give a signal to noise between 15 to 20 at λ 2.2μ, as compared with the sky background. Unfortunately confirmation or a calibration for this observation was not possible, owing to subsequent cloud cover. The observation of comet Kohoutek was limited to 10 minutes on the one night only, but the result was considered particularly encouraging.

5.10 Design improvements resulting from the previous observations

The first diagonal flat frame, 'S1' in figureF5.03, was modified such that the flat can now slide up into a housing on the box lid; in this position, the telescope beam passes via a slot in the mirror 'S2' to a focus before eyepiece 'E2'. This eyepiece was mounted on a horizontal slide with three adjustable preset positions: one central, and one either side, corresponding in total to the amplitude of sky-comparison used (usually 25mm). Some minor changes were made to the offsetting eyepiece facilities, but the other major improvement was the addition of an artificial star (F5.12).

The artificial star as shown in figure F5.12 consists of a small filament lamp and adjoining tapered light pipe tapered to a needle point and blackened along its length. This point projects through a no.67 hole in a ground perspex screen; the screen can be separately illuminated to form a continuous extended source, as an alternative to the point source just described. The field is limited by a stop ring which holds a Kodak gelatine No. 37 filter; the whole unit is mounted at the focus of a simple 30mm diameter lens which projects an image of the screen and point in an F/8 beam to the field lens in the photometer box. The unit is mounted in a fully adjustable mounting and is supported by an X-Y slide arrangement with rack-pinion, as shown in figure F5.12a. This assembly is located on the end inside wall of the photometer box at 'A' in figure F5.03, and can be seen by the photometer detector through any of the optical systems via the field lens when the mirror'S1' is in its raised position.

The artificial star proved invaluable for routine instrumental laboratory tests, and for measurements of detector comparisons and characteristics.

A laser bolting frame was also installed, such that a laser may be bolted either to the outside of the end wall of the box, to define the optic axis, or at the cryostat face plate in place of the cryostat, again defining the optic axis to assist laboratory alignment of the equipment.

A complete set if circuit diagrams for the present photometer is given in chapter 6.

No references have been found for optical systems similar to those previous described.

CHAPTER 6

6. The electronic circuits developed for the infrared photometer.

Contents:

THE ELECTRONIC CIRCUITS DEVELOPED FOR THE INFRARED PHOTOMETER

6.01 The block layout. F6.01

The block layout diagram F6.01 shows the system at the time of writing; the signal processing circuits are discussed in this chapter, while the servo system is discussed in chapter 7. Both the signal channel and the reference channel show a number of changes from the block layout diagram F3.07. In these diagrams switches are denoted by 'sw', and pin contacts by 'c', attenuators by 'p', and socket pins by 'B'.

6.02 The HT attenuator circuit. F6.02

The bias battery attenuator circuit shown in F6.02 is symmetrical about the earth point 'B93' so as to reduce pick-up on the cable to the cryostat, and to help reduce the effect of switching spikes and other transients or capacitance leakage effects from upsetting the cooled F.E.T. in the preamplifier. The signal channel is capable of detecting 10 nv, at the input, and so switched attenuators were used in place of continuously variable potentiometers to attenuate the 90v battery supplies; three switch ranges enabled coarse and fine adjustment to be made to the bias. Low-noise wire-wound resistors are used throughout, together with a choice of two smoothing capacitor values; without the capacitors, battery voltage fluctuations at very low frequency become very serious. The unit is earthed through the preamplifier.

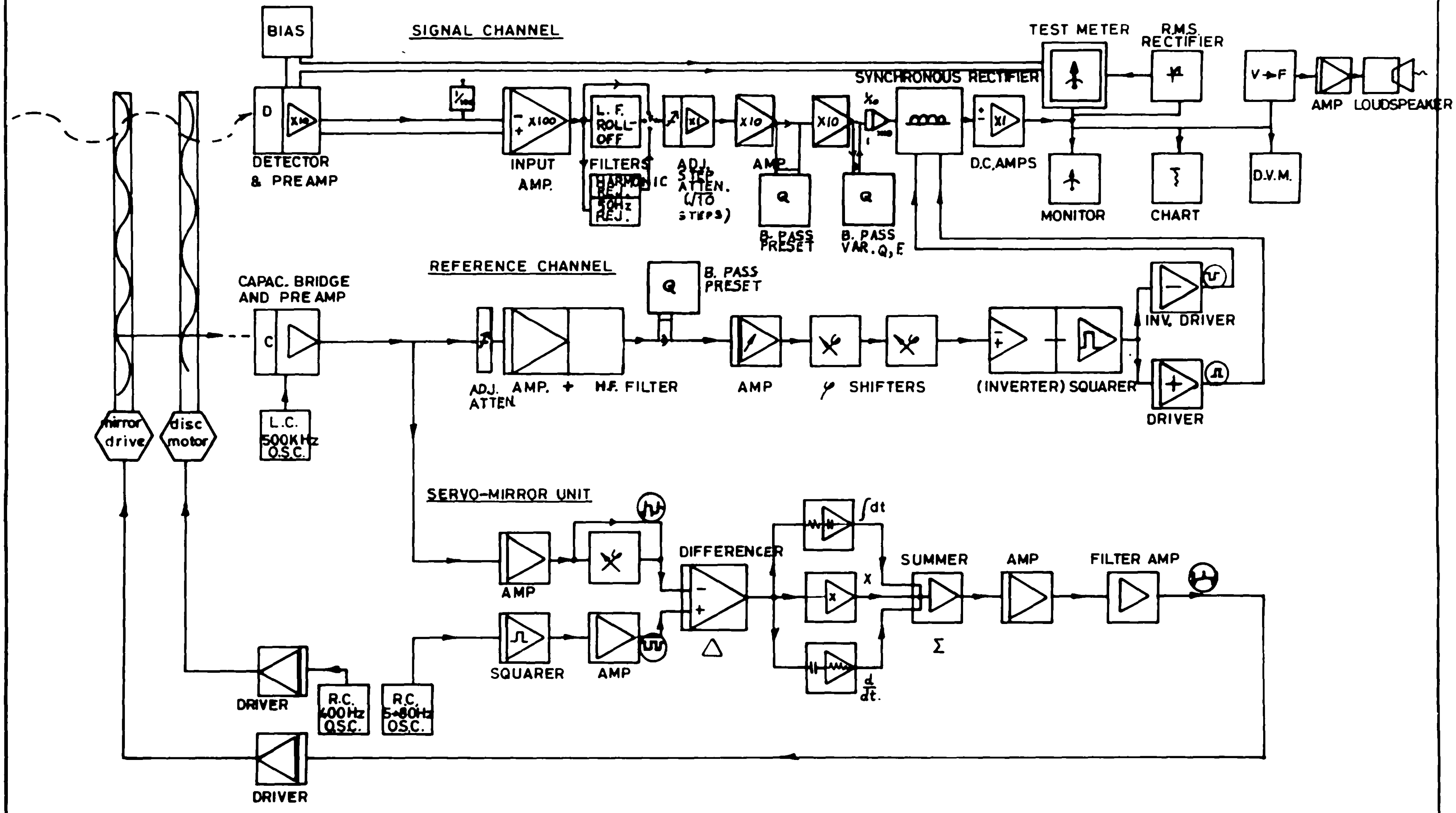

F.6.01 ***BLOCK LAYOUT OF PHOTOMETER CIRCUITS***

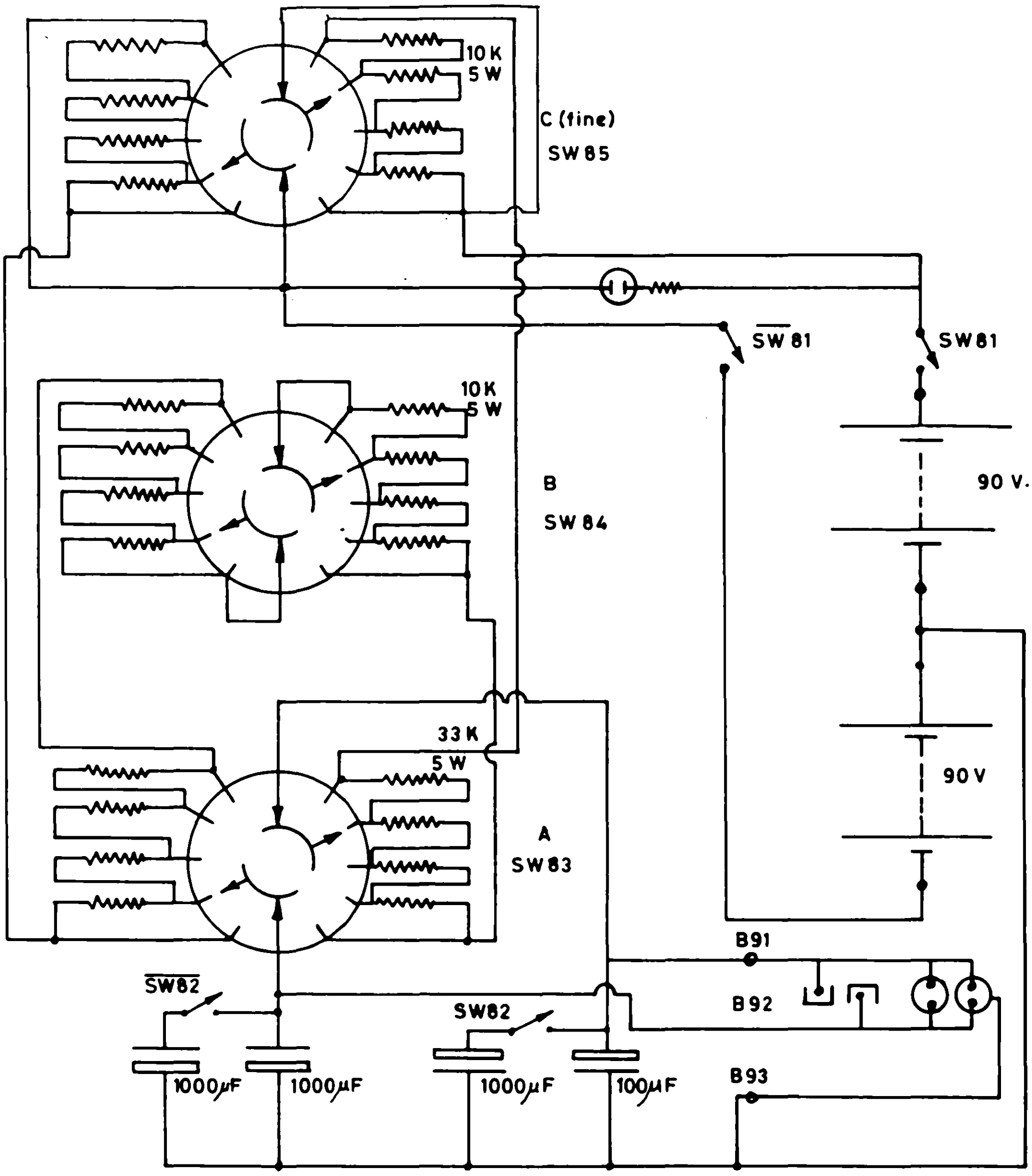

F.6.02 H.T. ATTENUATOR CIRCUIT

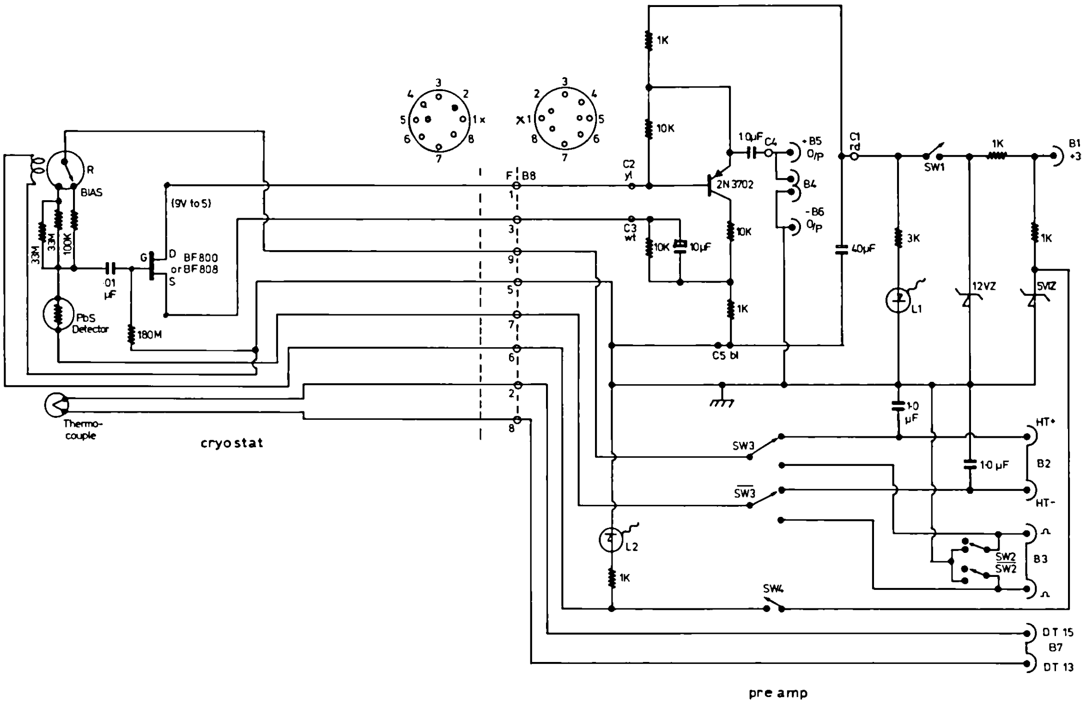

F. 6.03 DETECTOR HEAD AND PREAMPLIFIER CIRCUIT

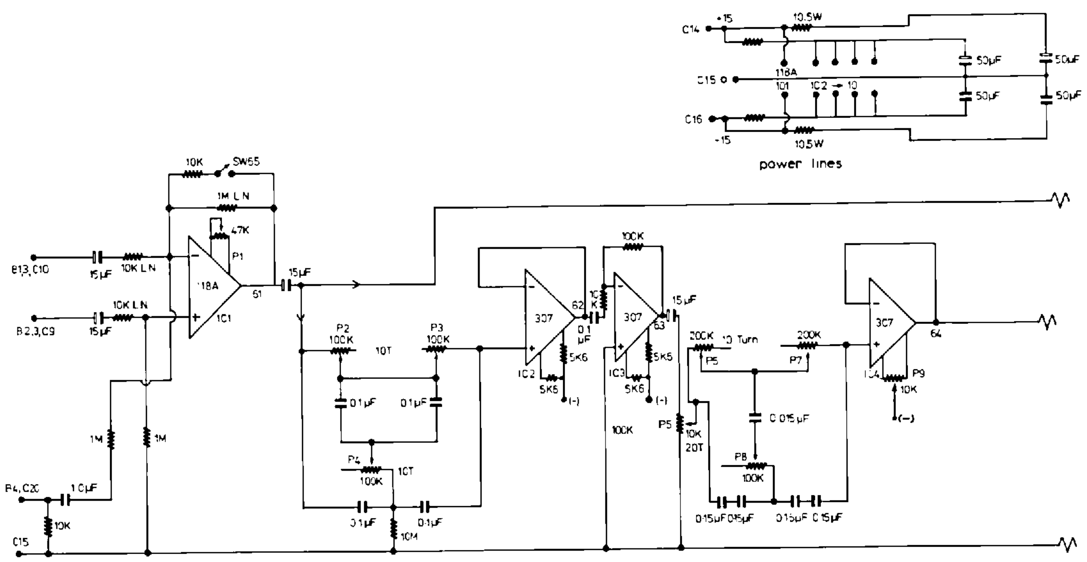

LOW NOISE DIFFERENTIAL INPUT
X 100 AMPLIFIER AND TEST
ATTENUATOR

50 Hz REJECT EILTER
(OPTIONAL)

TUNABLE REJECTION FILTER
(FOR 3rd HARMONIC SUPPRESSION)
(OPTIONAL)

F 6 04 a SIGNAL CHANNEL CARD

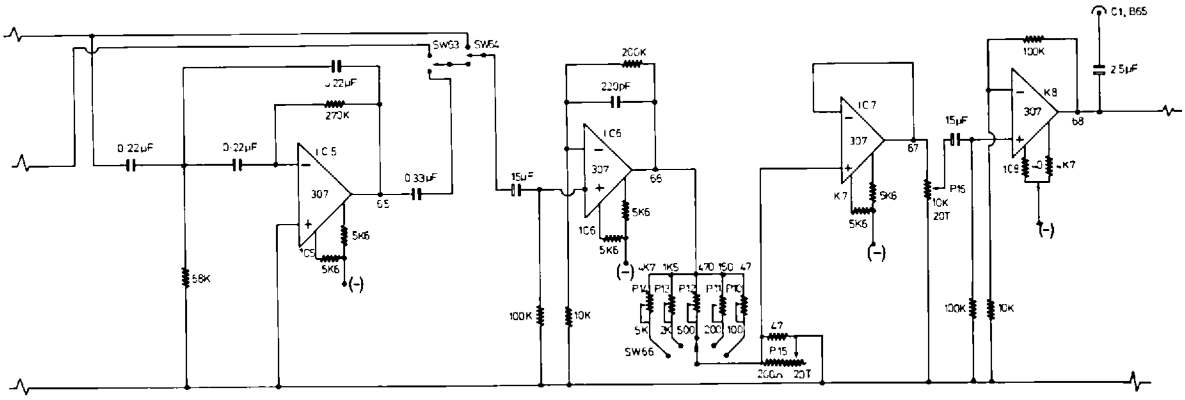

LOW FREQUENCY REJECT FILTER
(OPTIONAL)

SWITCHED GAIN MAIN AMPLIFIER

F.6.04 b SIGNAL CHANNEL CARD (cont.)

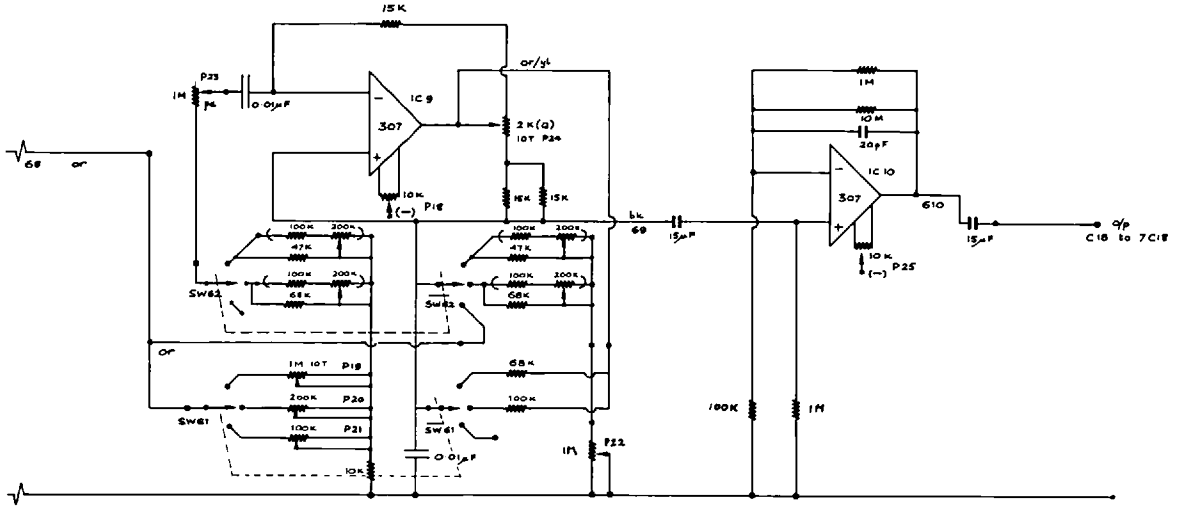

VARIABLE Q, VARIABLE PASS FREQUENCY
BAND PASS FILTER, SWITCHES LINKED WITH REF. FILTER

BOOSTER AMPLIFIER

F.6.04c SIGNAL CHANNEL CARD (cont.)

CARD 7 - VARIABLE - Q.f. BANDPASS FILTER

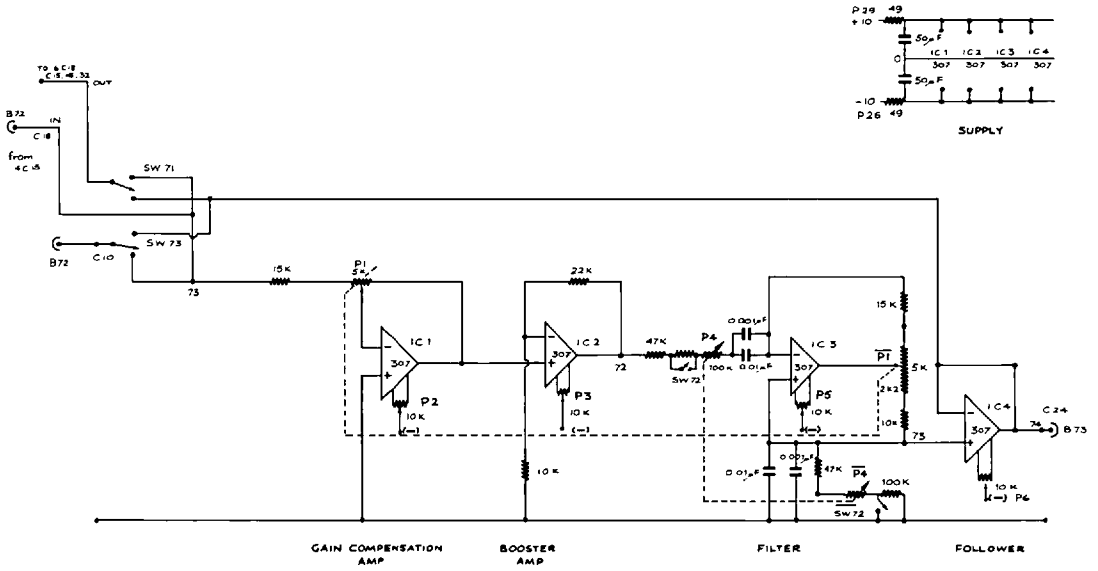

F.6.05 VARIABLE FREQUENCY, BAND PASS, VARIABLE Q FILTER (100 → 460 Hz)

6.03 The detector head and preamplifier circuit F6.03

This unit is built in two sections; the low noise F.E.T. is mounted in the cryostat near the detector; F.E.T. BF800 has a very low noise current while BF 808 has a very low noise voltage, these characteristics vary with temperature and gate load and so the lowest noise F.E.T. should be selected by experimental comparison; in practice this is not a critical factor. Preamplifier roll-off is given by the .01 μF capacitor and 180M F.E.T. gate bias load resistor. The detector bias voltage load resistor is mounted like the F.E.T., and may be switched from one of two values by relay R; the relay when not powered switches in the higher bias used with the cooled detector (no power is then dissipated by the relay to cause heating). A thermocouple probe monitors the detector head temperature. The remaining preamplifier stages are housed in a box fixed to the outer valve plate of the cryostat, which contains the X10 voltage amplifier stage for driving the line to the main amplifier.

This box also contains the detector bias line from the H.T. attenuator together with some line hum suppression capacitors, and a switch to connect over to the (cell + bias) resistance measuring circuit (see multimeter F6.11).

6.04 The Signal channel card. F6.04

The first stage of the signal channel uses an 'Analog Devices 118A' low noise operational amplifier and low noise resistors. This amplifier is operated in common mode rejection between the amplifier and dummy line, in order to minimise pick-up on the line; the unit is set for a voltage gain of 100, but can be switched to X1 or used with a $^1/100$ attenuator input. All the remaining I.Cs. are of type T.I. 2N307 (replacements for the original T.I. 2N709).

The optional filter block shown in F6.04a was in practice rarely used, but contains a tunable 50Hz reject (notch) filter and a similar filter at first used for carrier third harmonic suppression. Another optical filter is used only for cases of bad $\frac{1}{f}$ noise, and is shown in F6.04b; this low-frequency roll-off filter operates at about 3Hz with 6db/octave roll-off.

Variable signal gain is achieved from switching between five preset attenuators (in steps of $\sqrt{10}$) after a X20 amplifier; the attenuator is matched to a X10 amplifier via a buffer amplifier, and so the attenuated signal is amplified with variable gain without a change in system frequency response. The switched preset band-pass filter was used in conjunction with the identical common switched unit in the reference channel, but in practice this filter proved unnecessary. The signal amplifier card concludes with a further X10 booster to give signal levels in the range of 0.1 to 10 volts.

6.05 The variable Q tunable band-pass filter. F6.05

This experimental filter was built for investigating the effect of different carrier waveforms and could be used for harmonic suppression; it has a continuously variable Q from 2 to 100, and a nominal frequency

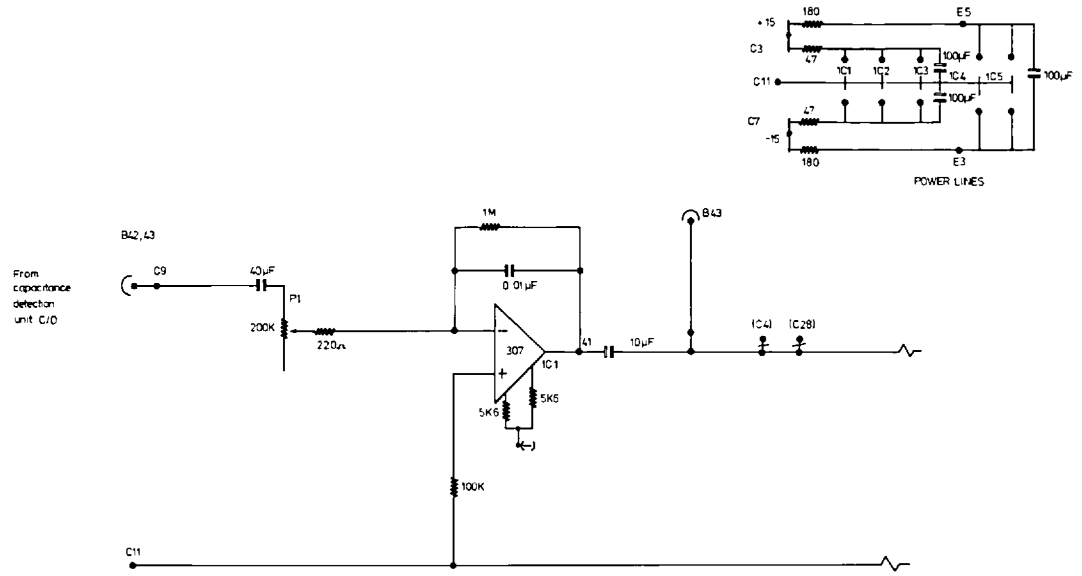

input integrating amplifier

F.6.06a REFERENCE CHANNEL CARD

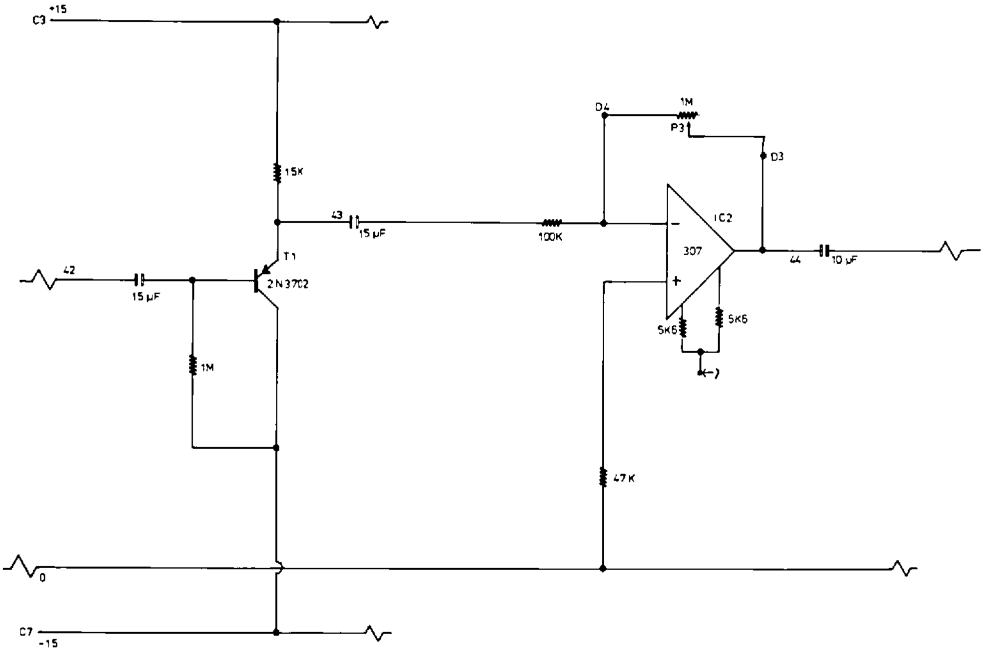

EMITTER FOLLOWER AND ADJ GAIN AMPLIFIER

F.6.06b REFERENCE CHANNEL CARD (cont.)

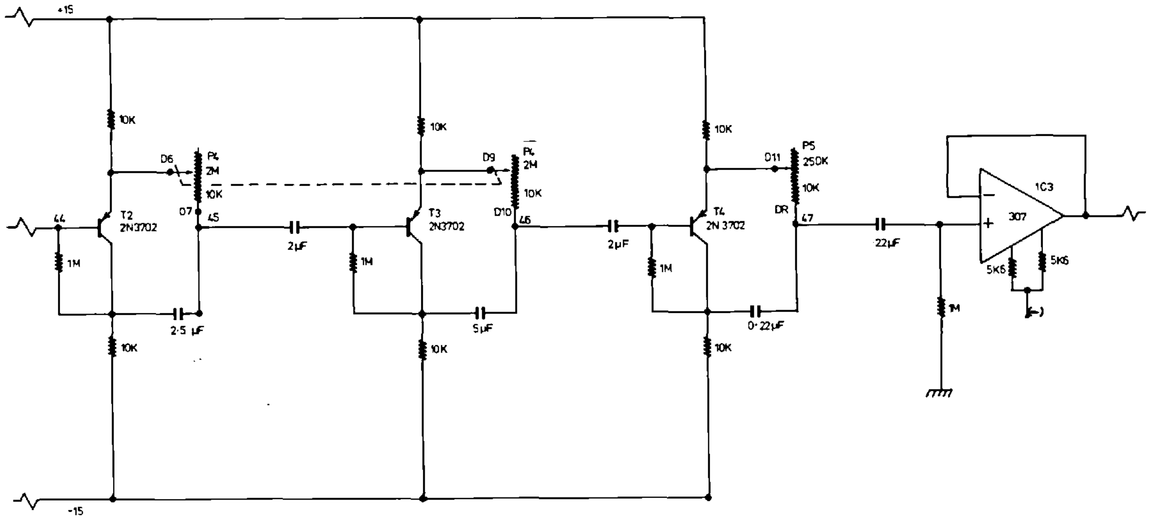

two ganged phase shifters and one phase shifter and follower

F.6.06c REFERENCE CHANNEL (cont)

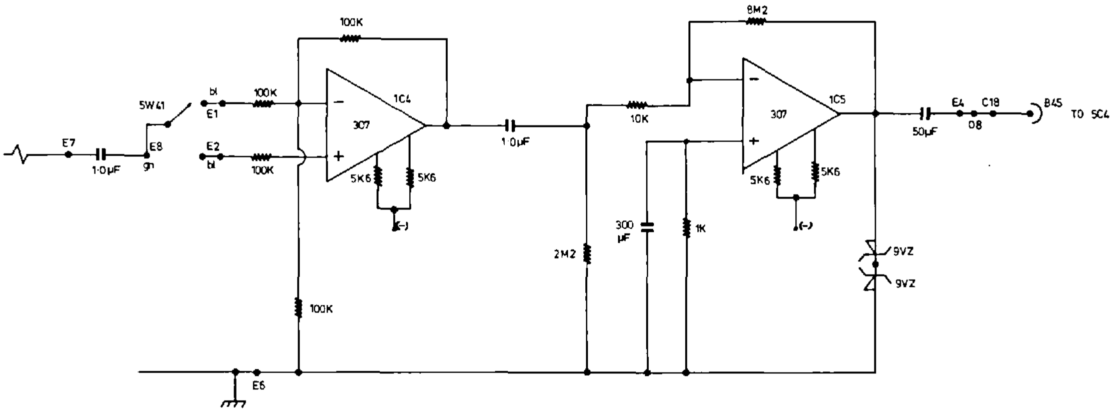

PHASE INVERTER AND SQUARER

F.6.06d REFERENCE CHANNEL (cont.)

range of 100 to 460Hz. The filter may be switched into the output of the main amplifier or operated separately; in practice, all filters were switched out during astronomical observations.

6.06 The reference channel card. F6.06

The input stages of this card have been considerably altered since the phototransistor reference detector was replaced by a capacitance bridge. The input stage is now a high frequency filter amplifier, the filter is necessary to remove possible high harmonics in the reference waveform which would otherwise prove a problem in the phase shifters. A follower connects this to the next stage; originally this stage was a preset switched band-pass filter identical to that in F6.04c, used to maintain the relative phase with the signal channel, but this was later removed as it proved to be a source of cross channel interference, and was later quite unnecessary. A variable gain amplifier is used to set the reference level gain, and this is then followed by three phase shifters; two are ganged together to provide coarse phase adjustment.

The phase shifters are of an original design based on an R-C bridge, taking advantage of the phase-antiphase outputs of a transistor (this circuit may not be designed around a single I.C. where there is only one phase of output). With reference to the negative rail, the output voltage to input voltage ratio is:

$$\frac{\frac{1}{j\omega c}}{r + \frac{1}{j\omega c}} - \frac{R}{R+R} \qquad \text{E6.01}$$

where 'R + R' denote the two reference resistors, 'c' the capacitance and 'r' the variable resistance for phase adjustment; then this becomes

$$\frac{1}{1+j\omega rc} - \frac{1}{2} = \frac{1 - j\omega rc}{1 + j\omega rc} = \frac{(1 + \omega^2 r^2 c^2)^{\frac{1}{2}} e^{-j\theta}}{(1 + \omega^2 r^2 c^2)^{\frac{1}{2}} e^{+j\theta}}$$

$$= e^{-2j\theta} \quad \text{where } \tan\theta = \omega rc \qquad \text{E6.02}$$

It is seen that there is no resultant change of amplitude through the network, and the phase change is $2\tan^{-1}\omega rc$; it is clear from this relation that the harmonic content of such a carrier must be very restricted, so as to prevent gross waveform distortions.

The phase shifters are buffered before passing to an inverting or non-inverting unit gain amplifier for phase anti-phase selection, and then to a squarer amplifier. The squarer amplifier is a high gain diode clipped amplifier with high D.C. feedback to ensure equal mark-space ratio.

The circuit was found to be far more stable (less prone to oscillation) than the original circuit containing the Schmitt trigger.

SYNCHRONOUS RECTIFIER CARD 5

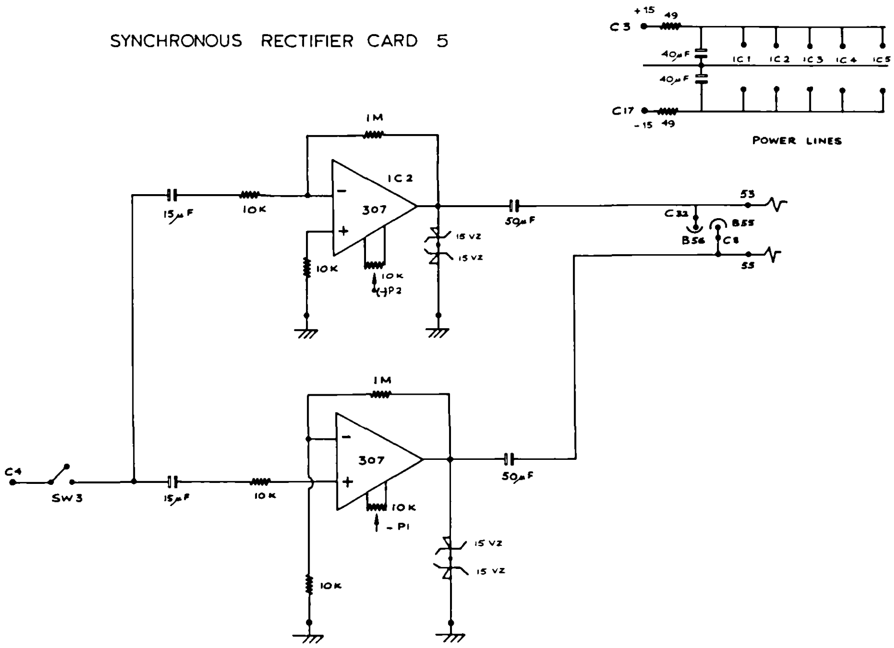

INVERTING AND NON-INVERTING DRIVER AMPLIFIERS

F.6.07a SYNCHRONOUS RECTIFIER CARD

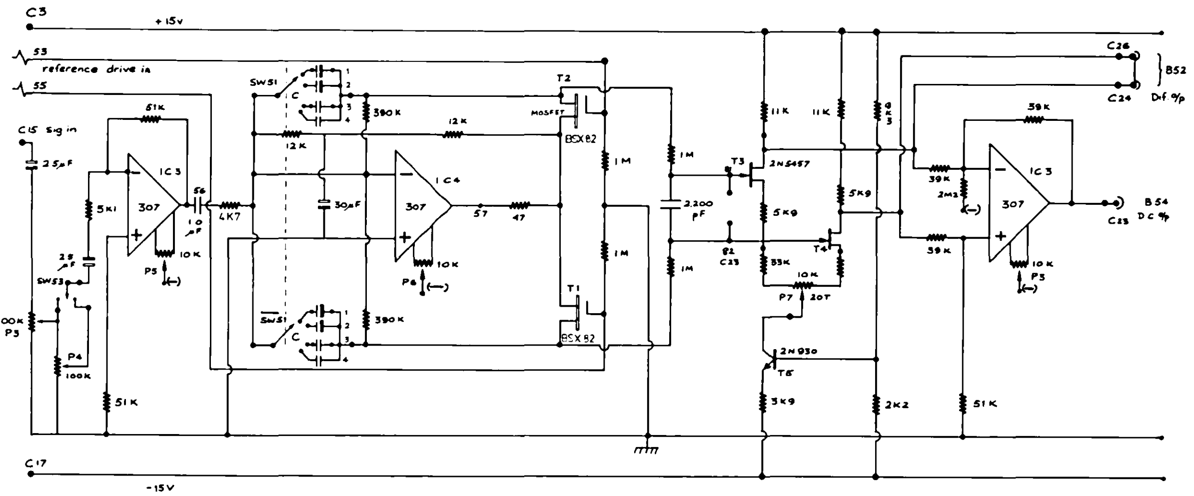

C = 1 [250µF
2 25µF
3 2·5µF
4 0·25µF

F.6.07b SYNCHRONOUS RECTIFIER AND DC CURRENT AMPLIFIERS

6.07 The synchronous rectifier card. F6.07

Several synchronous rectifiers were tried, but that found most successful, is that of P. Williams (R6.05), giving particularly good noise rejection and stability. On the card (F6.07) the signal passes through an attenuator and amplifier to provide optional additional gain, then into the active switch synchronous rectifier; the switching is provided by insulated gate MOSFETS driven by the split reference channel square wave via an inverting and a non-inverting amplifier of F6.07a. As can be seen, the switching to the integrating capacitors is done symmetrically in the feedback loop of an operational amplifier; the 30μF capacitor controls the low frequency roll off. Integration times of 0.1 sec to 100 secs are available in steps of X10 (corresponding to changes of X 10 in the signal/noise); the high frequency performance roll-off is determined by the 2200pF capacitor. 'P7' provides adjustable D.C. offsetting of the rectified signal; the two rectified antiphase D.C. outputs are differenced in the output amplifier.

6.08 The output monitor. F6.08

This card provides a monitoring facility for the output of the synchronous rectifier; the meter was offset to read zero output for mid scale; the potentiometers provide adjustment for range and offset.

OUTPUT MONITOR CARD 2

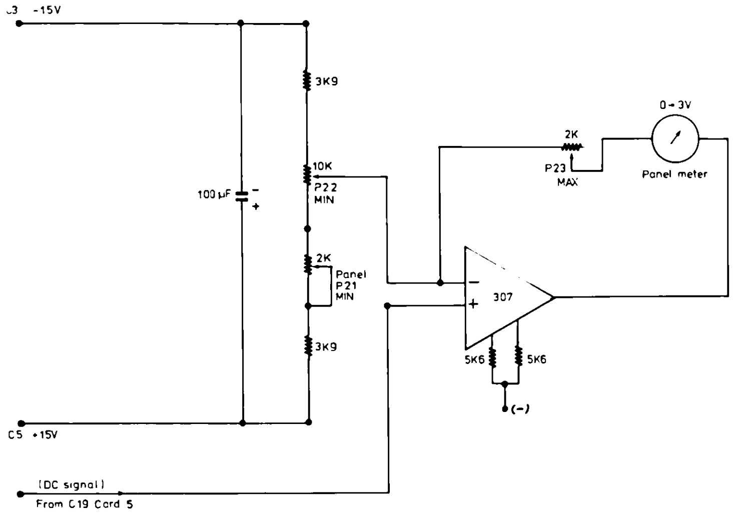

F.6.08 METER AND METER DRIVER

TEST OSCILLATOR BOARD CARD 3

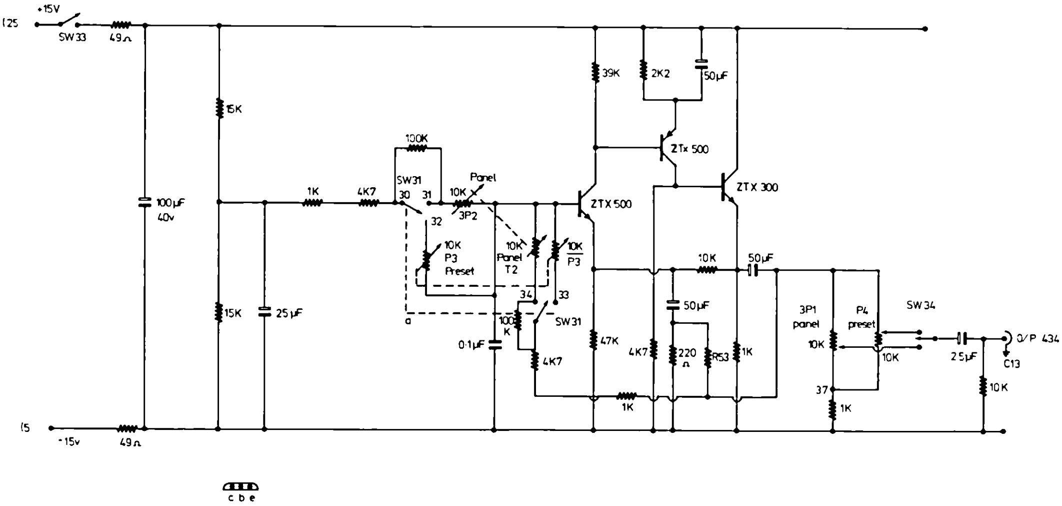

F.6.09 113 → 455 Hz LOW DISTORTION OSCILLATOR WITH COARSE AND PRESET FINE CONTROLS

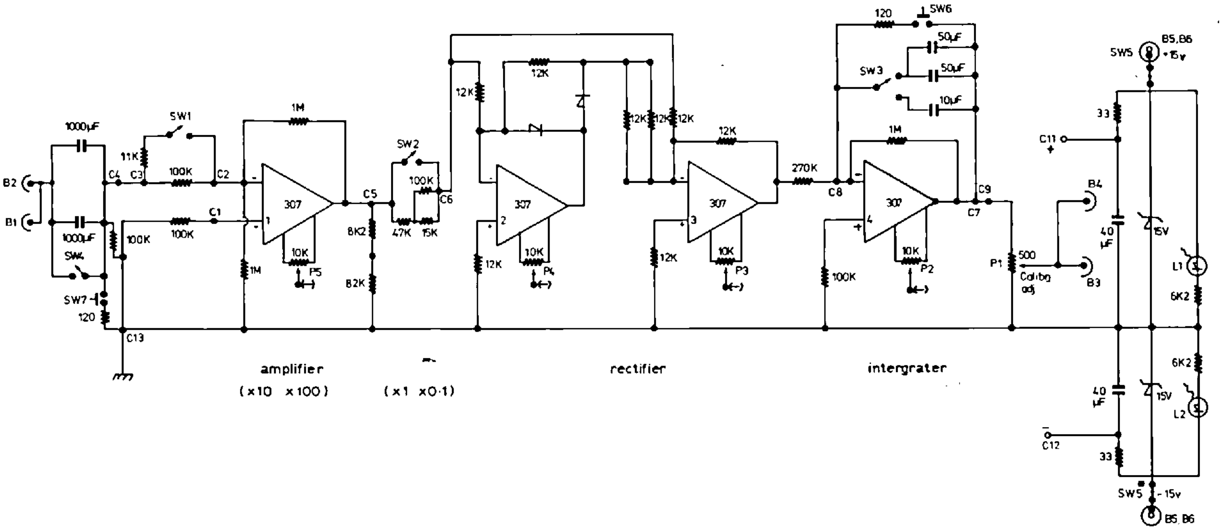

F.6.10 R.M.S. RECTIFIER

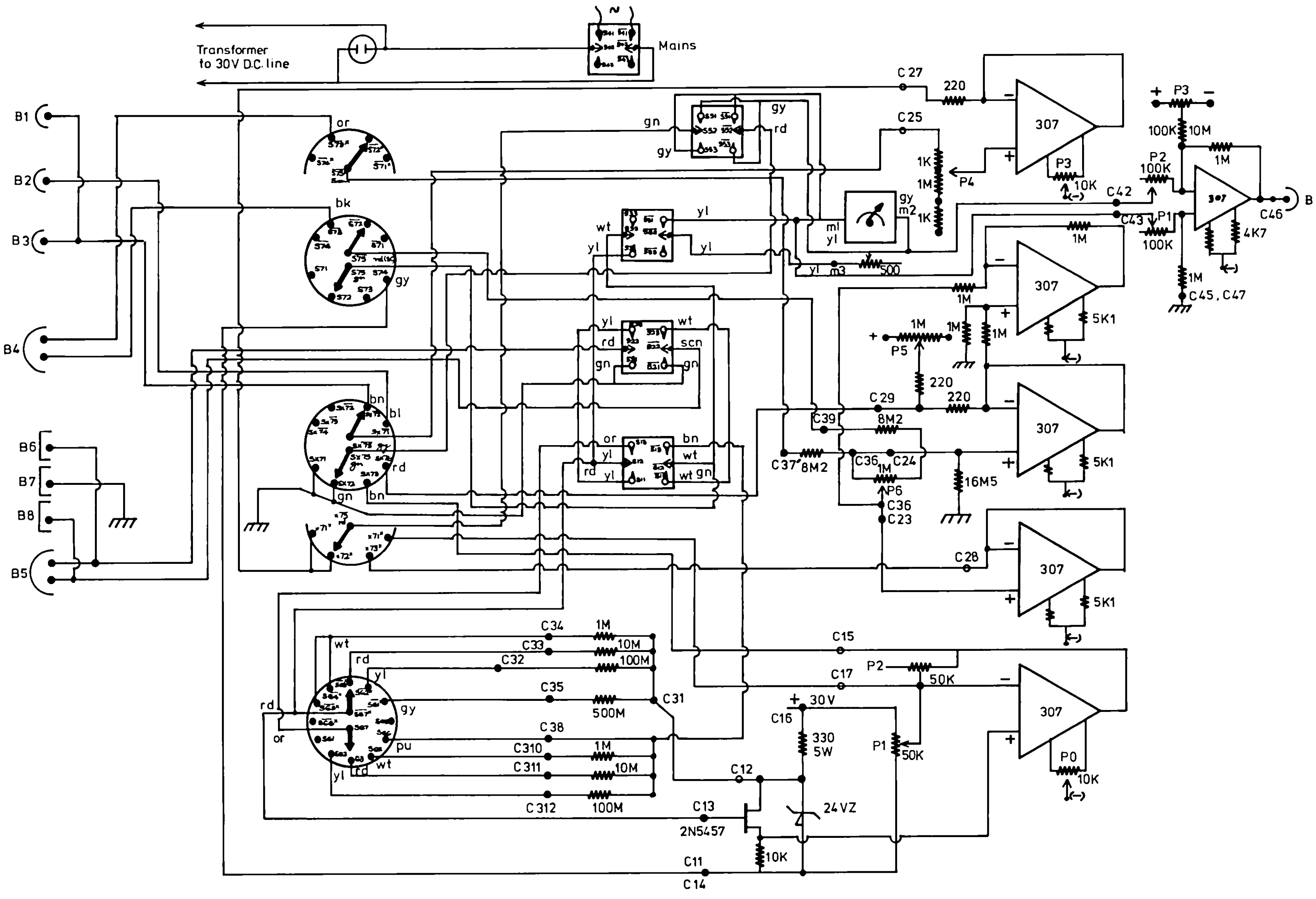

F.6.11 MULTIMETER CIRCUIT

6.09 The test oscillator. F6.09

This is provided in the signal electronics rack for testing circuits and calibrating gain; it is of a simple Wien bridge transistor design, with coarse and fine frequency ranges.

6.10 The R.M.S. rectifier. F6.10

This circuit was used to measure the noise from the synchronous rectifier in the detector signal/noise tests. The first amplifier provides several gain settings, and an input capacitor can be used to block the D.C. signal component (this is bypassed when calibrating the meter with a known D.C. voltage). The diode feedback of the perfect diode circuit, followed by a summing amplifier, provides full wave rectification of the input waveform, which is then integrated with either a 3 sec. or 30 sec. time constant; and fed to a meter.

6.11 The multimeter. F6.11

This is a test and monitoring facility that proved particularly useful; it includes two 1v to 3v range voltage monitoring inputs, usually connected to the signal output from the synchronous rectifier, and the rectified noise output from the R.M.S. rectifier. The circuit angles of a 150 volt range differential input for monitoring the detector bias voltage, and a F.E.T. follower with preset biased gate for measuring the resistance of the detector with a bias resistance. The 2N5457 F.E.T. is gate positive biased by standard resistors (1M, 10M, 100M, 500M) switched from 'SW6', which may be compared with a similar set of standards to the negative rail (effectively reducing the bias), and the output meter is then adjusted to read halfscale; the detector + bias resistance is measured in the same way as compared with the standard calibrated values. All the necessary calibrations and range selection, as well as mode (Ω,v, etc), is controlled from panel switches; the mode switch enables the user to measure consecutively the output noise, signal, bias voltage, and detector with bias resistance, from a single meter.

6.12 Reference oscillator circuit. F6.12

This is just a Wien bridge circuit with a low distortion feedback amplitude control, and an optional squaring circuit. The unit is used mostly to drive the chopper disc via a power amplifier and transformer, and has stepped octave frequency ranges from 2Hz up to about 2kHz.

6.13 Main power lines and transformers. F6.13

This unit contains two sets of symmetrical power supplies and a ± 51v line for biasing the solenoid originally used for driving the mirror unit; the drive signal is supplied via a power amplifier and transformer 'T2'; the second power supply is stabilised and operated at ± 15 volts and is used for the power amplifiers previously mentioned. Transformer 'T3' is used to step up the voltage from a power amplifier in order to drive the disc chopper previously mentioned.

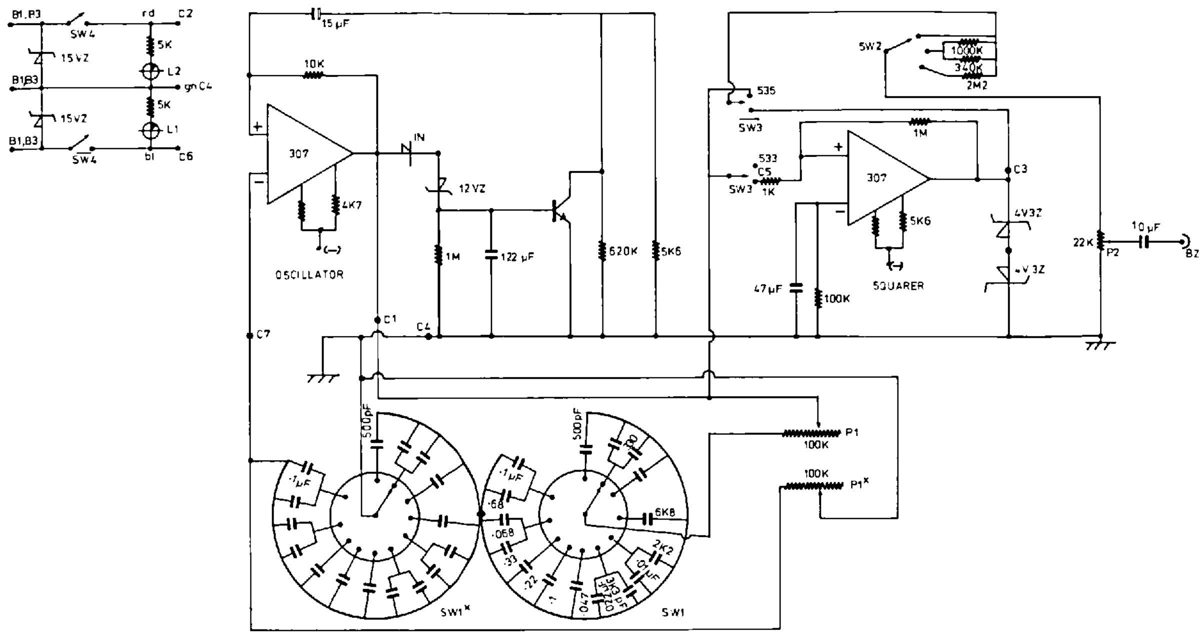

F. 6.12 REFERENCE OSCILLATOR CIRCUIT

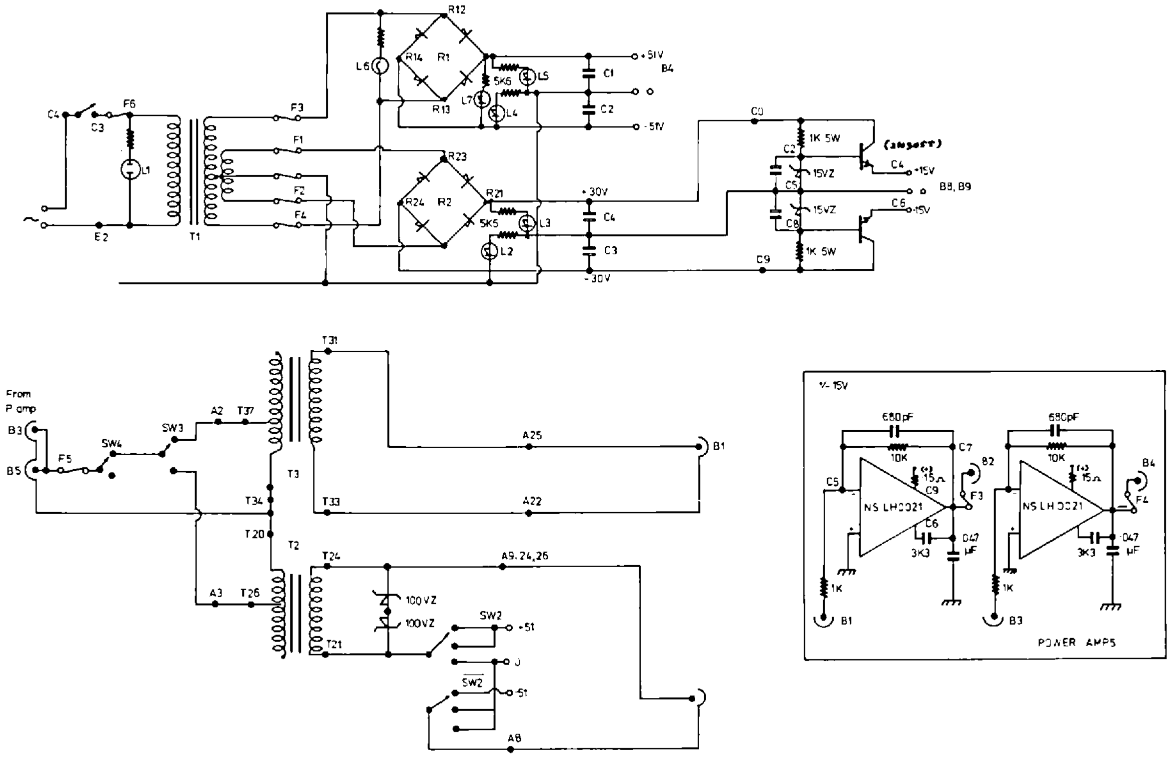

F. 6.13 MAIN POWER LINES AND TRANSFORMERS

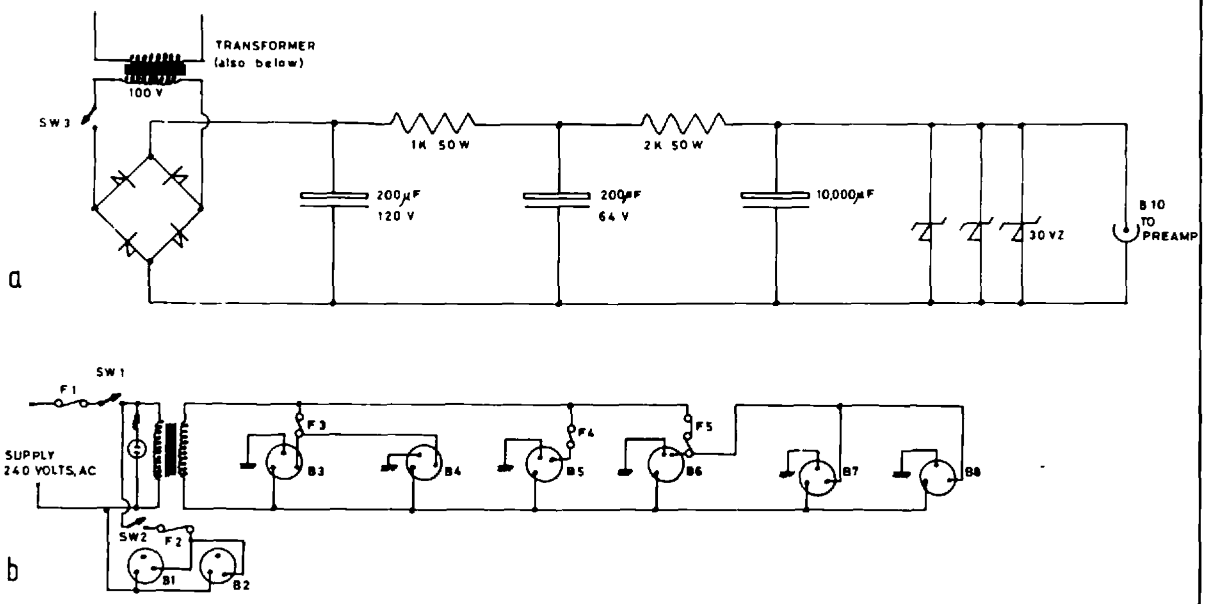

F. 6.14 *PRE AMP POWER SUPPLY AND DISTRIBUTION BOX*

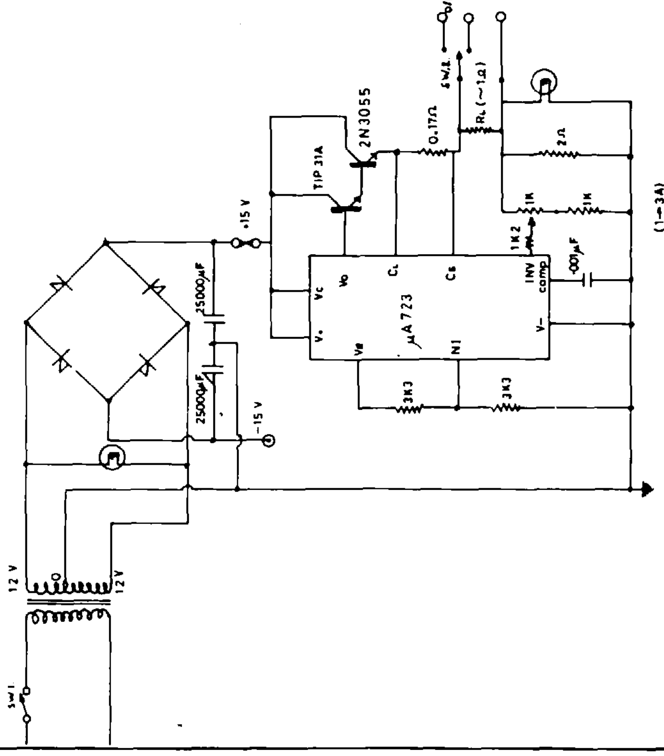

F. 6.15 *CURRENT STABILISED POWER SOURCE FOR CALIBRATION LAMP*

6.14 The preamplifier power supply and distribution box. F6.14

This unit is a fuse box and a well smoothed power supply for the preamplifier.

6.15 The current stabilised power supply for a calibration lamp. F6.15

This unit was built originally as a constant current supply for a calibration lamp, but later supplied the artificial star. It has a voltage range from 1 to 10v. at 5A. and is stable to 1 in 10^3; the output voltage is set by a vernier potentiometer.

6.16 General electronics specifications

Table 6.1 shows the general electronics specification, while T6.2 gives the output to input scaling ratios for the various gains and time constants; T6.2 is used in chapter 9.

Figure F6.16 shows the measured signal channel frequency response; as mentioned, the system was usually operated without any filters.

6.17 System noise specification (excluding preamplifier)

F6.17 shows the main amplifier noise (mostly originating in the first stage of the input resistor), and the synchronous rectifier switch noise (seen as a train of transients) which is only of concern when the carrier frequency is about 10^3Hz. At room temperature the carrier frequency was usually set at 30Hz, but was lowered to about 5Hz with a good cooled detector (see chapter 8). The preamplifier noise is about 10X the main amplifier noise.

6.18 Calibration curves for the high resistance ohm meter

F6.18 shows the multi-meter resistance range calibrations for the D.V.M. output and the panel meter. These curves were used to obtain estimates of the detector resistance, at room temperature, and also when cooled.

6.19 Conclusion

The circuits described were evolved over a considerable period of time; in some cases, many different circuit designs were investigated; those presented here were considered the most satisfactory; the relative advantages of the various possible filter designs are not discussed here for reasons of brevity.

A reading list is given at the end of this chapter. A complete set of layout diagrams is available separately.

Table T6.1

Electronic Specification Table

Amplifier (no preamplifier):

Gain : $G1 = 1.0 \times 10^3$ (+, -) according to input

$G2 = 3.16 \times 10^3$

$G3 = 1.0 \times 10^4$

$G4 = 3.16 \times 10^4$

$G5 = 1.0 \times 10^5$

Preamplifier gain: + 10.0
-ve o/p is dummy

preamplifier freq. resp.: 1 db pt. < 5Hz

main amplifier freq. resp.: 1 db pt. < 1Hz

Filter attenuation :

f Hz :	3.8	7.5	15	30	50	60	120	650	750	850
L.f. roll off :	0.40	0.82	0.95	0.95	1.0	1.0	1.0	1.0	1.0	1.0
50Hz reject + a harmonic reject		1.27	1.10	0.45	0.0	0.27	0.75	0.5	0.0	0.50
					(Q = 2.0)				(Q = 6.4)	

fixed band psss filter: 1, $f_{01} = 300\text{Hz}: Q_{11} = 2.7, Q_{12} = 5.5, Q_{13} = 9.5$

2, $f_{02} = 410\text{Hz}: Q_{21} = 2.7, Q_{22} = 5.5, Q_{23} = 9.5$

Tunable filter band pass: var. Q, f

Synchronous rectifier frequency response:

1 db < 5Hz

F.S.D. = 1.0v pp. ≡ 1.0v pp from amp. X1 or $X\frac{1}{10}$

Table T6.1 (contd.)

Time constants :

T :	1	2	3	4
τsec	0.1	1.0	10.0	100.0
Δ f Hz	3.3	.33	.035	.0033

Noise meter:

AC/DC: A.C. $\tau = 2000\mu F \times 100k = 200$ sec 0.8×10^{-3} Hz.

Integration $\tau =$ 3, 30 sec ≡ $53, 503 \times 10^{-3}$ Hz

(270k x 10μF, 100μF)

gain: x 1.0, x 10.0

Frequency response: flat

Table T6.2

Instrument constants as used for referring output to input

Signal in μV P

Switch setting \ Gain setting:	G1	G2	G3	G4	G5
$\frac{1}{10} \times \frac{1}{100}$	10^5	$\sqrt{10} \times 10^4$	10^4	$\sqrt{10} \times 10^3$	10^3
$\frac{1}{100}$	10^4	$\sqrt{10} \times 10^3$	10^3	$\sqrt{10} \times 10^2$	10^2
$\frac{1}{10}$	10^3	$\sqrt{10} \times 10^2$	10^2	$\sqrt{10} \times 10$	10
X1	10^2	$\sqrt{10} \times 10$	10	$\sqrt{10}$	1

Noise meter $^1/\sqrt{\text{Hz}}$ q

Switch setting \ Integration setting:	1	2	3	4
X1	$1.74/\sqrt{10}$	1.74	$1.74/\sqrt{10}$	1.74
X10	$.174/\sqrt{10}$	.174	$1.74/\sqrt{10}$	1.74
X10 X 10	$.0174/\sqrt{10}$	.0174	$.174/\sqrt{10}$	.174

$$\left\{ \begin{array}{l} E_{2.2} = 0.52/\text{area of field, } (\times\ 0.0796/\text{arc}^2\text{min}) \\ E_{1.65} = 0.62/\text{area of field, } (\times\ 0.0796/\text{arc}^2\text{min}) \end{array} \right\} *$$

* (see chapter 9)

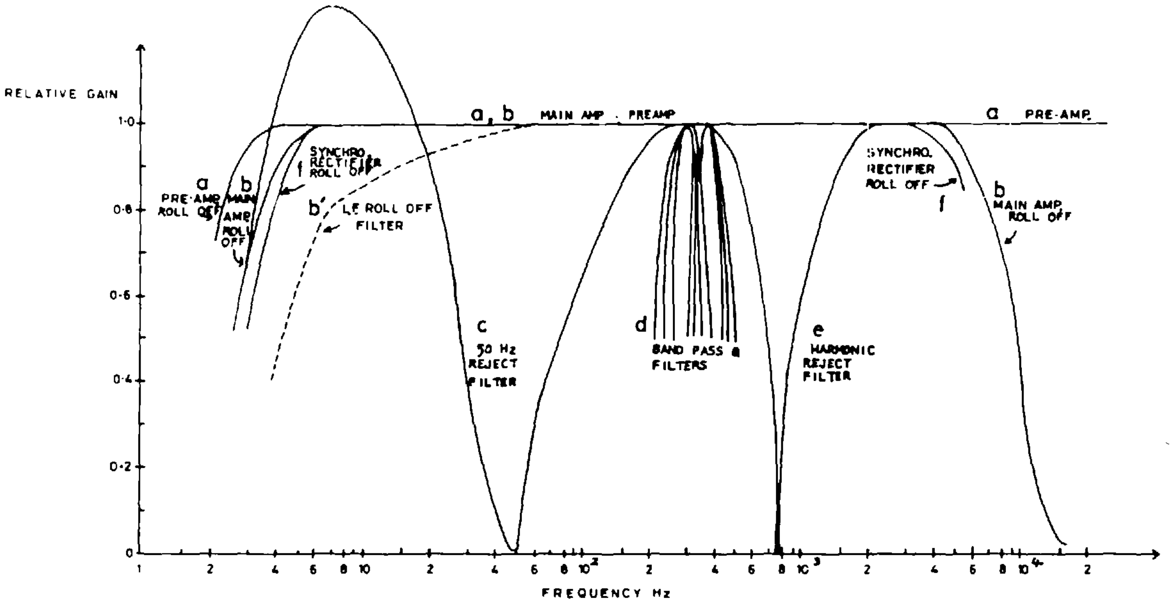

F.6.16 *SIGNAL CHANNEL FREQUENCY RESPONSE*

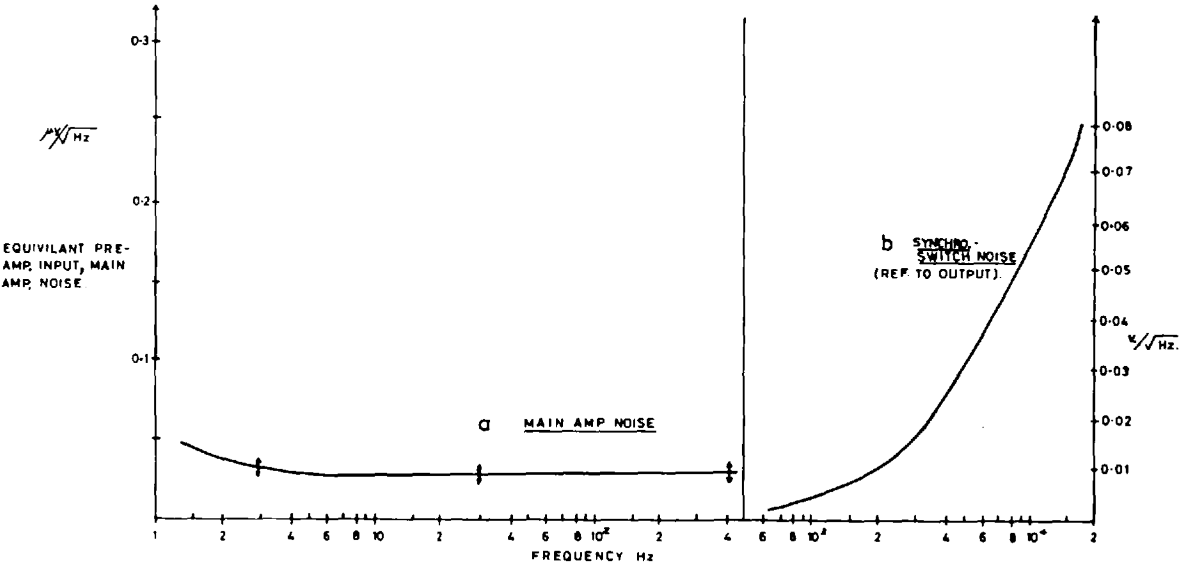

F.6.17 *SIGNAL CHANNEL NOISE REFERRED TO INPUT OF PRE-AMPS.*

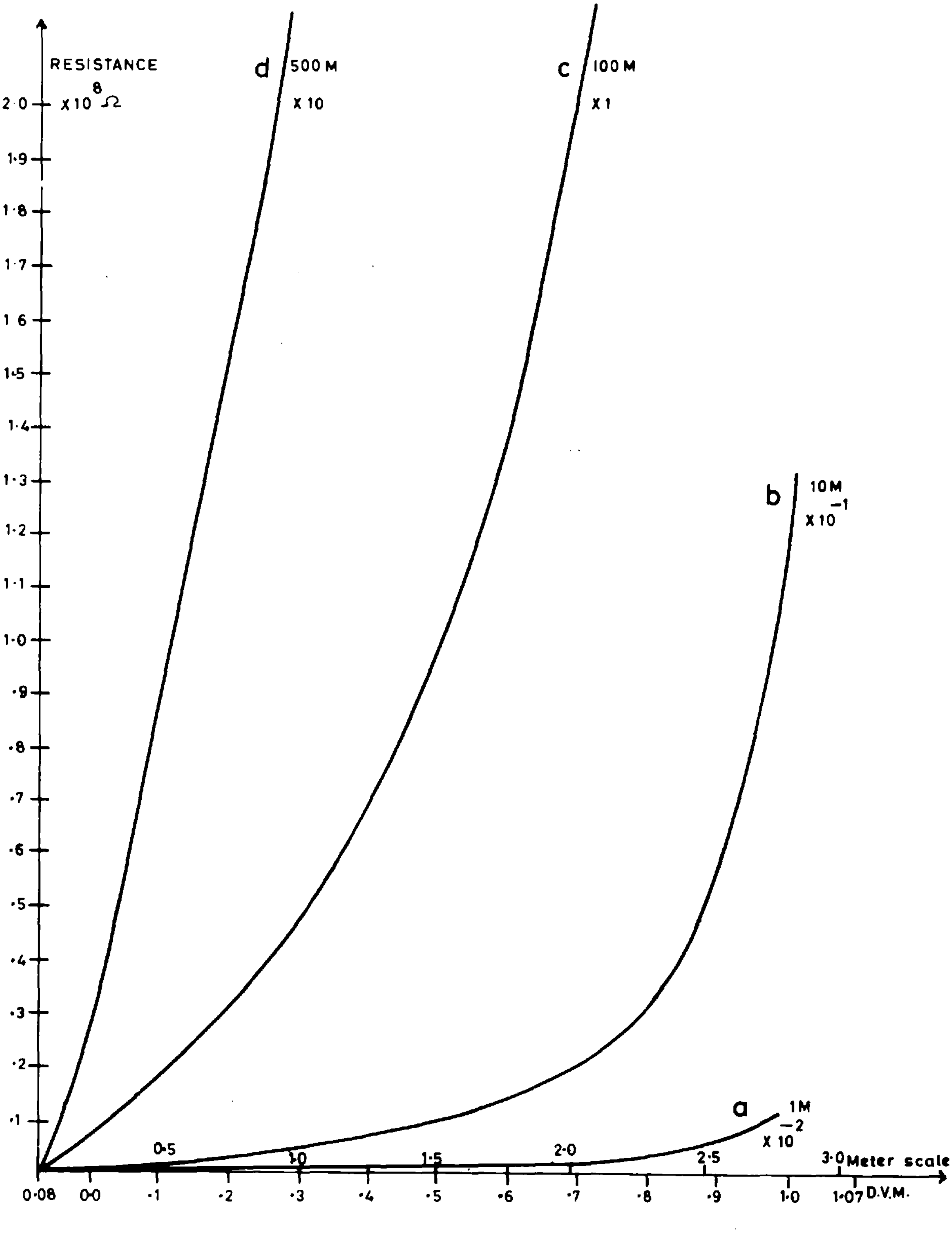

F.6.18 ***CALIBRATION CURVE FOR HIGH RESISTANCE Ω METER***

References for chapter 6

R6.01 McCullock, D. 'Low noise preamplifiers for a silicon target vidicon (S.T.V.) camera' 'ROE' report (1974)

R6.02 Texas Instruments. 'Low noise junction F.E.T. data sheets'.

R6.03 Smith, L., and Sheingold, D.H., 'Noise and operational amplifier circuits'. Analog Dialog (1969), 3, 1, 1, 5-9

R6.04 Philbrick Nexus Research Inc. 'Applications manual for operational amplifiers' 1968.

R6.05 'National Semiconductor'. applications sheets 83.

R6.06 Williams, P. 'A phase-sensitive detector with high noise immunity'. J.S.I. (1970), 3, 441-443

CHAPTER 7

7. A servo control system for the photometer sky-comparison mirror unit, and some design changes made for adaptation of the photometer for use on the Tenerife 60" flux collector.

Contents:

A SERVO CONTROL SYSTEM FOR THE PHOTOMETER SKY-COMPARISON MIRROR UNIT, AND SOME DESIGN CHANGES MADE FOR ADAPTATION OF THE PHOTOMETER FOR USE ON THE TENERIFE 60" FLUX COLLECTOR

7.01 The need for a servo system

It was mentioned in chapter 5, that the vibrating mirror amplitude was found to be unstable and so a servo system was built to control this mirror motion. The sinusoidal scanning motion of the mirror is inefficient; most of the scanning time is spent in the mirror travelling between the two field apertures; a square waveform increases the dwell time and reduces the travel time, thus increasing the proportion of time spent integrating the required source. Due to the resonance and rapid roll off frequency response of the drive unit, a square wave motion may only be attained by servo control.

7.02 A new capacitance-bridge position detector

The capacitance detection system previously described was originally designed for sensing the motion of the disc-chopper, and later for sensing the motion of the solenoid armature; the circuit was A.C. coupled and very non-linear (capacitance varies inversely with the plate gap width), and so quite unsuited for use as a position detector with the servo system.

CAPACITANCE DETECTOR SYSTEM FOR SERVO CONTROL CDSI

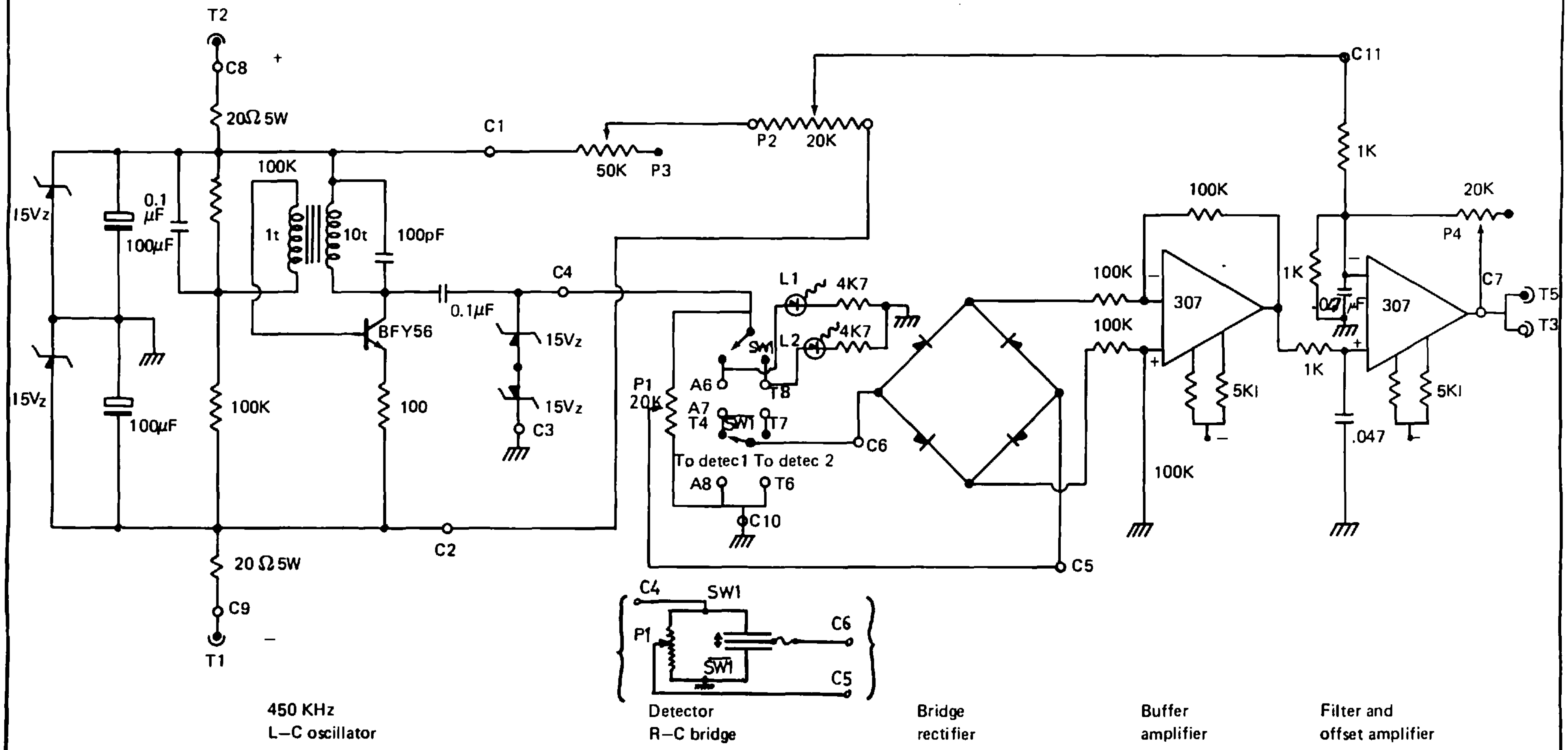

F. 7.01 CAPACITANCE DETECTOR SYSTEM FOR SERVO CONTROL

A new capacitance detection system was designed and built as shown in figure F7.11, and is a simplified version of that described in R7.01. The L.C. 450 kHz oscillator as previously used now drives an R-C bridge, where the two capacitance arms consisting of three parallel capacitor plates (from supply, to output, to earth) are balanced by an adjustable resistance potential divider; the moving capacitor plate moves closer to one plate at the expense of the other, and so registers twice the change in capacitance for the same geometry as a single armed system (one pair of capacitor plates). The bridge can be accurately balanced and the system is insensitivie to atmospheric changes as these will affect both capacitance arms equally.

Consider a resistance/capacitance combination as originally used; for a potential 'V_1' dropped across a series resistance capacitance combination, the observed potential 'V_0' dropped across the capacitance alone is

$$\frac{V_0}{V_1} = \frac{\frac{1}{j\omega c}}{R + \frac{1}{j\omega c}}$$

where R is the resistance; c, the capacitance. E7.01

Now the capacitance of a parallel plate capacitor of plate area 'A', dielectric 'k', and plate separation 'd' is:

$$C = \frac{kA}{d} \qquad \text{E7.02}$$

which when substituted in E7.01 gives

$$\frac{V_o}{V} = \frac{d}{d+kAj\omega R} \qquad \text{E7.03}$$

This is a hyperbolic function of 'd,' and is only linear for very small displacements.

Now consider the capacitance bridge combination of F7.01, where the two capacitance arms are 'C_1' and 'C_2' and the resistance arms are 'R_1' and 'R_2'. Then the bridge output compared to the input is

$$\frac{V_o}{V_1} = \frac{\frac{1}{j\omega c_2}}{\frac{1}{j\omega c_1}+\frac{1}{j\omega c_2}} - \frac{R_2}{R_1+R_2} \qquad \text{E7.04}$$

Substituting for 'c' from E7.02 we have

$$\frac{V_o}{V_1} = \frac{d^2/kAj\omega}{\frac{d_1}{kAj\omega}+\frac{d_2}{kAj\omega}} - \frac{R_2}{R_1+R_2} \qquad \text{E7.05}$$

but $R_1 + R_2 = R$ (constant) E7.06

and $d_1 + d_2 = d$ (constant) E7.07

Then $$\frac{V_o}{V_1} = \frac{d_2}{d} - \frac{R_2}{R} \qquad \text{E7.08}$$

If this is set to zero; then a displacement from this position by 'x' makes

$$\frac{V_o}{V_1} = \frac{d_2}{d} + \frac{x}{d} - \frac{R_2}{R} = \frac{x}{d} \qquad \text{E7.09}$$

The output of the bridge is then linear with the displacement and independent of the dielectric; in this design, the fixed capacitor plate gap width 'd' is usually about 10 x the displacement amplitude, and the voltage supplied to the bridge is 30v at 450 kHz.

The capacitance bridge can be replaced by the disc chopper detector previously described, appropriately matched, by operation of switch Sw1 and monitored by L.E.Ds L1 and L2. In order to remove the 450 kHz carrier frequency, the bridge output is full-wave rectified and then referred to ground with the differential buffer amplifier; the resultant signal is then filtered to remove the 450 kHz carrier frequency, but not enough to cause any noticeable phase shift of the 5 to 30 Hz displacement modulation frequency or its harmonics as in the case of square wave modulation. In practice the roll-off point and rate for this h.f. filter was found to be quite critical; the component values shown are considered to be the optimum. Offsetting is applied by virtual earth summation at this filter amplifier; the amplifier also includes a variable gain setting. Bridge balance is adjusted with P1, biasing and offsetting with P2 and voltage gain with P4. This system is most satisfactory, a 0.8mm armature displacement can give rise to several

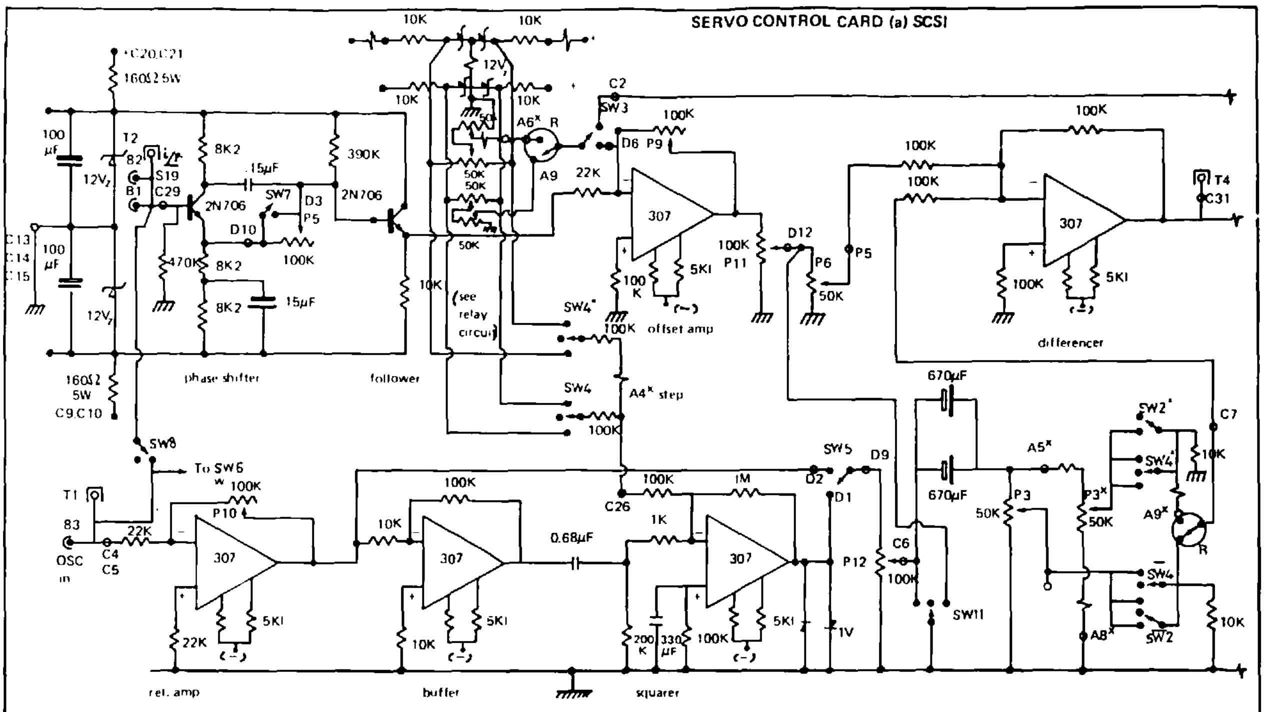

F.7.02a SERVO CONTROL CARD

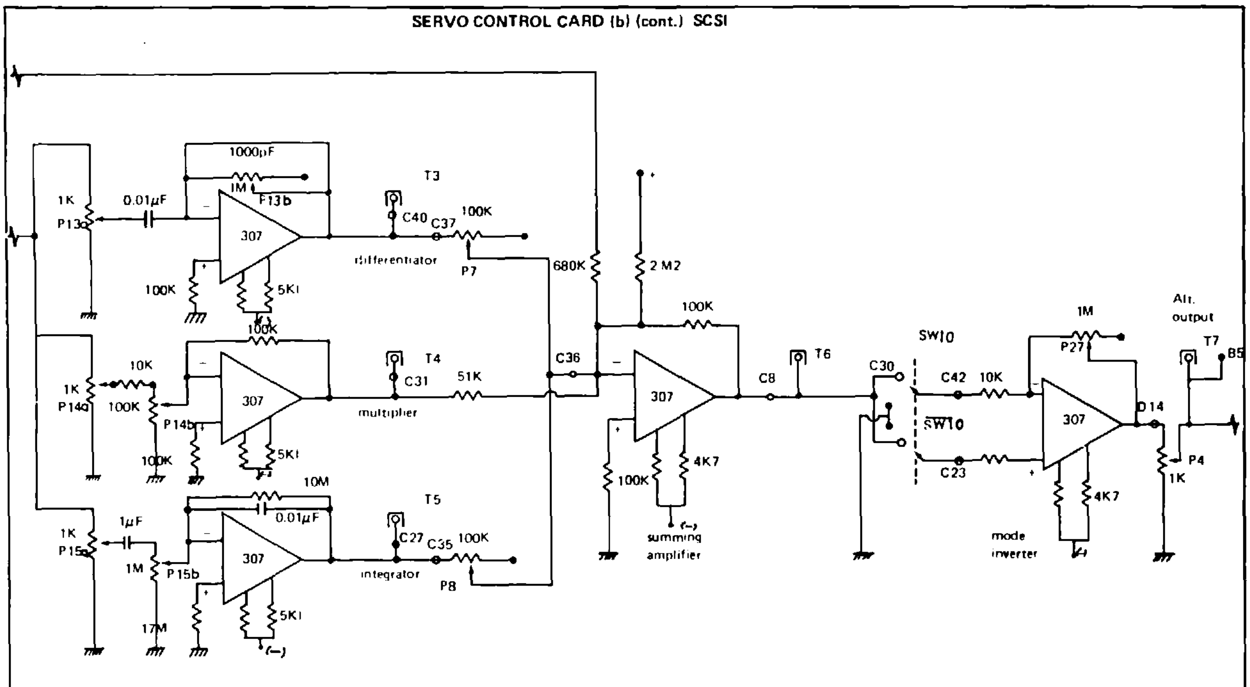

F.7.02b SERVO CONTROL CARD

SERVO CONTROL CARD (c) (cont.) SCSI

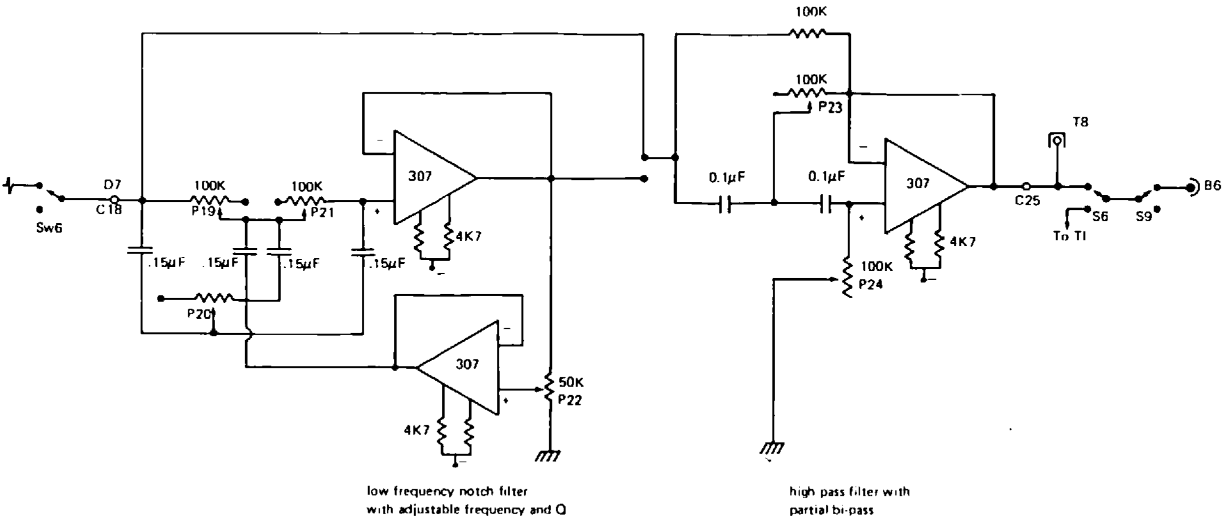

F. 7.02c SERVO CONTROL CARD

SERVO CONTROL SCSI Relay and remote control unit

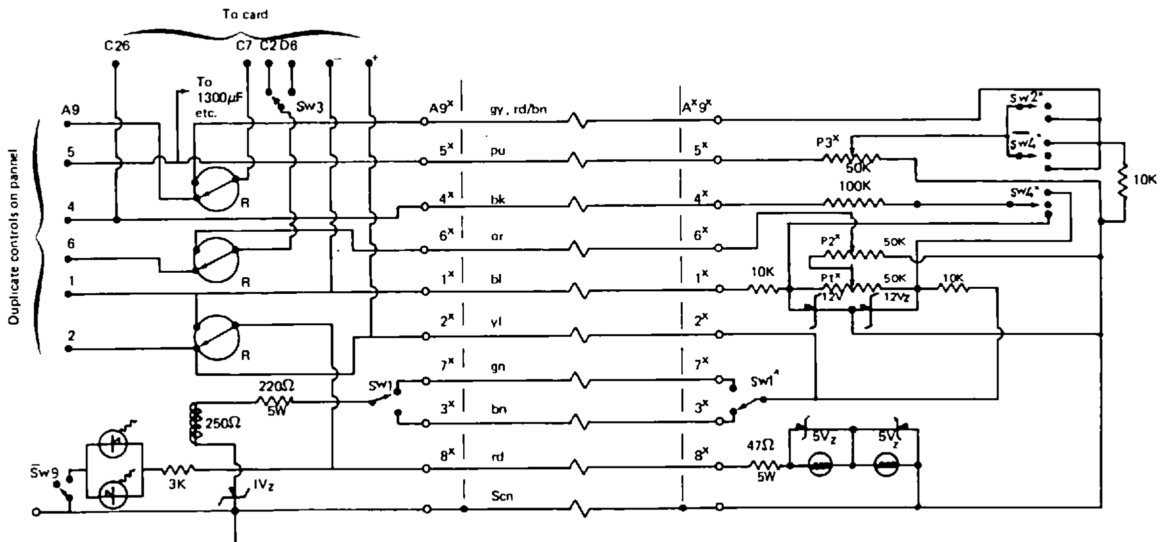

A pannel socket pinface

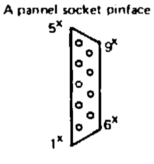

F. 7.03 SERVO CONTROL RELAY AND REMOTE CONTROL UNIT

SERVO CONTROL SCSI Power lines and indicators

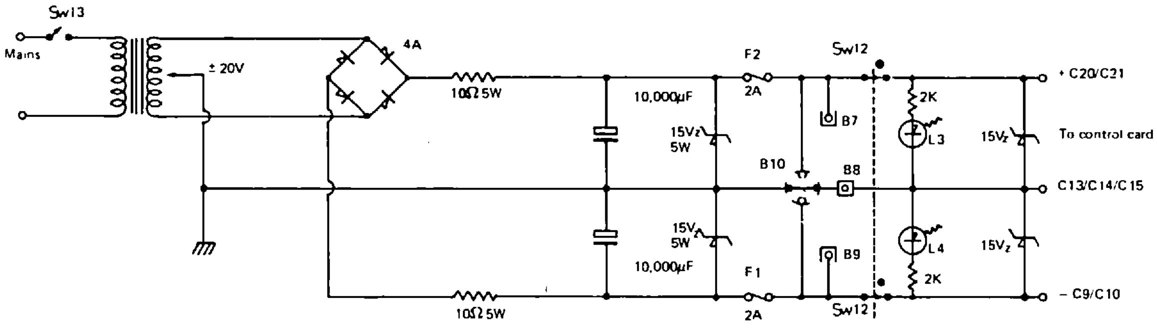

F.7.0 4 SERVO CONTROL POWER LINES AND INDICATORS volts change on the output, and the frequency response is from 0 Hz to 1 kHz or more. The whole circuit is housed in a small box in the photometer close to the mirror unit, and the bridge on the drive armature is connected to the circuit by a triax cable where the bridge supply is on the centre core, the screen is earth, and the middle screen is the bridge output; this arrangement minimises stray capacitance effects.

7.03 The servo control unit

The block layout diagram F6.01 shows the servo control layout, which is shown in detail in F7.02 and resembles the circuit given in reference R7.02; the capacitance bridge output is fed to the control unit input via a long cable. A phase shifter was used in initial tests on the servo system, but later abandoned; however this phase shifter at first proved vital in order to compensate for phase changes produced by the solenoid drive transformer. This phase shifter is a modified version of that shown in F6.06c,so as to pass a D.C.voltage without change in gain.

Position control is obtained by summing in a variable voltage at the offset amplifier shown in F7.02a, or with the summing amplifier in F7.02b. The reference waveform is supplied from an oscillator connected to an adjustable-gain amplifier; the output waveform may be switched to the reference attenuator to provide amplitude control, or to a squarer and then to the reference attenuator, depending on the choice of a sine wave or square wave reference. The squarer includes a stepping facility so that the square reference may be held in either of its two states (this is useful in setting up the photometer on a star). Comparison between the real signal waveform from the capacitance bridge and the generated reference waveform is made in the differencer (here, this is a summing amplifier, as the signal is already suitably inverted).

The. error signal then is split between a proportional multiplier, differentiator to provide velocity damping, and integrator to provide D. C. control and high frequency roll off (the time constants and gains are adjustable), and all three summed (see F7. 02b).

An optional inverting or non-inverting amplifier is used to select the phase, and the signal may be directed to the power amplifier at this stage, but a more satisfactory waveform was obtained by including the high pass filter with a partial bypass.. The adjustable low frequency notch filter, in F. 702c, was used to compensate for the solenoid spring resonance, but was later removed (see next section). Figure F7. 03 shows the remote control unit normally bolted to the photometer; this duplicates the essential controls of the main panel; these include the reference amplitude and on/off, the square-wave, step-hold switch, and offsetting control; the unit can be removed and control then reverts to the main panel. The unit has a relay cut in/out that may be operated from the panel or the unit itself. The servo control power supplies are shown in figure F7. 04.

The servo unit has several test facilities for setting up and fault finding; one is a possible combination of the input channel to the oscillator channel, another is a shorting switch for either of the differencer inputs. The unit may be operated in open or closed loop mode, and in correct operation the open loop gain is at least a factor of three greater than the closed loop gain at the fundamental carrier frequency (5 Hz - 10 Hz) as measured from the output of the capacitance bridge detector; the difference in the gain of the two modes is an indication of the amount of feedback. As with all servo systems, the frequency response and hence gain is limited by the phase-shift/frequency characteristic; oscillations set in at the frequency where the phase shift is π .

7.04 Initial trials with the servo system

When the servo system was first operated, it was found that the phase setting for optimum D.C. stability corresponded to a condition of considerable A.C. instability, and vice versa. With the servo loop closed, the maximum amplitude of motion attained with a 7w. power amplifier was only about 30% of that required; the A.C. instability increased, and the amplitude decreased still further in the square wave drive mode. The mirror position control did not function as expected, due to the A.C. coupling of the necessary step up transformer to the solenoid, and it was considered that this was also the likely cause of the gross low frequency phase shifts just described.

An attempt was made to overcome the lack of D.C.control problem by replacing the solenoid armature with a new armature with a 15 Ω coil winding; the step up transformer was then removed, and the drive current applied to this coil winding, while the D.C. constant field current was applied as before to the solenoid coil. This was expected to remove the low frequency phase shifts, but in practice it was found that the amplitude of motion was severely limited by the limited power dissipation of armature coil. Several different armatures were made: one of nylon, one of Tufnol, and one of steel; the additional field concentration from the steel armature proved the most successful, but even here, the thermal dissipation problem proved too severe. Magnetic rectification does not occur providing the permanent field induced in the armature exceeds the peak amplitude of the alternating armature field.

7.05 Power limitations on an armature winding

Consider a closely wound coil of wire of diameter 'd' on a former of length 'l' and of radius 'r', wound to a radius 'r + t,' with a total number of turns 'N.'

Then $N = nm$ where E7.01

$t = md$ E7.02

and $l = nd$ E7.03

Then from E7.01, E7.02, E7.03

$$N = \frac{l\,t}{d^2} \propto \frac{1}{d^2} \qquad \text{E7.04}$$

Let v = applied potential and i = coil current.

(a) <u>if v = constant</u>

$$i \propto \frac{\text{wire cross section area}}{\text{wire length}} \propto \frac{d^2}{N} \qquad \text{E7.05}$$

Then $Ni \propto d^2$ E7.06

And $W \propto i$ E7.07

hence from E7.07, E7.07

$$W \propto \frac{d^2}{N} \propto \underline{d_4} \qquad \text{from (E7.04)} \qquad \text{E7.08}$$

(b) <u>If W = constant</u> (e.g. maximum power for an amplifier)

$$i^2R = \text{constant} \qquad \text{E7.09}$$

hence $i^2 \propto \frac{1}{R}$ E7.10

and as $R \propto \frac{N}{d^2}$ E7.11

Then $i^2 \propto \frac{d^2}{N}$ E7.12

hence $i \propto \frac{d}{\sqrt{N}}$ E7.13

and $Ni \propto d\sqrt{N}$ E7.24

Then from E7.04 <u>Ni = constant</u> E7.15

Now Magnetic field $B \propto \mu Ni$ E7.16

where μ is the magnetic susceptibility.

Then in 'a', for <u>constant</u> <u>voltage, and μ</u>

from E7.06 $B \propto d^2$ E7.17

and $W \propto d^4$ E7.08

and in <u>b</u> for <u>constant power W and μ</u>

from E7.25 B = constant E7.18

In practice the power is restricted by the thermal dissipation of the coil, and the coil size is also geometrically restricted, and so case 'b,' applies; then the magnetic field is not a function of any of the coil parameters considered and so is restricted, and is the same for all such coil designs.

7.06 Power necessary to produce a square wave of given amplitude and frequency

Consider a square wave of amplitude 'a', and fundamental frequency $\omega/2\pi$, including harmonics up to m.

Then the displacement is given by:

$$x_m = \frac{4}{\pi} a \left\{ \sin \omega t + \frac{1}{3} \sin 3\omega t + \frac{1}{5} \sin 5\omega t + \dots\dots + \frac{1}{m} \sin m\omega t \right\} \tag{E7.19}$$

$$\dot{x}_m = \frac{4}{\pi} a\omega \left\{ \cos \omega t + \cos 3\omega t + \cos 5\omega t + \dots\dots + \cos m\omega t \right\} \tag{E7.20}$$

$$\ddot{x}_m = -\frac{4}{\pi} a\omega^2 \left\{ \sin \omega t + 3 \sin 3\omega t + 5 \sin 5\omega t + \dots\dots + m \sin m\omega t \right\} \tag{E7.21}$$

The series may be written :

$$x_{\hat{m}} = \frac{4}{\pi} a \sum_{m=1}^{\hat{m}} \frac{\sin m\omega t}{m} \tag{E7.22}$$

where m = 2n - 1 (odd only) E7.23

$$\dot{x}_{\hat{m}} = \frac{4}{\pi} a\omega \sum_{m=1}^{\hat{m}} \cos m\omega t = \frac{4 a\omega}{\pi} \left\{ \frac{\cos \frac{m+1}{2} \omega t \sin \frac{m\omega t}{2}}{\sin \frac{\omega t}{2}} \right\} \tag{E7.24}$$

and $$\ddot{x}_{\hat{m}} = -\frac{4}{\pi} a\omega^2 \sum_{m=1}^{\hat{m}} m \sin m\omega t \tag{E7.25}$$

The maximum displacement and acceleration occurs when $\dot{x} = 0$ then :

$$\cos\frac{\hat{m}+1}{2}\,\omega\,t\,\sin\frac{\hat{m}\omega t}{2} = 0 \qquad \text{E7.26}$$

and $\hat{m}\omega t \neq 0$, so the first root is $\omega t = \pi/_{\hat{m}+1}$ E7.27

and the second is $\omega t = {}^{2\pi}/_{\hat{m}}$ E7.28

The acceleration at a zero velocity point is then:from E7.24 and E7.26,

$$\ddot{x}_{\hat{m}} = \frac{4}{\pi}\,\frac{a\omega^2}{\sin\frac{\omega t}{2}}\left\{\begin{matrix}\frac{\hat{m}}{2}\cos\frac{\hat{m}\omega t}{2}\quad\cos(\hat{m}+1)\frac{\omega t}{2}\\ -\frac{(\hat{m}+1)}{2}\sin\frac{(\hat{m}+1)}{2}\,\omega\,t\,\sin\frac{\hat{m}\omega t}{2}\end{matrix}\right\} \qquad \text{E7.29}$$

and where $\omega t = \pi/_{\hat{m}+1}$

then $$\ddot{x}_{\hat{m}_1} = -\frac{2}{\pi}\,a\,\omega^2\,(\hat{m}+1)\,\frac{\sin\frac{\hat{m}\pi}{2(\hat{m}+1)}}{\sin\frac{\pi}{2(\hat{m}+1)}} \qquad \text{E7.30}$$

The power for mass M to reach a velocity $\hat{\dot{x}}$ in a time T

$$P_{1/4} = \frac{M}{T}\int_0^{\hat{\dot{x}}}\dot{x}\,d\dot{x} \qquad = \frac{1}{2}\,\frac{M}{T}\,\hat{\dot{x}}^{\,2} \qquad \text{E7.31}$$

$$= \frac{M}{2T}\;\frac{4^2a^2\omega^2}{2}\left[\left(\frac{\cos\frac{\hat{m}+1}{2}\,\omega\,t\;\frac{\sin\hat{m}\omega t}{2}}{\sin\frac{\omega t}{2}}\right)^2\right]_0^T \qquad \text{E7.32}$$

$\dot{x}$ is a maximum for t = 0 and is zero for $T = \frac{\pi}{\omega(\hat{m}+1)}$, $\frac{2\pi}{\omega\hat{m}}$, etc.

For a well-damped motion, then take $T = \frac{\pi}{\omega(\hat{m}+1)}$

Then the total power =

$$\bar{p} = \frac{8Ma^2\omega^3}{\pi^3}(\hat{m}+1)\hat{m}^2 \qquad \text{E7.33}$$

And from E7.30 the maximum force $\hat{F} = -M\frac{2}{\pi}a\omega^2(\hat{m}+1)\frac{\sin\frac{\hat{m}\pi}{2(\hat{m}+1)}}{\sin\frac{\pi}{2(\hat{m}+1)}}$ E7.34

and as $\hat{m} \to \infty$

$$\hat{F} \to -M\frac{2}{\pi}a\omega^2(\hat{m}+1)\hat{m} \qquad \text{E7.35}$$

Substituting some values in E7.33 and E7.35, where M = 42 gms, a = 0.4mm, $\hat{m} = 9$, f = 30Hz

Then

$p = 9.4$ watts

and $\hat{F} \simeq 34$ newtons

It is clear from this that a considerable amount of force is necessary to maintain a square waveform to the 9th harmonic. The power and force relations for a sine wave of the same amplitude are ;

$$\bar{p} = \frac{4Ma^2}{\pi} \omega^3 \qquad \text{E7.36}$$

$$\hat{F} = -Ma\omega^2 \qquad \text{E7.37}$$

substituting in the above values form a, M, ω :

$\bar{P} = 0.018$ watts

$\hat{F} = 0.60$ newtons

The relative advantage in the integrated signal,obtained with an ideal square wave sky-chop,compared to a sine wave of the same amplitude, is $\frac{4}{\pi} \triangleq 1.27$, and so the increase in optical efficiency is ~27%.

7.07 A new drive unit and bearing assembly

The previous sections have shown the limitations of a solenoid drive unit as used with the servo system; as a result of this investigation, it was decided to replace the solenoid drive by a commercial 'Ling vibrator' drive unit which worked on the loudspeaker magnet principal; the coupling transformer was then dispensed with.

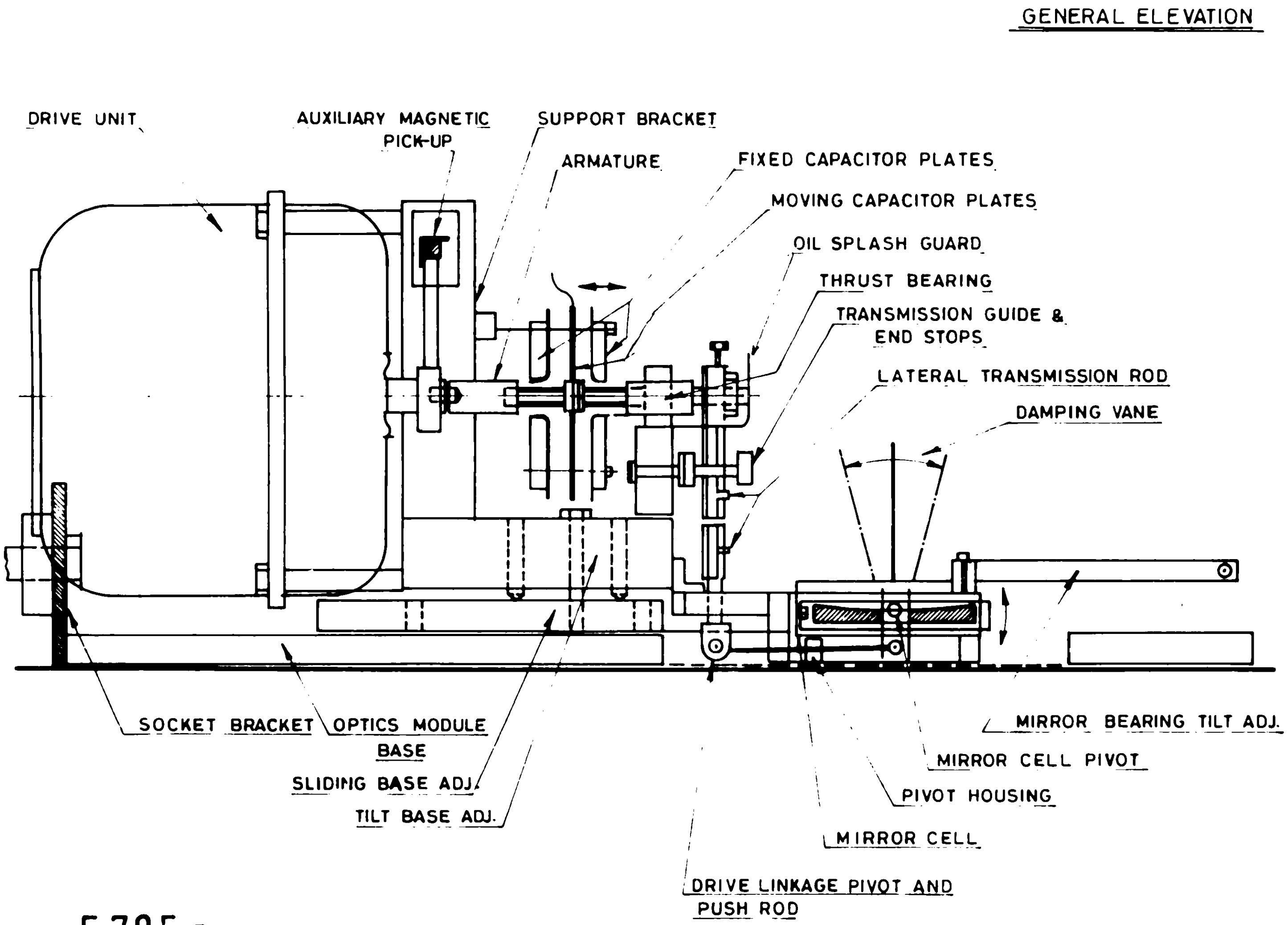

F.7.05a

DRIVE ASSEMBLY, CAPACITANCE POSITION DETECTION BRIDGE, AND MIRROR HOUSING.

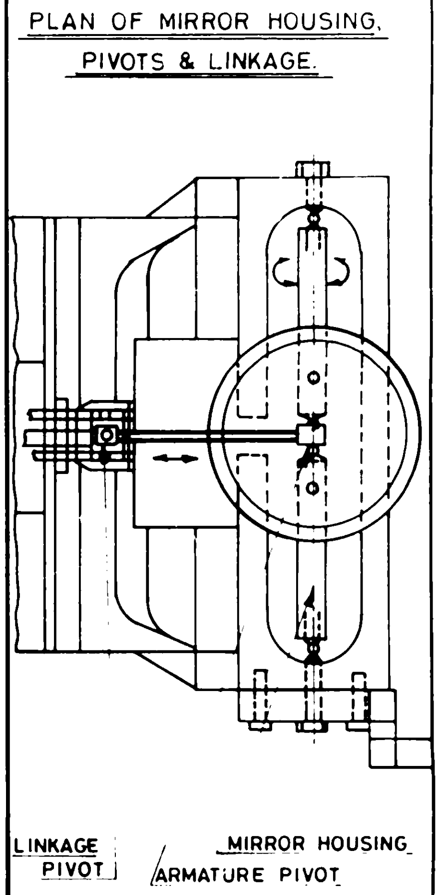

F.7.05b

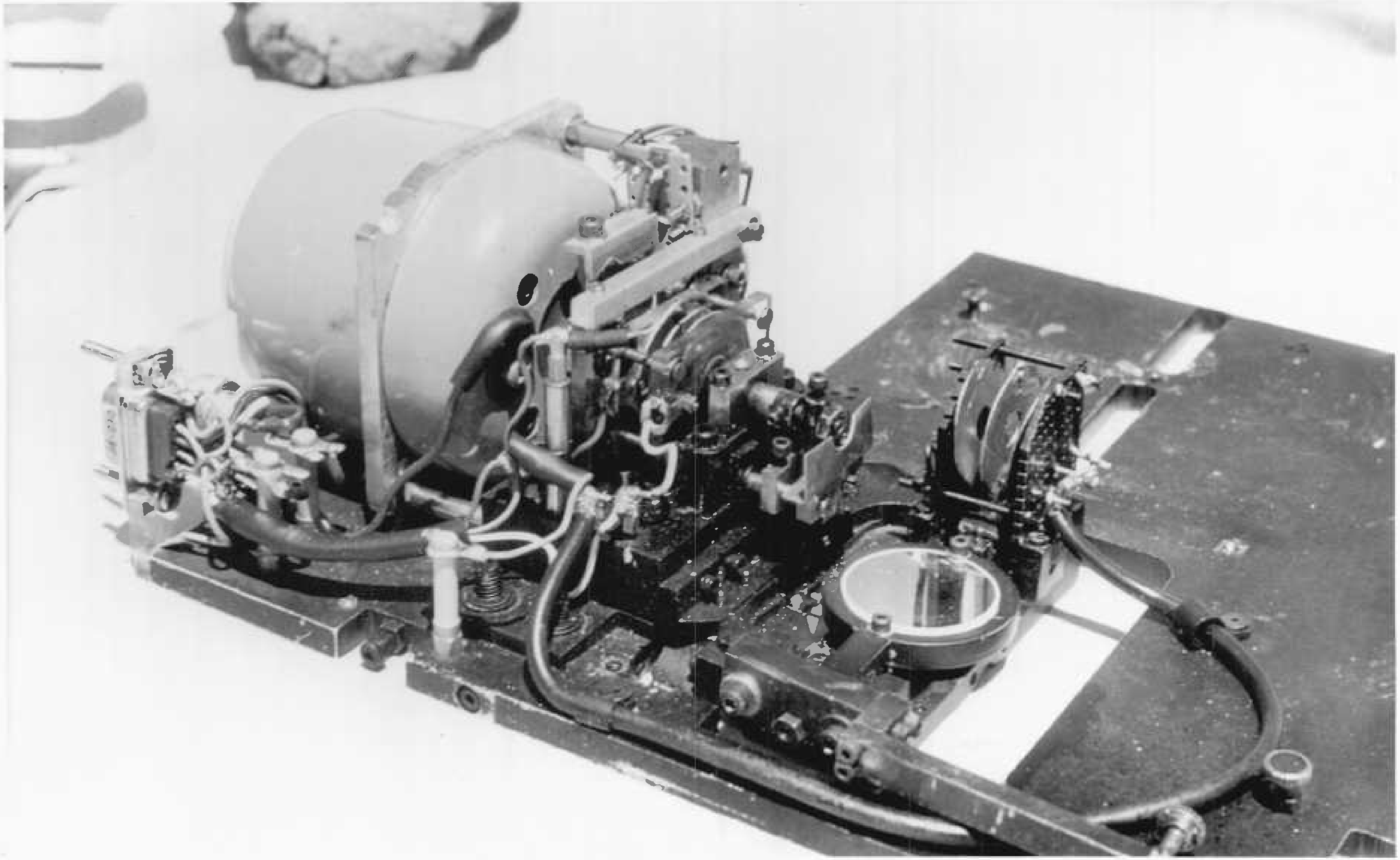

P7.1

THE MIRROR DRIVE UNIT AND LINKAGE SHOWING THE CAPACITANCE POSITION DETECTOR PLATES AND DAMPING VANE

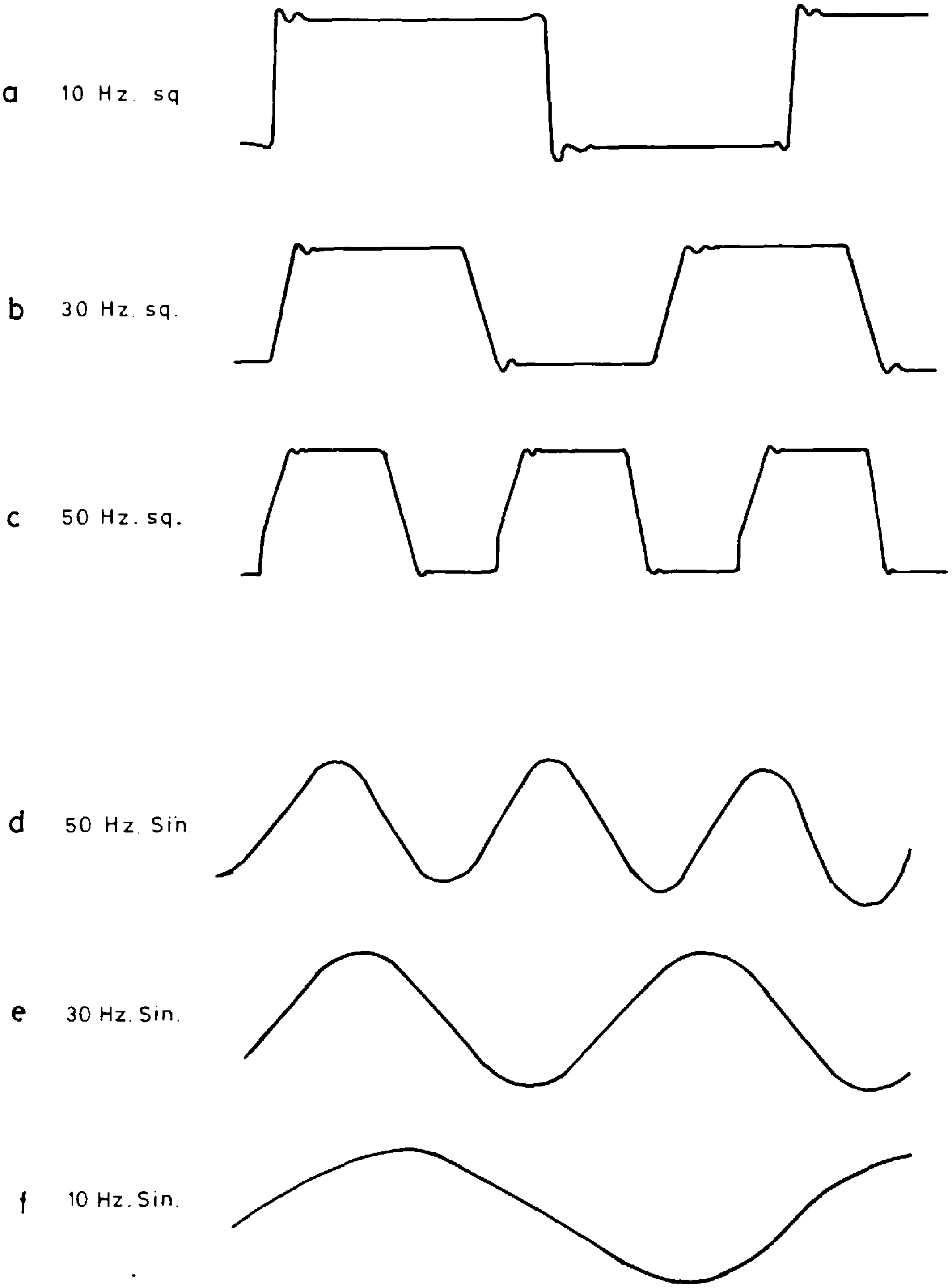

F.7.06 VIBRATING MIRROR, WAVE FORMS FROM CAPACITANCE BRIDGE OUTPUT

Figure F7.05 shows the new drive unit, armature, capacitance bridge vanes, mirror linkage,and mirror cell assembly. This modification, together with some optical changes to be described were made shortly before the photometer was used on the 60" Tenerife flux collector. A photograph of the assembly is given in P. 7. 1, where the optics of the two-spherical mirror module has been removed to show the base plate for the module, and the complete drive assembly; the mirror pivot linkage is the same as in P5. 4. There are several features to note; besides the three capacitance plates (the middle one is attached to the armature), there in an optional magnetic resistor pickup. The armature is fitted with end limit stops, and the location of the brass bush thrust bearing is fully adjustable; the whole unit has tilt and also slide adjustment on the module base; the mirror pivot frame can also be tilted along the pivot axis from the horizontal, to facilitate optical alignment; the armature has a screw length adjustment, and also the outer capacitor plates have a limited range of adjustment.

The unit illustrated proved to be very successful, and when used with the servo system without transformer and phase shifters, gave a very stable sinusoidal waveform with a 0.8mm armature throw for up to 100Hz, and a satisfactory square wave at this amplitude up to 60Hz, see figure F.7.08. The square wave showed some slight asymmetry as well as overshoot, and in practice the mirror overshoot exceeded that indicated by the capacitance bridge, which was mostly caused by flexure of the main linear drive armature and wear on the brass thrust bearing; the pivot linkage was not responsible for any of the overshoot. The slight asymmetry can be reduced by increasing the capacitor plate separation; the square wave profiles shown in F7.06 are recorded from the output of the capacitance bridge, with the servo damping factor critically adjusted to minimise ringing. An attempt was made to overcome the mirror overshoot problem by including the mirror in the servo loop. The second set of capacitor plates shown in P7. 1 and F7.05, attached to the mirror pivoted armature, were used for this purpose as an alternative to the parallel plates described; unfortunately this proved very unsatisfactory, both increasing the asymmetry and instability. These plates, although abandoned from their original purpose, were found to help damp the mirror by the viscous damping effect produced by their motion in air.

The armature linkage pivot and lever system reduces the inertial mass of the mirror and cell by 30% of its gravitational mass; the total inertial mass of the complete moving armature and linkage assembly was estimated at 42 gms. A 0.8mm armature displacement produces an 25mm image displacement in the focal plane.

7.08 Adaptation of the photometer for use with the Tenerife 60" flux collector

On successful application for observing time on the Tenerife 60" flux collector, it was decided to make a few changes to the optical system to take full advantage of the slower F ratio. At F/12.8, the reduced

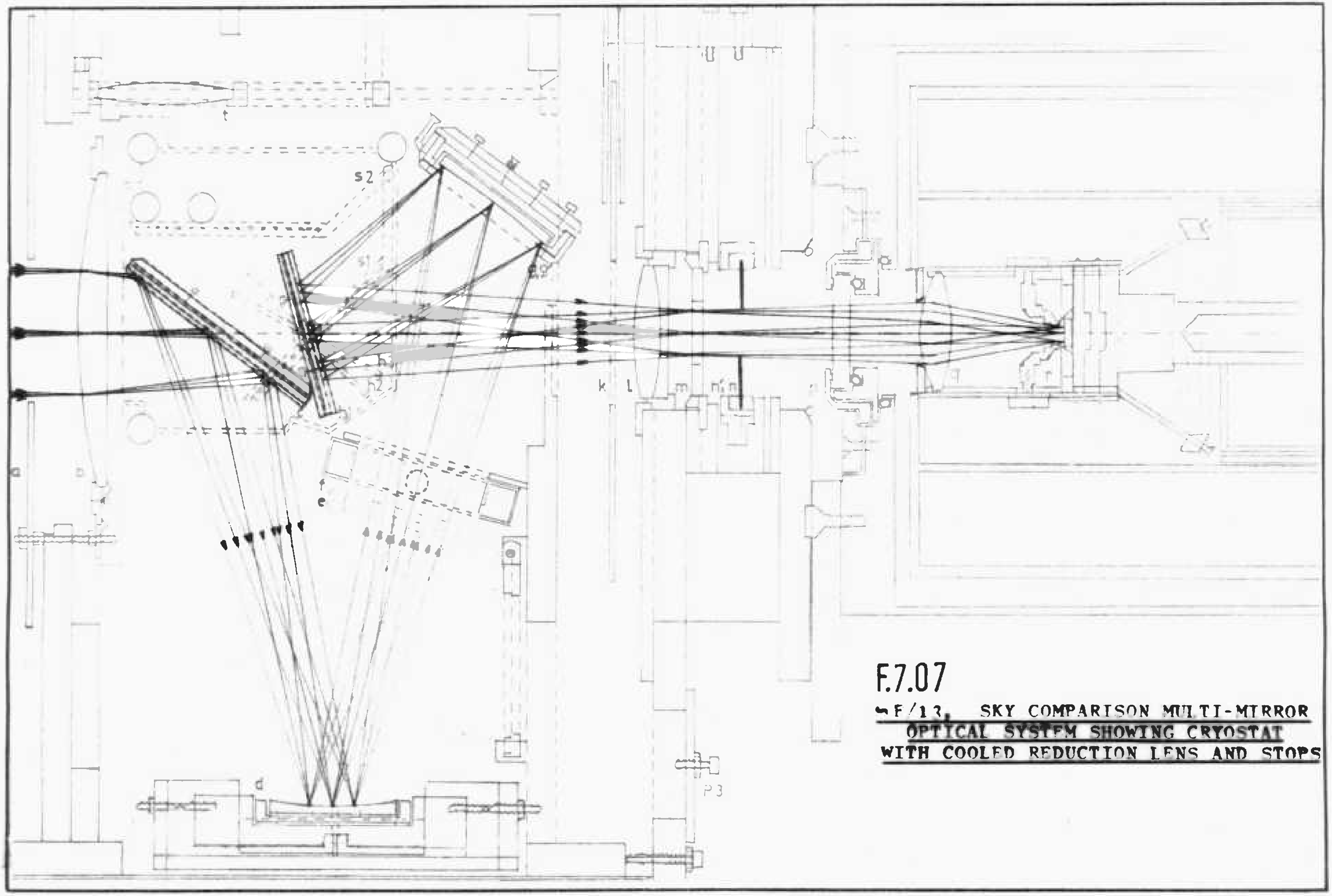

F.7.07

F/13, SKY COMPARISON MULTI-MIRROR OPTICAL SYSTEM SHOWING CRYOSTAT WITH COOLED REDUCTION LENS AND STOPS objective stop is approximately 10mm in diameter, and with this in mind, the final reduction lens was then placed inside the cryostat as shown in figure F7.07, thus eliminating the need for the light pipe of figure F5.11, and hence improving the optical transmission by 30% at λ 1.65 μ. The increase in collimation space slightly increases the reduction ratio, giving a 4mm reduced field for the 25mm focal plane field; this enabled the 25mm^2 area detector to be replaced by a 16mm^2 area detector with a consequent lower intrinsic noise level. A new objective stop was introduced in front of the reduction lens 'q' in the cryostat, which therefore decreases the solid angle of view at room temperature as seen by the detector; the 10mm objective stop enables 13mm diameter interference filters to be used in the collimated beam without obscuration. This change of the pre-detector optics, and consequent change in detector size, enabled a number of new detectors to be tried out and compared; this is discussed in the next chapter. The new optics and detector head assembly is shown in photograph P7. 2, and the instrumental profiles, as determined with the artificial star, for this optical system are shown in figures F7.08, F7.09; the F7.10 profiles include the square-wave R.A. sky-comparison-chop convolution. Photograph P7. 3 shows the complete electronics as used at the time of the observations made with the 60" flux collector, and P7. 4 shows the complete assembled photometer with cryostat and alignment laser.

A new adaptor flange was made specially for interfacing the photometer to the 60" flux collector at an F/12.8 focus.

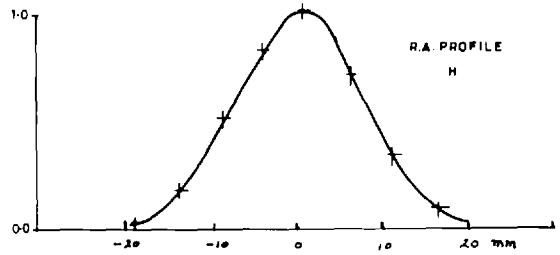

F.7.08a

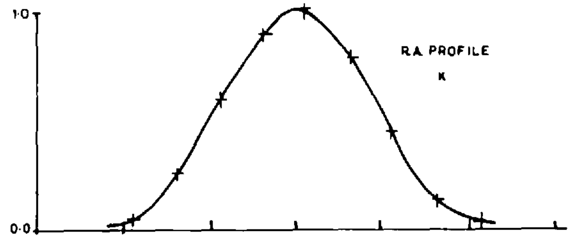

F.7.08b

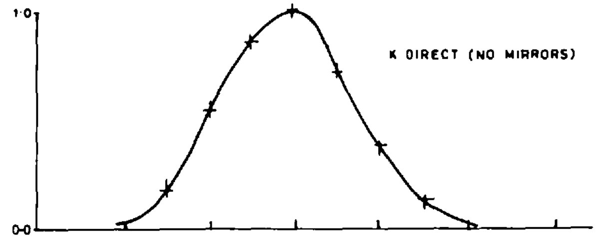

F.7.09

INSTRUMENT PROFILE DETERMINED WITH ARTIFICIAL STAR DISC CHOPPED

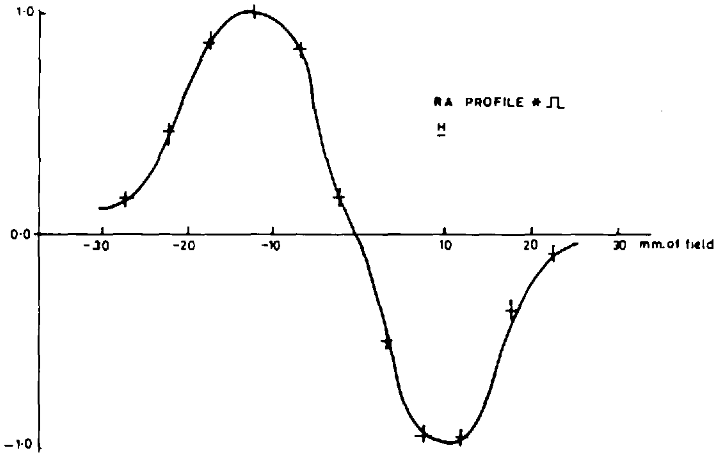

F.7.10a

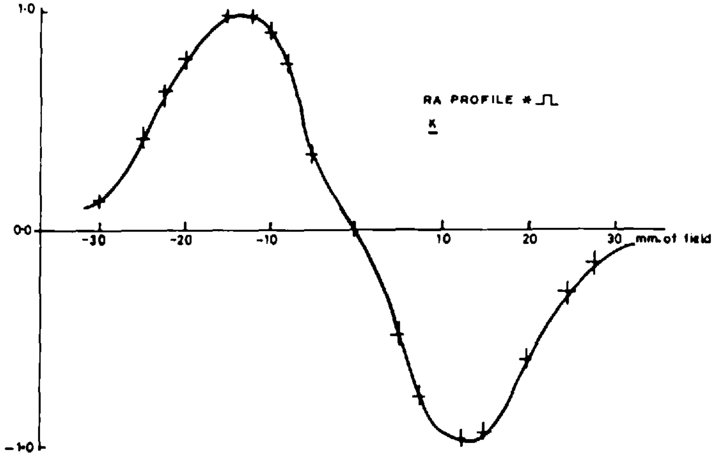

F.7.10b

INSTRUMENTAL PROFILE DETERMINED WITH ARTIFICIAL STAR

P7.2

THE DETECTOR, BIAS NETWORK, FET ASSEMBLY WITH THE COOLED PRE-DETECTOR F/12.8 OPTICS

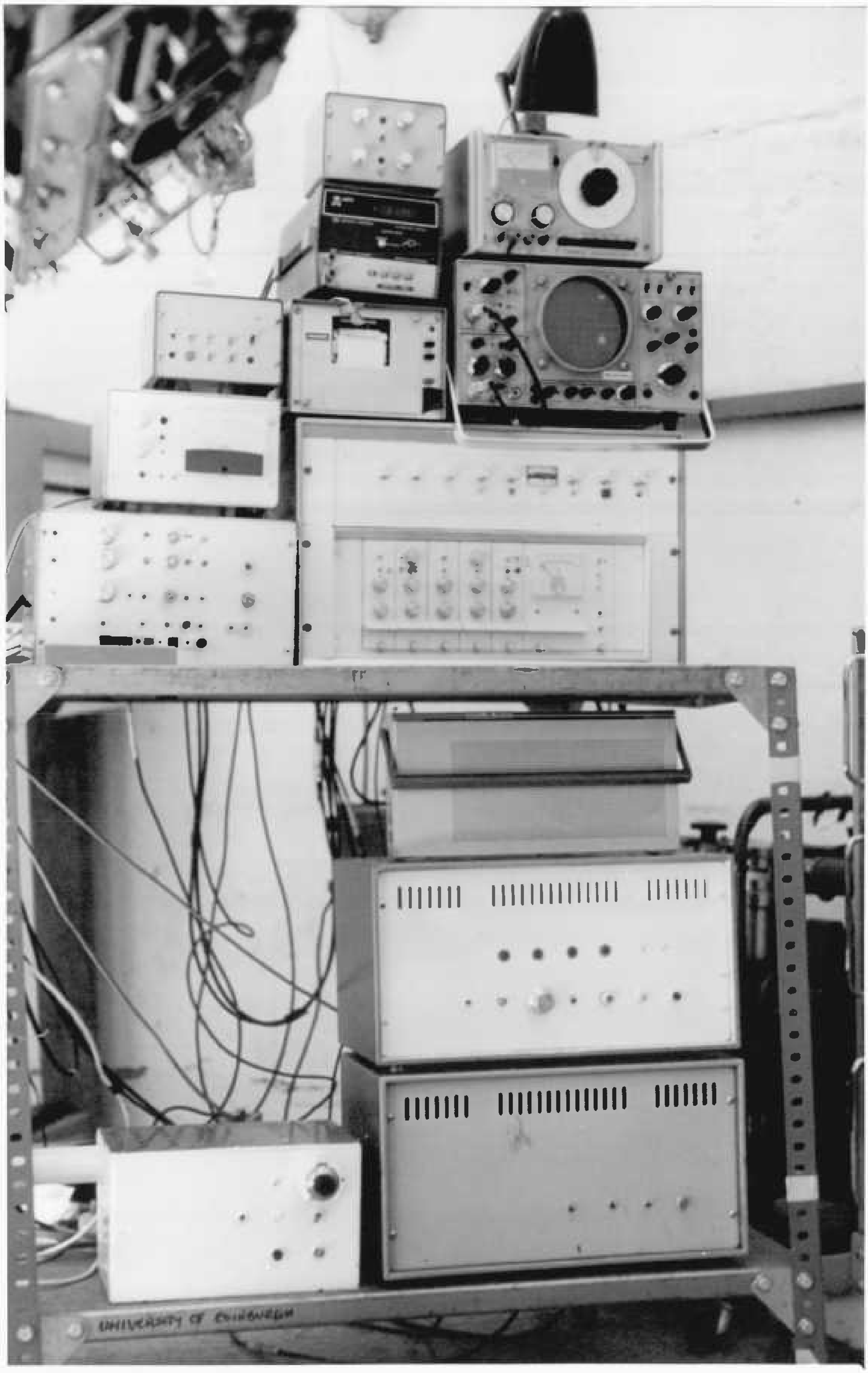

P7.3

GENERAL VIEW OF THE PHOTOMETER ELECTRONICS AS USED WITH THE 60" FLUX COLLECTOR

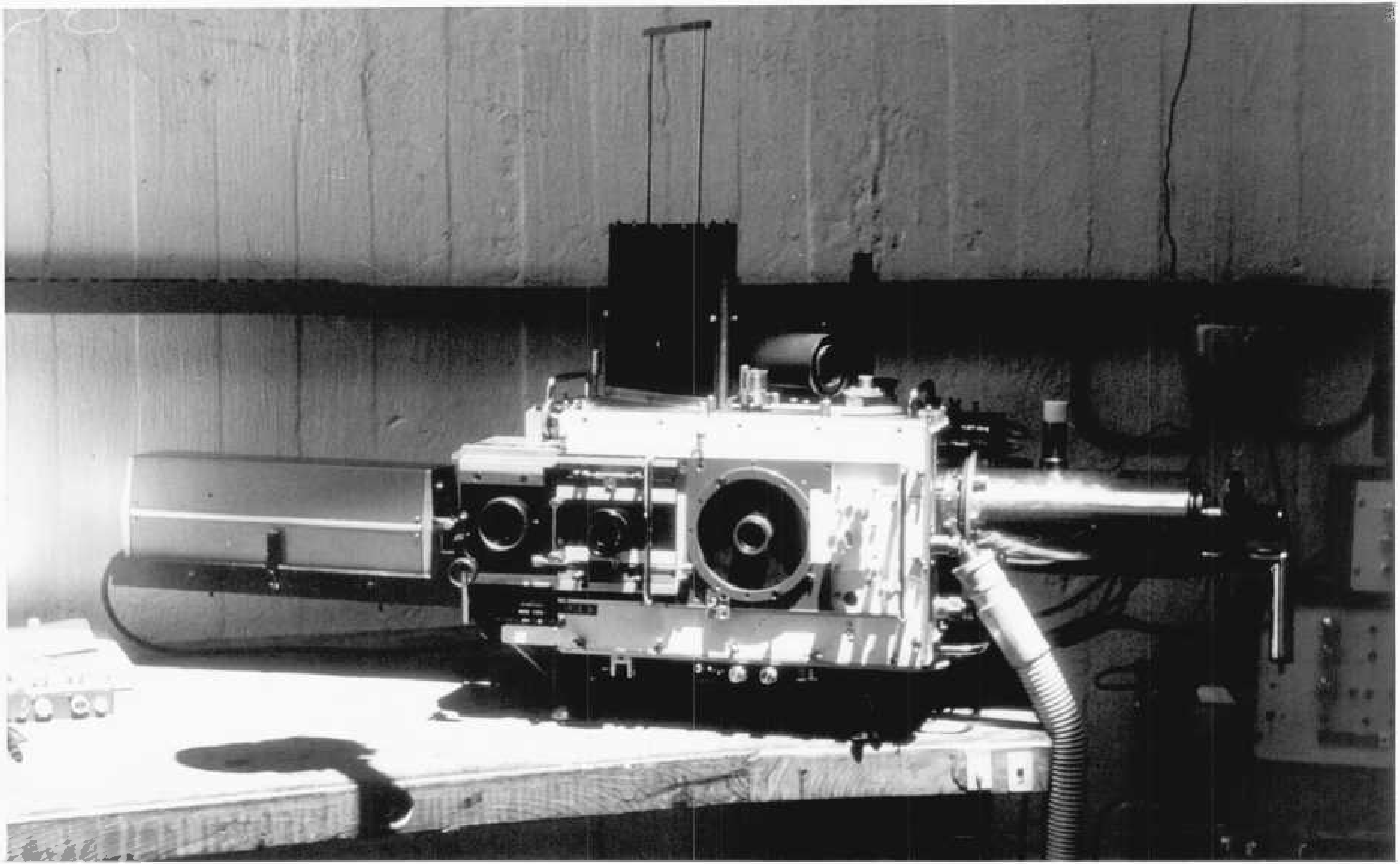

P7.4
THE WIDE FIELD INFRARED PHOTOMETER SHOWING THE MAIN PANEL

References to Chapter 7

R7.01 Schofield, J.W. 'A linear capacitance micrometer'. J.S.Inst. (1972), 5, 822-825

R7.02 Fahrback, U., Kaussecker, K., Lemke, D. 'A new chopper design for astronomical infrared photometry'. Astron. and Astrop. (1974), 33, 265-267

CHAPTER 8

8. The optimisation and calibration of PbS detectors used with the infrared photometer.

Contents:

8. THE OPTIMISATION AND CALIBRATION OF PbS DETECTORS USED WITH THE INFRARED PHOTOMETER

8.01 Introduction

This chapter concerns the optimisation and calibration of PbS-plate detectors used with the bias network described in chapter 6. Expressions for the general signal-to-noise characteristics of PbS detectors have been the subject of many papers (R8.01 - R8.09); the characteristic curve for a given detector is then specified by its fixed parameters : specific detectivity 'D^*' and time constant '$\tau = R.C.$' The equations given in the literature, are usually generalised, and do not usually include noise sources other than those from the detector.

In chapter 5, it was noticed that the signal-to-noise for the PbS detector used with the photometer biasing network, showed an optimum when the bias resistance was considerably lower than that of the detector resistance; this result was also confirmed by the manufacturer, but opinion at R.O.E. was divided on this issue. This result was not obvious from a study of the literature, but has been noticed by several fellow astronomers working with very high impedance PbS detectors. It was therefore decided to carry out an independent study of the signal-to-noise characteristics of the photometer bias circuit and detector, in order to establish a mathematical expression to describe the observed phenomena, and to provide a satisfactory explanation for all the noise sources observed, specific to this circuit.

This development of a semi-empirical relation for the bias-circuit signal-to-noise characteristic was originally to have been included here as a preface to the optimisation and calibration of several selected PbS detectors later used for the intended astronomical observations. The discussion has now been more appropriately supplied as an appendix to this thesis; the expression obtained for the signal-to-noise is used in this chapter to establish a suitable optimum operating point for the detector used in chapter 9. The relations determined in the appendix, mostly conform to those given in the literature (see R8.03), in the discussed presented the bias resistor network is treated as an additional noise source, which is not often considered. Such a treatment shows why the optimum signal-to-noise does not occur when the ratio of cell resistance to bias resistance (β) is equal to unity, but in this case, is closer to $10 < \beta < 50$.

A comparison was made of several detectors, and one detector was calibrated in the laboratory. One detector was selected for use for observations and was optimised.

8.02 The signal-to-noise function for the PbS detector and bias network, and the optimum operating point

The reader is referred to the appendix for a derivation of this semi-empirical expression for the signal-to-noise of a PbS detector and bias network:

$$\frac{\Delta e}{\varepsilon} = K\, r_c\, V \rho \Big/ \left\{ \varepsilon_o^{\,2} + 1.28^2 \times 10^{-2}\, r_c \rho \frac{T}{295} + k_{Tf}^2\, 1.4^2 \times 10^{-4}\, V\, r_c^{\,2} \rho^2 (\alpha^2 + \beta^{-2}) \right\}^{\frac{1}{2}}$$

E8.72

Where Δe = signal voltage at the preamplifier input

ε = noise voltage at the preamplifier input

K = sensitivity constant for the detector

r_c = detector resistance

V = total bias voltage

ε_o = preamplifier noise voltage at preamp. input

T = absolute temperature

k_{Tf} = a function of temperature and frequency parameter determination
from measurement : = 1.0 at 295°K and 0.141 at 200°K
30Hz 5 Hz

α = ratio of detector current noise to that of a comparable metal film resistance

β = ratio of detector resistance to bias resistance

and

$$\rho \equiv \beta(1+\beta)^{-2} \left\{ \frac{1+2\gamma}{1+\beta} + \frac{\gamma^2+\delta^2}{(1+\beta)^2} \right\}^{-\frac{1}{2}} \qquad \text{E8.70}$$

where

γ = ratio of detector resistance to F.E.T. gate load resistance

δ = product of detector resistance and detector capacitance (cell time constant)

21 Jy

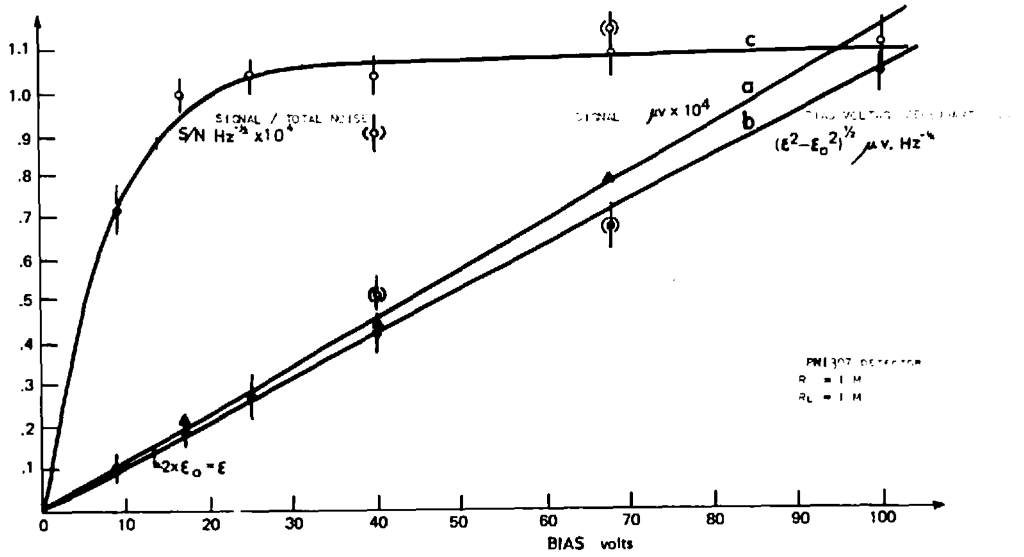

F. 8.14 OBSERVERVED SIGNAL, NOISE & SIGNAL/ NOISE AS A FUNCTION OF BIAS VOLTAGE FOR A Pb.S. DETECTOR, 23°C

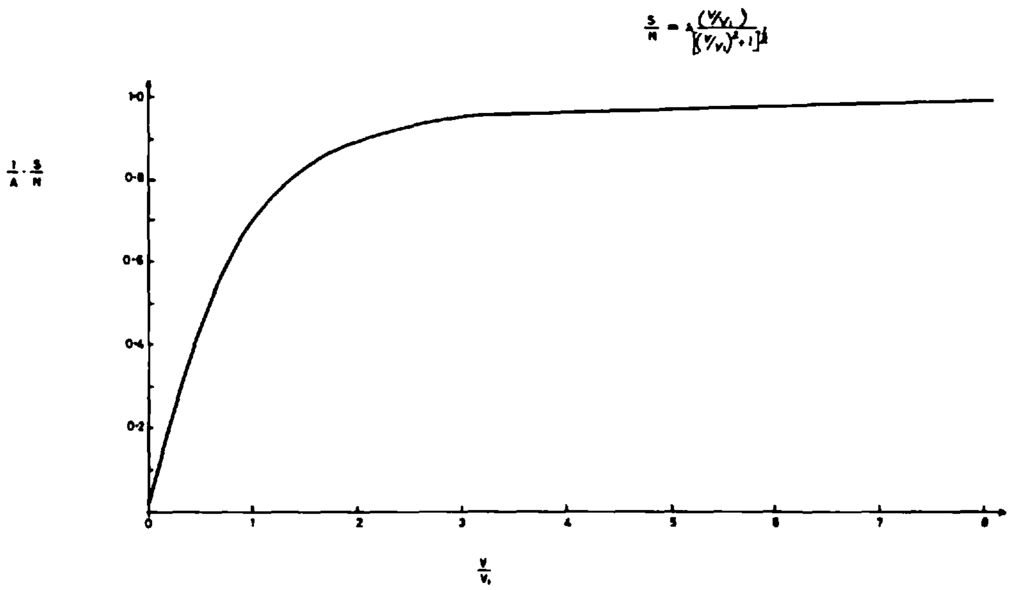

F.8.15 *THEORETICAL SIGNAL/NOISE AS A FUNCTION OF BIAS VOLTAGE.*

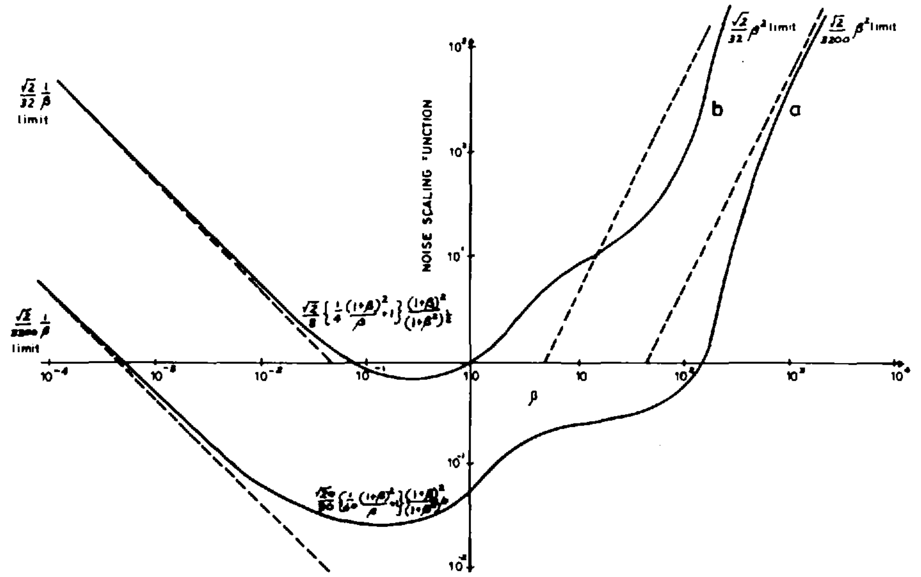

F.8.16 THEORETICAL CURVES FOR BIAS VOLTAGE TO SCALE NOISE LEVEL FROM ZERO VOLTS NOISE.

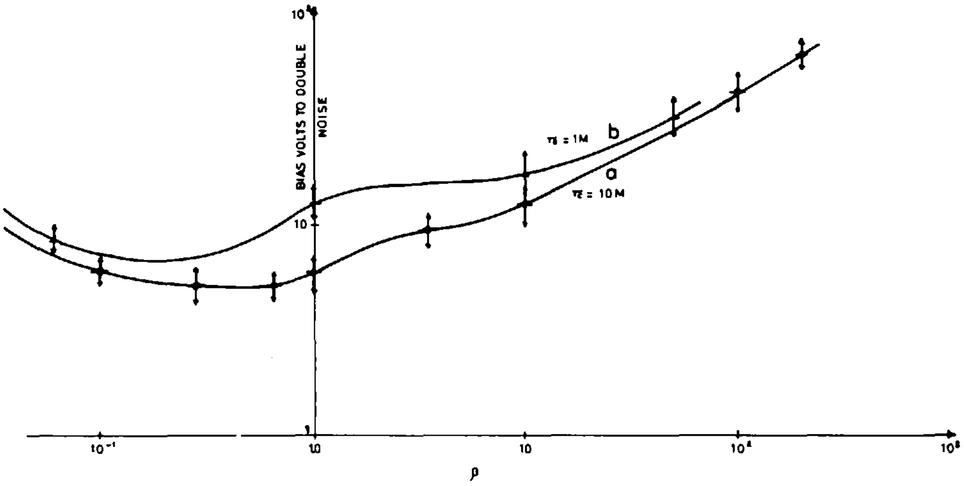

F.8.17
OBSERVED BIAS VOLTAGE TO DOUBLE THE NOISE LEVEL FROM ZERO VOLTS BIAS NOISE AT 22°C FOR TWO PbS DETECTORS.

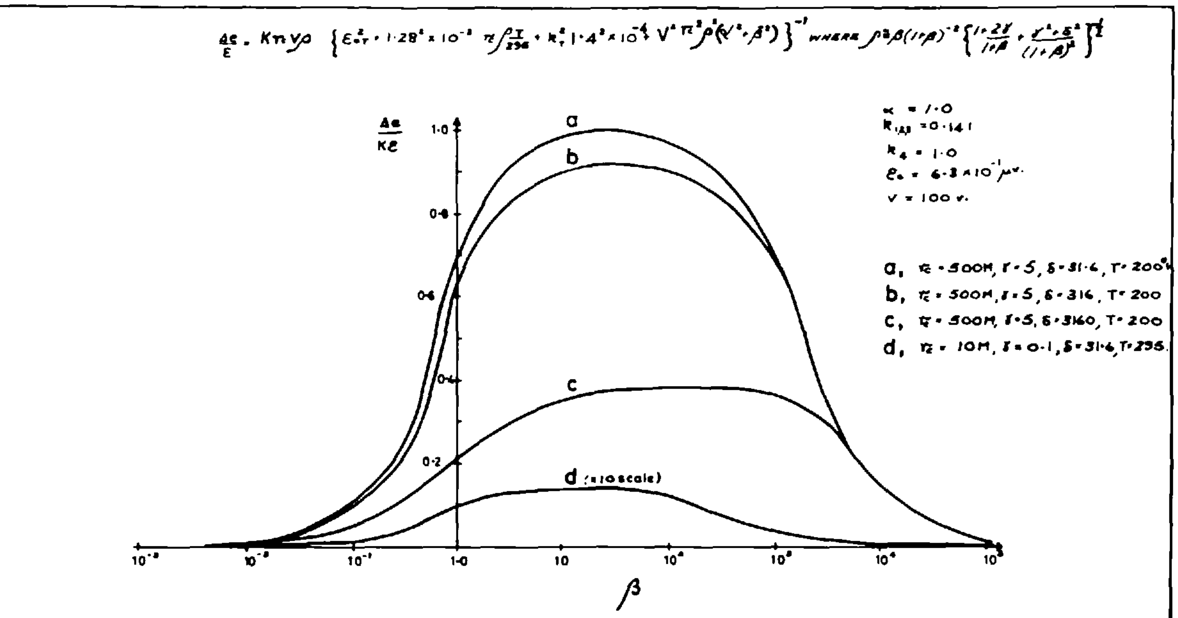

F.8.19

THEORETICAL CURVES REPRESENTING THE SIGNAL/NOISE AT CONSTANT (100 V.) BIAS VOLTAGE AS A FUNCTION OF β.

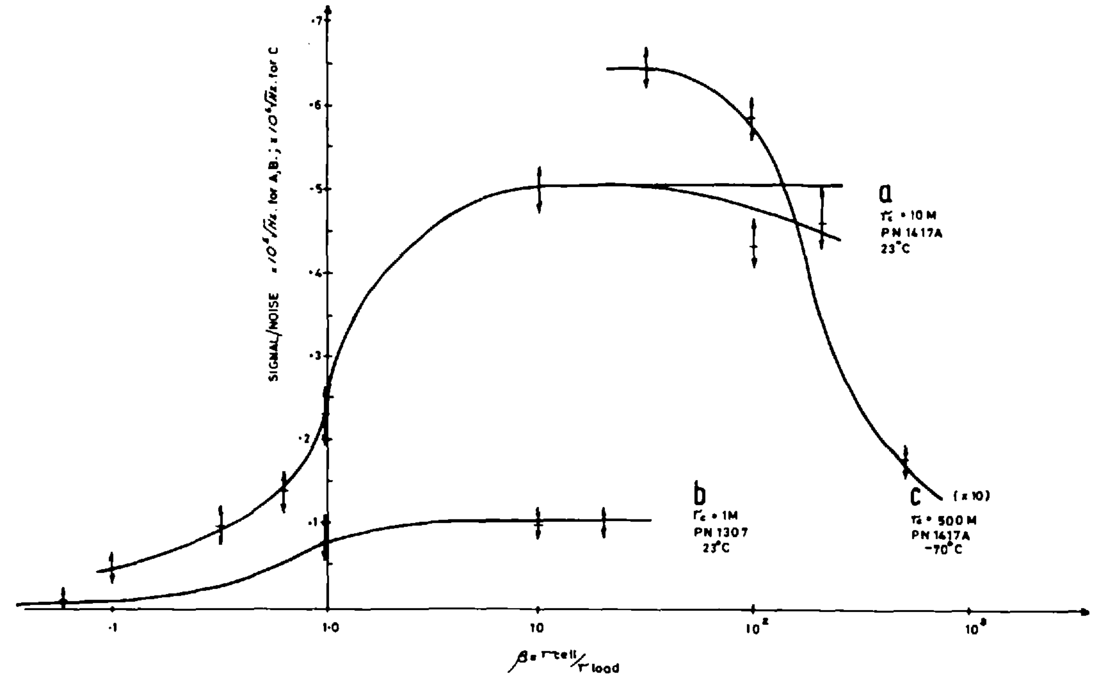

F.8.20 OBSERVED SIGNAL/NOISE AS A FUNCTION OF BIAS RESISTANCE FOR TWO DETECTORS

This expression (E8.72) is first given in appendix A8.07; the voltage dependence of this function (E8.73, A8.08) is plotted in F8.15 and the corresponding observed performance of a PbS detector and bias network with bias voltage is shown in F8.14. It is clear from these curves that there is little advantage in setting the noise level greater than three times the zero bias voltage noise. The derived bias voltage required to increase the zero volts bias noise by 'm'(E8.76, A8.09) is shown as a function of β in F8.16 and the observed corresponding function is plotted in F8.17.

Equations E8.70 and E8.72 were used to plot the signal/noise curves figure F8.19 as a function of β for a fixed 100v bias. Three cases for a cooled detector were considered: $\delta = 31.6, 316, 3160$; the lowest value was chosen as the least to have any significant effect on the final curve, when $r_c = 500$ and $\gamma = 5$, for a working $\beta \sim 10$. The order of magnitude jumps of δ correspond to order of magnitude increases in frequency or of capacitance; at a frequency of 5 Hz and $r_c = 500M$, then $\delta = 31.6$ corresponds to a cell capacitance of 2KpF. The value of $k_{Tf} = 0.141$ was determined from measurement of noise from the cooled detector (PN1417A); if the value of k_{Tf} for the detector (PN1307) at room temperature is taken as 1.0, then the data in figure F8.14 gives $\alpha = 2.6$ for that detector, (it then has 2.6 x the noise expected from the equivalent pure resistance). Temperature dependence of k_{Tf} requires further investigation, but appears to be a reciprocal power, or inverse exponential function.

The curves 'a, b, c' in figure F8.19, obtained from E8.70 and E8.72, show the sigmoid shape of curve F8.18 (A8.10) for $\beta \lessdot 20$, with the most rapid change at $\beta = 0.8$, and a gradual fall off as $\beta \rightarrow \infty$, most rapid at 2×10^3. The fall off at high β is mostly produced by the predominance of preamplifier noise, while the effect of capacitance is to attenuate the whole curve, but less so at high β where the load resistance is small; the capacitance attenuation becomes very significant for $\delta \gg 300$ in the case considered. Curve 'd' at 10 x scale shows the signal/noise for the same detector parameters but here at room temperature. In figure F8.20, some measurements of signal/noise for two real detectors have been plotted as a function of β. In curve 'a' the detector (PN1417A) is at room temperature, and in curve 'b' (shown $^1/10$ scale) is cooled to about 200°K, and shows a 13 fold increase in signal/noise for $\beta = 30$ and also shows the effect of preamplifier noise at high β. Curve 'c' is for a different detector at room temperature, showing how the intrinsic sensitivity of different detectors vary. Measurements were unfortunately restricted for curve 'b' due to the problem of changing the load resistor in the cryostat in vacuum while in a cooled state. The curves F8.20 in general confirm the semi-empirical curves of F8.19 and so also of the semi-empirical equations F8.14 and F8.15, and confirm the domain of the optimum signal/noise as $10 < \beta < 50$ and not $\beta = 1.0$ as would have been expected if the detector were the only source of noise; $\beta = 1.0$ is close to the point of most rapid change. The optimum operating point for the detector is then $10 < \beta < 50$ and V is such that $\varepsilon_V \gg \varepsilon_o$.

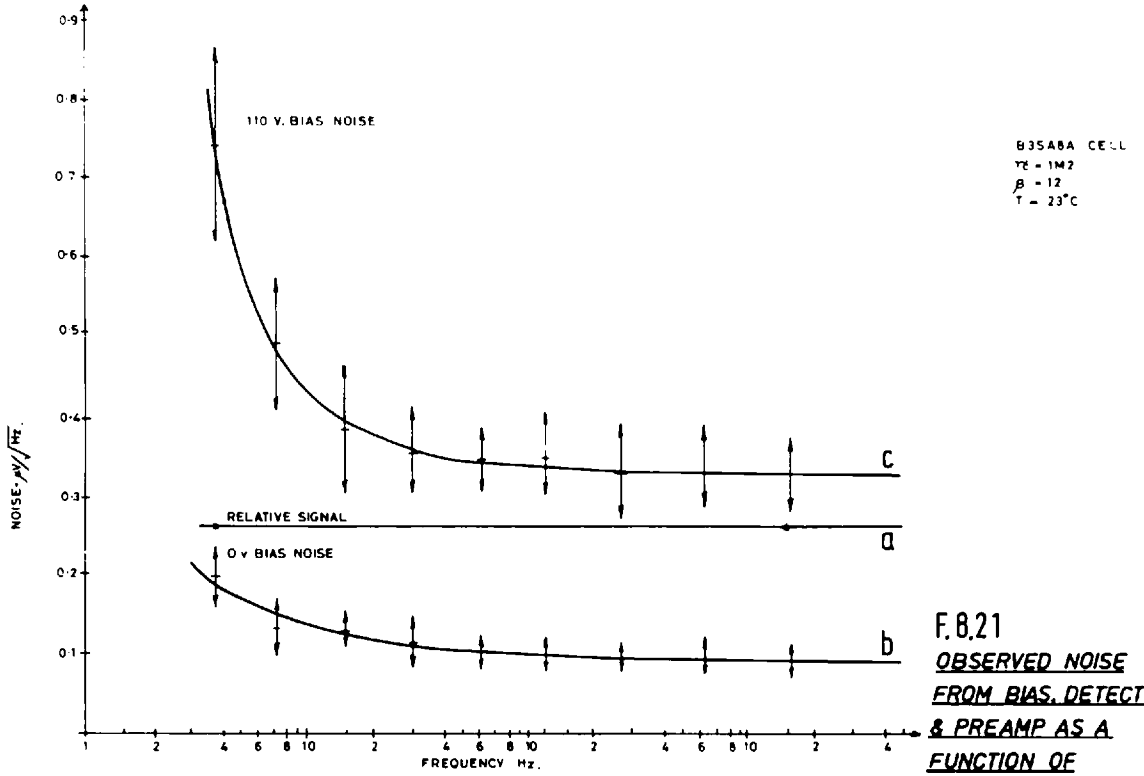

F.8.21 ***OBSERVED NOISE FROM BIAS, DETECTOR & PREAMP AS A FUNCTION OF FREQUENCY***

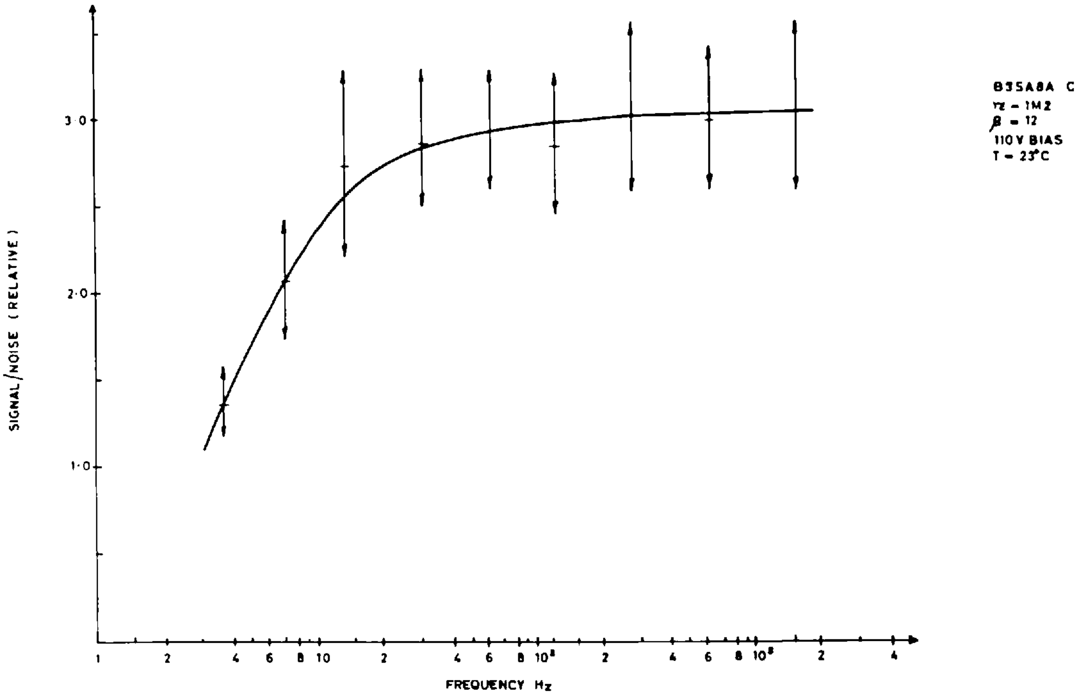

F.8.21d ***OBSERVED SIGNAL/NOISE FOR BIASED DETECTOR, AT 23°C., AS A FUNCTION OF FREQUENCY.***

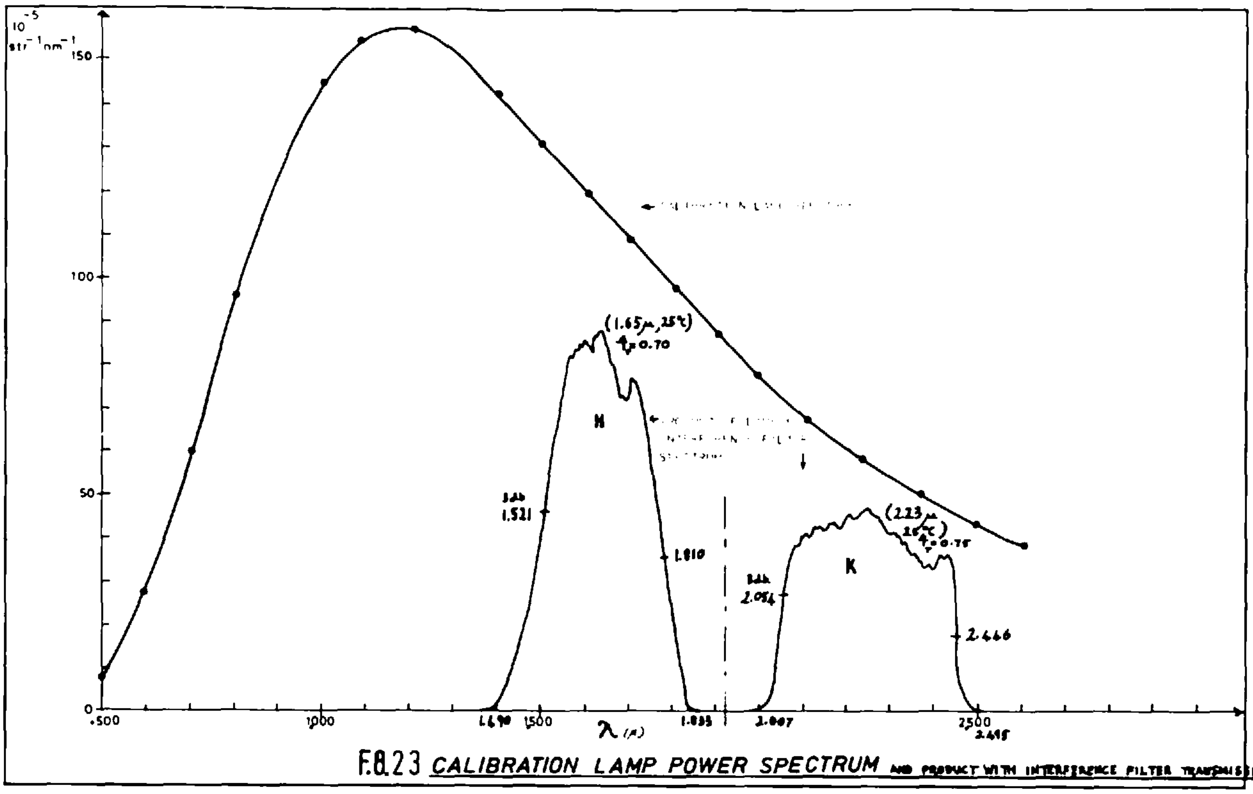

F.8.23 CALIBRATION LAMP POWER SPECTRUM AND PRODUCT WITH INTERFERENCE FILTER TRANSMISSION

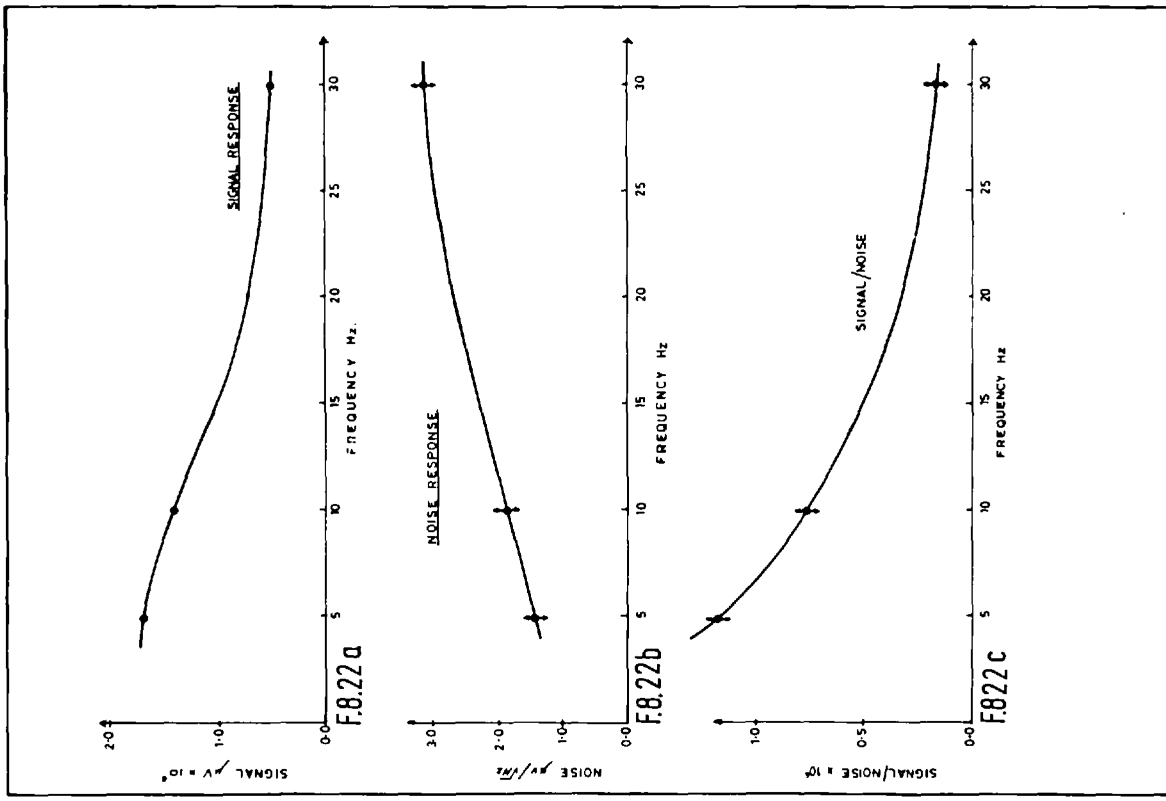

F.8.22a

F.8.22b

F.8.22c

OBSERVED FREQUENCY RESPONSE OF BIASED DETECTOR PN1417A WHEN COOLED TO ~ -70°C, $\beta = 18{\cdot}2$, $\tau_c = 16$ MS.

8.03 Effect of operating frequency on signal/noise

Figure F8.21 shows the effect of operating frequency on a room temperature detector, while figure F8.22 shows the frequency effect on a cooled detector; note how at room temperature, the $^1/f$ detector noise results in a signal/noise low frequency roll-off below 10Hz; all other room temperature measurements were made at 30Hz. As expected, at -70°C the signal/noise improves with reduction of frequency; the optimum is possibly a little less than 5 Hz; this is the attenuation effect produced by capacitance when the detector resistance is high. All other measurements were made at 5 Hz, that is just above the roll-off-frequency of the instrument electronics.

8.04 Comparison of detectors

Measurements on the cooled detector PN1417 and on other detectors for comparison, were all made in Tenerife, and so were necessarily restricted; a table of the measured performance of various PbS detectors is shown in T8.1 ; the best detector (PN1417A) was used for the astronomical measurements in chapter 9, while B3SA8A was the original detector used in 1973 and the subject of laboratory calibration.

8.05 Detector laboratory calibration

A lead sulphide plate (B3SA8A) was mounted on an optical bench and disc-chopped against a standard calibration lamp. The W.O.T.A.N. tungsten lamp was supplied by a constant current power supply; the detector was biased as in the photometer, and the signal from the calibrated

Table T8.1

Comparison of detectors

Detector :	B3SA8A	B3SA8B	PN1417A	PN1417B	PN1307	units
resistance:	1M0	1M0	10M6	9M8	1M0	Ω
load :	1M0	1M0	9M4	9M4	1M0	Ω
Noise(23°C):	.070	.072	.239	.221	.071	$\mu V/\sqrt{Hz}$
H.T. bias V :	17	17	8	8	8	V
Inc. in noise to V :	2.2	2.1	2.6	4.6	2.0	X
Signal in broad band	10×10^3	9.5×10^3	149×10^3	152×10^3	21.4×10^3	μV
signal $\lambda 1.65\mu$:	1.7×10^3	1.77×10^3	30.5×10^3	24.3×10^3	3.7×10^3	μV
" $\lambda 2.2\mu$:	$.51 \times 10^3$	$.409 \times 10^3$	11.2×10^3	9.1×10^3	0.89×10^3	μV
Signal relative to broad-band (b.b.) at $\lambda 1.65\mu$:	.17	.186	.204	.160	.173	
" $\lambda 2.2\mu$:	.051	.043	.075	.060	.0418	
$(2.2\mu)/(1.65\mu)$:	.30	.23	.37	.38	.24	
$S/N(\lambda 1.65\mu)$:	11.0×10^3	11.7×10^3	49.1×10^3	23.9×10^3	26.1×10^3	$\sqrt{Hz}$
$S/N(\lambda 2.2\mu)$:	3.3×10^3	2.71×10^3	18.0×10^3	8.95×10^3	6.27×10^3	$\sqrt{Hz}$

T8.2 Laboratory calibration for a PbS detector

$f(\lambda)$ is the filter transmission function

$B(\lambda)$ is the lamp emission function

(detector area)$^{\frac{1}{2}}$ detector resistance	B3SA8A: 5.0mm 1M	PN1417A: 4.0mm 10M at 295°K, 500M at 200°K	
solid angle of detector, subtended at lamp : Ω :	4.3 x 10^{-6}st		
waveband:	λ 1.65μ, H	λ 2.2μ, K	units
$R = \sum_{\lambda} f(\lambda)B(\lambda)\,\Delta(\lambda)$:	0.226	0.162	w/st
:-R Ω :	0.973	0.698	μ
B3SA8A detector:- output from X10 preamp. at 30 bias :	52	52	mV
:-sensitivity at 30v bias :	5.3	7.45	mV/μ
noise at 30v bias :	0.35	0.35	μv/$\sqrt{\text{Hz}}$
:-noise equivalent power 295°K :	6.60 x 10^{-5}	4.70 x 10^{-5}	μw/$\sqrt{\text{Hz}}$
:- D*(30, 1) 295°K : for 5mm area detector	7.58 x 10^{9}	1.06 x 10^{10}	cm$\sqrt{\text{Hz}}$ /w
telescope collection area:	1.71	1.71	m^2
† filter band width : $\Delta\lambda$:	.291	.409	μ
† filter transmission :	.65	.45	
total transmission (x0.3):	.20	.135	
:- total area x transmission:	0.333	0.231	m^2

Table T8.2 (contd.)

B3SA8A detector (contd.)	λ 1.65μ, H	λ 2.2μ, K	units
:- noise equiv. flux on telescope mirror or b.w.:	1.98 x 10^{-10}	1.28 x 10^{-11}	w/m^2
:-noise eq. flux for 1μ b.w. :	6.80 x 10^{-10}	4.96 x 10^{-10}	w/m$^2\mu$
flux unit. limit at 295°K:	620	800	F.U.
From T8.1 the S/N advantage of PN1417A over B3SA8A is :	4.46	5.45	
when cooled there is a further x 13 advantage making overall :	58.0	70.9	
Then for PN1417A detector	-		
∴ n.e.p. of detector at 200°K :	1.14 x 10^{-6}	6.63 x 10^{-7}	μw/$\sqrt{\text{Hz}}$
:-D*(5, 1) : with a 4mm area detector	3.51 x 10^{11}	6.01 x 10^{11}	cm$\sqrt{\text{Hz}}$ /w
:- flux limit at 200°K :	10.7	11.3	F.U.
:-‡ flux limit at 200°K, 50 secs integration :	0.60	0.64	F.U.

† see F8.23

‡ 1 Hz b.w. = 0.16 sec integration

Then for 50 secs integration, limit is scaled by x 5.64 x 10^{-2}

preamplifier was noted and compared with the known source (luminosity curves were supplied). The detector was calibrated with both λ 1.65μ and λ 2.2μ interference filters; the filters were of known transmission profiles, the integrated transmission having been established (see figure F8.23). Unfortunately these were not the same filters as used in Tenerife. A sensitivity for the detector was established (see T8.2:), and the noise for this bias was measured (where the noise exceeded the zero volt bias noise by an amount $>$ 3); a noise equivalent flux power and D^* was then obtained. The detector was then cooled in the cryostat and the increase in sensitivity noted (using a local source); the noise equivalent power for the cooled detector was then established (T8.2′).

Given the telescope collecting area, and allowing for the transmission of the telescope and instrument optics, a limiting sky brightness could then be estimated. A summary of the findings is given in table T8.02, and the expected performance of another detector such as that used for the Tenerife observations (PN1417A) was made by scaling the relative signal/noise values given in table T8.1. The estimated flux limit for the Tenerife flux collector with the photometer, dusty telescope mirrors, and the cooled PN1417A detector (see T8.02), agrees with the observed minimum error bars in the astronomical data section of chapter 9.

8.06 Conclusion

This chapter has been concerned with the determination of a semi-empirical function representing the signal/noise for a detector-noise limited PbS detector together with the optimisation of the function parameters (the bias conditions). The function thus obtained showed satisfactory agreement with the detectors tested, and can be regarded as being representative for all such detector-bias arrangements several detectors were compared and one was calibrated. The best detector was selected and optimised for astronomical use.

Further information particularly useful in appreciating the behaviour of PbS and other infrared detectors can be found in the listed references (R8.01 - R8.09).

References for Chapter 8 (see appendix for further discussion)

R8.01 Lummis, F.L., Petritz, R.L. 'Noise, time-constant, and Hall studies of lead sulphide photoconductive films'. Phys. Rev. Jan. 1975, 105, 2, 502

R8.02 'Infrared radiation detectors'. Nasa Technical translation, Nasa TTF197, 93

R8.03 Humphrey, J.N. 'Optimum utilization of lead sulphide detectors under diverse operating conditions'. Applied Optics 1965, 4, 665.

R8.04 Putley, E.H., Martin, D.H. 'Detectors'. Spectroscopic Techniques, N. Holland (1966) C.4. 113-151.

R8.05 'Study of technological requirements associated with interferometric infrared astronomy'. Space Division Hawker Siddeley Dynamics Ltd. Report HSD TP7 491

R8.06 Putley, E.H. 'Solid state devices for infrared detection'. J.S.Inst. (1966) 43, 857

R8.07 Smith, R.A., Jones, F.E. R.R.E. Journal, Ap. 1967, 35

R8.08 Smith, R.A., Jones, F.E., Chasmar, R.P. 'The detection and Measurement of infrared radiation'. Oxford (1968)

R8.09 Smith, R.A. 'Semiconductors'(Cambridge Univ. Press) (1961) C7

CHAPTER 9

9. Observations made on the Tenerife 60" flux collector. and general conclusions.

Contents:

OBSERVATIONS MADE ON THE TENERIFE 60" FLUX COLLECTOR, AND GENERAL CONCLUSIONS

9.01 Preliminary preparations

Observing time on the 60" flux collector was successfully applied for in early 1975, and it was after this application that the solenoid system was replaced by the Ling vibrator drive unit, and the servo system became fully operational. It was also at this time that the F/12.8 optics system was built and new detectors of a slightly smaller size than previously used, were ordered.

9.02 Conditions on site

A number of problems were encountered after shipment of the photometer to Tenerife; the equipment suffered in the hands of the Spanish customs, and also several solder joints and card contacts came adrift in transit; other problems included the interfacing flange holes not matching with the telescope bolt holes, and also the instrument flange had been drilled with clearance holes rather than the specified topped size holes; all these problems were successfully overcome during the first week on site.

The photometer,together with its extension pipe, proved to be a little too heavy for the telescope such that the condition of minimum slip of the R.A. drive clutch corresponded to a state of considerable unbalance, then requiring only 1 Kg wt. force to move the telescope in negative R.A. but a full body weight to move it in positive R.A. The R.A. and Dec. readouts were found to be inconsistent, giving unrepeatable positions within a few arcmins, which in the case of subsequent sky R.A. incremental scans, produced apparent shifting of peak signals on repeated scans, and in cases where there was no visible object in view, large uncertainties in location.

The weather during the observing period of 25 July to 2 August proved to be far from ideal, with considerable intermittent cloud on all nights except for the 2 August, when observations were prematurely terminated by a fracture of the Ling drive unit coil winding. Atmospheric dust persisted for the whole period which made finding difficult when the moon was up, but this was less of a problem at the end of the month. On many nights, the intensity readings at λ 2.2 μ of reference stars showed rapid, as well as longer term fluctuation, corresponding to varying attenuation by thin cloud; on most nights the clouds cleared and readings steadied towards morning, but unfortunately most of the objects of interest lay close to the galactic plane, and hence were early evening objects.

Wind and the large optical aberrations in the flux collector did not present inconvenience due to the extensive field of the photometer; the full field aperture (measured from star trailing) was 4.0 arcmins.

9.03 Detector selection

The detectors did not arrive until the photometer was on site, and due to an error by the manufacturer of replacements for the spherical mirrors, the mirrors were not aluminised satisfactorily until two days before leaving R.O.E.. Hence both mirrors and detectors were mounted and installed on site. Fortunately, no particularly bad problems were encountered, and the detectors fitted into their mounting blocks with only a little packing. A comparison was made of all five detectors at room temperature as previously discussed, and signal to noise tests carried out (see previous chapter). Some acoustic pickup was experienced at this point, and found to be dependent on the orientation of the cryostat; it was subsequently eliminated after some selective use of araldite to fix down the load resistors and f.e.t. clamp.

The cryostat behaved satisfactorily on cooling, without any excessive vacuum leaks; the temperature hold time proved to be about four or five hours for $\sim 23^{0}$C(room temperature). The detector temperature was monitored from the cell resistance, as no digital thermometer was available (although the detector head was provided with a thermocouple probe).

9.04 Alignment procedure and field of view

Initial alignment was carried out with the laser from the artificial star side of the photometer in the usual way. The artificial star was then used to compare the field of view of the various detectors in both H and K bands as seen directly or through the multi-mirror optics. It was thus confirmed that a .4mm detector with the F/12.8 optical system was still limited by the field stop iris, but that due to chromatic aberration of the reducer lens 'n', the image spread at K . was noticeably broader than that at H (see F9.01 to F9.02); attempts were made to optimise this.

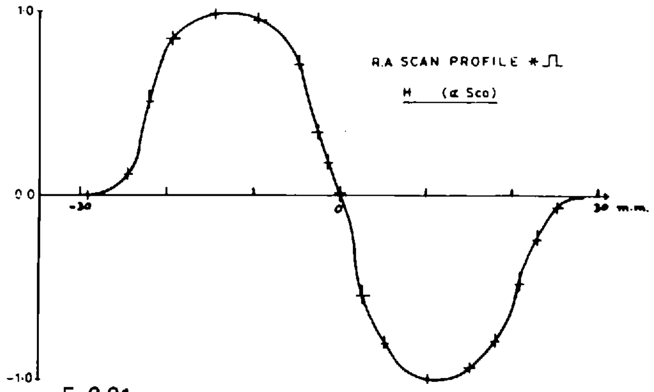

F. 9.01a

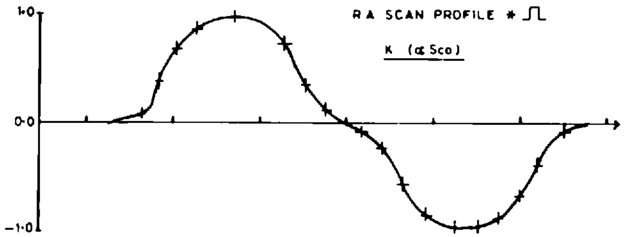

F. 9.01b

INSTRUMENTAL PROFILES

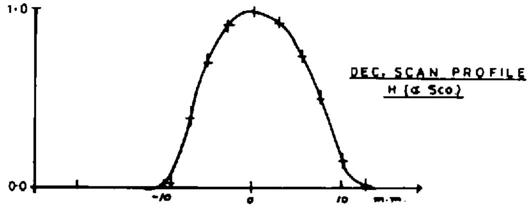

F. 9.02a

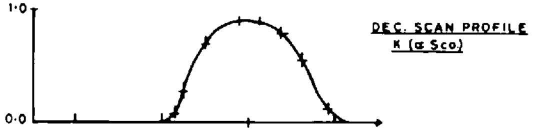

F. 9.02b

INSTRUMENTAL PROFILES

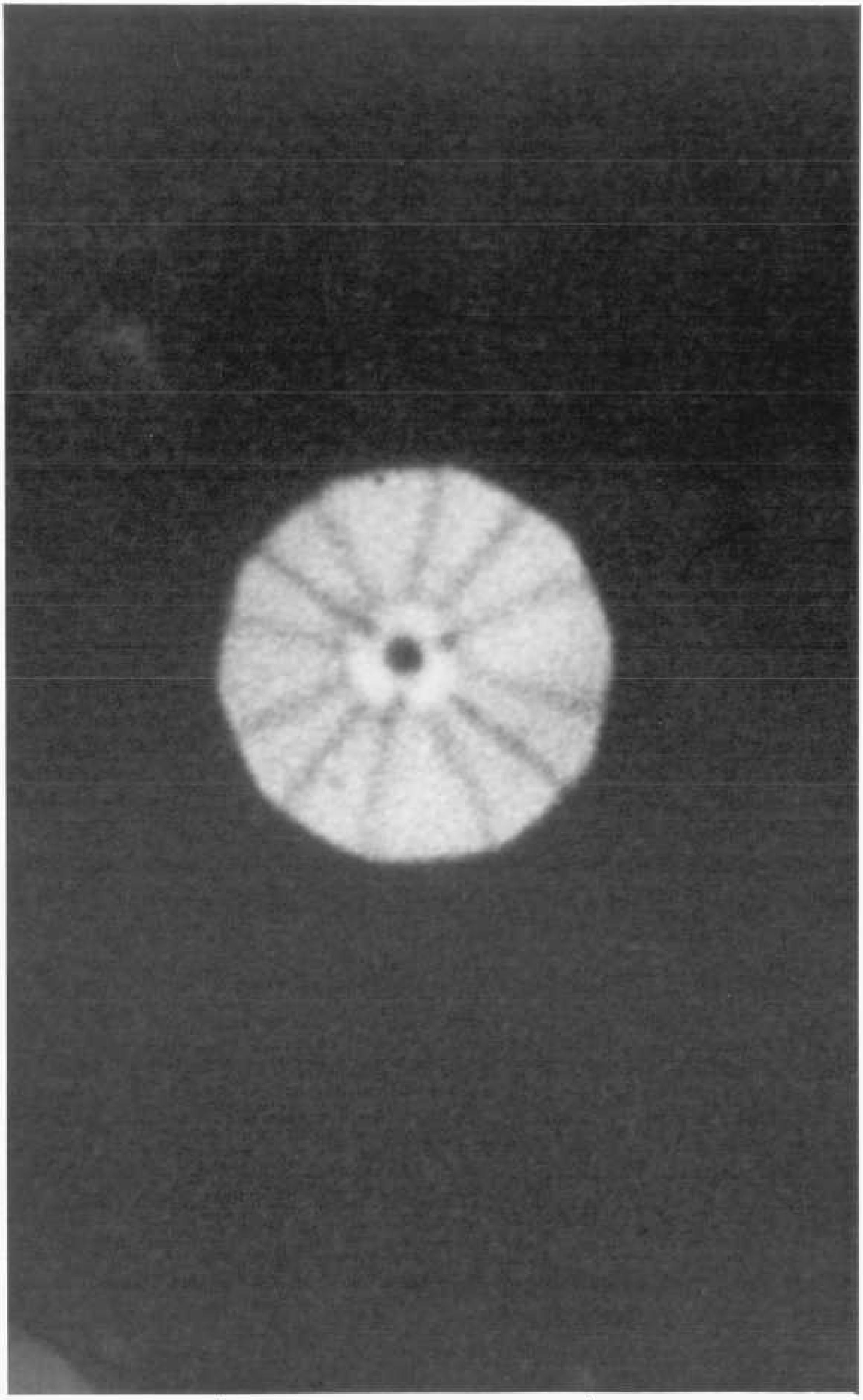

P9.2

THE 60" FLUX COLLECTOR MIRROR COVERS SEEN THROUGH THE ENTIRE OPTICAL SYSTEM OF THE TWO SPHERICAL MIRROR SKY COMPARISON WIDE FIELD INFRARED PHOTOMETER FROM THE FINAL OBJECTIVE STOP

Once the photometer was mounted on the telescope, (frontispiece P9. 1) further alignment adjustments of the field mirror were found necessary to bring the image of the primary mirror into coincidence with the photometer aperture stop iris; the final result of this adjustment can be seen in photograph P9. 2, where an image of the flux collector primary mirror cover is seen in coincidence with the aperture stop iris. Note that there is some astigmatism, but the image is remarkably satisfactory, and at no point can the edge of the mirror be seen (otherwise spurious signals would be generated when sky- chopping). The aperture stop under these circumstances was set to 9.5mm; the laser when placed in this position, with the first diagnal flat in place, was easily adjusted by means of the same flat, to illuminate the centre of the telescope secondary while at all times passing along the principal axis of the folded optics system. The illumination of the telescope secondary by the laser was particularly steady in the sky-chop mode.

The 10" finder telescope cross-wires were brought into coincidence with the photometer cross-wire systems and also the main photometer, by location of a bright star. The normal cross-wire position was arranged to be that for the image to be in the centre of the positive R.A. field aperture on a square-wave 4 arcmin sky-chop, and phased to give a positive maximum signal. The observations were all made at a chopping frequency of 5Hz, which was found to be as close as could be attained to the optimum signal-to-noise for the detector when used in its cool state of ~ -70°C.

9.05 Method of sampling

It was found that most bright stars gave signal-to-noise ratios of greater than 10, with a 3 second integration time, but most other sources gave no obvious signal without much longer integration. The available chart recorder was found to be unreliable and also in view of the long integrations necessary, it was decided to use a digital voltmeter with four-figure display and hold facilities, together with a printer borrowed on site. The printer could be operated from the D.V.M. manually or at various fixed sampling rates, the slowest being once a second. After some experimenting the most satisfactory method of recording data was found to be that using the D.V.M. in the one second sampling mode with the synchronous rectifier time constant set at 3 seconds; sampling was continued for periods up to 100 seconds, for later averaging. A longer time constant was available but not used as an instantaneous readout for monitoring was considered more satisfactory; by this means, interference transients and cloud attenuation could be more readily monitored, and accurate numerical analysis of the data could be carried out at a later date.

In the case of sources smaller or equal to the field stop diameter (4 arcmins), sampling of the data was carried out as described, here with the object first in the positive R.A. aperture, then in the negative R.A. aperture and labelled respectively 0, -1. In the case of more extended sources, and also occasionally for some point sources as above, scans in R.A. were executed in increments of 4 arcmins from positive to negative R.A.

the number of increments, and of samples per increment was preset according to the source. In some cases return scans were executed, in which case the data on return was treated separately as a separate scan. Scans were usually made in R.A., and in some cases these were repeated at ± 4 arcmin. intervals in declination. The central emission source usually was labelled '0' and sometimes used as the start of a scan, but quite often the first scan point was allocated a negative number corresponding to the number of increments of R.A. away from the central source.

It had been hoped to interface the 'Interdata Nova' computer directly to the analog synchronous rectifier output, via the available 'C.A.M.A.C.' boards, such that the computer could terminate sampling once a preset standard error had been reached, but unfortunately the 'C.A.M.A.C.' suffered a major failure and was not available .

9.06 Data reduction

Averaging of the data was at first attempted on an electronic calculator, but the calculation of standard deviation and errors in the mean proved very tedious and prone to error, so a simple computer program was prepared which averaged up to 100 data points and calculated the standard deviation and error in the mean. The evening's data was typed into the 'Nova' computer on site each following day, and all the data was satisfactorily reduced before finally leaving the site.

Further processing of the data was necessary in order to present the results in a form corresponding to the spatial intensity of the source. The general equation set up for this purpose is directly obtained from a mathematical analog of the sky chopping and scanning process.

In the following argument, 'n' represents the increment sky position, running between minimum and maximum values of 'n' and 'n', 'I' is the 'true' intensity of the source integrated over the field of view, 'S' is the signal output from the photometer when the source is placed in the + ve R.A. aperture, and 'e', 'v' are offset and pickup voltages accordingly.

This shows that for a source smaller than the field stop, it is sufficient to subtract the signal readings for the source in the two apertures and divide by two, to give a scale intensity independent of offsets and pickup. For scans, subsequent intensities are generated by addition of all previous intensities, subtracting the mean each time, using the first minimum sample number as the arbitrary zero. It should be noticed that if the scan column of signal values is added in reverse order to that specified, then the resultant intensities correspond to the inverse about the datum level of the original intensities but displaced by one scan increment.

Data reduction

A model for the instrument

Behaviour of instrument for a star:

Sample scan point No. n	Intensity I_n	difference $\Delta_n = I_n - I_{n+1}$	signal $S_n = k\Delta_n + kv + e$
3	I_s		
2	I_s	0	$kV + e$
1	I_s	0	$kV + e$
0	$I_s + I^*$	I^*	$kI^* + kV + e$
-1	I_s	I^*	$-kI^* + kV + e$
-2	I_s	0	0
-3	I_s	0	0

for a set $\check{n} \leqslant n \leqslant \hat{n}$

In general:

Hence

$$\frac{S_n}{k} = I_n - I_{n+1} + e/k + V \qquad \text{E9.01}$$

$$I_n = I_{n+1} + \frac{S_n}{k} - e/k - V$$

and

$$\sum_{n=\check{n},}^{\hat{n}} I_n = \sum_{n=\check{n},}^{\hat{n}} I_{n+1} + \sum_{n=\check{n},}^{\hat{n}} S_n/k - (\hat{n} - \check{n} + 1)(e/k + V)$$

$$V + e/k = \frac{\sum_{n=\check{n}}^{\hat{n}} S_n}{K\,(\hat{n} - \check{n} + 1)} \equiv \frac{\bar{S}}{k}$$

$$\underline{\underline{\bar{S} = \sum_{n=\check{n}}^{\hat{n}} S_n/(\hat{n} - \check{n} + 1)}} \qquad \text{E9.02}$$

$$\text{hence} \quad \underline{\underline{k\,I_n = S_n - \bar{S} + k\,I_{n+1}}} \qquad \text{E9.03}$$

$$\text{or} \quad k\,I_n = \sum_{j=n}^{\hat{n}} S_j - \bar{S}\,(\hat{n} - \check{n} + 1) + k\,I_{\hat{n}}$$

For points far from source, $I_{\hat{n}} = I_{\hat{n}+1} = I_s$ E9.04

and for a datum, $I_{\hat{n}} \equiv 0$; also $k = {}^{1}/pg$

For a star two samples taken $n = 0, -1$; then from E9.03

$$kI_o^* = kI_1^* + S_o - \bar{S} = S_o - \bar{S} = S_o - \frac{S_o}{2} - \frac{S_{-1}}{2} = (S_o - S_{-1})/_2$$

$$kI_{-1}^* = kI_o^* + S_{-1} - \bar{S} = S_o - \bar{S} + S_{-1} - \bar{S} = S_o + S_{-1} - S_o - S_{-1} = 0$$

$$\text{where } \bar{S} = \frac{S_o + S_{-1}}{2}, \qquad \underline{\underline{\text{hence } kI_o^* = (S_o - S_{-1})/_2}} \qquad \text{E9.05}$$

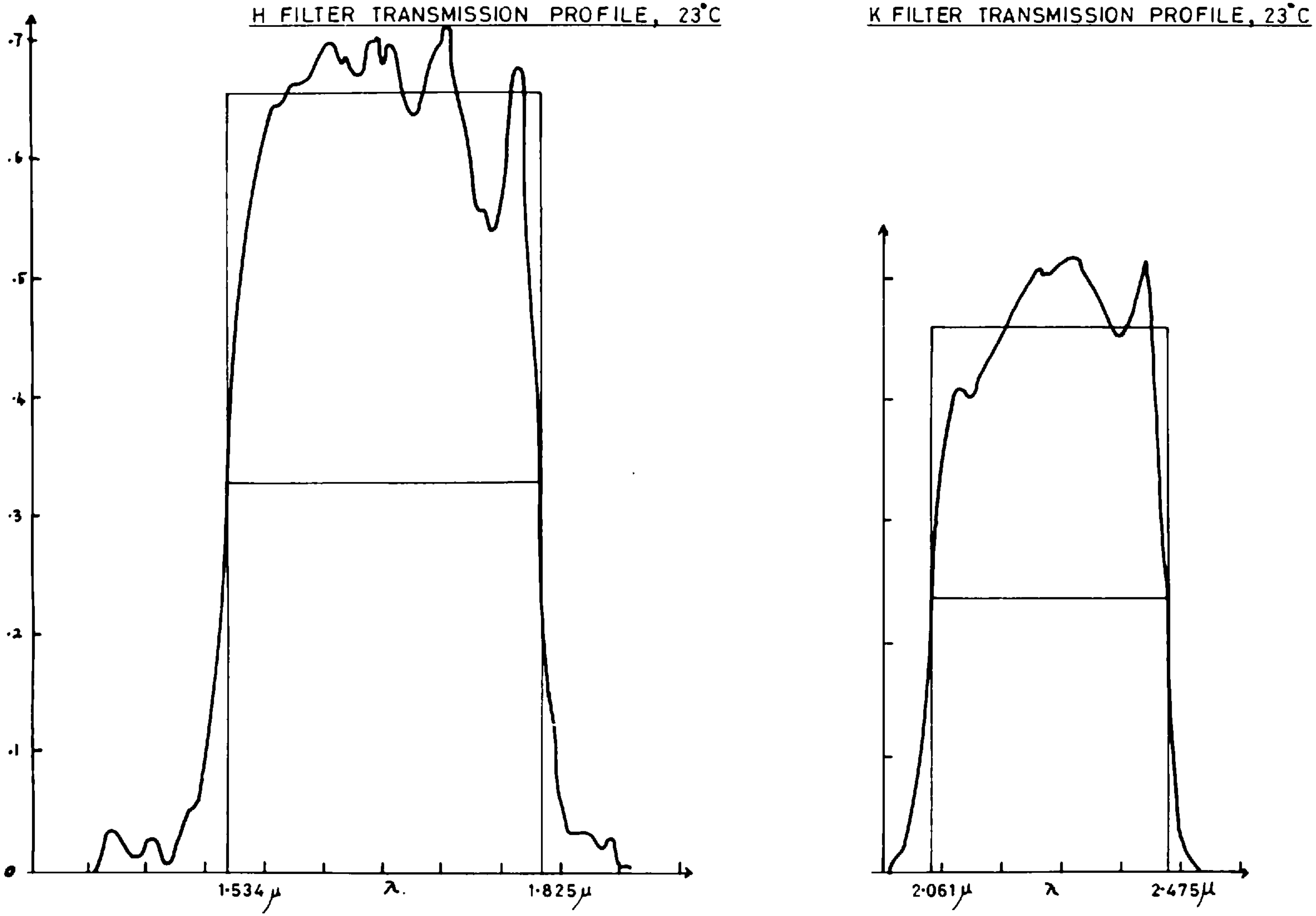

H FILTER TRANSMISSION PROFILE, 23°C

Eq. WIDTH = 0·291μ
TRANSMISSION = 0·65

F. 9.03a

K FILTER TRANSMISSION PROFILE, 23°C

Eq. WIDTH = 0·409μ
TRANSMISSION = 0·45

F. 9.03b

INTERFERENCE FILTER TRANSMISSION PROFILES

9.07 Instrumental profile correction and summary

Instrumental profiles can be seen in figures F9.01, F9.02 obtained by trailing α Sco across the field. The profiles are approximately Gaussian, in appropriate cases convoluted by the square-wave sky-chop; the square-wave mirror motion can be seen in diagram F7.06, as given by the mirror position display. The instrumental profile is largely determined by the final focusing optics before the detector; the profiles obtained on the 20" telescope with the light-pipe prior to the detector approximate to that of a truncated trapezoid, which is a more satisfactory profile due to the increased region of constancy. With the Gaussian profile, a star near the edge of the field contributes little signal as compared with that near the centre; for this reason, an extended uniform field would generate a deceptively low signal as compared with a central reference star. The appropriate scaling factor is determined below for a uniform field by integrating the volume under the three dimensional instrumental profile curve, here numerically approximated to a finite set of concentric cylinders. For any real source showing variation in brightness on a scale less than the field of view, the scaling factor will tend towards the unity value of a point source, but no allowance for this has been made in the data presentation.

(a) Instrumental profile constant

The interference filter transmission profiles are shown in F9.03.

Consider a star $I^{*} \equiv 1.0$ at location $k = 0$, (F9.04a)

This, by definition of the normalised profile, gives an effective signal intensity $\mathcal{S}_0 = f(o) = 1.0$

(No allowance is made here for the chopping function).

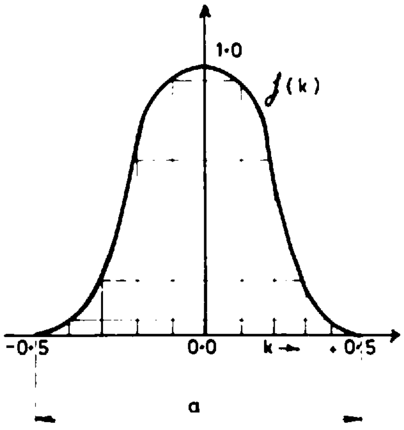

F. 9.04a

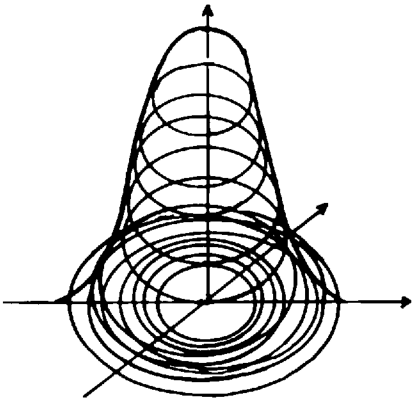

F. 9.04b

INSTRUMENTAL PROFILE INTEGRATION

In general $\mathcal{S}(k) = f(k)$

Consider a row of stars $I(k)$

$$\text{Then} \qquad \mathcal{S} = \sum_{k=-1/2}^{+1/2} f(k)\ I(k) \tag{E9.07}$$

$$\mathcal{S}_{\delta k \to \infty} = \int_{-1/2}^{+1/2} f(k) \left(\frac{I(k)}{dk} \right) dk$$

This is the area under the profile curve (F9.04a).

Consider a uniform field of such stars, then '$\mathcal{S}$' becomes the volume of rotation under the profile curve (assuming R.A. and Dec.profiles are the same).

The volume may be segmented into concentric cylinders (F9.04b).

$$\mathcal{S} = \sum_{k=0}^{1/2} 2\pi \quad k \quad \frac{\delta I(k)}{\delta a} \quad f(k)\ \delta k$$

$$\text{where,} \qquad \frac{\delta I_k}{\delta a} = \text{intensity/area} \qquad \equiv i_k$$

$$\mathcal{S}_{\delta k \to 0} = \int_0^{1/2} 2\pi\, i(k) f(k)\ \delta k \tag{E9.08}$$

<u>If</u> $\int_v I(k)\ dv = I^*$

and the field is evenly illuminated: $i_k = \dfrac{I^*}{\pi (\frac{1}{2})^2}$

$$\mathcal{S} = \sum_{k=0}^{1/2} 2\pi\ k\, f(k) \quad \frac{I^*}{\pi (\frac{1}{2})^2} \quad \delta^k \tag{E9.09}$$

In the instrumental profiles shown, a good approximation may be made with only a few cylinders,

then $$\mathcal{S} = \frac{I^*}{\pi (x_{\frac{1}{2}})^2} \pi \sum_{k=0}^{1/2} \cdot (x_{k+1}^2 - x_k^2) f(k) \equiv I^* E \qquad \text{E9.10}$$

then the equivalent intensity for a point source in the centre of the field is $\mathcal{S}/_E$

For an extended object $\mathcal{S}^0 = I^0 E$

for a central star $\mathcal{S}^* = I^*$

$$\frac{I^0}{I^*} = \frac{\mathcal{S}^0}{\mathcal{S}^*} \qquad \text{E9.11}$$

From figure F9.01: $E_{\lambda\, 1.65\mu} = 0.62$, $E_{\lambda\, 2.2\mu} = 0.52$

Most real cases of sources are neither uniform nor stellar,, and so E then lies closer to 1.0.

(b) <u>Scaling factors</u>

The intensities of observed objects and comparisons must be scaled for the appropriate air masses, in each case referred to the zenith, including the amplifier gain scaling (table T6.2). Noise measurements must also be scaled for r.m.s. rectifier gain (T6.2).

g = air mass

p = amplifier inverse gain } see table T6.2

q = rectifier inverse gain }

e.g.

$$I^{*} = p^{*} g^{*} (S_o - S_{-1})/_2 \qquad E9.12$$

hence

$$\frac{I^o}{I^*} = \frac{p \; g^o (k^o I_n^{\;o})}{p^* \; g^*(S_o^* - S_{-1}^*)E/_2} \qquad E9.13$$

(c) Summary

for a set $\check{n} \leqslant n \leqslant \hat{n}$

scan: $$k I_n = \sum_{j=n}^{\hat{n}} S_j - \bar{S}(\hat{n} - \check{n} + 1) + kI$$

or $$kI_n = S_n - \bar{S} + kI_{n+1} \qquad E9.03$$

where $$\bar{S} = \sum_{n=\check{n}}^{\hat{n}} S_n/(\hat{n} - \check{n} + 1)$$

$$I_{\hat{n}} = 0 \qquad E9.04$$

For a star. $n = 0, -1$

$$k I_o^* = (S_o^* - S_{-1}^*)/_2 \qquad E9.05$$

For scaling

$$\frac{I^o}{I^*} = \frac{p^o\,g^o}{p^*\,g^*\,E}\;\frac{k^o\;n^o}{(S^*_o - S^*_{-1})/_2} \qquad \text{E9.13}$$

where: E is instrumental area profile function constant.

g is air mass ratio

p is reciprocal gain

9.08 Presentation of the data

Each diagram, F9.05 to F9.15, is drawn as a set of steps, the height of each representing the mean intensity of the source integrated over a 4 arcmin.diameter field expressed in μ volts (left hand scale) from the detector for the settings and bandwidths used and determined as previously described. The scan position increment numbers appear across the diagrams, and the datum level is usually taken as zero for the minimum R.A. scan position. In each diagram, a scale height is given for 1 flux unit as determined by the signal from a nearby bright star, corrected to bring it to the same air mass as the source; the instrumental profile scaling constant obtained from figure F9.03 has also been included in the expressed scaling figure. The error bars indicate the error in the mean for each mean, and the number of samples in the mean is given to the right of each figure. Date, object catalogue no. and filter band appear in that order at the head of each diagram; together with, where possible, the scale, expressed as the number of flux units to 1.0μ V. The characteristics of the interference filter profiles are not considered here a critical factor, and are not included in any reduction as the filters used for the observations were particularly narrow band; this can be seen from the filter profile scans. The filter scans F9.03 also show the equivalent ideal flat top filter best fitting the real profile; the 3 db points are for equal area rather than equal transmission. Some useful discussions on filter radiometry and transmission profiles may be found in M. Menel's paper, R9.01.

Table T9.01

Standards used:

Name	Johnson list			Others			Author
	I	J	K	J	H	K	
6134 α Sco	-1.89	-1.73	-3.86		-3.77	-3.92	±.02 Hyland
7001 α Lyr	.10	.04	.02	.00	.00	.00	Grasdalen
7557 α Aql	.53	.44	.27	.21	.19	.11	Grasdalen
8308 Peg	.57	.04	-.77				
165 And	1.72	1.28	.52				

(see R9.02)

Crossing Points

1 F.U. = 10^{-26} w/m^2 Hz =	1.10 x 10^{-12} w/m^2 µ	0.62 x 10^{-12}
1 F.U. (α Sco) =	m 7.8	m 7.0

Aperture = 12.6 arc min^2

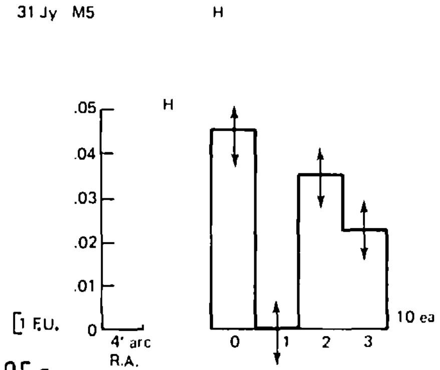

F. 9.05a N.G.C. 5904,H

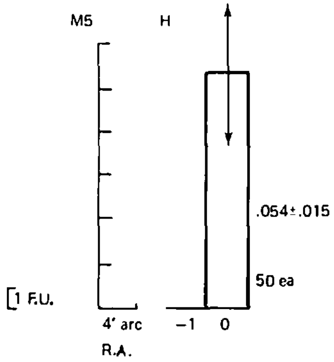

F.9.05b N.G.C. 5904,H

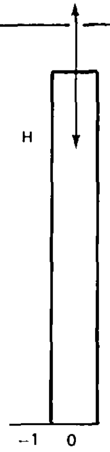

F.9.05c N.G.C. 5904, H

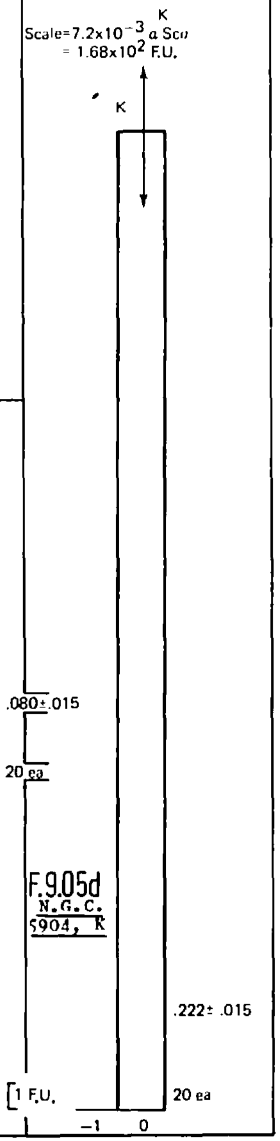

F.9.05d N.G.C. 5904, K

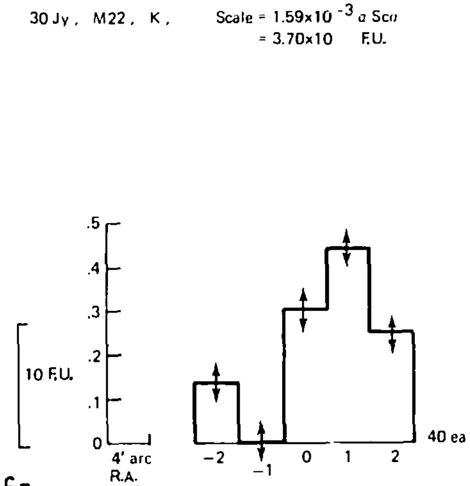

F.9.06a N.G.C. 6656,K

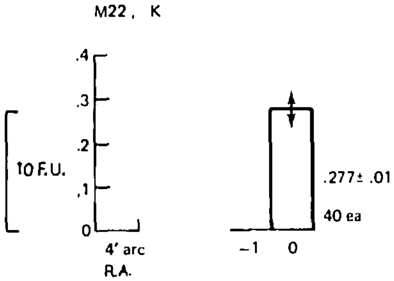

F.9.06b N.G.C. 6656,K

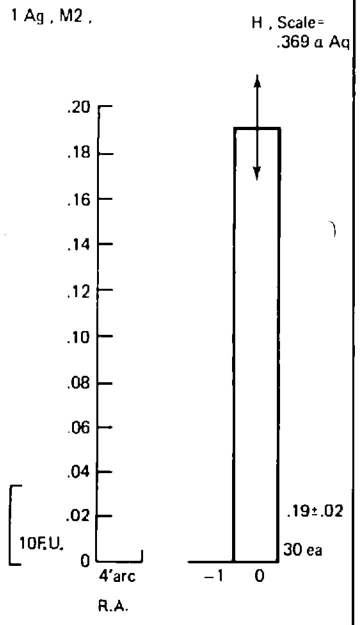

F.9.07a N.G.C. 7089,H

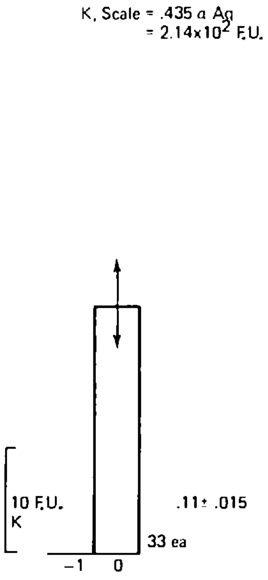

F.9.07b N.G.C. 7089,K

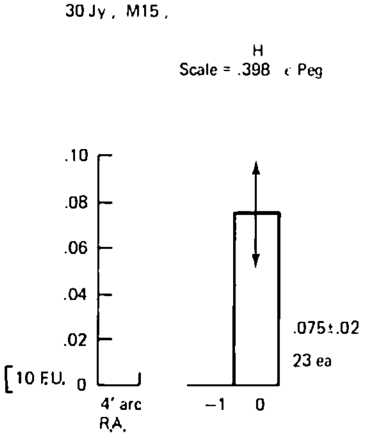

F. 9.08 a N.G.C. 7078,H

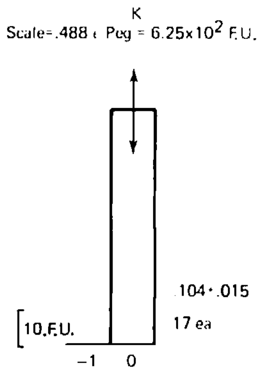

F. 9.08 b N.G.C. 7078,K

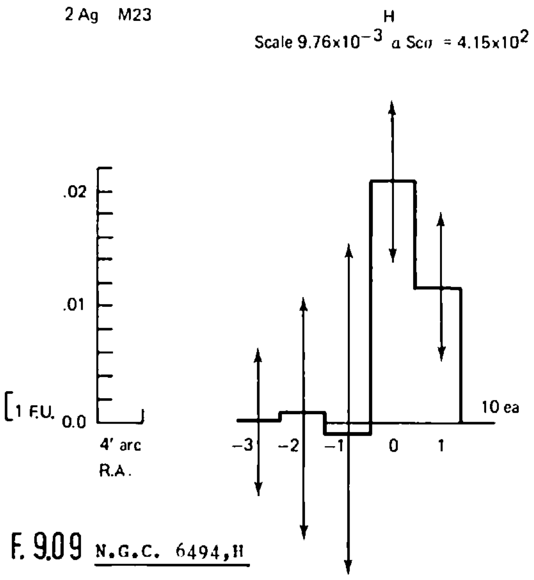

F. 9.09 N.G.C. 6494,H

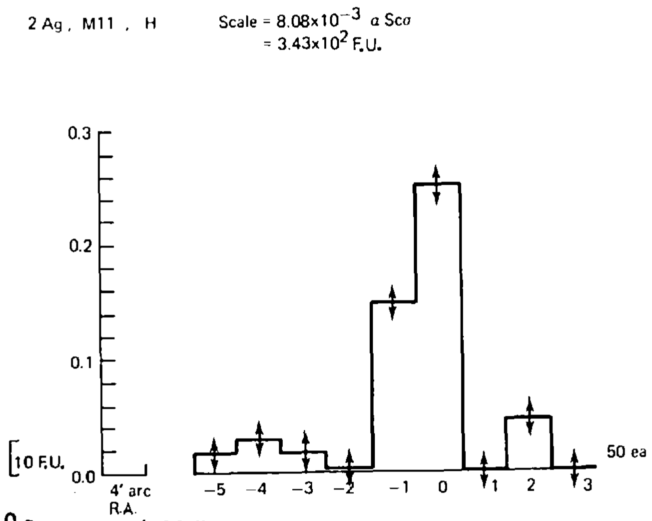

F.9.10a N.G.C. 6705,H

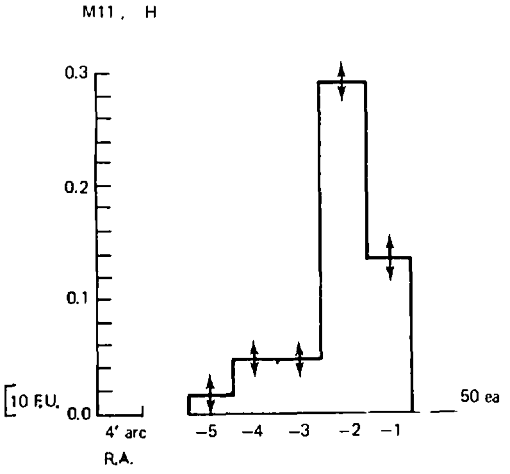

F.9.10b N.G.C. 6705,H

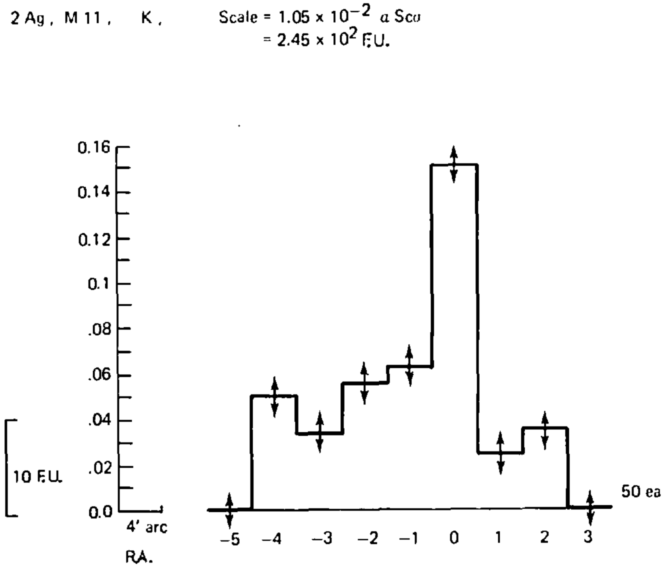

F.9.10c N.G.C. 6705,K

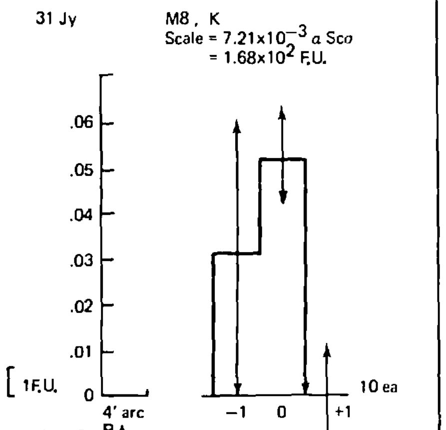

F.9.12a N.G.C.6523,K

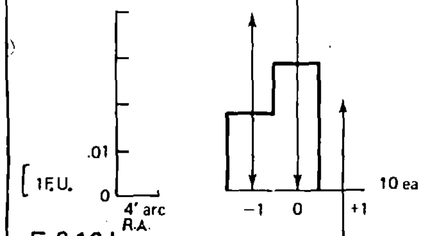

F.9.12b N.G.C.6523,K

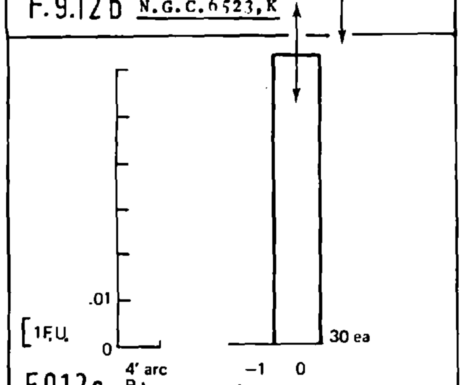

F.9.12c N.G.C.6523,K

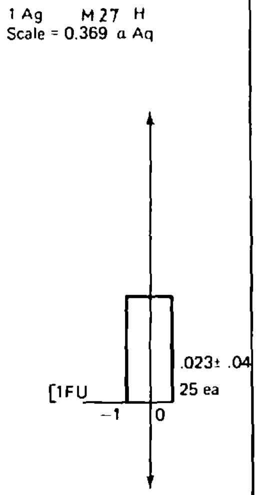

F.9.13 N.G.C. 6853,H

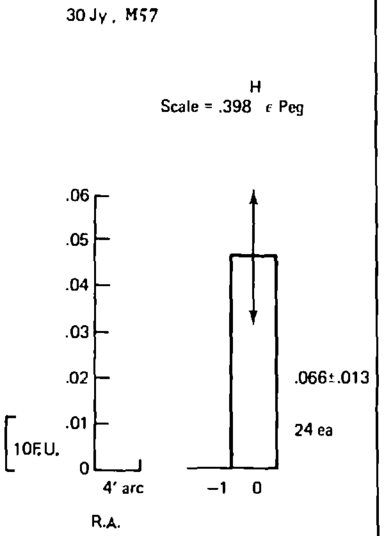

F.9.11a N.G.C. 6720,H

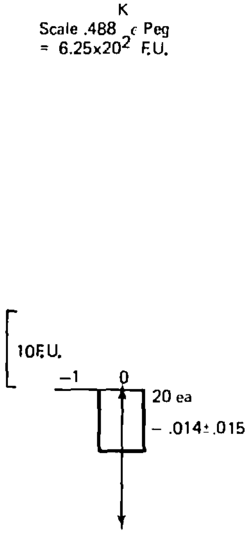

F.9.11b N.G.C. 6720,K

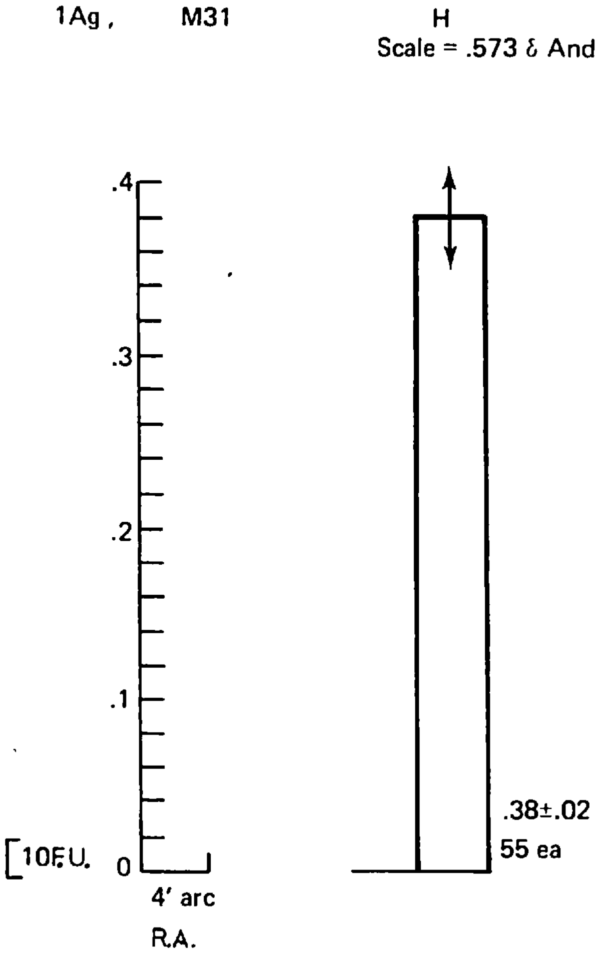

F.9.14a N.G.C. 224,H

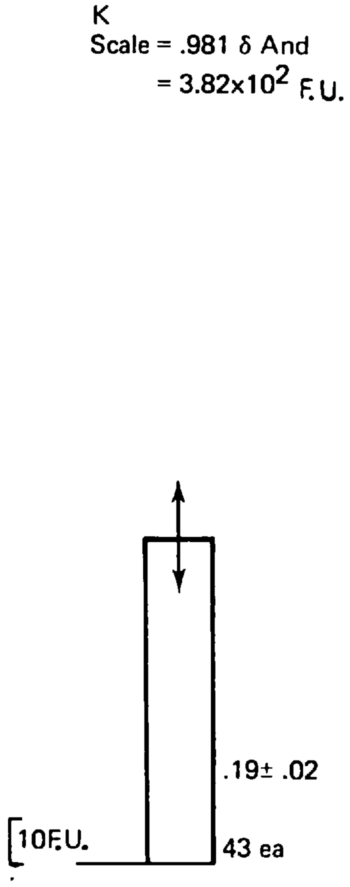

F.9.14b N.G.C. 224,K

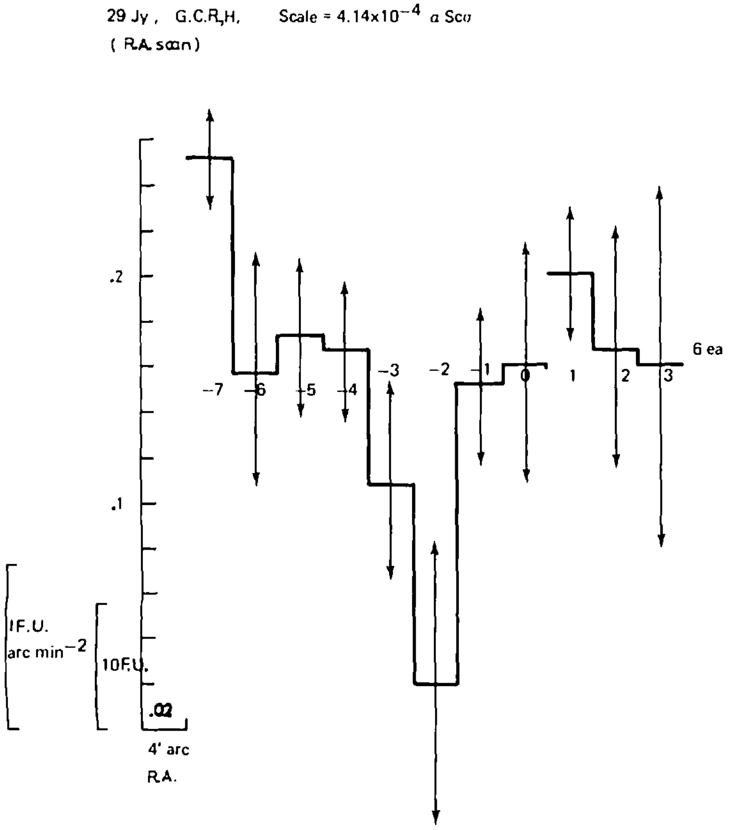

F. 9.15a G.C.R., H

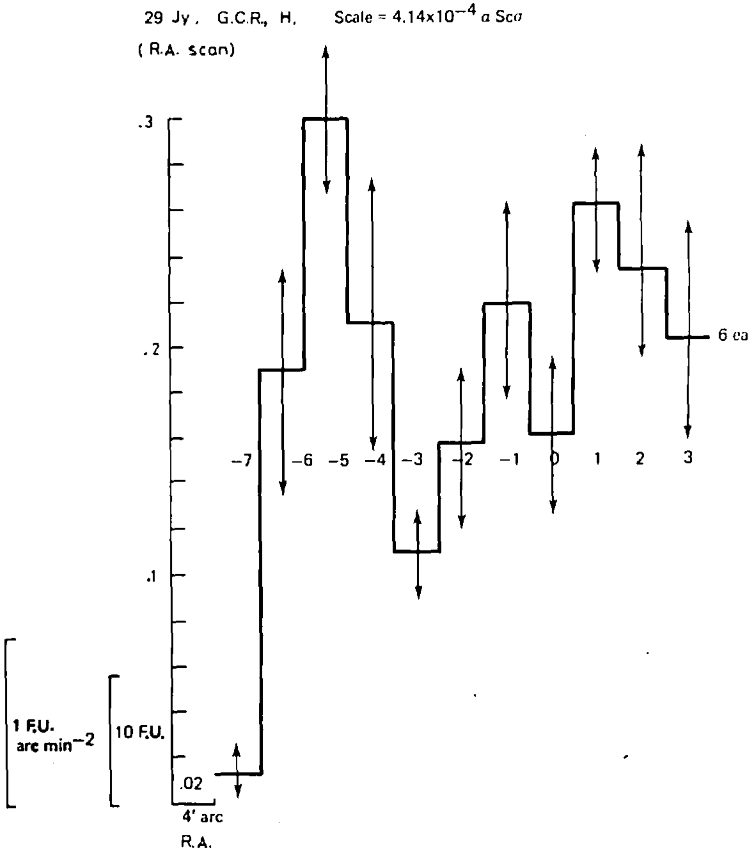

F.9.15b G.C.R., H

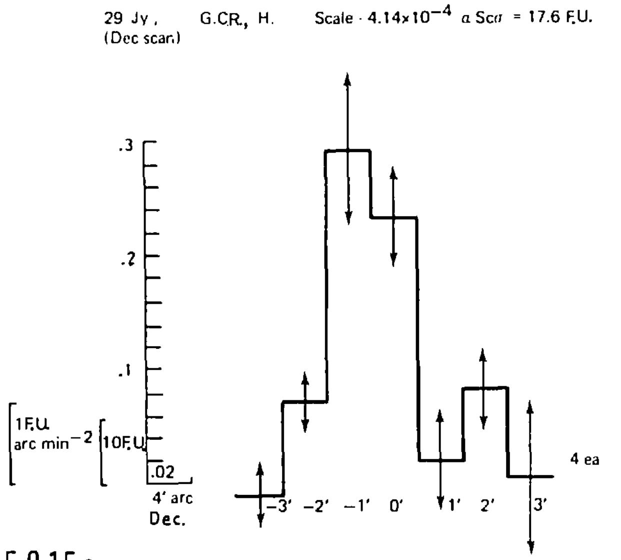

F.9.15c G.C.R., H

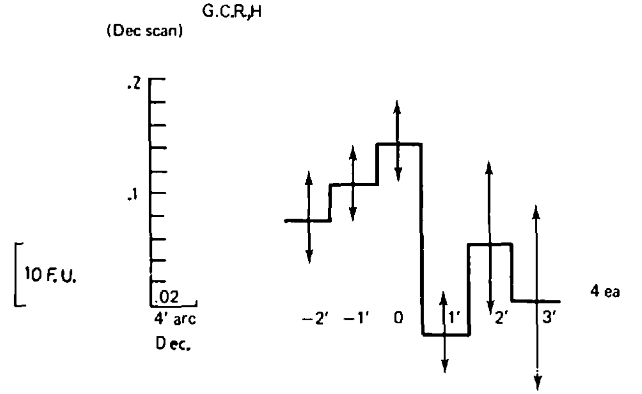

F.9.15d G.C.R., H

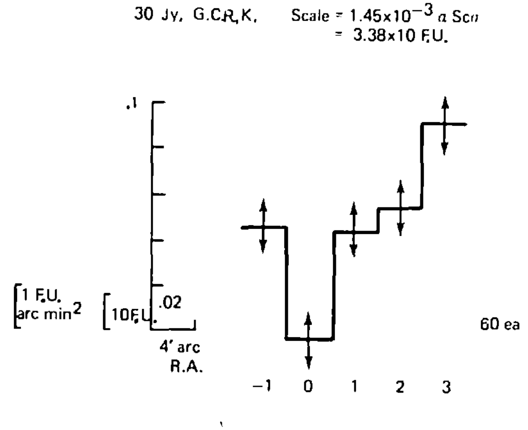

F.9.15e G.C.R., K

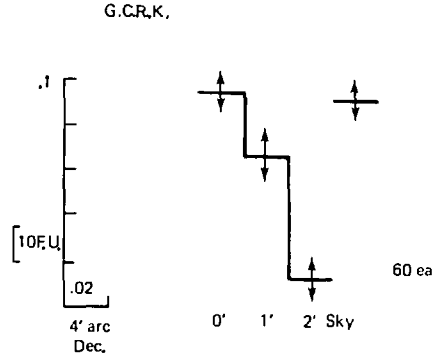

F.9.15f G.C.R., K

9.09 Discussion of the presented data

A glance at the figures F9.05 and F9.15 shows that significant signals were detected from most of the objects observed, but intensity values appear to show some inconsistency, credited in all cases to variable attenuation by thin cloud. Scans in negative, then positive R.A. show a position slip due to the unrepeatability of the telescope location; the increments for all scans are determined by the R.A. position readout.

(a) The galactic centre

Attempts to locate the galactic centre were foiled by the unreliability of the telescope position readouts; many attempts were made by offsetting from X Sag. but it was soon decided that the time would be more profitably spent studying visible objects, of which the brighter nearer globular clusters proved particularly suited to the 4 arcmin field. The milky way does show significant emission (F9.15) but repeatability is not good; presumably the field shown was bordering on the galactic nucleus source. The galactic centre has been well mapped by Becklin, Neugebauer, and Low et al (R9.03, R9.04, R9.05); they have made extensive mappings at various infrared wavelengths and many others have also made observations (R9.06 - R9.11). It had been hoped to observe the infrared continuous extended emission region out further from the nucleus than shown on the Neugebauer map.

Table T9.2 H, K intensities and magnitudes of the objects observed (bracketed H values are inferred where no H magnitude values were found for the reference stars)

Date	Object	NGC No.	Integrated mean, (Pg .) visual	dimn. arcmin.	dist. parsecs.	Spec.	H intensity F.U.	error ±	No. samples per mean	K intensity F.U.	error ±	No. samples per mean	H magnitude	error	No. samples per mean	K magnitude	error	No. samples per mean	B-V	V	V-K	H-K
Globular Clusters																						
31 Jy	M5	5904	(6.69) 6.2	19.9	7.66K	d, F5	10.0	1.0	10	37.2	2.3	20	(5.30)	-.10 +.11	10	3.07	-.07 +.07	20	.72	5.97	2.90	.61
							12.0	3.3	50				(5.10)	-.26 +.35	50							
							[illegible]	[illegible]	[illegible]				[illegible]	-.19 [illegible]	20							
30 Jy	M22	6656	(6.15) 5.9	17.0	3.09K	VII,F6				15.7,8.9	2.5	40				4.01,4.62	-.16 +.19	40	1.00	5.05	1.04	
										10	0.4	40				4.47	-.04 +.04					
1 Ag	M2	7089	(6.94) 6.3	11.7	9.05K	d,F3	52.3	5.5	30	22.9	3.3	33	(3.50)	-.11 +.12	30	3.57	-.15 +.17	33	.68	6.26	2.69	-.07
30 Jy	M15	7078	(6.96) 6.0	12.3	9.51K	d,F3	62	17	23	65	13	17	3.32	-.26 +.35	23	2.45	-.20 +.24	17	.68	6.08	3.63	.87
Open Clusters																						
2 Ag	M23	6494	6.9	25	1.38K	e(o.c.)	8.0,4.5	2.3	10				5.50,6.15	-.27 +.37	10							
2 Ag	M11	6705	6.3	10	1.74K	g(o.c.)	46.3,78.7	1.9	50	14.5,34.5	0.9	50	3.60,2.97	-.03 +.03	50	4.10,3.05	-.03 +.03	50				-.14
							90,44	2.5	50				2.91,3.69	-.03 +.03								
Planetary nebulae																						
30 Jy	M57	6720	9.3neb 14.7*	14 x 1	660	cont*	39.2	11	24	(-8.8)	8.8	20	(3.82)	-.27 +.36	24	> 4.6		20				
	M27	6853	7.6neb 13.4*	8 x 4	300		(5.1)	8.8	25				(6.03)	-1.1 ~	25							
Diffuse nebulae																						
31 Jy	M8	6523	6.8*	1 x 0.6	770	e O5.e*				4.8,4.7	4	10				5.29,4.65	-.41 +.67	10				
										2.6,4.3	4.3	10				5.96,5.42	-.75 ~	10				
										9.8	1.5	30				4.42	-.16 +.18	30				
Galaxies																						
1 Ag	M31	224	4.8	(160x35)		G5	158	10	55	73	7	43	(2.30)	-.07 +.07	55	2.34	-.10 +.11	43	.92	3.69	1.35	-.04

(b) Globular Clusters

Four globular clusters were studied, together with two open clusters, most in both H and K bands, and several were scanned in R.A. M5 shows a particularly large flux in K (F9.05d) and some strange fluctuation in the R.A. scan (F9.05a); this may be explained by the particularly heavy cirrus that interupted observations several times on 31 July. Each step shown is the mean of many samples, as previously mentioned; the error bars shown are the error in the mean for the set, the intervals are in units of 4 arcmins, of R.A.

M22 (F9.06), like M5, shows a clear core in the infrared, but emission extends out as far as that given for visual wavelengths, see table T9.02 and R9.14, R9.15. All the clusters show an infrared excess, but M22 less so than the others.

M2 (F9.07) shows a surprisingly low flux in K; again this may be attributed to intermittent cirrus in the early evening of 1 August; variation in transparency are more noticeable at K and longer wavelengths than at H.

M15 (F9.08), was not studied in much detail, but gives an H excess consistent with those observed for M5 and M2, and also a similarly consistent K excess.

M15 has been well studied at λ 10μ (R9.13), where a strong point source has been detected, and also at λ 2.4μ and λ 4.7μ (R9.12a), together with several other globular clusters. Table T9.2 shows the accepted V & (B-V) magnitude for these objects (ref. R9.14 : C. Alaino, 'Atlas of Globular Clusters', and R9.15 : A Beevar, 'Atlas of the 1950.0 Catalogue) and the H, K, and (V-K) values determined from these observations; however these latter values are critical of the crossing points for the magnitude scale (ref. R9.02, Thomas, Hyland Robinson) and no corrections have been applied for interstellar reddening affects. Despite these reservations, the infrared excesses given as (V-K) are in reasonable agreement with those published by Grasdalen (R9.12a : 'Near infrared magnitudes and V-K colours of 13 globular clusters'); all his objects are small and fairly distant, limited by his 35 arcsec. field aperture. Grasdalen quotes a mean (V-K) of 2.2 for his clusters with a mean E(V-K)/E(B-V) of 2.5; the uncorrected excesses given here tend to be greater, with the exception of M22. The letter of Hansen and Hesser (R9.12b : Nature October 1975), describes λ 2.4 μ and λ 4.7 μ observations of eight globular clusters with a 10 arcsec. aperture, of which several show strong emission from their central 100 arcsec. nuclei; they also find that the observed infrared excesses may be satisfactorily explained by radiation from stellar sources with $T_{eff} > 1000^0K$.

Open clusters M23 (F9.09) and M11 (F9.10) were scanned, both showing a central emission peak with extensive emission further out to the visual limit. In the case of M11, discrepancy between F9.10a and F9.10b is due to the telescope clutch clipping, the agreement otherwise being satisfactory. Note in K, the emission is less centralised (F9.10c), though this may not be significant; both objects show an infrared excess.

(c) Planetary nebulae

Two planetary nebulae were observed, see (F9.11) (F9.13), one of which, M57 (F9.11), the ring nebula, was detected at H but not at K. Planetary nebulae have been detected in the infrared before, including the planetary NGC7027 known to be an infrared source (R9.16), but more usually strongest infrared emission is observed from the condensed types, ref (R9.17, R9.18, R9.19). No reference has been found for the large planetary nebula M57 (NGC6720); the source is most likely to be nebular - degraded radiation from the star, but some nebular infrared lines may be expected beyond λ 3μ (R9.20); it is unlikely that such an object would show up with a much smaller field aperture.

(d) Diffuse nebulae

It is unfortunate that the Orion nebula M42 was not accessible, as this has been the authors' primary concern for previous less successful observing attempts. M8 is a known infrared source (R9.22) and has been studied in several infrared bands; M17 and other compact HII regions are known sources of infrared emission (R9.21, R9.23 - R9.27). Most of the emission in M8 is thought to originate from the star Herschel 36, and the remainder from the nebulosity in the immediate vicinity; in R9.22 the source is quoted at a K magnitude of 6.8 for an 11 arcsec. beam. Observations here (F9.12) were hampered by cloud, and for the 4 arcmin. beam K magnitudes varied between 5.4 and 4.4. for the central emission; some emission was seen beyond this 4 arcmin. centre which must be from the nebulosity; R9.28 discusses expected infrared diffuse-nebular emission.

(e) Galaxy M31

The central 4 arcminutes of the nucleus of M31 gave a particularly strong signal, again showing an infrared excess (F9.14) but as expected less than for the globular clusters; there is less abundance of luminous red giants in such a galactic nucleus than in some globular clusters. The (H-K) value appears negative (may be explained by temperature changes in the detector at the end of a run). Many galaxies have now been detected in the infrared (R9.29 - R9.34).

(f) General discussion

In all cases except for M8 and M57, the infrared emission may be satisfactorily explained as stellar in origin (R9.12a, b) produced by luminous red giants; for M8 and M57 the emission may be degraded from optical wavelengths by the nebulosity.

The results obtained for globular cluster M15 (NGC7078) are in reasonable agreement with those presented by Hansen and Hesser in their letter to Nature (R9.12b). There is considerable scope here for further study of the spatial distribution of this infrared excess in globular clusters, and to the establishment of the relevant infrared extinction coefficients.

9.10 Conclusion: Some possible astronomical applications

The data has verified that the photometer is capable of producing astronomical results, and that it should be possible to carry out specific research programs using the wide-field or wide sky-chopping advantages of the instrument. This is particularly true for globular clusters, which could be more extensively studied with a smaller field while using the large throw of the sky-comparison for a blank sky reference, thus enabling such objects to be mapped more readily than with a more limited throw instrument. Observation of globular clusters in the infrared is of increasing interest (R9.12a, b); some show considerable excess at λ 2.2μ to λ 10μ. The available wide-field lends itself to infrared survey work, possibly for the study of the radio arcs, general emission from the milky way, and extensive nebulosity; the instrument is capable of operation at R to K bands, but would require some modification to cover the K band.

It is most unfortunate that news about comet 1975h (Kobashi-Berger-Milan) did not reach the Tenerife site as this would have been favourably placed for observation at the time the other observations were made. The photometer is especially suited to observation of comets due to the large available field; comet Kotoutek as previously mentioned was observed in H with this photometer on the 20" R.O.E. telescope for a brief moment in between clouds in January 1974, but without record. Coarse mapping of comets near perihelion could be quickly and easily accomplished, on a day-to-day basis if the opportunity arose. (R.9.35)

9.11 Suggested improvements

(a) General optical system

The optical system was found to be very satisfactory, with only a 40 to 30% H or K light radiation loss from all the combined mirror surfaces involved in the sky-comparison system. The final reduction lens, when placed in the cryostat in the absence of the light pipe, gave significantly better throughput and a better field reduction (4.0mm detector field as opposed to 5.0mm field), as determined by the ray traces; this method is only applicable for the F/12.8 beam, and so a larger reduction lens and cryostat window would be required for F/8. The instrumental profile obtained with the system was considered to be rather unsatisfactory as compared with that previously obtained with the light-pipe arrangement; it is therefore suggested that when the instrument is used again for astronomical observations, the final reduction optics should be modified from that shown in F2.19 to that of F2.20. The final objective lens, like a light-pipe, ensures that the detector responds equally to point images in all parts of the original field. In order to maintain the reduction ratio required for the 4.0mm detector, the collimation space would probably have to be increased together with the diameters of the window and field reduction lens; this may present some difficulty and so a compromise lens location may be preferred. The addition of the further objective lens introduces more light loss but this would be offset by a reduction in final objective image and detector size with consequent reduction in detector noise.

The two reference lamps on their turntable were not used; their function is replaced by the artificial star, which has proved to be particularly useful for measurements of signal response, instrumental profile, mirror reflectivities, and alignment. With the exception of the direct access vision eyepiece at the telescope focus, the remaining wide field and offsetting eyepieces were not found practical on the 60" telescope; the turntable eyepieces with their view through the mirror sky comparison or direct system were found very useful. An indicator light system for the various mirror positions would be particularly useful.

(b) Sky-comparison system

The two spherical-mirror principle was considered very satisfactory and adaptable, while the two parallel-mirror system alternative discussed in chapter 5 is considered less satisfactory in its present form due to the more limited field throw. Several improvements are suggested here to increase the repeatability and efficiency of the spherical mirror motion.

The armature displacement readout from the capacitance bridge is not a faithful indication of the mirror position: There is some flexibility in the insulated section of the armature supporting the capacitance plates and wear in the brass bearing (which should be replaced by a steel ball-race thrust bearing); the mirror was observed to overshoot by a significant proportion of its throw; this was noticed from eyepiece V with the artificial star, and was also observed when using a stroboscopic light source.

The mirror-cell linkage was found to be satisfactory but the ball-pivot bearings had to be screwed tight to avoid any slack, which if overdone resulted in noticeable frictional damping on the drive unit armature. The obvious alternative to servo controlling the drive armature is to servo the mirror cell itself; this led to the construction of the second capacitance bridge with a moving vane fixed to the mirror cell armature, see F7.05. This system proved unsatisfactory partially due to the non-linear behaviour of the pivoted bridge vane gap and partially due to bearing slackness; as mentioned, the vane proved useful to increase the air damping.

None-linearities in the servo system and consequent asymmetry in the armature position profile largely result from the non-linear change of capacitance with capacitance-bridge gap-width and possible inequality of the mean gap-widths; this effect may be considerably reduced by increasing the capacitance plate separation. Position drift was also noticed, which was especially bad for the first hour after switching on the servo system; the most likely cause is voltage drift in the rails and consequent offset voltage drift in the capacitance detection output stage; the bridge itself compensates for atmospheric changes. The need for an adjustable offset arises from the bridge rectifier stage. This stage may be replaced by a synchronous rectifier circuit triggered by the carrier frequency waveform; this should improve the stability and the sensitivity of the detection circuits.

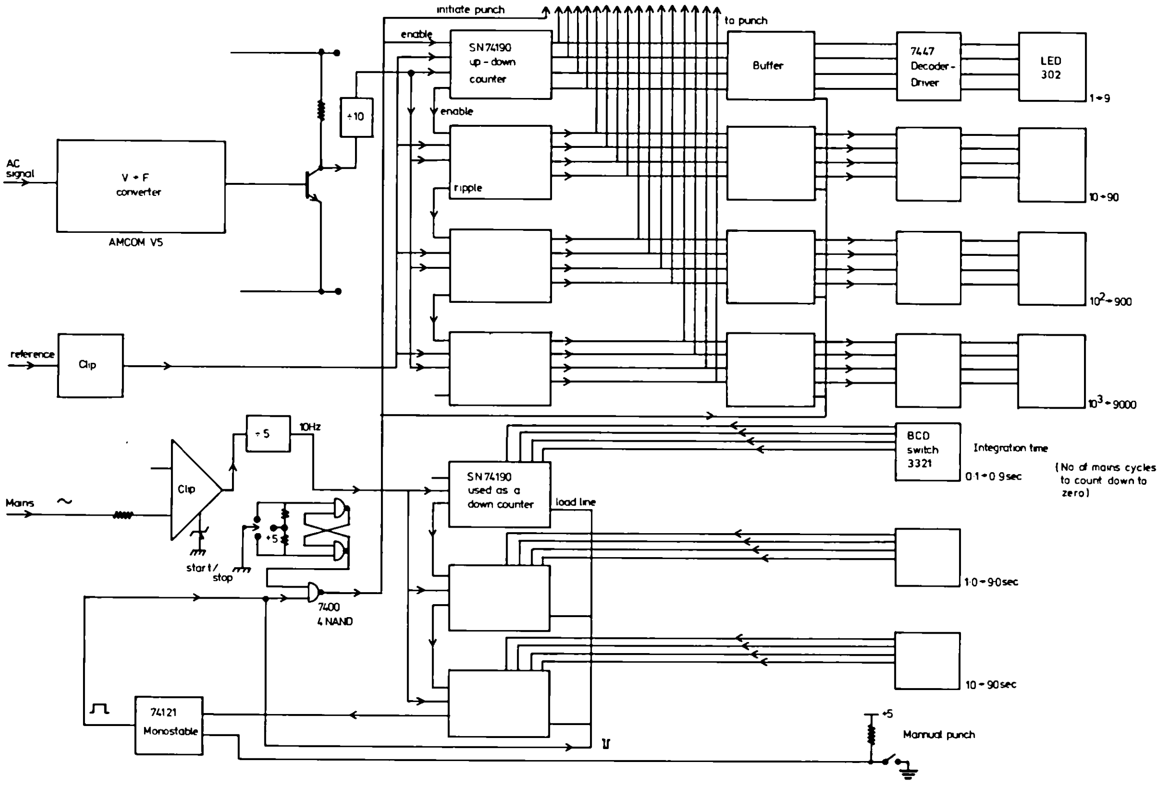

F.9.16 DIGITAL SYNCHRONOUS RECTIFIER CIRCUIT

Another improvement to the servo circuit would be to provide finer amplitude for the reference square-wave, and mirror amplitude, possibly with voltage control operation such that the mirror motion amplitude and position could be operated from a pre-programmed controller. This would allow automatic scanning over the full 50mm scan field for a much smaller field aperture (possibly using a small detector). This facility would allow automatic mapping to be carried out on extended objects such as globular clusters (providing that the field transmission function was allowed for in the data processing).

(c) General electronics

The signal processing electronics could be improved to reduce the signal drift and improve noise rejection and integration times could be made unlimited by performing the synchronous rectification with digital up-down counters after digitising the signal via an A to D converter. A circuit is suggested in F9.16; although in its present form the circuit is probably unsatisfactory, it could be the basis for a much improved signal processor. An analog readout would be necessary as a monitor, while continuous noise readout together with the rectified integrated signal output could be used to trigger the closing gate on the counter. Integration would continue to a preset signal-to-noise; signal strength would then be indicated by the time taken to integrate to a preset value. An alternative would be to allow the 'Nova' computer (if available) to sample and average the signal regularly until a preset standard error in the mean is attained. (This was to be attempted on site but for the untimely failure of the C.A.M.A.C. interfacing boards).

(d) Cryostat improvements

The cryostat is particularly difficult to fill with a coolant such as dry ice and acetone. Dry ice made on site from CO_2 cylinders proved to be more powdery than crushed CO_2 blocks and therefore more easily mixed into a slurry in the cryostat funnel, but the cryostat narrow coolant tube proved a considerable hindrance and should be widened.

The interchangeable detector mounting arrangement and fixed head preamplifier were considered very satisfactory; the relay continued to operate in the cooled environment but was normally kept in the off position so as not to contribute to the heat gain. The thermal hold time was about 4 hours and could be improved (it was about 10 hours when the cryostat was used at R.O.E. in January 1974 at a room temperature of $0^{o}C$). The cryostat developed a small leak while on site but otherwise the vacuum seals were found satisfactory, and no atmospheric condensation on the cryostat window was ever observed.

Replacement of the detector bias network by a virtual earth detector arrangement would eliminate the bias noise and capacitance effects, and so would be a well worthwhile improvement.

References for Chapter 9

Filter radiometry

R9.01 Menat, M. 'Applied filter radiometry'. Infrared P. (1971), 11, 133-146.

Calibration stars

R9.02 Thomas, J.A. Hyland, A.R., Robinson, G. 'Southern infrared standards and absolute calibration of infrared photometery.' Mon. Not. R. astr. Soc. (1973), 165, 201-211

Galactic Centre Infrared emission

R9.03 Becklin, E.E., Neugebauer, G. 'High resolution maps of the galactic centre that 2.2μ and 10μ'. Ap.J. (1975), 200, L71- L74

R9.04 Becklin, E.E., Neugebauer, G. '1.65μ - 19.5μ observations of the galactic centre'. Ap. J. (1969), 157, 63

R9.05 Rieke, G.H., Low, F.J. 'Infrared maps of the galactic nucleus' Ap. J. (1973), 184, 415-425.

R9.06 Sutton, E., Becklin, E.E., Neugebauer, G. '34μ observations of the Eta Carina' G 333.6 - 0.2 and the galactic centre'. Ap.J. (1974), 190, L69 - L70

R9.07 Spinrad, M., Liebert, J., Smith, M.E., Schweizer, F., Kuhi, L. 'The detection of the galactic nucleus at one micron'. Ap.J. (1971), 165, 17-21

R9.08 Low, F.J., Kleinmann, D.E., Forbes, F.F., Aumann H.M. 'The infrared spectrum, diameter, and polarization of the galactic nucleus'. Ap.J. (1969), 157, L97 - L101

R9.09 Becklin, E.E., Neugebauer, G. '1.65μ to 2.2μ observation of the galactic centre'. Ap.J. (1969), 157, L31 - L36

R9.10 Rieke, G.H., Harper, D.A., Low, F.J., Armstron, K.R. '350μ observations of sources in HII regions, the galactic centre, and NGC 253. Ap.J. (1973), 183, L67 - L71

R9.11 Lequeux, J. 'The nature of the far-infrared radiation from the galactic centre'. Ap.J. (1970), 159, 459-462.

Globular Clusters - infrared emission

R9.12a Grasdalen, G.L. 'Near-infrared magnitudes and (V-K) colours of globular clusters.' Astron. J. (1974), 79, 10, 1047-1051

R9.12b Hansen, O.L., Hesser, J.E. 'Observations of eight globular clusters at 2.3 and $4.7 \mu m$'. Nature, 257 (1975), 568-569

R9.13 MacGregor, A.D., Phillips, J.P., Selby, M.J. 'The detection of M15 at 10.2μ.' Mon. Not. R. astr. Soc. (1973), 164, 31-33

R9.14 Alairo, C. 'Atlas of Globular Clusters'.

R9.15 Becvar, A. 'Atlas of the heavens catalogue 1950.0.'

Planetary nebulae - infrared emission

R9.16 Gillett, F.C., Low, F.J., Stein, W.A. 'Infrared observations of the planetary nebula NGC 7027'. Ap.J. (1967), 149, L97-L100

R9.17 Gillett, F.C., Stein, W.A. 'Infrared studies of the galactic nebulae NGC 6523, NGC 6572, BD 30^{0} 3639'. Astron. J. (1970), 159, 817-819

R9.18 Gillett, F.C., Knacke, R.F., Stein, W.A. 'Infrared studies of galactic nebulae II, The compact nebulae IC 4997, VV8, F.G. Sag.'. Ap.J. (1971), 163, L57-L59

R9.19 Neugebauer, G., Garmire, G. 'Infrared observations of nebula K3-50'. Ap. J. (1970), 161, L91-L94

R9.20a Flower, D.R. 'On the infrared line spectra of planetary nebulae'. Mon. Not. R. astr. Soc. (1970), 147, 245-252

Diffuse nebulae, HII regions. Infrared emissions

R9.21 Kleinmann, D.E., Wright, E.L. 'A new Infrared source in M17'. Ap.J. (1973), 185, L131-L133

R9.22 Woolf, N.J., Stein, W.A., Gillett, F.C., Merrill, K.M., Becklin, E.E., Neugebauer, G. 'The infrared sources in M8'. Ap.J. (1973), 179, L111-L115

R9.23 Wynn-Williams, C.G., Becklin, E.E., Neugebauer, G. 'Infrared studies of HII regions and OH sources'. Ap.J. (1974), 187, 473-485

R9.24a Becklin, E.E., Frogel, J.A., Kleinmann, D.E., Neugebauer, G. Perssan, S.E., Wynn-Williams, C.G. 'Infrared emission from the southern HII region H2-3'. Ap.J. (1974), 187, 473-485

R9.25 Becklin, E.E., Frogel, J.A., Neugebauer, G., Perssan, S.E., Wynn-Williams, C.G. 'The HII region G333.6-0.2, a very powerful 1-20μ source'. Ap.J. (1973), 182, L125-L129

R9.26 Gillett, F.C., Farrest, W.J., Merrill, M., Capps, R.W., Saifer, B.T. 'The 8-12μ spectra of compact HII regions.' Ap.J. (1975), 200, 609-620

R9.27 Gillett, F.C., Stein, W.A. 'Infrared studies of galactic nebulae II, B Stars associated with the nebulosity'. Ap.J. (1971), 161, 77-82

R9.28 Osterbrock, D.E. 'Expected infrared spectra of gaseous nebulae'. Ph.Tr. R. Soc. A. (1969) 1150, 246, 241

Other galaxies - infrared sources

R9.29 Glass, I.S. 'The J, H, K, L colours of galaxies'. Mon. Not. R. astr. Soc. (1973), 164, 155-168

R9.30 Frogel, J.A., Person, S.E., Aaronson, M, Becklin, E.E., Matthews, K., Neugebauer, G. 'The [V-2.2μ] colours of elliptical galaxies'. Ap.J. (1975), 200, L23-L126

R9.31 Johnson, H.L. 'Infrared photometry of galaxies'. Ap.J. (1965), 143, 187-191

R9.32 Rieke, G.H., Low, F.J. 'The infrared spectrum of NGC 1068'. Ap.J. (1975), 199, L13-L17

R9.33 Becklin, E.E., Frogel, J.A., Kleinmann, D.E., Neugebauer, G. Ney, E.P., Strecker, D.W. 'Infrared observations of the core of centaurus A NGC 5128'. Ap.J. (1971), 170, L15-19

R9.34 Barbridge, G.R., Stein, W.A. 'Cosmic sources of infrared radiation'. Ap.J. (1970), 160, 573-593

Supplement list

R9.24b Frogel, J.A., Perssan, S.E. 'Compact infrared sources associated with southern HII regions'. Ap.J. (1974), 192, 351-368

R9.20b Cohen, M., Barlow, M.J. 'An infrared photometric survey of planetary nebulae'. Ap.J. (1974), 193, 401-418.

Comets

R9.35 Ney, E.P. 'Infrared observations of comet Kohoutek near perihelion'. Ap.J. (1974), 189, L141-L143.

APPENDIX TO CHAPTER 8

8. Determination of the signal-to-noise expression for the PbS detector and bias network.

Contents:

DETERMINATION OF THE SIGNAL-TO-NOISE EXPRESSION FOR THE PbS DETECTOR AND BIAS NETWORK

A8.01 Introduction

In this appendix a semi-empirical expression for the signal-to-noise of a PbS detector and bias network is obtained, including all the noise sources in the network. Signal response characteristics are developed from simple theory, while the noise characteristics are based on a combination of this theory and careful measurements. Most of the early noise measurements were made with a dummy cell - (a wire wound resistor) with the usual detector bias network, at room temperature. This allowed more flexibility, and as was later shown, a real detector (the only one available up to the time of the observations in Tenerife) behaves similarly. Measurements made with a cooled detector were more restricted, but as is shown, the data points agreed well with the derived characteristics (see main chapter 8).

A8.02 Detector responsivity relations

A PbS detector is a purely photo-electric device, and not a bolometer; for the purpose of the following argument, it is sufficient to regard it as a two state system, with a lower non-conductive, and an upper conductive state, neither of which is normally saturated.

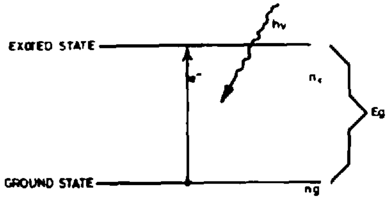

F.8.01 ENERGY STATE DIAGRAM FOR A Pbs DETECTOR

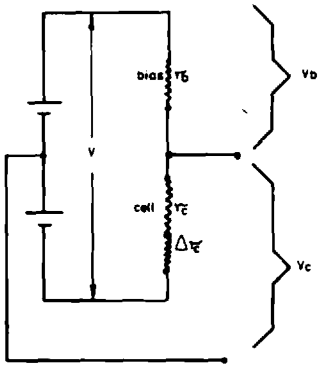

F.8.0 2 a DETECTOR BIAS CIRCUIT

DETECTOR SIGNAL SOURCE

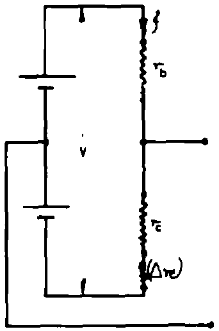

F.8.02a′ BASIC BIAS CIRCUIT WITHOUT OUTPUT LOAD

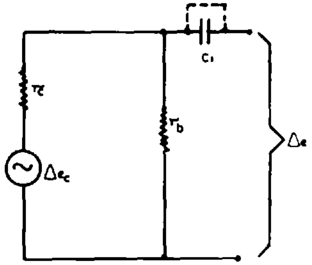

F.8.02 b AC EQUIVILENT CIRCUIT

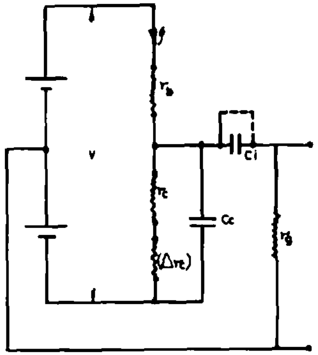

BASIC CIRCUIT MODIFIED BY OUTPUT LOAD

F.8.0 3 a

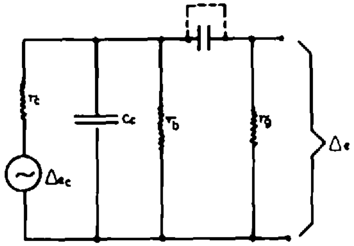

AC EQUIVILENT CIRCUIT

F.8.03 b

DETECTOR SIGNAL ATTENUATION

Detector responsivity

This is a well established relation (R8.03 p667) but a simple derivation is given here (see figure F8.01).

r_c = dctector resistance

n_g = no. of electrons in ground state

n_c = no. of electrons in conduction state

Δn_c = increase in no. of electrons in conduction state produced by a change in energy.

Δr_c = is the change in detector resistance produced by Δn_c.

From simple probability theory, the probable change of no. of sites in the upper state is proportional to the no. of lower filled sites and the no. of vacant upper state sites.

$$\frac{\Delta n_c}{n} \propto \frac{n_g}{n} \frac{(n - n_c)}{n} = \frac{n_g^2}{n^2} \qquad \text{E8.01}$$

where $(n - n_c)$ = no. of vacant conduction sites.

$$\frac{\Delta r_c}{r_c} = \frac{\Delta n_c}{n_c} \propto \frac{n_g^2}{n_c} \propto \frac{n^2 + n_c^2 - 2\,n\,n_c}{n_c}$$

$$\propto \frac{n^2 + n_c^2}{n_c} - 2n$$

$$\propto \frac{n^2 + n_c^2}{n_c} \qquad \text{E8.02}$$

Detector is not near saturation,

then $n_c < n$, $\therefore$ $n_c^{\,2} \ll n^2$

so $$\frac{\Delta r_c}{r_c} \propto \frac{n^2}{n_c} \propto \frac{1}{n_c}$$ E8.03

But r_c = cell resistance $\propto$ ${}^1/$conductivity

i.e. $r_c \propto {}^1/n_c$

$$\Rightarrow \underline{\underline{\frac{\Delta r_c}{r_c} \propto r_c, \quad \frac{\Delta r_c}{r_c} = K r_c}}$$ E8.04

Signal $\Delta e = \Delta r_c I_c$ where $I_c = {}^{V_c}/_{r_c}$ (I_c = cell bias current
V_c = cell bias voltage)

$$\Rightarrow \Delta e = \frac{\Delta r_c}{r_c} V_c \propto r_c . V_c$$

So $\underline{\underline{\Delta e = K r_c V_c}}$ (Then responsivity $\propto r_c$, see R8.03) E8.05

Now $r_c \propto \frac{1}{n_c}$ and $n_c \propto e^{-E_g/kT}$, $\Rightarrow n_{cT} \doteq n_{co} e^{-E_g/kT}$., (where

$$E_g = h\nu_p = \frac{hc}{\lambda_p}$$

So $\Delta e \propto r_c V$ and $r_{cT} = r_{co} e^{E_g/kT}$

Then $$\underline{\underline{r_{cT_2}/r_{cT_1} = e\left\{\frac{Eg}{k}\left(\frac{1}{T_2} - \frac{1}{T_1}\right)\right\}}}$$ E8.06

A8.03 Effect of bias on signal

see figure F8.02

I = bias current through cell

r_b = bias resistance

V = total bias voltage

Δr_c = a small change in r_c produced by radiation

A, $\Delta r_c = 0$

$$I_c = \frac{V}{r_b + r_c}, \quad V_c = r_c I_c = \frac{V r_c}{r_b + r_c} \qquad \text{E8.07}$$

B, $r_c \neq 0$

$$I_c^* = \frac{V}{r_b + r_c + \Delta r}, \quad V_c^* = I_c^* (r_c + \Delta r_c) =$$

$$\frac{V (r_c + \Delta r_c)}{r_b + r_c + \Delta r_c} \qquad \text{E8.08}$$

Let Δe = voltage change across r_b from resistance change Δr_c,

Then

$$\frac{\Delta e}{V} = \frac{V_c^* - V_c}{V} = \frac{r_c + \Delta r_c}{r_b + r_c + \Delta r} - \frac{r_c}{r_b + r_c}$$

$$= \frac{r_b r_c + r_c^2 + r_b \Delta r_c + r_c \Delta r_c - r_b r_c - r_c^2 - r_c \Delta r_c}{(r_b + r_c + \Delta r_c)(r_b + r_c)}$$

$$= \frac{r_b \quad \Delta r_c}{(r_b + r_c \quad r)(r_b + r_c)} \qquad \text{E8.09}$$

let $r = r_b + r_c$

$$\frac{\Delta e}{V} = \frac{r_b \Delta r_c}{r^2 (1 + \frac{\Delta r_c}{r})} = \frac{r_b \ \Delta r_c}{r^2} (1 + \frac{\Delta r_c}{r})^{-1} \qquad \text{E8.10}$$

$$\simeq \frac{r_b}{r^2} \Delta r_c \quad (1 - \frac{\Delta r_c}{r} + \cdots \ )$$

but $\frac{\Delta r_c}{r} \ll 1$

Hence $$\frac{\Delta e}{V} = \frac{r_b}{r^2} \Delta r_c = \frac{r_b r_c}{(r_b + r_c)^2} \frac{\Delta r_c}{r_c} ,$$

Then $$\underline{\Delta e} = V \frac{r_b r_c}{(r_b + r_c)^2} K r_c , = V_c K r_c \frac{r_b}{r_b + r_c} \qquad \text{E8.11a}$$

(see equation (9) of R8.03 p667)

This takes a maximum when $r_b = r_c$, then

$$\underline{\Delta \hat{e}} = \frac{V K r_c}{4} \qquad \text{E8. 11b}$$

A8.04 The effect of cell capacitance and gate load on signal

(see figures F8.02, F8.03)

c_c = cell capacitance

c_i = coupling capacitance

r_g = F.E.T. gate bias resistance

Δe_c = cell signal voltage

Δe = output signal voltage

From E8.11, $\Delta e = \dfrac{Kr_c V_c r_b}{r_b + r_c}$

and $\Delta e = \dfrac{\Delta e_c \, r_b}{r_b + r_c}$

$$\underline{\Delta e_c = Kr_c V_c} \qquad \text{E8.12}$$

The D.C. conditions of bias are the same in modified case

but now r_b becomes $r_b//r_g//C_c$ where // means'in paralel circuit with'

and r becomes $r_c + r_b//r_g//C_c$

Then r_b becomes $\dfrac{r_b r_g/j\omega c}{r_b r_g + \dfrac{r_g}{j\omega c} + \dfrac{r_b}{j\omega c}} = \dfrac{r_b r_g}{r_g + r_b \, j\,\omega\, c_c + (r_b + r_g)}$ E8.13

$$\text{Then } \Delta e = \frac{Kr_c V_c \dfrac{r_b r_g}{r_g - r_b \, j\omega c_c + r_b + r_g}}{\left\{ \dfrac{r_b r_g}{r_c + r_g r_b j \; c_c + r_b + r_b} \right\}}$$

$$= \frac{K\ r_c\ V_c}{1 + r_c(j\ \omega\ + \frac{1}{r_b} + \frac{1}{r_g})}$$

$$= K\ r_c\ V\ \frac{r_c}{(r_c + r_b)(1 + r_c(j\omega C_c + \frac{1}{r_b} + \frac{1}{r_g}))}$$

$$= \frac{K\, r_c\ \frac{r_c}{r_b}}{(1 + \frac{r_c}{r_b})\ (1 + j\,\omega\, r_c c_c + \frac{r_c}{r_b} + \frac{r_c}{r_g})} \qquad E8.14$$

Define parameters:

$$\beta \equiv \frac{r_c}{r_b}, \quad \gamma \equiv \frac{r_c}{r_g}, \quad \delta \equiv \omega\, r_c c_c$$

$$\delta = \omega\ \tau_c$$

where ω = signal modulation frequency
and τ_c = detector time constant

Then
from E8.14
$$\Delta e = \frac{K\ \ r_c\ \ V\beta}{(1+\beta)(1+\beta+\gamma+j\,\delta)} = K\ \frac{r_c V\beta}{(1+\beta)^2}\,(1 + \frac{\gamma + j\,\delta}{1+\beta})^{-1}$$

$$|\Delta e| = K\, r_c\ \frac{V\beta}{(1+\beta)}\ ((1+\beta)^2 + \gamma^2 + 2\,\gamma\,(1+\beta) + \delta^2)^{-\frac{1}{2}}$$

$$|\Delta\ e| = K r_c V\ \frac{\beta}{(1+\beta)^2}\ \left\{1 + \frac{2\,\gamma}{1+\beta} + \frac{\gamma^2 + \delta^2}{(1+\beta)^2}\right\}^{-\frac{1}{2}} \qquad E8.15$$

But if $\delta = 0$

$$\Delta\ e = K\, r_c\ V \frac{\beta}{(1+\beta)^2}\ \ (1 + \frac{\gamma}{1+\beta})^{-1} \qquad E8.16$$

Approximations to signal function

$$\alpha \equiv \frac{r_c}{r_c + r_b}, \quad \beta \equiv \frac{r_c}{r_b}, \gamma \equiv \frac{r_c}{r_g}, \varsigma \equiv \omega r_c c_c$$

From E8.15

$$\left|\frac{\Delta e}{KV}\right| = \frac{r_c \beta}{(1+\beta)^2} \left\{ 1 + \frac{2\gamma}{1+\beta} + \frac{\gamma^2 + \varsigma^2}{(1+\beta)^2} \right\}^{-\frac{1}{2}} \qquad \text{E8.17}$$

$$= \frac{r_c \beta}{(1+\beta)^2} \left\{ 1 - n \frac{\gamma}{1+\beta} - \frac{\gamma^2 + \varsigma^2}{2(1+\beta)^2} + \frac{3}{2} \frac{\gamma^2}{(1+\beta)^2} + \frac{3}{8} \frac{(\gamma^2 + \varsigma^2)^4}{(1+\beta)^4} \right.$$

$$\left. + \frac{3}{2} \frac{\gamma(\gamma^2 + \varsigma^2)}{(1+\beta)^3} + \frac{\sim 0}{(1+\beta)^3} + \cdots \right\}$$

$$= \frac{r_c \beta}{(1+\beta)^2} \left\{ 1 - \frac{\gamma}{1+\beta} + \frac{\gamma^2 - \varsigma^2/2}{(1+\beta)^2} - \cdots \right\} \qquad \text{E8.18}$$

In the absence of ς :

$$\frac{\Delta \epsilon}{KV} = \frac{r_c \beta}{1+\beta} (1 + \beta + \gamma)^{-1}$$

$$= \frac{r_c \beta}{(1+\beta)^2} \left\{ 1 + \frac{\gamma}{1+\beta} \right\}^{-1} \qquad \text{E8.19}$$

$$= \frac{r_c \beta}{(1+\beta)^2} \left\{ 1 - \frac{\gamma}{1+\beta} + \frac{\gamma^2}{(1+\beta)^2} - \frac{\gamma^3}{(1+\beta)^3} + \cdots \right\} \qquad \text{E8.20}$$

if $\gamma \ll 0, \quad \delta \simeq 0$, then $\frac{\Delta e}{KV} \rightarrow \frac{r_c\beta}{(1+\beta)^2} \left(1 - \frac{\gamma}{1+\beta}\right)$

if $\gamma \ll 0, \quad \delta \neq 0$, then $\frac{\Delta e}{KV} \rightarrow \frac{r_c\beta}{(1+\beta)^2} \left(1 - \frac{\gamma}{1+\beta} - \frac{\delta^2}{2(1+\beta)^2}\right)$

The signal voltage function given by equation E8.15 is used in the determination of the noise function, but unlike the signal, the noise has several sources which must be taken separately.

A8.05 Noise sources and a derivation of a noise characteristic expression

Several sources were identified from measurements made on the bias resistor network and preamp: All measurements were made with the R.M.S. calibrated integrating rectifier connected to a synchronous rectifier

(a) Noise from the preamplifier, in excess of the main amplifier noise: This was isolated by shorting the preamplifier input. It is the lower asymptotic value of the noise / . total effective resistance curve F8.04.

$$\varepsilon_0 \simeq 6.3 \times 10^{-2} \quad \mu V/\sqrt{Hz} \pm 10\%$$

This is equivalent to a Johnson noise resistance of $r_{eq.} = \varepsilon_0^{\,2}/4kT\Delta\nu = \varepsilon_0.^2/1.28^2 \times 10^{-20} \simeq 300K$. The constant will take on different values according to environmental temperature of the preamplifier F.E.T.. The F.E.T. was selected for its very low noise properties when cooled.

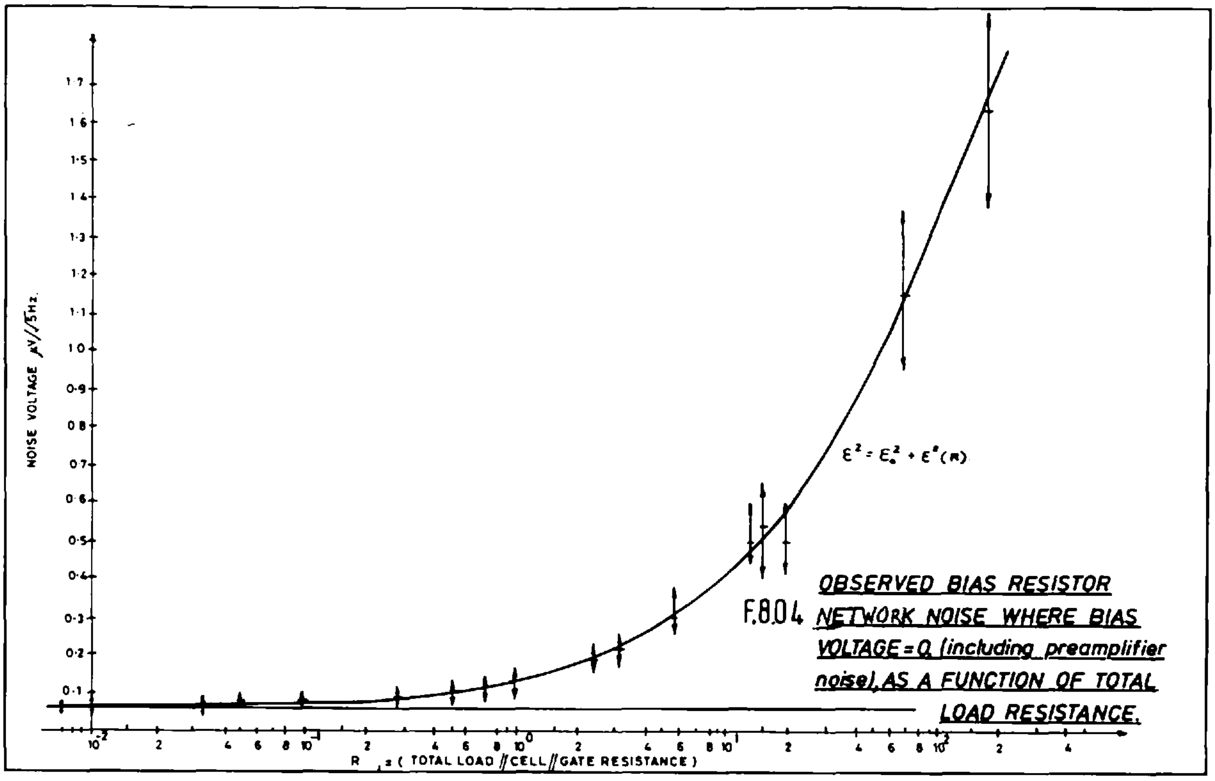

F.8.0.4 *OBSERVED BIAS RESISTOR NETWORK NOISE WHERE BIAS VOLTAGE = 0 (including preamplifier noise), AS A FUNCTION OF TOTAL LOAD RESISTANCE.*

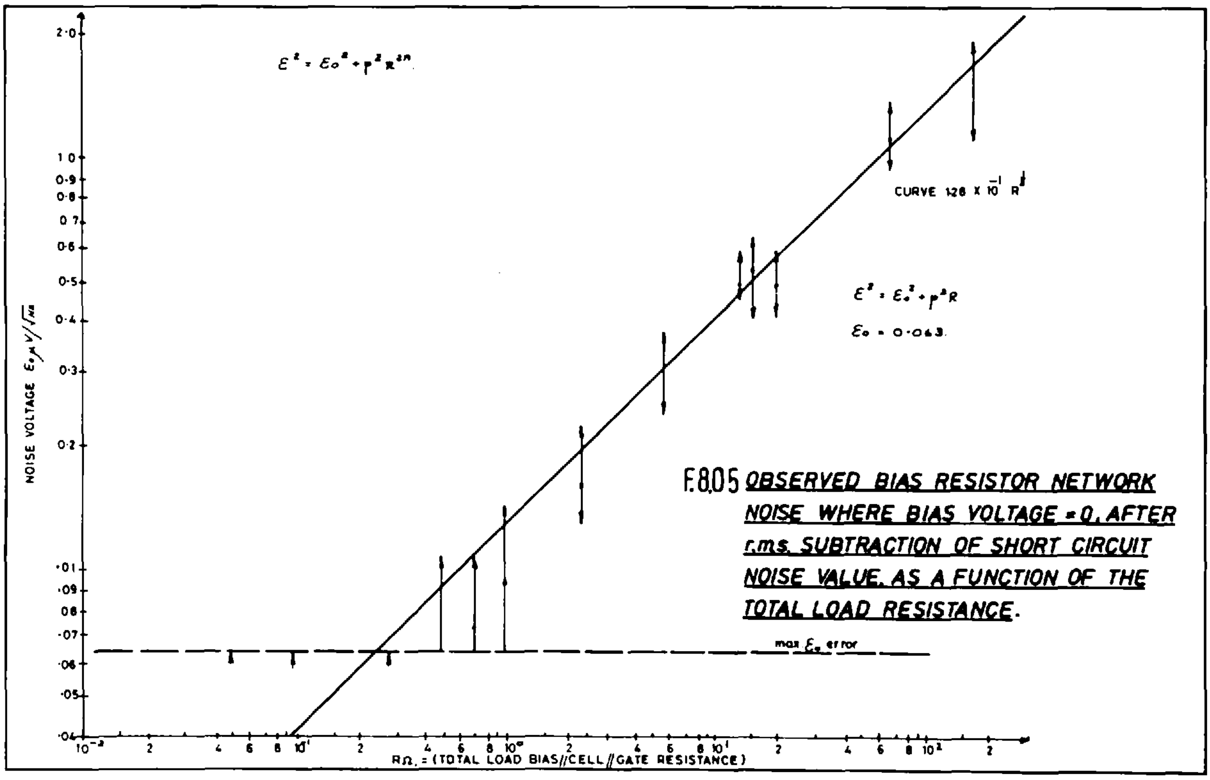

F.8.0.5 *OBSERVED BIAS RESISTOR NETWORK NOISE WHERE BIAS VOLTAGE = 0, AFTER r.m.s. SUBTRACTION OF SHORT CIRCUIT NOISE VALUE, AS A FUNCTION OF THE TOTAL LOAD RESISTANCE.*

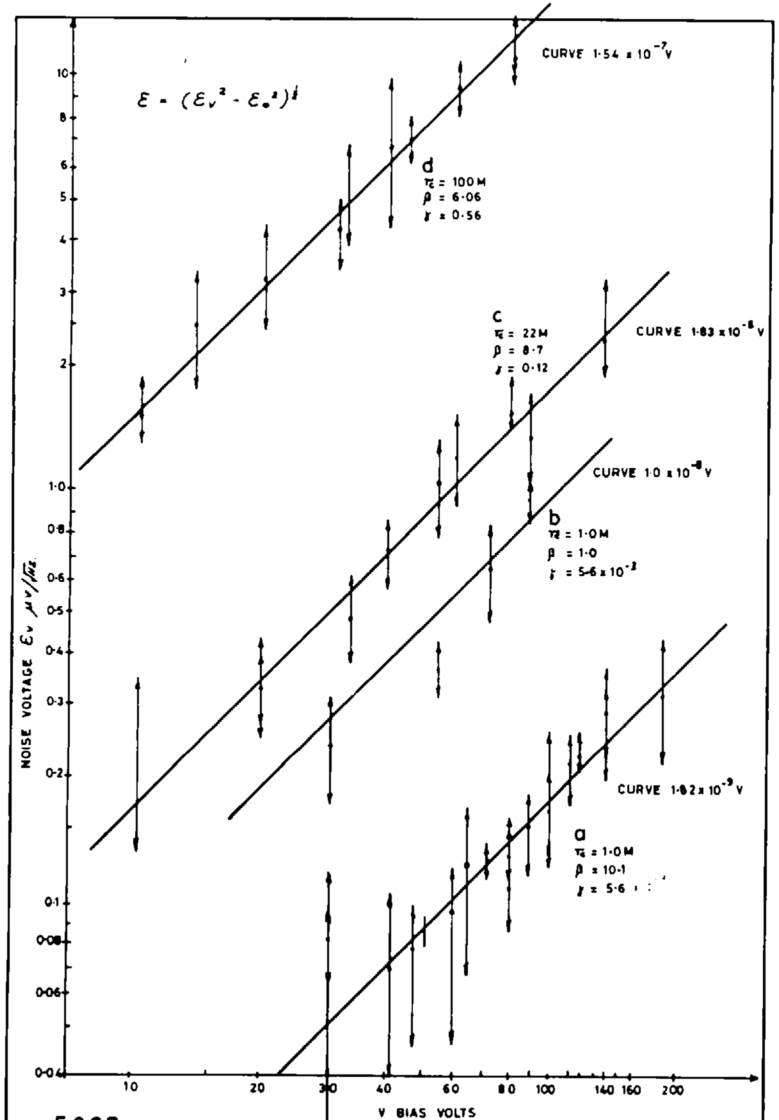

F.807

OBSERVED BIAS RESISTOR NETWORK NOISE AS A FUNCTION OF BIAS VOLTAGE WITH ZERO BIAS NOISE - r.m.s. SUBTRACTED.

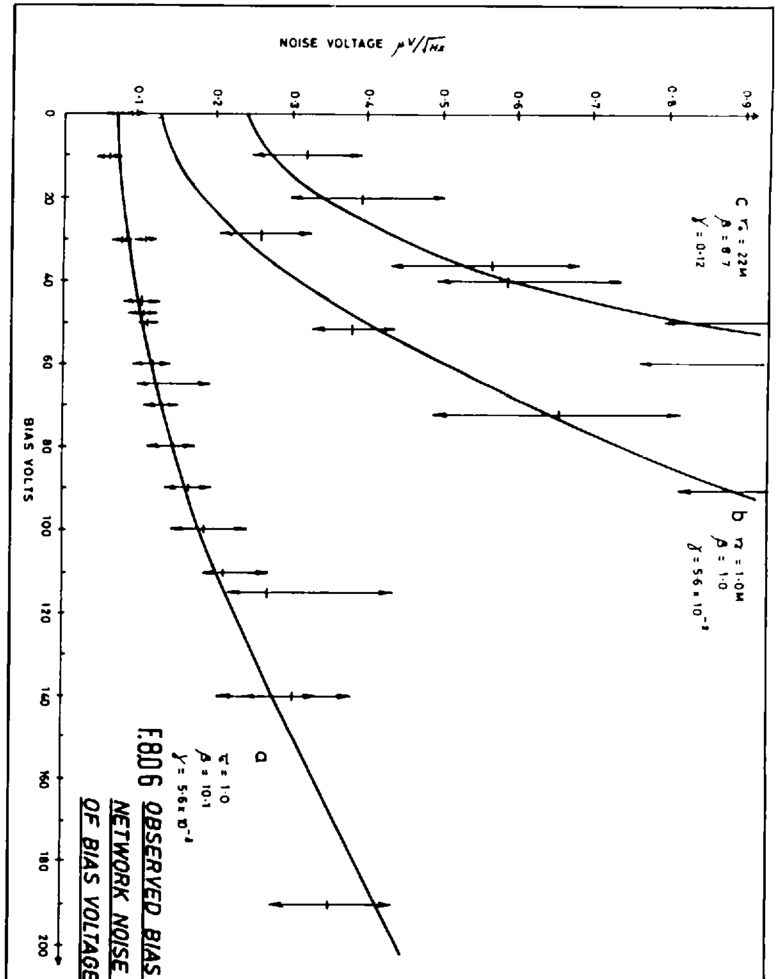

F.806 OBSERVED BIAS RESISTOR NETWORK NOISE AS A FUNCTION OF BIAS VOLTAGE.

(b) Noise dependent on the input load resistance:

This is isolated by subtracting the preamplifier noise power:

$$\mathcal{E}_{(R)}^{2} = \mathcal{E}^{2} - \mathcal{E}_{o}^{2} \qquad \text{E8.21}$$

The function $\mathcal{E}$ (R) was determined from log-log plot F8.05, where:

$$R \equiv r_{//} = r_{c}(1 + \beta + \gamma + j\,\delta)^{-1} \qquad \text{E8.22}$$

It was found that the curve $\mathcal{E}_{(R)} = 1.28 \times 10^{-1}\, R^{\frac{1}{2}}\, \mu v/\sqrt{Hz} \pm 15\%$ E8.23

where R is in MΩ, gave a good fit to the data points.

This function agrees well with that for Johnson resistance noise and no other noise mechanism is required.

(c) Noise dependent on the bias voltage and resistance:

This was isolated by measurement of $\mathcal{E}$ as a function of bias voltage, then subtracting the zero volts noise power. F8.06.

$$\mathcal{E}_{(VR)}^{2} = \mathcal{E}^{2} - \mathcal{E}_{(0R)}^{2} \qquad \text{E8.24}$$

The log-log plots of F8.07 show that the curve $\mathcal{E}_{(VR)} = PV^{n}$ is a good fit to the data points when n = 1.0. This agrees with that expected for current noise (see R8.08 p199). Dependence of this noise component on cell resistance and bias ratio β was determined by curve fitting, the first attempt is shown in F8.10 where for a constant r_c, the noise voltage, bias-dependent component is reduced to a standard 100v bias and scaled by a theoretical β function and plotted against β. Successive attempts guided by the following theoretical argument, enabled the function to be fully determined.

No photon-generated noise was observed when measurements were made with a real detector.

(d) Bias supply noise

This increases as the bias supply attenuation is reduced, i.e. as the bias voltage is increased and the R.C. smoothing time constant is reduced. It is only seen as excess flicker noise at very low frequency, $\sim \frac{1}{20}$ Hz, but contains high harmonics at high bias voltages, $V \sim 150$v. See figure F8.04.

$$V = \frac{ER_c}{R}$$

$$\text{and} \quad \mathcal{E}_o = \frac{\mathcal{E}_s \, R_c // C_c}{(R-R_c) + R_c // C_c} = \frac{\mathcal{E}_s}{1 + (R - R_c)(\frac{1}{R_c} + j\omega C)}$$

$$= \frac{\mathcal{E}_s}{1 + (\frac{R}{R_c} - 1)(1 + j\omega R_c C)} \qquad \text{E8.25}$$

and if $\omega R_c C \gg 1$, and $R \neq R_c$,

$$\text{Then} \quad \mathcal{E}_o = \frac{\mathcal{E}_s}{1 + (\frac{R}{R_c} - 1)^2 \omega^2 R_c^{\,2} C^2)^{\frac{1}{2}}} \triangleq \frac{\mathcal{E}_s}{(\frac{R}{R_c} - 1)\,\omega\, R_c C} \qquad \text{E8.26}$$

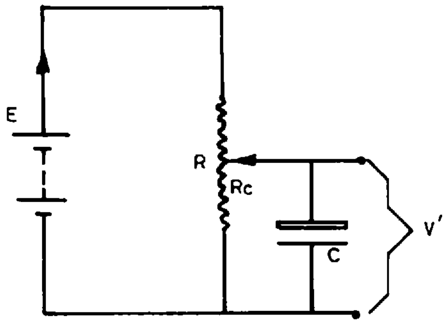

ONE ARM OF THE BIAS VOLTAGE ATTENUATOR CIRCUIT

F.8.08a

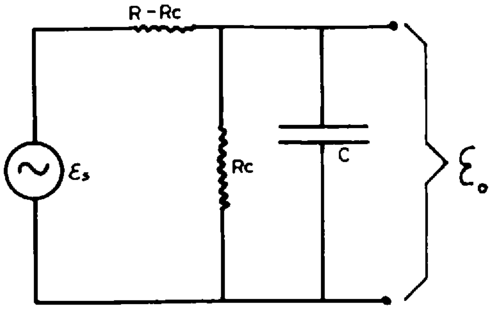

A.C. EQUIVALENT CIRCUIT

F.8.08b

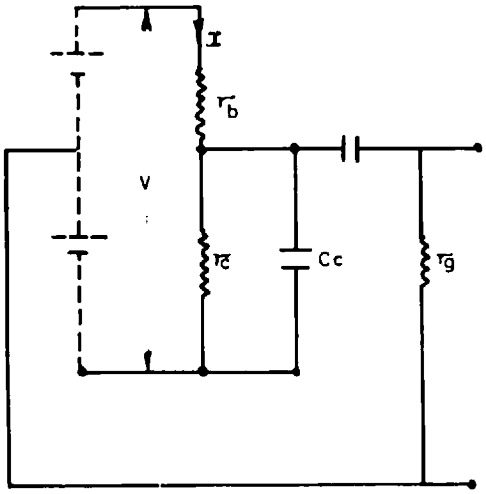

GENERAL DETECTOR BIAS CIRCUIT

F.8.09a

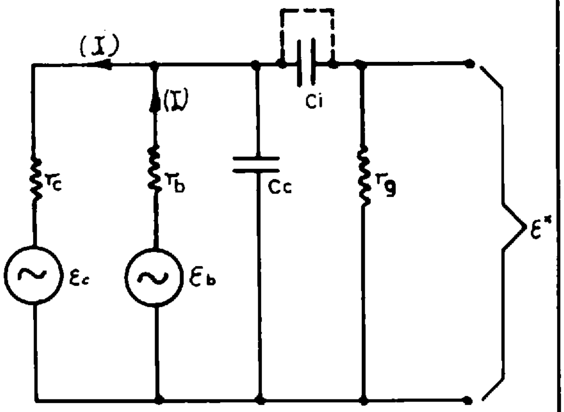

A.C. EQUIVALENT CIRCUIT FOR NOISE

F.8.09b

NOISE SOURCES AND THEIR ATTENUATION

(e) Contact Noise

This is again proportional to the voltage and seen as excess flicker noise, but can be cured by cleaning all contacts.

(f) Synchronous rectifier switch noise

This is on the output of the synchronous rectifier and shows as a rectified ripple (not random), it is only serious above 5kHz, see F6.17, and is not a true noise. These switching spikes were detected by the noise meter only at these higher frequencies.

A8.06 Determination of the bias generated noise function of bias voltage resistance and bias resistance ratio.

Bias current generated noise (see figure F8.09)

$$\mathcal{E}_3 = \mathcal{E}_3(V, R)$$

Unlike resistor noise, we must treat the source resistors separately but the current is common to both so the noise is correlated.

$$V_b = \frac{r_b}{r_b + r_c} V \quad \ldots\ldots \text{ E8.27, and } \quad V_c = \frac{r_c}{r_b + r_c} V \qquad \text{E8.28}$$

$$\mathcal{E}_b^* = \mathcal{E}_b \frac{(r_c//C_c//r_g)}{r_b + (r_c//C_c//r_g)} = \mathcal{E}_b \left\{ 1 + \frac{r_b}{r_c//C_c//r_g} \right\}^{-1} \qquad \text{E8.29}$$

and

$$\mathcal{E}_c^* = \mathcal{E}_c \frac{(r_b//C_c//r_g)}{r_c + (r_b//C_c//r_g)} = \mathcal{E}_c \left\{ 1 + \frac{r_c}{r_b//C_c//r_g} \right\}^{-1} \qquad \text{E8.30}$$

Now $$\frac{r_c}{r_b // c_c // r_g} = \frac{r_c}{r_b} + j\omega c_c r_c + \frac{r_c}{r_g} = \beta + j\delta + \gamma \qquad \text{E8.31}$$

and $$\frac{r_b}{r_c // c_c // r_g} = \frac{r_b}{r_c} + j\omega c_c r_b + \frac{r_b}{r_g} = \frac{1}{\beta} + j\frac{\delta}{\beta} + \frac{\gamma}{\beta} \qquad \text{E8.32}$$

Then $$\mathcal{E}_b^{x} = (1 + \frac{1}{\beta}(1 + \gamma + j\delta)^{-1}\mathcal{E}_b = \beta(\beta + 1 + \gamma + j\delta)^{-1}\mathcal{E}_b$$

$$= \frac{\beta}{1+\beta}\left\{1 + \frac{\gamma + j\delta}{1+\beta}\right\}^{-1}\mathcal{E}_b \qquad \text{E8.33}$$

and $$\mathcal{E}_c = (1 + \beta + \gamma + j\delta)^{-1}\mathcal{E}_c = \frac{1}{1+\beta}\left\{1 + \frac{\gamma + j\delta}{1+\beta}\right\}^{-1} \qquad \text{E8.34}$$

Let the noise function:

$$\mathcal{E}_c = Q\, f(r_c)\, V_c \qquad \text{E8.35}$$

and $$\mathcal{E}_b = Q\, f(r_b)\, V_b \qquad \text{E8.36}$$

(Linearity with V has already been established)

now from E8.28, $$V_c = V\frac{r_c}{r_c + r_b} = \frac{V}{1 + \frac{r_b}{r_c}} = \frac{V}{1 + \frac{1}{\beta}} = \frac{\beta V}{1+\beta} \qquad \text{E8.37}$$

and from E8.27, $$V_b = \frac{V r_b}{r_c + r_b} = \frac{V}{\frac{r_c}{r_b} + 1} = \frac{V}{1+\beta} \qquad \text{E8.38}$$

Then from E8.35, E8.37, $\mathcal{E}_c^* = Q\, f(r_c) V \dfrac{\beta}{(1+\beta)^2} \left(1 + \dfrac{\gamma + j\delta}{1+\beta}\right)^{-1}$ E8.39

and from E8.36, E8.38, $\mathcal{E}_b^* = Q\, f(r_b)\, V \dfrac{\beta}{(1+\beta)^2} \left(1 + \dfrac{\gamma + j\delta}{1+\beta}\right)^{-1}$ E8.40

If the sources are unrelated:

$$|\mathcal{E}|^2 = |\mathcal{E}_c^*|^2 + |\mathcal{E}_b^*|^2 \qquad \text{E8.41}$$

Hence $\mathcal{E} = \dfrac{QV\beta}{(1+\beta)^2} \left\{ 1 + \dfrac{2\gamma}{1+\beta} + \dfrac{\gamma^2 + \delta^2}{(1+\beta)^2} \right\}^{-\frac{1}{2}} \left(f^2(r_b) + f^2(r_c)\right)^{\frac{1}{2}}$ E8.42

and if we assume $f(r_b) = f\left(\dfrac{r_c}{\beta}\right)$, where $f(r_c) = r_c^{\,n}$ E8.43

Then $\mathcal{E} = \dfrac{QV\beta\, r_c^{\,n}}{(1+\beta)^2} \left\{ 1 + \dfrac{2\gamma}{1+\beta} + \dfrac{\gamma^2 + \delta^2}{(1+\beta)^2} \right\}^{-\frac{1}{2}} \left(1 + \dfrac{1}{\beta^{2n}}\right)^{\frac{1}{2}}$ E8.44

If the sources are related:

Then $|\mathcal{E}| = |\mathcal{E}_c^* + \mathcal{E}_b^*|$ E8.45

and $\mathcal{E} = \dfrac{QV\beta}{(1+\beta)^2} \left\{ 1 + \dfrac{2\gamma}{1+\beta} + \dfrac{\gamma^2 + \delta^2}{(1+\beta)^2} \right\}^{-\frac{1}{2}} \left(f(r_c) + f(r_b)\right)$ E8.46

if $f(r_b) = f\left(\dfrac{r_c}{\beta}\right)$, where $f(r_c) = r_c^{\,n}$, E8.43

Then $= \underline{\underline{\dfrac{QV\beta r_c^{\,n}}{(1+\beta)^2}\left\{1+\dfrac{2\gamma}{1+\beta}+\dfrac{\gamma^2+\delta^2}{(1+\beta)^2}\right\}^{-\frac{1}{2}}\left(1+\dfrac{1}{\beta^n}\right)}}$ E8.47

<u>Asymptotic values:</u>

The function:

$$\underline{g(\beta) = \frac{\beta}{(1+\beta)^2}\left(1+\frac{1}{\beta^{2n}}\right)^{\frac{1}{2}}} \qquad \text{E8.48}$$

takes the value

$$g(1) = \frac{\sqrt{2}}{4} = 0.35353, \text{ for all n}$$

and also $g(\frac{1}{2}) = \frac{2}{9}\,(1+2^{2n})^{\frac{1}{2}}$

It also has limits :

$$g(\beta \to 0) \to \frac{1}{\beta} \text{ for all n,} \qquad \text{E8.49}$$

$$g(\beta \to 0) \to \frac{\beta}{\beta^n} = \frac{1}{\beta^{n-1}}, \qquad \text{E8.50}$$

and if n = 1, g (B 0) 1

g (β) has a maximum when:

$$(1+\hat{\beta})^2\left\{\hat{\beta}\,\tfrac{1}{2}\left(1+\frac{1}{\hat{\beta}^{2n}}\right)^{-\frac{1}{2}}\left(\frac{1}{\hat{\beta}^{2n+1}}\right)+\left(1+\frac{1}{\hat{\beta}^{2n}}\right)^{\frac{1}{2}}\right\} =$$

$$\hat{\beta}\left(1+\frac{1}{\hat{\beta}^{2n}}\right)^{\frac{1}{2}} 2\,(1+\hat{\beta}) \qquad \text{E8.51}$$

Then $(1+\hat{\beta})\,(\tfrac{1}{2}\,(1+\frac{1}{\hat{\beta}^{2n}})^{-1}\,\hat{\beta}^{-2n}+1 = 2\hat{\beta}$

$$(1+\hat{\beta})\left\{1+\frac{1}{2(1+\hat{\beta}^{2n})}\right\} = 2\hat{\beta}$$

$$1+\frac{1}{2(1+\hat{\beta}^{2n})} + \hat{\beta} + \frac{\hat{\beta}}{2(1+\hat{\beta}^{2n})} = 2\hat{\beta}$$

$$\underline{\underline{\hat{\beta}-1-\frac{1+\hat{\beta}}{2(1+\hat{\beta}^{2n})} = 0}} \qquad \text{E8.52}$$

When $n \to \infty$, then $\hat{\beta} \to 1$, $\hat{g} \to \frac{\sqrt{2}}{4}$,

when $n \to 0$, then $\hat{\beta} - 1 \to \frac{1+\hat{\beta}}{2(2)} \Rightarrow \frac{3}{4}\hat{\beta} \to \frac{5}{4}$

then $\hat{\beta} \to \frac{5}{3}$, $\hat{g} \to \frac{15}{64}\sqrt{2}$

<u>The function</u>

$$\underline{\underline{h(\beta) = \frac{\beta}{(1+\beta)^2}\left(1+\frac{1}{\beta^n}\right)}} \qquad \text{E8.53}$$

Takes the value $h(1) = \frac{2}{4} = \frac{1}{2}$ for all n

and also $h(\tfrac{1}{2}) = \frac{2}{9}(1+2^n)$

It has limits:

$$h(\beta \to \infty) \to \frac{1}{\beta} \text{ for all n} \qquad \text{E8.54}$$

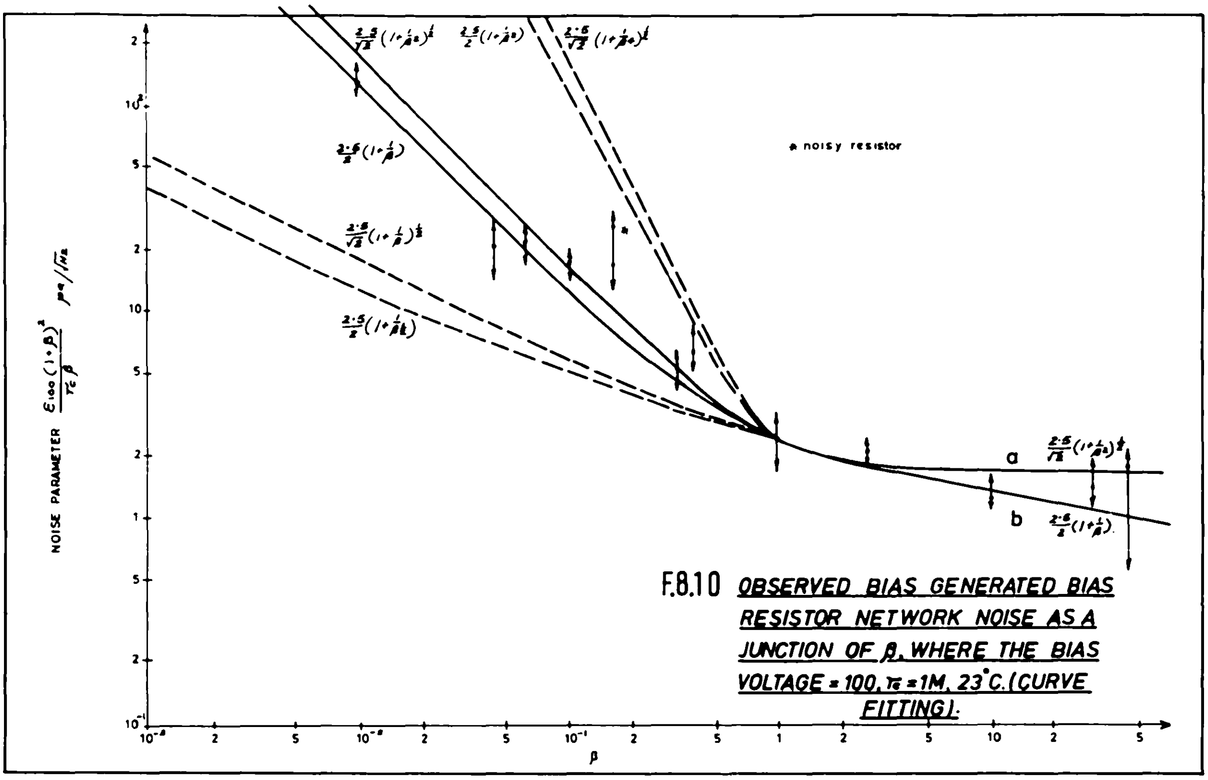

F.8.10 OBSERVED BIAS GENERATED BIAS RESISTOR NETWORK NOISE AS A JUNCTION OF β, WHERE THE BIAS VOLTAGE = 100, r_G = 1M, 23°C. (CURVE FITTING).

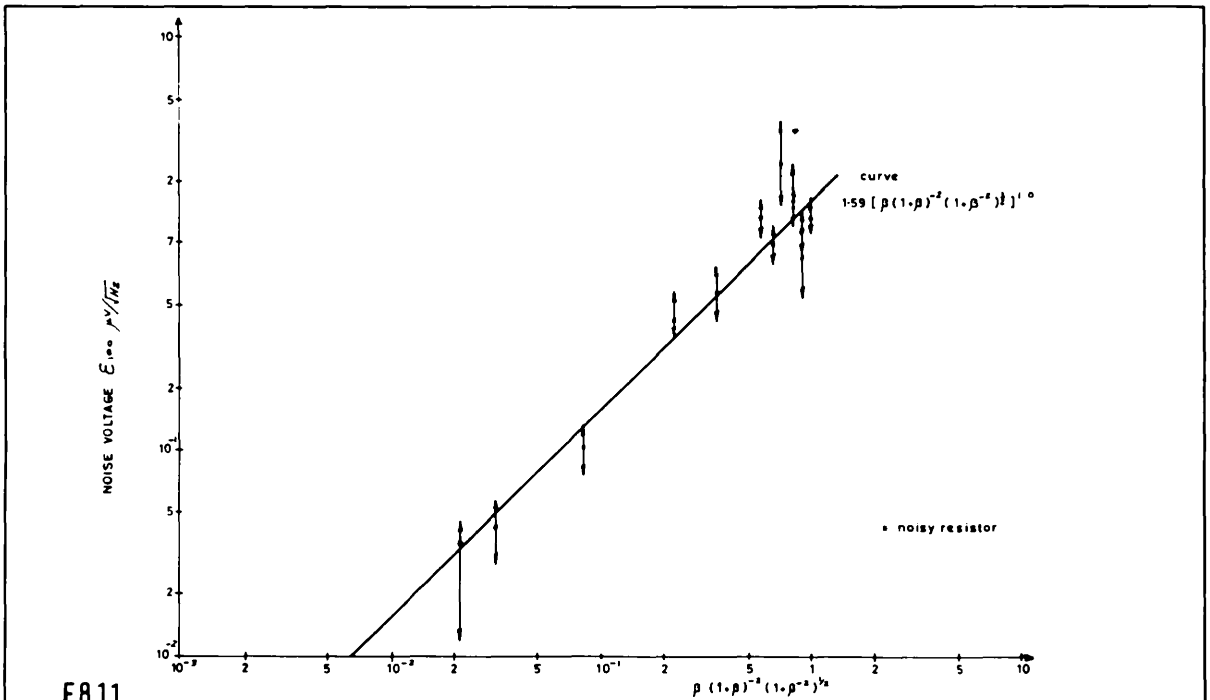

F.8.11
OBSERVED BIAS GENERATED BIAS RESISTOR NETWORK NOISE AS A FUNCTION OF β, WHERE THE BIAS VOLTAGE = 100, 23°C, (r_G = 1M) — (CURVE FITTING).

and $h(\beta \to 0) \to \frac{\beta}{\beta^n} = \frac{1}{\beta^{n-1}}$ ... E8.45, for n = 1 $h(\beta \to 0) \to 1$

$h(\beta)$ has a maximum when:

$$(1+\hat{\beta})^2 \left\{ \hat{\beta}\left(\frac{1}{\hat{\beta}^{n+1}}\right) + \left(1+\frac{1}{\hat{\beta}^n}\right) \right\} = \hat{\beta}\left(1+\frac{1}{\hat{\beta}^n}\right) 2(1+\hat{\beta}) \qquad \text{E8.55}$$

$$(1+\hat{\beta})\frac{1}{\hat{\beta}^n} + (1+\hat{\beta})\left(1+\frac{1}{\hat{\beta}^n}\right) = 2\left(1+\frac{1}{\hat{\beta}^n}\right)$$

$$\frac{(1+\hat{\beta})}{1+\hat{\beta}^n} + 1+\hat{\beta} = 2\hat{\beta}$$

$$\hat{\beta} - 1 - \frac{1+\hat{\beta}}{1+\hat{\beta}^n} = 0 \qquad \text{E8.56}$$

When $n \to \infty$, then $\hat{\beta} \to 1$ and $\hat{h} \to \frac{1}{2}$

when $n \to 0$, then $\hat{\beta} \to 1$, $\hat{h} \to \frac{1}{2}$

In figure F8.10 noise values were measured for various values of β, at constant r_c; the voltage generated component was isolated by subtracting the noise power for zero volts, and then this value was reduced to that for a standard 100v bias, multiplied by the signal reciprocal attenuation $\bar{\beta}$ function and then plotted, (E8.16). In the case considered, both γ' and ζ are negligible, and the departure of the

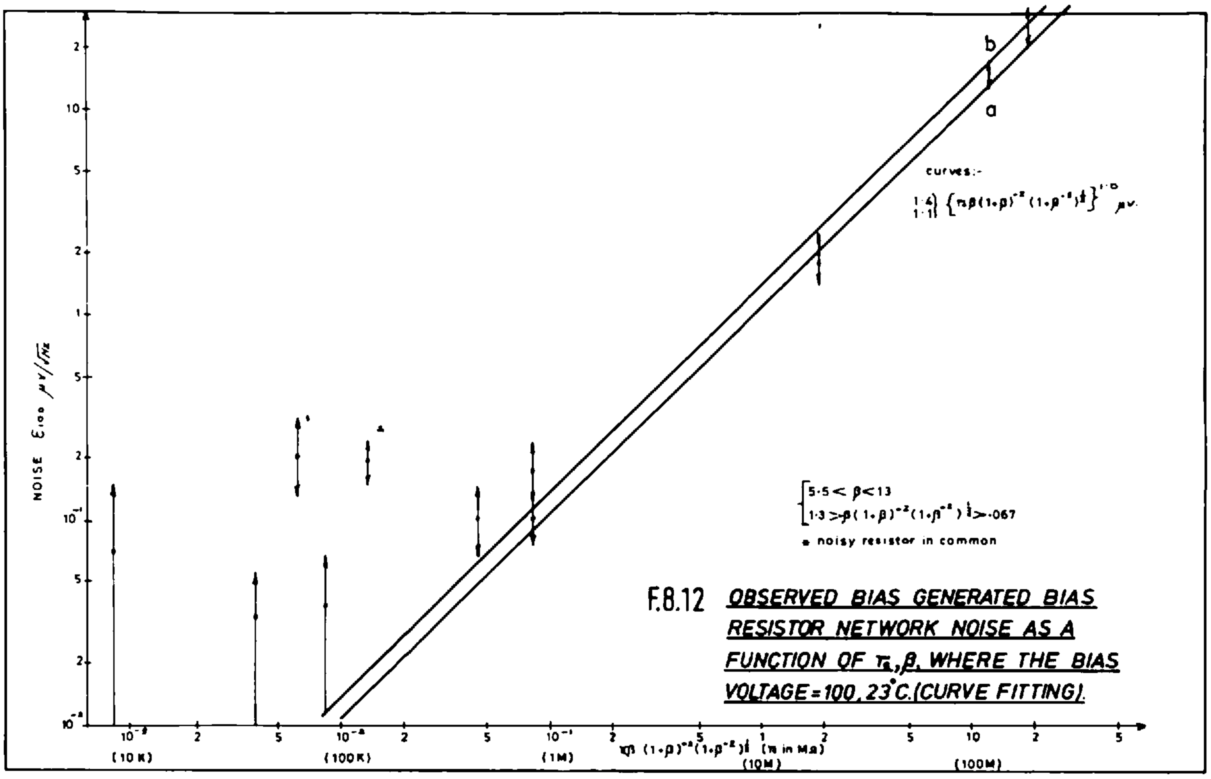

F.8.12 OBSERVED BIAS GENERATED BIAS RESISTOR NETWORK NOISE AS A FUNCTION OF r_s, β, WHERE THE BIAS VOLTAGE=100, 23°C.(CURVE FITTING).

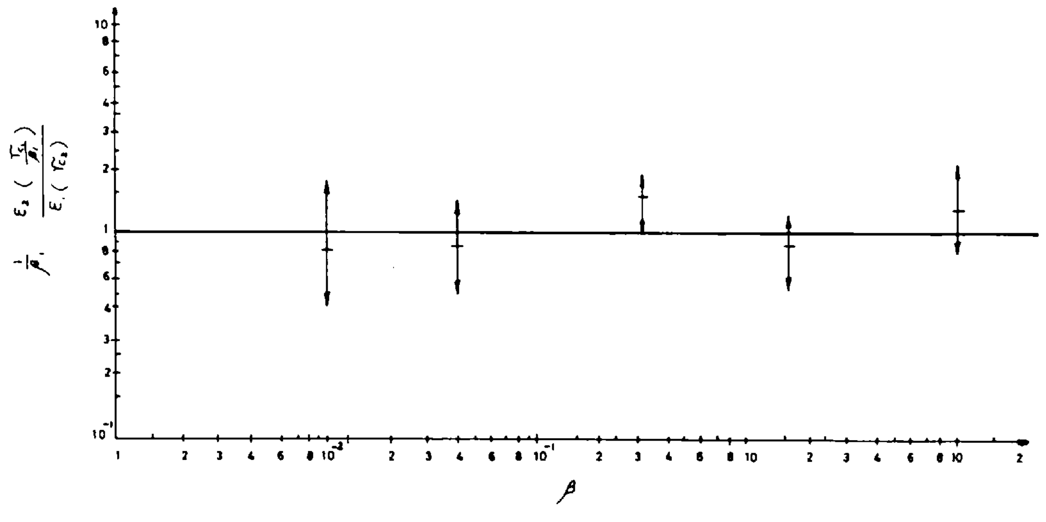

F.8.13 THE OBSERVED RATIO OF BIAS GENERATED BIAS NETWORK NOISE VOLTAGE AT 100V. BIAS FOR RECIPRICAL POINTS OF β (CONSTANCY INDICATES SYMMETRY IN β)

best fit curve from constancy indicates that this noise component does not behave like the signal function; this is as expected from the previous argument. The residual β function ratio is clearly close to $\frac{2.5}{2}(1+\frac{1}{\beta})$ or $\frac{2.5}{\sqrt{2}}(1+\frac{1}{\beta})^{\frac{1}{2}}$, which fits well with equations E8.37 or E8.43 with the value n = 1. This data has been replotted in F8.11, where the reduced bias voltage noise generated component is plotted as a function of $\beta\,(i+\beta)^{-2}\,(1+\beta^{-2})^{\frac{1}{2}}$; note that the fit to the line n = 1.0, is very good. The equations E8.44 and E8.47 predict that the dependence of cell resistance r_c should then also be linear; in figure F8.12 more noise data has been plotted treated as before, but here β was held within restricted limits while r_c was used as the principal variable. The best fit curve again confirms the linear r_c dependence. It may be noticed that the equation E8.44 and E8.47 where n = 1, have the property that a value : $\mathcal{E}(\frac{r_c}{\beta}) = \frac{1}{\beta}\mathcal{E}(r_c)$; this was used to test the data over a wide range of β, as in figure F8.13.

Having established this relationship, it was realised that detector bias-generated noise would not necessarily follow the same behaviour, (the noise-generating mechanism is not necessarily the same).

A More general noise function

Let us consider a more general noise function to replace E8.44 and E8.47.

Let $\mathcal{E}_c' \equiv$ cell noise $= P\, I_c^{\,m}\, r_c^{\,n} \equiv r_c\, i_c$ E8.57

where $I = V/r_c + r_b$

Then the voltage noise generated at the cell

$$= P \left\{ \frac{V}{r_c + r_b} \right\}^m r_c^{\,n} \tag{E8.58}$$

at the gate of the F.E.T. :-

$$\frac{\mathcal{E}}{\left(1 + \frac{\gamma + J\delta}{1+\beta}\right)} \equiv P \left\{ \frac{V}{(r_c + r_b)} \right\}^m r_c^{\,n} \cdot \frac{r_b}{r_b + r_c} \tag{E8.59}$$

$$= P \frac{V^m r_c^{\,n-m}}{(r_c + r_b)^m \, r_c^{-m}} \cdot \frac{r_b}{r_b + r_c}$$

$$= P \frac{V^m r_c^{\,n-m}}{(1 + \frac{1}{\beta})^m (1+\beta)}$$

$$\mathcal{E}_c = \frac{V^m r_c^{\,n} \beta^m}{r_c^{\,m} (1+\beta)^{m+1}} \left\{ 1 + \frac{\gamma + J\delta}{1+\beta} \right\}^{-1} \tag{E8.60}$$

$$\text{and } \mathcal{E}_b = \frac{Q V r_c}{(1+\beta)^2} \left\{ 1 + \frac{\gamma + J\delta}{1+\beta} \right\}^{-1} \tag{E8.61}$$

$$\text{and if } \mathcal{E} = (|\mathcal{E}_b|^2 + |\mathcal{E}_c|^2)^{\frac{1}{2}} \tag{E8.41}$$

If m = 1, then

$$\mathcal{E}_c = \frac{P V r_c^{\,n} \beta}{r_c (1+\beta)^2} \left\{ 1 + \frac{\gamma + J\delta}{1+\beta} \right\}^{-1} \tag{E8.62}$$

$$\mathcal{E}_3 = (|\mathcal{E}_b|^2 + |\mathcal{E}_c|^2)^{\frac{1}{2}} = Q V r_c \frac{\beta}{(1+\beta)^2} \left\{ 1 + \frac{2\gamma}{1+\beta} + \frac{\gamma^2 + \delta^2}{(1+\beta)^2} \right\}^{-\frac{1}{2}} X$$

$$\left\{ \frac{1}{\beta^2} + \frac{P^2}{Q^2} \frac{r_c^{\,2n}}{r_c^{\,4}} \right\}^{\frac{1}{2}} \tag{E8.63}$$

At the time of these measurements, only one PbS detector was available, and so exhaustive tests on the detector noise function were not possible; however the bias voltage dependence of the signal and also of that component of the noise was established as plotted in figure F8.14. The voltage dependence in both cases is clearly linear, which would suggests that the bias resistor and detector noise functions are the same. The suggested appropriate noise function is therefore that given combining the preamplifier noise power, the Johnson noise power of E8.23 and of either current noise E8.44 or E8.47, but with the $(1 + \frac{1}{\beta})$ or $(1 + \frac{1}{\beta^2})^{\frac{1}{2}}$ replaced by $(\alpha + \frac{1}{\beta})$ or $(\alpha + \frac{1}{\beta^2})^{\frac{1}{2}}$ where α represents the excess noise of the PbS detector over its pure resistance equivalent. Then the noise functions agree well with that given in the literature (R8.03 equation 16), but in these expressions all the bias network noise sources have been included.

A8.07 Noise sources; summary of findings:

$$\varepsilon_0 = 0.063\,\mu\ \mathrm{V}/\sqrt{\mathrm{Hz}} \text{ at } 30\ \mathrm{Hz} \qquad \text{E8.64}$$

E8.23; $\varepsilon_1 = 1.28 \times 10^{-1}\, r_{/\!/}^{\frac{1}{2}}$, where $r_{/\!/} = \dfrac{r_b r_c}{r_b + r_c} = r_c\,(1 + \frac{1}{\beta})^{-1} = r_c\,\beta\,(1+\beta)^{-1}$

$\mu\ \mathrm{V}/\sqrt{\mathrm{Hz}}$

In general:

$$\varepsilon_1 = 1.28 \times 10^{-1}\, r_c^{\frac{1}{2}}\, \beta^{\frac{1}{2}}\, (1+\beta)^{-1}\, (1 + 2\gamma(1+\beta)^{-1} + (\gamma^2 + \delta^2)(1+\beta)^{-2})^{-1/4}$$

$\mu\mathrm{V}/\sqrt{\mathrm{Hz}}$

(r_c in MΩ) E8.65

From F8.15 and E8.44 at 23°C and 30Hz:

$$\varepsilon_2 = 1.4 \times 10^{-2}\ \mathrm{V}\ r_c\beta\,(1+\beta)^{-2}(\alpha^2 + \beta^{-2})^{\frac{1}{2}}\, (1 + 2\gamma(1+\beta)^{-1} +$$

$$(\gamma^2 + \delta^2)\,(1+\beta)^{-2})^{-\frac{1}{2}} \qquad \text{E8.66}$$

and $$|\varepsilon|^2 = |\varepsilon_0|^2 + |\varepsilon_1|^2 + |\varepsilon_2|^2 \qquad \text{E8.67}$$

where: $\alpha \equiv \dfrac{\text{equivalent noise resistance}}{\text{resistance}}$

$$\beta \equiv \frac{r_c}{r_b}$$

$$\gamma \equiv \frac{r_c}{r_g}$$

$$\delta \equiv r_c\, c_c$$

or from E8.63,

$$\mathcal{E}_2 = 1.4 \times 10^{-2}\, V\, r_c\, \beta\, (1+\beta)^{-2}(1 + 2\gamma(1+\beta^{-1}) + (\gamma^2 + \delta^2)\,(1+\beta)^{-2})^{-\frac{1}{2}} \times$$

$$(P\, r_c^{\,2n-4} + \beta^{-2})^{\frac{1}{2}} \qquad \text{E8.68}$$

From E8.15: Signal $\Delta e = K\, r_c\, V\, \beta\, (1+\beta)^{-2}\, (1 + 2\gamma(1+\beta)^{-1} + (\gamma^2 + \delta^2)\,(1+\beta)^{-2})^{-\frac{1}{2}}$

.... E8.69

Let $$\underline{\underline{\rho \equiv \beta\,(1+\beta)^{-2}\,(1 + 2\gamma(1+\beta)^{-1} + (\gamma^2+\delta^2)\,(1+\beta)^{-2})^{-\frac{1}{2}}}} \qquad \text{E8.70}$$

The signal/noise ratio at room temperature may then be expressed:

$$\Delta e/\mathcal{E} = K\, r_c V \rho \Big/ \left\{ \mathcal{E}_o^{\,2} + 1.28^2 \times 10^{-2} r_c + k_{Tf}^2 1.4^2 \times 10^{-4} V^2 r_c \rho^2 (\alpha^2 + \beta^{-2}) \right.^{\frac{1}{2}}$$

.... E8.71

at room temperature, 22°C, $k_{Tf} = 1$

For other temperatures, r_c will take up different values:

$$\frac{r_T}{r_{295}} \sim e^{-T/295}$$

and the constant in the Johnson noise term will become $1.28^2 \times 10^{-2} \times \frac{T}{295}$

k_{Tf} is a constant, dependent on temperature and frequency, and at $T = 200^{o}K$ observed to be $\simeq$ 0.141 for the detector used; it contains a $\frac{1}{f}$ component. $\mathcal{E}_{oT}$ may reduce in value on cooling.

Then:

$$\frac{\Delta e}{\mathcal{E}} = K\ r_c V \rho \Big/ \left\{ \mathcal{E}_{oT}^{\ 2} + 1.28^2 \times 10^{-2}\ r_c \rho\ \frac{T}{295} + k_{Tf}^{\ 2} \times 1.4^2 \times 10^{-4} \times V^2 r_c^{\ 2} \rho^2 (\alpha^2 + \beta^{-2}) \right\}^{\frac{1}{2}} \qquad \text{E8.72}$$

where $k_{Tf} = k\ (T,\ f)$

and $\alpha = \alpha(f)$, where there is a constant and a $\frac{1}{f}$ frequency component.

A8.08 Voltage dependence of signal/noise

Let us consider the voltage dependence of function. E8.70

Then

$$\frac{\Delta e}{\mathcal{E}} = \frac{V K\ r_c \rho / (\mathcal{E}_o^{\ 2} + 1.28^2 \times 10^{-2}\ r_c \rho \frac{T}{295})^{\frac{1}{2}}}{\left\{ 1 + \dfrac{V^2 k_{Tf}^2 1.4^2 \times 10^{-4} r_c^{\ 2} \rho^2 (\alpha^2 + \beta^{-2})}{\mathcal{E}_o^{\ 2} + 1.28^2 \times 10^{-2}\ r_c \rho \frac{T}{295}} \right\}}$$

$$= \frac{A\ \dfrac{V}{V_1}}{\sqrt{1 + \dfrac{V^2}{V_1^{\ 2}}}}$$ where A, and V_1 are fixed parameters. E8.73

This function is plotted in figure F8.15 (see main text chapter 8), and shows good agreement with the observed curve F8.14

The limit as $V \rightarrow \infty$, of $\frac{\Delta e}{\mathcal{E}}$ is $K\ /k_{Tf} \times 1.4 \times 10^{-2}(\alpha^2 + \beta^{-2}) = A$

and is dependent of ρ, but a large ρ will tend to reduce the rate at which this limit value is approached.

A8.09 The voltage required to increase the zero bias volts noise by m.

Now from E8..72

$$\mathcal{E}_{oT}^{\ 2} + 1.28^2 \times 10^{-2} \frac{T}{295} r_c + k_{Tf}^2 1.4^2 \times 10^{-4} V_m^{\ 2} (\alpha^2 + \beta^{-2})\ r_c^{\ 2\ \ 2}$$

$$= m^2 \left\{ \mathcal{E}_{oT}^{\ 2} + \frac{1.28^2 \times 10^{-2}\ Tr_c\rho}{295} \right\}^{\frac{1}{2}}$$

$$\Rightarrow \quad V_m = \frac{\left\{ \frac{\mathcal{E}_{oT}^{\ 2}}{r_c^{\ 2} \rho^2} + \frac{1.28^2 \times 10^{-2} T}{r_c \rho\, 295} \right\}^{\frac{1}{2}} \quad \left\{ m^2 - 1 \right\}^{\frac{1}{2}}}{k_{Tf} 1.4 \times 10^{-2} (\alpha^2 + \beta^{-2})^{\frac{1}{2}}} \qquad \text{E8.74}$$

When $\gamma = \delta = 0$ and $\alpha = 1$, then $\rho = \frac{\beta}{(1+\beta)^2}$

and $(\alpha^2 + \frac{1}{\beta^2})^{\frac{1}{2}} = (\frac{1+\beta^2}{\beta^2})^{\frac{1}{2}}$

$$\text{Then } V_m = \frac{(m^2 - 1)^{\frac{1}{2}}}{k_{Tf}1.4 \times 10^{-2}} \left\{ \frac{\mathcal{E}_o T^2}{r_c^2} \frac{(1+\beta)^4}{\beta \ (1+\beta^2)^{\frac{1}{2}}} + \frac{1.28^2 \times 10^{-2} T(1+\beta)^2}{295\, r_c \, (1+\beta^2)^{\frac{1}{2}}} \right\}$$

$$= \frac{1.28^2}{k1.4} \ \frac{T}{295} \ \frac{1}{r_c} \ (m^2 - 1)^{\frac{1}{2}} \left\{ \frac{\mathcal{E}_o T^2}{r_c} \frac{295 \qquad (1+\beta)^4}{T \times 1.28^2 \times 10^{-2} \ \beta(1+\beta^2)^{\frac{1}{2}}} + \frac{(1+\beta)^2}{(1+\beta^2)^{\frac{1}{2}}} \right\} \qquad \text{E8.75}$$

$$\cong g \ \frac{(m^2 - 1)^{\frac{1}{2}}}{r_c} \ \frac{(1+\beta)^2}{(1+\beta^2)^{\frac{1}{2}}} \left\{ \frac{g_2}{r_c} \ \frac{(1+\beta)^2}{\beta} + 1 \right\} \qquad \text{E8.76}$$

as $\beta \to \infty$, $V_m \to g_1 \dfrac{(m^2 - 1)^{1/2}}{r_c^2} \ g_2 \ \beta^2$

and as $\beta \to o$, $V_m \quad g_1 \dfrac{(m^2 - 1)^{1/2}}{r_c^2} \ g_2 \ \dfrac{1}{\beta}$

when $\beta = 1$, $V_m = \dfrac{g_1 \ 4(m^2 - 1)^{1/2}}{r_c} \ \dfrac{.4}{\sqrt{2}} \left\{ \dfrac{g_2}{r_c} \times 4 + 1 \right\}$

The representative curves:

$$\frac{\sqrt{2}}{8} \left\{ \frac{1}{4} \ \frac{(1+\beta)^2}{\beta} + 1 \right\} \frac{(1+\beta)^2}{(1+\beta^2)^{\frac{1}{2}}}$$

$$\text{and} \quad \frac{\sqrt{20}}{80} \left\{ \frac{1}{40} \quad \frac{(1+\beta)^2}{\beta} + 1 \right\} \frac{(1+\beta)^2}{(1+\beta^2)^{\frac{1}{2}}}$$

are plotted in figure F8.16 (see main text chapter 8) and can be compared with observed data for two biased PbS detectors, in figure F8.17. Comparison of the observed and theoretical curves shows their similarity.

A8.10 The dependence on β of the signal to noise function

Consider the limit of equation E8.71

$$\left(\frac{\Delta e}{\varepsilon}\right)_{V \to \infty} = K \quad /k_{\tau f} 1.4 \text{ x } 10^{-2} (\alpha^2 + \beta^{-2}) = \frac{K}{k_{\tau f} 1.4 \text{ x } 10^{-2}} \text{ x } \frac{\beta}{(1+\alpha^2\beta^2)^{\frac{1}{2}}} \qquad \text{E8.77}$$

or for a general case:

$$\left(\frac{\Delta e}{\varepsilon}\right)_{v = V_m} = \frac{K}{k_{\tau f} i.4 \text{ x } 10^{-2}} \quad \frac{(m^2 - 1)^{\frac{1}{2}}}{m} \quad \frac{\beta}{(1+\alpha^2\beta^2)^{\frac{1}{2}}} \qquad \text{E8.78}$$

when $\alpha = 1$, then:

$$\left(\frac{\Delta e}{\varepsilon}\right)_{v = V_m} = \frac{K}{k_{\tau f} 1.4 \text{ x } 10^{-2}} \quad \frac{(m^2 - 1)^{\frac{1}{2}}}{m} \quad \frac{\beta}{(1+\beta^2)^{\frac{1}{2}}} \qquad \text{E8.79}$$

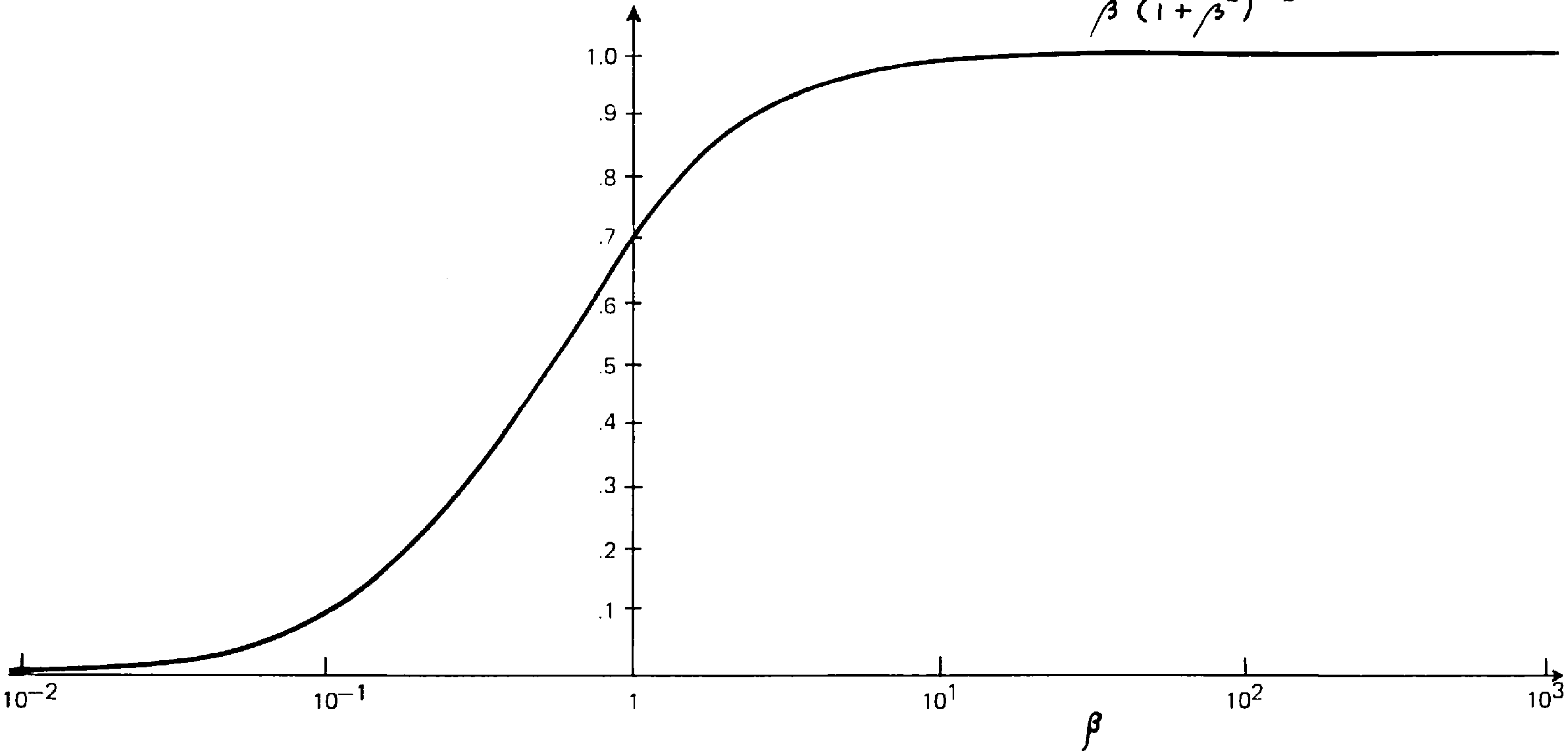

F.8.18 THE ASYMPTOTIC LIMIT FUNCTION $\beta(1+\beta^2)^{-1/2}$

The function $\frac{\beta}{(1+\beta^2)^{\frac{1}{2}}}$ is plotted in figure F8.18

Note that at $\beta = 1$, the asymptotic function (F8.18) takes the value $\frac{1}{\sqrt{2}}$ as to be expected for the sum of two equal noise sources (detector + bias resistors).

In practice for large β and constant V, then $\mathcal{E}_0$ (preamplifier noise) is not insignificant and produces a departure of the signal-to-noise function from that of the curve F8.18. The function of β for a practical constant bias voltage V = 100v is plotted in figure F8.19, and is discussed and compared with the measured behaviour of two biased detectors. The expression E8.70, E8.72 agrees with that given by Humphrey (R8.03 equation 22) where the preamplifier noise and the bias network noise have been included, and the detector is not background radiation noise limited.

A reference list is given at the end of the main text for chapter 8.